Université Sorbonne
Paris Cité

université PARIS DIDEROT PARIS 7

THÈSE DE DOCTORAT

DE L'UNIVERSITÉ SORBONNE PARIS CITÉ

PRÉPARÉE À L'UNIVERSITÉ PARIS DIDEROT

LABORATOIRE MATÉRIAUX ET PHÉNOMÈNES QUANTIQUES

Ecole doctorale n° 564: physique en Ile de France

Gallium Arsenide optomechanical disks approaching the quantum regime

Par William HEASE

Thèse de doctorat de Physique

Dirigée par Ivan FAVERO

Présentée et soutenue publiquement à Paris le 25 / 11 / 2016 devant la commission d'examen composée de:

Mme.	Isabelle SAGNES,	Présidente du jury
M.	Sébastien HENTZ,	Rapporteur
M.	Xavier CHECOURY,	Rapporteur
M.	Bahram DJAFARI-ROUHANI,	Examinateur
M.	Brahim LOUNIS,	Examinateur
M.	Samuel DELÉGLISE,	Examinateur
M.	Christophe VOISIN,	Examinateur
M.	Ivan FAVERO,	Directeur de thèse

Remerciements

La modeste contribution à l'avancée des connaissances scientifiques que représente cette thèse n'aurait pu se faire sans l'aide des autres. Si ces quatre années passées au laboratoire MPQ de l'université Paris Diderot on constitué une expérience si enrichissante pour moi, c'est avant tout grâce à l'excellente ambiance de travail qui y règne, et à la qualité des interactions entre collègues.

Je tiens tout d'abord à remercier mon directeur de thèse, Ivan Favero. Sa grande culture scientifique, sa rigueur et sa droiture ont certainement contribué à rendre ma tâche plus facile. Je le remercie aussi pour sa relecture très rigoureuse de mon mémoire. Merci au chef d'équipe, Giuseppe Leo, qui a toujours montré de l'intérêt pour ma recherche. Merci aussi à Sara Ducci pour son enthousiasme et sa bonne humeur.

Je tiens à remercier très chaleureusement les collègues doctorants et post-doctorants qui m'ont accompagné pendant ce travail de thèse. Merci tout d'abord aux « opto-mécaniciens » : merci à Chris, pour sa motivation à toute épreuve et son sens de l'humour indéfectible, à Trung, pour m'avoir transmis la rigueur indispensable à la micro-fabrication, à David pour son franc parler et pour avoir cru au feedback optomécanique. Merci à Biswarup, pour sa patience et sa bonne humeur quotidienne, à Pierre pour sa créativité et nos débats passionnés, et enfin à Mehdi pour son pragmatisme et son efficacité. Merci à Eduardo pour ces quatre années d'opto-mécanique en parallèle et pour son extraordinaire potentiel comique. Merci à Evelio pour son cubanisme communicatif, à Lucien pour son décalage permanent, et à Samantha pour son enthousiasme, sa curiosité et sa motivation. Je tiens aussi à remercier les collègues qui ont travaillé dans un autre domaine. Merci à Silvia et Cécile, pour leur caractère bien trempé, merci à Claire et Guillaume, nos deux amoureux du labo, merci à Fabien et Andreas pour nos geekeries. Merci à Alessio pour son aide précieuse en informatique. Merci à Alice pour nos discussions vidéoludiques (surtout pour m'avoir fait réaliser que je termine des jeux entiers sans rien comprendre à la trame narrative), à Valerio pour les charmantes expressions qu'il m'a apprises en Italien, à Natália pour nos discussions philosophiques. Merci aussi à Chérif, Giorgio, Jonathan, Oleksandr, Alok, Daniele, Zara, Allegra, et aux autres.

J'aimerais remercier tout particulièrement les ingénieurs salle blanche, qui ont été d'une aide très précieuse tout au long de ma thèse. La fabrication ayant constitué une part importante de ma thèse, on peut imaginer le rôle crucial qu'ils ont joué dans l'avancée de mon travail. Merci donc à Pascal, pour son sens de l'humour qui tombe toujours à pic, à Christophe pour son aide précieuse en chimie, et à Stéphane pour sa disponibilité et sa gentillesse.

Merci aux personnels des ateliers de mécanique et d'électronique qui m'ont apporté leur savoir-faire et leur expérience. Merci à Patrick et à Martial pour leur efficacité et leur gentillesse, ainsi qu'à Marc pour son enthousiasme.

Merci à Jocelyne, Joëlle et Sandrine du service comptabilité pour les bonnes rigolades, et merci à Anne pour m'avoir inculqué ce bon principe : « ce qui est fait n'est plus à faire ». Merci à Carlo, directeur du laboratoire, pour son dynamisme. Merci aussi à Joëlle Taieb et à Sylvie Hénon.

Je tiens enfin à remercier mes proches, sans qui cette petite aventure n'aurait pas été possible. Merci à mes frères pour avoir fait semblant de s'intéresser à ma thèse, à mes grands parents pour m'avoir donné le goût de la science, ainsi qu'à mes parents pour leur amour et leur soutien infaillible.

Résumé

Le but de cette thèse est d'atteindre l'état de mouvement fondamental sur des disques optomécaniques en arseniure de gallium. La mécanique quantique prévoit en effet que la quantité d'énergie d'un système physique (mécanique ou autre) ne peut jamais être réduite totalement à zéro. Il existe cependant un état de plus basse énergie, que l'on appelle l'état fondamental.

L'effet physique utilisé pendant cette thèse pour extraire de l'énergie du système (et ainsi atteindre l'état fondamental) est le *couplage opto-mécanique*. Les micro-disques supportent des résonances optiques à symétrie axiale appelées *modes de galerie* ainsi que des résonances mécaniques appelées *modes de respiration*. Le couplage entre ces deux modes peut être intuitivement compris comme suit : lorsque le disque « respire » mécaniquement, la circonférence du disque ressentie par le mode optique change, ce qui induit un décalage de sa longueur d'onde de résonance. À l'inverse, le mode optique exerce une *pression de radiation* sur les parois du disque, qui peut amplifier ou atténuer le mouvement mécanique.

Le refroidissement opto-mécanique est d'autant plus efficace que les résonances (optique comme mécanique) ont de faibles taux de dissipation. Une grande partie de ce travail de thèse à donc été dédiée à la réduction de ces pertes. Des efforts technologiques ont permis d'obtenir des structures lisses et régulières, pour éviter la diffusion (et donc la dissipation) de lumière par rugosités. Afin de réduire la dissipation mécanique, une structure novatrice incluant des boucliers mécaniques à été développée, et à permis de réduire la dissipation mécanique d'un facteur 100.

L'état du système après refroidissement opto-mécanique dépend par ailleurs de sa température initiale. Il est donc avantageux de placer l'échantillon dans un cryostat. L'appareil utilisé au cours de cette thèse permet de refroidir l'échantillon jusqu'à une température de 2,6 K. Les expériences de photonique en environnement cryogénique imposant des contraintes en terme de stabilité, il a été nécessaire de d'opter pour une approche avec guide d'onde intégré. Le développement de guides d'ondes entièrement suspendus (voir chapitre 4) a permis d'apporter et de collecter la lumière depuis le disque de manière optimale.

Toutes ces efforts ont permis de descendre à un taux d'occupation mécanique de 30 quanta. Cependant de nombreuses améliorations peuvent encore être implémentées, afin d'ancrer ces résonateurs fermement dans l'état fondamental, ce qui permettrait d'effectuer par exemple des expériences d'intrication quantique.

Abstract

The main goal of this PhD work has been to reach the quantum ground state on gallium arsenide optomechanical disks. Quantum mechanics predict that the amount of energy within a given system cannot be brought to zero. Nevertheless a state of minimal energy exists, called the ground state.

The physical mechanism used to extract energy from the system (and thus reach the ground state) is the *optomechanical coupling*. The miniature ($\mu m - $ sized) disks support optical and mechanical resonances, respectively called *whispering gallery modes* and *radial breathing modes*. The coupling between these two modes can be intuited as follows: when the disk *breathes* mechanically, its perimeter increases. The optical mode evolves now in a wider cavity, and its resonance wavelength therefore changes. Conversely, the optical mode exerts radiation pressure on the disk boundaries, which can either amplify or damp the mechanical motion.

Optomechanical cooling is more efficient if the dissipation rates of the optical and mechanical resonances are low. An important part of this PhD work has therefore been dedicated to the reduction of dissipation. Technological efforts have been made to fabricate smooth and regular structures, so as to limit optical scattering. A novel approach consisting of a mechanical shield has allowed to reduce mechanical damping by a factor of 100.

The system state after optomechanical cooling depends on its initial temperature. It is therefore advantageous to place the system in cryogenic environment prior to starting the optomechanical cooling. The apparatus used throughout this PhD work can cool the optomechanical device down to 2.6 K. As optical experiments in cryogenic environment require a good mechanical stability, it is necessary to opt for fully integrated devices where the optomechanical resonator and the waveguide bringing the light to it are processed on the same chip. The development of fully suspended waveguides (see chapter 4) has moreover allowed to inject and collect light from the device more efficiently.

All these improvements have allowed to reach a state of 30 excitation quanta in the mechanical resonator. However many ideas can still be tried to keep enhancing the devices, so as to anchor them more firmly in the ground state. This would open the way to more advanced experiments, such as entanglement of mechanical oscillators.

Contents

Introduction **8**

1 Optomechanics : conceptual tools **12**
1.1 Optomechanics models . . . 12
1.1.1 Generic optomechanical system . . . 12
1.1.2 Mechanical spectrum optical readout . . . 13
1.1.3 Delayed force model . . . 14
1.1.4 Coupled dynamical equations for optomechanics . . . 16
1.1.5 Quantum model . . . 18
1.2 Optical forces on miniature mechanical devices . . . 23
1.2.1 Radiation pressure . . . 23
1.2.2 Electrostriction . . . 24
1.2.3 Photothermal forces . . . 25
1.3 Optomechanical coupling constants . . . 26
1.3.1 Reduction point r_0 and vacuum coupling g_0 . . . 26
1.3.2 Geometric and photoelastic g_{om} . . . 27
1.3.3 Thermo-optic effect . . . 28

2 Gallium arsenide optomechanical disks **29**
2.1 Optical modes of GaAs disks . . . 29
2.1.1 Whispering gallery modes . . . 29
2.1.2 Bending losses . . . 31
2.1.3 Scattering losses . . . 32
2.1.4 Absorption losses . . . 33
2.1.5 Thermooptic triangular envelope . . . 36
2.2 Mechanical modes of GaAs disks . . . 36
2.2.1 Modes of thin disks: analytic approach . . . 36
2.2.2 Numerical simulations of disk mechanical modes . . . 37
2.2.3 Mechanical losses in GaAs disks . . . 39
2.3 Optomechanical coupling in GaAs disks . . . 42
2.3.1 2D-axisymmetric g_0 calculations . . . 42
2.3.2 3D g_0 calculations . . . 43
2.3.3 Photothermal forces . . . 44

3 Design of "on chip" coupling to GaAs disks **46**
3.1 Coupled mode theory . . . 47
3.2 Straight and bent waveguides . . . 49
3.2.1 gallium arsenide (GaAs) waveguide design . . . 50
3.2.2 Bent waveguides . . . 51
3.2.3 Coupling simulations . . . 52
3.3 Global waveguide design . . . 53

3.3.1 Long waveguides devices . . . 53
3.3.2 Fully suspended waveguide devices . . . 55

4 Device fabrication **59**
4.1 Fabrication steps of long waveguide devices . . . 59
4.1.1 Epitaxial structure . . . 59
4.1.2 Definition of the resist mask . . . 61
4.1.3 ICP anisotropic etch . . . 63
4.1.4 Hydrofluoric acid under-etching . . . 65
4.1.5 E-beam resist removal . . . 66
4.2 Fully suspended waveguide devices . . . 67
4.2.1 General idea . . . 67
4.2.2 Photosensitive resist mask definition for the mesa . . . 68
4.2.3 Mesa etching . . . 70
4.3 Mechanically shielded devices . . . 74
4.3.1 Change in the e-beam resist thickness. . . . 74
4.3.2 ICP optimization . . . 75
4.3.3 Pedestal under-etch control . . . 77
4.3.4 Stiction problems . . . 80
4.3.5 E-beam resist removal (bis) . . . 83

5 Experimental setup **85**
5.1 The setup in general . . . 85
5.2 Cryostats . . . 85
5.2.1 Janis ST-300 cryostat . . . 86
5.2.2 Attocube cryostat . . . 88
5.3 Laser sources . . . 90
5.3.1 External cavity diode lasers . . . 90
5.3.2 Titanium sapphire laser . . . 91
5.3.3 Laser noise . . . 93
5.4 Amplification and detection . . . 94
5.4.1 Transduced signal and fluctuation-dissipation theorem . . . 94
5.4.2 Electronic spectrum analyzer . . . 96
5.4.3 Amplifiers . . . 96
5.5 Electro-optic modulators . . . 98

6 Mechanically shielded disk resonators **99**
6.1 Clamping losses of disk resonators . . . 99
6.1.1 Analytic formula . . . 99
6.1.2 Experimental measurements . . . 100
6.1.3 Acoustic Bragg reflectors . . . 101
6.2 Disks with mechanical shields . . . 102
6.2.1 Principle . . . 102
6.2.2 Numerical simulations . . . 103
6.2.3 Optimization with the genetic algorithm . . . 105
6.3 Realization of MS devices . . . 108
6.3.1 First generation of MS devices . . . 108
6.3.2 Compact MS structure (2^{nd} generation) . . . 108
6.3.3 Sub micrometer radius shielded disks . . . 111

7 Optomechanical measurements in cryogenic environment **113**
7.1 Brownian motion measurement at 3 K . . . 113
7.2 Intra-cavity power limitations . . . 114
7.2.1 Power limitation induced by TPA . . . 114
7.2.2 Power limitation induced by thermo-optic instability . . . 116
7.3 Mechanical mode thermalization . . . 118
7.4 Optomechanical cooling experiment . . . 119
7.4.1 Results . . . 119
7.4.2 Perspectives . . . 122
7.5 Optomechanically induced transparency . . . 122
7.5.1 Principle . . . 122
7.5.2 Experimental setup . . . 124
7.5.3 Experimental results . . . 126

Conclusion **129**

Glossary **131**

Bibliography **134**

Appendix **139**

A Electrostriction: derivation of the striction pressure **140**

B Brief presentation of the Finite Element method **141**

C Perfectly Matched Layers **143**

D Stabilization of the thermo-optic instability **145**

E Derivation of OMIT transmission expressions **147**

Introduction

Electromagnetic radiation carries momentum, which can be transferred to matter upon interaction with it. Johannes Kepler had supposed the existence of this momentum in the 17^{th} century, to explain the fact that comets tails were systematically deviated away from the sun. However the first experimental demonstrations of radiation pressure were not realized until the early 20^{th} century [1]. This demonstration was relying on the use of a *light mill* apparatus (see figure 1), and careful measurements had to be performed in order to de-correlate radiation pressure from thermal effects.

Figure 1 – Crooke's light mill. The vanes rotate on a low friction spindle and vacuum is made in the glass bulb. The vanes are black on one side, and mirror coated on the other. If light is shone on the apparatus from one direction, photons impinging on the black side of a vane will be absorbed, resulting on a momentum transfer of $\hbar k$ per photon (k is the wavenumber of the photon), while those impinging on a mirror coated side will be reflected, resulting in a momentum transfer $2\hbar k$. This net difference is in theory accountable for the rotation of the vanes. In first experiments though, the vanes were rotating in the wrong direction, because of thermal effects. Crookes invented this radiometer in 1873 but one had to wait 1901 to see an experimental demonstration of radiation pressure with such a device.

The field of optomechanics is dedicated to the study of the interaction between electromagnetic and mechanical degrees of freedom in physical systems. Radiation pressure plays a important role in this interaction, but we will see that other forces are also at play. Modern optomechanics initiated in the late 1960s with the works of Braginsky [2] in the context of sensitive interferometers. Braginsky showed that the retarded optical force leads to damping (or amplification) of the mechanical motion. The field rapidly expanded in the last decade thanks to a series of technical advances in micro-fabrication, optical coatings, lasers, and microwave techniques. Optomechanics bear close implications in:

- Gravitational interferometry. Very high sensitivity interferometers require to control the degree of interaction between light and mirrors forming the limits of the interferometer itself.

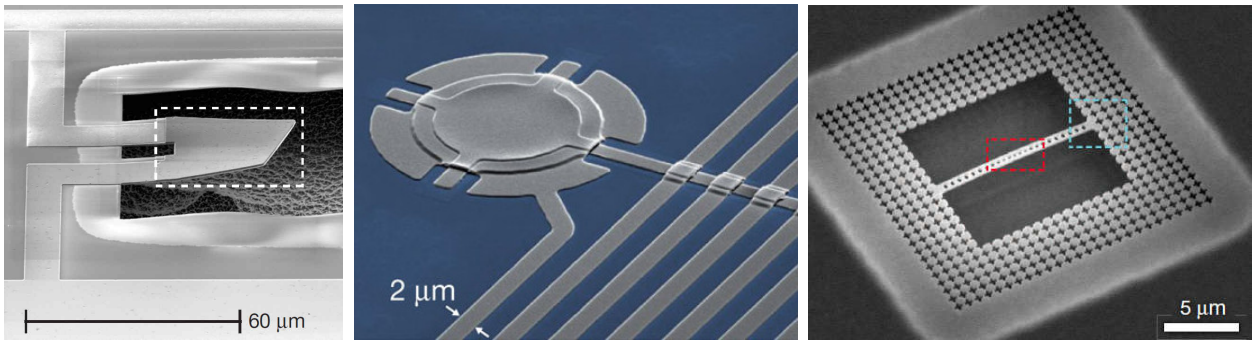

Figure 2 – Pioneering systems that prepared a mechanical mode in its ground state of motion. **Left:** AlN membrane sandwiched between two Al sheets that was used for pioneering mechanical ground state experiments [5]. Upon vibration, piezoelectric AlN changes the potential between the two aluminum sheets, potential then measured via a superconducting qubit. **Center:** detail of the superconducting microwave LC circuit used for the first experimental demonstration of optomechanical cooling to the quantum ground state [6]. The mechanical system is a thin (100 nm tick) aluminum membrane stretched 50 nm above the substrate, like a drum skin. When the membrane oscillates the gap distance to the substrate changes, which modifies the capacitance of the ensemble. The resonance frequency of the whole LC circuit is therefore modified. **Right:** optocmechanical nanobeam used in another demonstration of optomechanical ground state cooling [7]. The optical mode is localized in the red dashed region by the means of a photonic crystal structure. The same region also undergoes mechanical motion. The periodic structure surrounding the nano-beam acts as a pho**n**onic bangap which enhances the quality factor of the nanobeam mechanical mode.

Works by Braginsky and Caves [3, 4] established the fundamental limit on the optical position readout of a mass in motion.

- Quantum information. Optomechanical systems could be used for the realization of quantum transducers from optical to radio frequency photons. Optomechanical cooling also allowed to prepare systems in their quantum ground state of mechanical motion [5, 6, 7], which opens the gates to the realm of quantum manipulation of mechanical objects.

- Detection of small forces and masses. The development of micrometer scale optomechanical systems allows the detection of femtogram range masses that adsorb on the optomechanical system [8, 9]. Detection of small forces is also feasible, be it in the context of AFMs [10] or accelerometers [11].

This doctoral work is focused on the realization of an optomechanical system optimized for quantum ground state cooling. The idea is to make use of the optomechanical interaction in order to cool the system's mechanical oscillator from a rest state comprising many phonons, to its quantum ground state of motion (zero phonon, or more realistically less than one phonon). It has been known since Braginsky that the optomechanical interaction can lead to excitation or damping of a mechanical mode. More recent works [12, 13] developed a quantum theory of cavity optomechanics ground state cooling, which shows that ground state cooling is achievable, if some conditions are fulfilled.

However, experimental preparation of a mechanical system in its ground state was first achieved without resort to optomechanics [5]: a 6 GHz mechanical mode of a piezoelectric device (left panel of figure 2) was cooled, using a dilution cryostat, to a very cold temperature T_{bath} verifying $k_B T_{\mathrm{bath}} < \hbar\Omega_{\mathrm{m}}$ (with Ω_{m} the mechanical frequency), and measured by a Josephson phase qubit. One year later, first experimental realization of optomechanical cooling in the quantum ground state was achieved using on an aluminum membrane oscillating at 10 MHz, coupled to a superconducting microwave circuit [6] (see center panel of figure 2). The same year another demonstration of optomechanical ground state cooling was performed [7], this time exploiting mechanical and optical modes of a silicon nanobeam, respectively at 3.5 GHz and 1550 nm (figure 2 right panel).

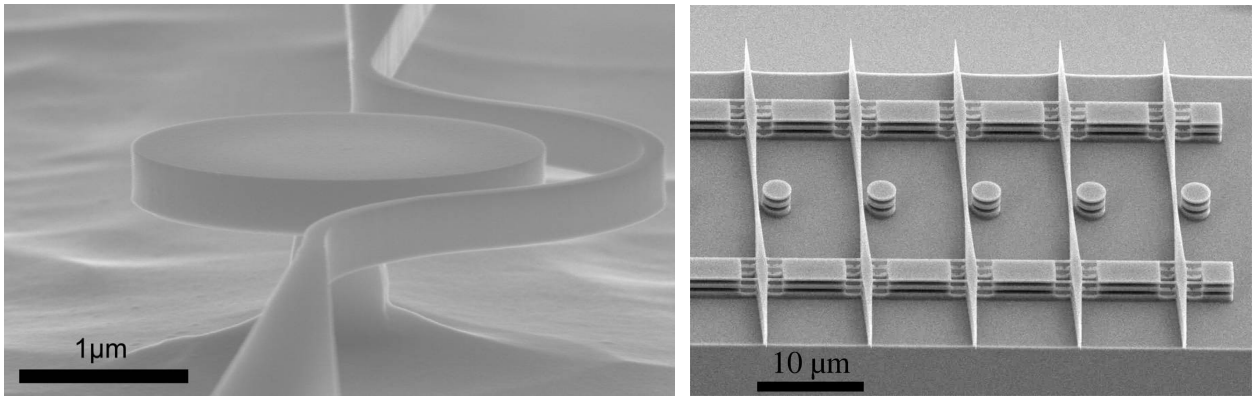

Figure 3 – scanning electron microscope (SEM) micrographs of systems used in our group for optomechanical cooling experiments. **Left:** close-up on a optomechanical disk resonator. The bended waveguide passing in the disk's vicinity can be seen. **Right:** section of a sample with several disk resonators and coupling waveguides.

The optomechanical systems used in our team are are GaAs miniature disks. They support optical modes in the near infrared (∼1550 nm) and mechanical modes in the few GHz range. They have their own specificities:

- the geometry: because of their disk shape, they support optical and mechanical modes that have an azimuthal symmetry.
- the material: the miniature disks are made of GaAs, a semiconductor belonging to the III-V family, which exhibits strong photoelastic effects, which is advantageous for photon-phonon interaction. In contrast to silicon, GaAs has a direct bandgap structure, which allows radiative recombination of electron-hole pairs. Interfacing of GaAs with other alloys (AlGaAs, InGaAs) allows the realization of quantum wells (or dots) which opens the possibility of interfacing optomechanics with optoelectronics.

GaAs miniature disks are *a priori* good candidates for optomechanical ground state cooling, because of their high mechanical frequency and high optical mode confinement. Efforts must however be developed in the fabrication process to raise optical and mechanical quality factors to a level as high as possible. The device fabrication developments in this perspective will represent a large part of this doctoral work.

Since the pioneering experiments in [6, 7], a wide variety of systems have been used to enforce or approach optomechanical ground state cooling [14, 15, 16, 17]. Figure 4 shows three of these systems. One similitude among all the systems presented in this introduction in the resort to micro (and nano) fabrication processes (even in ref [15] where microfabrication is outsourced to a commercial provider). Indeed, optomechanical cooling requires strong interaction between optical and mechanical degrees of freedom, which is better achieved by confining them in a small volume. Table 1 gathers the optomechanical parameters of most of the systems evoked through this introduction, as well as those of our GaAs miniature disks.

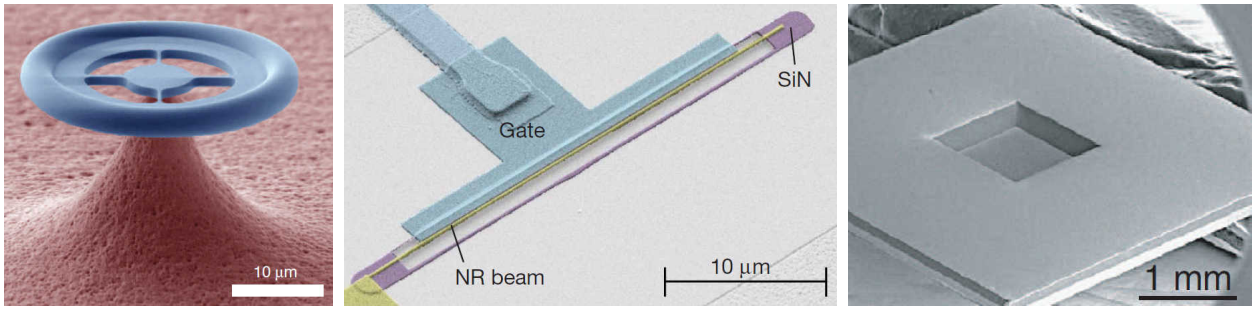

Figure 4 – Other systems that have approached the ground state of motion by optomechanical cooling. **Left:** silica micro-toroid resonator [14]. This system supports modes with azimuthal symmetry, like our GaAs disks. Very high optical quality factors in the 10^7 can be achieved, but mechanical quality factors are limited by intrinsic properties of silica. **Center:** Al/SiN beam resonator coupled to a superconducting microwave circuit [16]. The beam is 30 µm long and ∼150 µm thin, and has a mechanical quality factor of one million. **Right:** 50 nm thick SiN membrane. It has been inserted in the path of a millimeter sized optical Fabry-Pérot cavity [15], or in a 3D radio frequency cavity [17]. Phonon occupancy as low as $\bar{n}_{\mathrm{min}}$=0.2 was achieved in [15], which is the actual state of the art in continuous wave optomechanical cooling.

device	f_m (MHz)	Q_{opt}	$Q_{\mathrm{m}} \cdot f_{\mathrm{m}}$ (Hz)	$g_0/2\pi$ (MHz)	n_{cooled}
AlN slab [5]	6000	–	$1.5 \cdot 10^{12}$	–	0.07
Al "drum" membrane [6]	10	$3 \cdot 10^6$	$3.3 \cdot 10^{12}$	$2 \cdot 10^{-4}$	0.35
Si nanobeam [7]	3.6	$5 \cdot 10^5$	$3.6 \cdot 10^{14}$	0.91	0.8
Silica micro-toroid [14]	80	$2 \cdot 10^7$	$7.8 \cdot 10^{10}$	$3.4 \cdot 10^{-3}$	1.7
Al/SiN beam [16]	6	10^4	$6.3 \cdot 10^{12}$	–	3.8
SiN membrane [15]	1.5	$2 \cdot 10^8$	10^{13}	–	0.2
GaAs disks	100–5000	10^4–$5 \cdot 10^6$	$3 \cdot 10^{11}$–$6 \cdot 10^{13}$	0.05–2	–
One GaAs disk	1000	$3 \cdot 10^4$	$6 \cdot 10^{13}$	0.2	~ 20

Table 1 – Optomechanical parameters and phonon occupancy n_{cooled} obtained by optomechanical (OM) cooling for a variety of systems. The number of photons N_{cav} in the optical cavity (or microwave circuit) during cooling is not shown, although it impacts linearly the cooling power and can be several orders of magnitude higher in systems like [15] than is our GaAs disks. Q_{opt}: optical quality factor. Q_{m}: mechanical quality factor. f_{m}: mechanical frequency. $g_0/2\pi$: optomechanical coupling rate.

Outline of the thesis. **Chapter 1** is dedicated to the *canonical* theoretical framework of linear optomechanics. Two classical and a quantum model are presented. Optomechanical coupling phenomena are explained in a second part. **Chapter 2** presents GaAs miniature disks: the optical and mechanical modes are described, with an emphasis on loss phenomena. Techniques for quantitative optomechanical coupling computation in GaAs disks are shown. **Chapter 3** deals with the coupling of the optical modes of GaAs disks with an external waveguide bus, and focuses on developments carried in this domain. **Chapter 4** is dedicated to nano-fabrication. The tools and techniques used in the fabrication of our devices are described, as well as the developments carried during this doctoral work. **Chapter 5** presents the laboratory equipment and the techniques used for quantum optomechanical experiments and sample characterization. Performances of laser sources, cryostats, amplifiers, etc. are discussed. **Chapter 6** is focused on the fabrication of a new generation of devices incorporating a phononic shield for mechanical quality factor enhancement. The concept and experimental realizations will be treated. **Chapter 7** describes the optomechanical experiments realized with our GaAs miniature disk devices. Cooling results and present limitations are discussed.

Chapter 1

Optomechanics : conceptual tools

This first chapter will present the general framework of optomechanics. Several models with increasing level of sophistication will be presented, allowing for precise prediction of OM effects. In a second part the different phenomena by which light can exert a force on matter will be detailed. Finally in a third part several calculation schemes for OM coupling constants will be exposed.

1.1 Optomechanics models

In this section we re-develop standard optomechanics (OMs) models, and comment on their virtues and limitations. We discuss OM effects predicted by these models, and focus in particular on OM cooling. But let us first present a generic OM system.

1.1.1 Generic optomechanical system

In spite of the great diversity of OM systems that have been built in the last decade (materials used, sizes, geometries), a few parameters suffice in order to predict most OM effects. We will present these parameters in a generic OM system, which is simple to understand. The actual system we chose for our OMs experiments will be presented in the next chapter.

Figure 1.1 represents a generic OM system. It consists in a Fabry-Pérot optical cavity delimited by two mirrors. The left side mirror is partially reflecting (to allow for some light to enter the cavity). A monochromatic optical wave impinges on the system from the left, enters it and is reflected back and forth between the two mirrors. The field intensity can build up in the cavity only if a resonance condition is fulfilled. The set of wavelengths $\{\lambda_m\}$ satisfying the resonance condition is given by :

$$\exists m \in \mathbb{N} \mid 2L = \lambda_m m \tag{1.1}$$

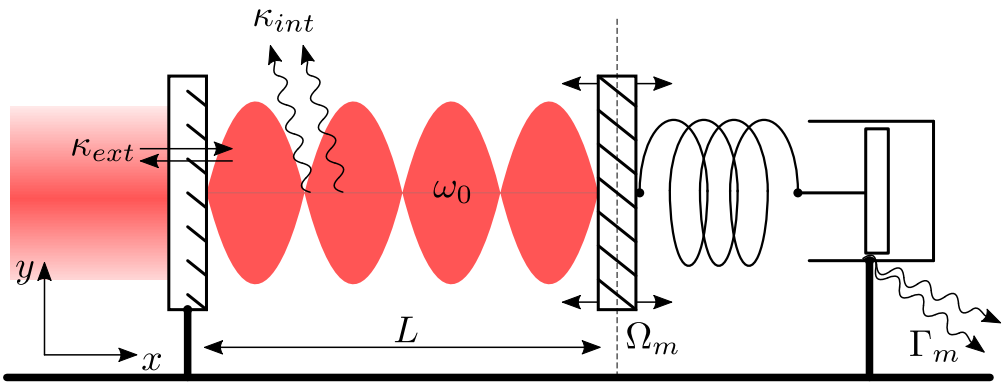

Figure 1.1 – Generic OM system.

where L is the optical cavity length, and λ is related to ω by : $\omega = \frac{2\pi c}{\lambda}$. The resonance condition takes a similar form in the disk OM systems we use as will be seen in chapter 2. The reflectance coefficient of the left-hand-side mirror is usually quite high, but not equal to 1, which implies an extrinsic loss rate κ_{ext}. It is defined such that the optical energy stored in a loss-less cavity decays as $e^{-\kappa_{\text{ext}}t}$ if the incident wave is shut off. The optical cavity mode also has an intrinsic loss rate, called κ_{int}, which corresponds to unwanted loss rates due to, e.g., linear and non-linear absorption in the cavity, scattering on the cavity edges, etc. κ_{ext} is a necessary loss channel, because it allows light to enter and leave the cavity so that measurements can be carried, whereas κ_{int} is in principle unwanted, as it corresponds to an "uncontrolled" loss of photons.

Let us now describe the mechanics of such a system. The left-hand-side mirror is rigidly clamped to the substrate, while the right-hand-side mirror can be translated along the x direction. Two elements link this moving mirror to the substrate : a spring, which makes the mirror oscillate left and right of its equilibrium position represented by the vertical dashed line, and a piston that induces mechanical losses. In the limit of small displacements the moving mirror's motion is that of a damped harmonic oscillator, with angular frequency Ω_{m} (determined by the spring stiffness and the mirror's mass) and damping rate Γ_{m}.

We now discuss how the optical and mechanical degrees of freedom interact. Let us assume that the moving mirror is in its equilibrium position and that the wavelength of the light sent in the cavity satisfies the resonance condition 1.1. When the mirror's position is shifted, the cavity length L is changed and does not satisfy the resonance condition anymore. The optical power circulating in the cavity therefore decreases. The radiation pressure force exerted on the mirrors decreases too, which induces a shift in the mirror's position. A bi-directional coupling thus exists between optical and mechanical degrees of freedom: the mechanics act on the optics which act on the mechanics... We parameterize this coupling with the *optomechanical frequency pull parameter* g_{om}, which quantifies the shift of the optical cavity's resonance angular frequency corresponding to a small change in the mirror's position ∂x, all other parameters being kept constant:

$$g_{\text{om}} = -\frac{\partial \omega_0}{\partial x} \tag{1.2}$$

The reader might notice that g_{om} only expresses the action of mechanics on the optics, the reverse action being apparently absent. We will see in section 1.3 that radiation pressure can actually be expressed as a function of g_{om}.

1.1.2 Mechanical spectrum optical readout

If the optical intensity impinging on the mirrors of the Fabry-Pérot cavity is low enough, the effect of radiation pressure on the mirrors motion can be neglected. However it is still possible to use the photons in order to read the moving mirror's motion properties. A monochromatic source is used to probe the optical cavity. The source's angular frequency ω_L is locked and slightly shifted from the optical cavity's resonance frequency ω_0 (see figure 1.2a). The cavity's resonance ω_0 is dithering around its central position because of the OM coupling with the disk's mechanical fluctuations. This results in a variation of the optical power reflected through the left hand side, partially transmitting mirror. In the disk/waveguide scheme used during this doctoral work, the waveguide transmission is actually the strict analog (see §3.1) of the Fabry-Pérot's reflection R. It can be deduced from figure 1.2a that the finesse of the Fabry-Pérot cavity has an impact on the readout sensitivity. Indeed, a higher finesse corresponds to Lorentzian modes of smaller width. The spectral slope (derivative) of the resonance flank is therefore steeper and the same ω_0 dithering will induce larger variations in the reflected power. The varying optical power is collected on a photo-diode that converts it into electric current. It is then possible to observe the time trace of the transmitted intensity (figure1.2b). Our OM system, which is mechanically coupled to the substrate at temperature T, undergoes a random, "Brownian" trajectory that makes the reflected power time-trace look erratic.

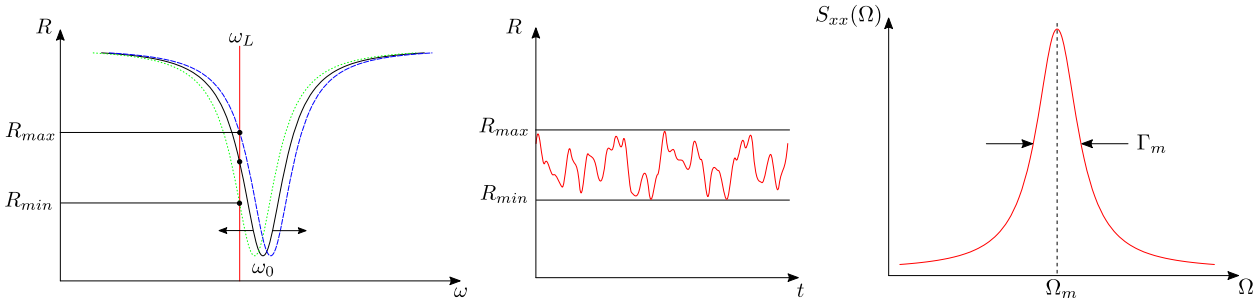

(a) Optical transduction (b) Time trace (c) Spectral power density

Figure 1.2 – Principle of OM motion readout.

Often in our experiments the photo-current delivered by the photo-diode is not observed in the time domain. It is sent in an electrical spectrum analyzer in order to directly obtain its power spectral density. The damping rate Γ_{m} of the mechanical mode of interest is the full width at half maximum (FWHM) of the resonance appearing in the power spectral density (see figure 1.2c).

1.1.3 Delayed force model

In this section and the two next, we present theoretical models of OM interactions. We start with the delayed force model. This model is the simplest, but it already grasps essential phenomena. Its shortcomings in terms of predictions will be dealt with by the following models.

The total loss rate of photons in the optical cavity is $\kappa = \kappa_{\mathrm{int}} + \kappa_{\mathrm{ext}}$, so that the average lifetime of a photon in the optical cavity is $\tau = 1/\kappa$. Let's assume that the moving mirror has been still for a long time such that the optical intensity within the cavity has reached a stationary regime under external laser pumping. Now we shift swiftly the position of the moving mirror. Although the new stationary optical intensity within the cavity will evolve, this change is not immediate. The characteristic response time τ is needed in order for the new stationary intensity to be established in the cavity. There is a time delay between a shift of the mirror's position and the resulting change in optical force acting on the mirror, hence the name "delayed force" (radiation pressure is proportional to the optical intensity within the cavity).

Let us call $F_{\mathrm{opt}}(x_0)$ the optical force corresponding to the mirror at position x_0. If the mirror "jumps" to a position x_1 at time t_1, the evolution of the optical force thereafter will be:

$$F'_{\mathrm{opt}}(t) = F_{\mathrm{opt}}(x_0) + h(t-t_1)[F_{\mathrm{opt}}(x_1) - F_{\mathrm{opt}}(x_0)] \tag{1.3}$$

where $h(t) = 1 - e^{-t/\tau}$ is a temporal response function, which in the simplest approximation can be taken as a decaying exponential. F'_{opt} is a function of time while F_{opt} depends on the position. The value of $F'_{opt}(t)$ tends to $F_{\mathrm{opt}}(x_1)$ for $t \gg \tau$. Now considering a series of N swift shifts from position x_{n-1} to x_n happening at times t_n :

$$F'_{\mathrm{opt}}(t) = F_{\mathrm{opt}}(x_0) + \sum_{n=1}^{N} [F_{\mathrm{opt}}(x_n) - F_{\mathrm{opt}}(x_{n-1})] h(t-t_n) \tag{1.4}$$

In this description, the mirror's motion can be seen as a continuous series of infinitesimal jumps, so that we can reformulate equation 1.4 as an integral [18]:

$$F_{\mathrm{opt}}(t) = F_{\mathrm{opt}}(x_0) + \int_{t_0}^{t} \frac{dF_{\mathrm{opt}}(x(t'))}{dt'} h(t-t')dt' \tag{1.5a}$$

$$= \int_{-\infty}^{t} \frac{dF_{\mathrm{opt}}(x(t'))}{dt'} h(t-t')dt' \quad \text{if} \quad (t-t_0) \gg \tau \tag{1.5b}$$

Now that we have an expression for the optical force acting on the system at time t, let us consider the mechanical equation of motion :

$$m\ddot{x}(t) + m\Gamma_{\rm m}\dot{x}(t) + Kx(t) = F_{\rm th}(t) + F_{\rm opt}(t) \tag{1.6}$$

where m is the system's mass, K is the spring's stiffness, $m\Gamma_{\rm m}\dot{x}(t)$ is the dissipative force, and $F_{\rm th}$ is the thermal Langevin force generating the Brownian motion. We wish now to solve equation 1.6 is Fourier domain. The time derivative of $F_{\rm opt}$ can be expressed as:

$$\frac{dF_{\rm opt}(x(t)')}{dt'} = \left.\frac{dF_{\rm opt}(x)}{dx}\right|_{\langle x\rangle} \frac{dx(t')}{dt'} = \nabla F_{\rm opt}\dot{x}(t) \tag{1.7}$$

with $\nabla F_{\rm opt}$ the optical force's gradient at the mirror's mean position $\langle x\rangle$. The Fourier transform or equation 1.6 is thus:

$$\begin{aligned} -m\Omega^2\tilde{x}(\Omega) + \Gamma_{\rm eff}\, im\Omega\tilde{x}(\Omega) + K_{\rm eff}\,\tilde{x}(\Omega) & \\ = F_{\rm th} + \int_{-\infty}^{+\infty} dt e^{-i\Omega t}\left[\int_{-\infty}^{t} \nabla F_{\rm opt}\dot{x}(t')h(t-t')\right] & \end{aligned} \tag{1.8}$$

with $\tilde{x}$ the Fourier transform of x. Using the following property of Fourier transforms:

$$\int_{-\infty}^{+\infty} dt e^{-i\Omega t}\left[\int_{-\infty}^{t} f_1(t')f_2(t-t')dt'\right] = \tilde{f}_1(\Omega)\tilde{f}_2(\Omega) \tag{1.9}$$

Equation 1.6 can be reformulated as:

$$\begin{aligned} -m\Omega^2\tilde{x}(\Omega) + \Gamma_{\rm eff}\, im\Omega\tilde{x}(\Omega) + K_{\rm eff}\,\tilde{x}(\Omega) & \\ = F_{\rm th} + i\Omega\nabla F_{\rm opt}\tilde{x}(\Omega)\tilde{h}(\Omega) & \end{aligned} \tag{1.10}$$

The expression of h is $h(t) = 1 - e^{-t/\tau}$, and its Fourier transform is:

$$\tilde{h}(\Omega) = \frac{1}{i\Omega(1 + i\Omega\tau)} \tag{1.11}$$

Equation 1.6 can therefore be re-written as [19]:

$$-m\Omega^2\tilde{x}(\Omega) + \Gamma_{\rm eff}\, im\Omega\tilde{x}(\Omega) + K_{\rm eff}\,\tilde{x}(\Omega) = F_{\rm th} \tag{1.12a}$$

$$\text{with} \begin{cases} \Gamma_{\rm eff} &= \Gamma_{\rm m}\left(1 + Q_{\rm m}\frac{\Omega_{\rm m}\tau}{1+\Omega^2\tau^2}\frac{\nabla F_{\rm opt}}{K}\right) \\ K_{\rm eff} &= K\left(1 - \frac{1}{1+\Omega^2\tau^2}\frac{\nabla F_{\rm opt}}{K}\right) \end{cases} \tag{1.12b}$$

$\Omega_{\rm m}$ is the mechanical frequency verifying $K = m\Omega_{\rm m}^2$, $Q_{\rm m} = \Omega_{\rm m}/\Gamma_{\rm m}$ is the mechanical quality factor. A few remarks on equations 1.12 :

- equation 1.12a is now in frequency space Ω. $F_{\rm th}(\Omega)$ has a flat spectral power so we can drop its Ω dependency.
- the $F_{\rm opt}(\Omega)$ term cannot be found in equation 1.12a. This is because it is included in the *effective* damping and stiffness coefficients $\Gamma_{\rm eff}$ and $K_{\rm eff}$ (equation 1.12b). These effective coefficients account for the influence of the retarded optical force on the mechanical system.
- $\Gamma_{\rm eff}$ and $K_{\rm eff}$ still have an Ω dependency, but we usually consider the harmonic response of one mechanical mode, within a typical frequency span of a few $\Gamma_{\rm m}$. On such a span the frequency variations of $\Gamma_{\rm eff}$ and $K_{\rm eff}$ are negligible because $\Gamma_{\rm m} \ll 1/\tau$, and we can approximately take $\Gamma_{\rm eff} = \Gamma_{\rm eff}(\Omega_{\rm m})$ and $K_{\rm eff} = K_{\rm eff}(\Omega_{\rm m})$.

The delayed force model predicts that the coupling between optics and mechanics modifies the properties of the mechanical oscillator. Its stiffness constant is modified, which leads to a shifted resonance frequency, and its dissipation constant is modified too. For a negative ∇F_{opt} – which can be achieved by slightly detuning the laser source on the blue flank ($\omega_L > \omega_0$) of the Fabry-Pérot cavity optical resonance – the value of Γ_{eff} can be brought to zero, so that mechanical dissipation virtually disappears. The mechanical motion is harmonic and permanent, sustained by the action of the optical force. In this so-called *self oscillation* regime, the oscillation amplitude of the system grows tremendously with respect to the Brownian motion regime, and adopts a finite value set by non-linear effects saturating the motion, which are absent in our linear model.

In the case $\omega_L < \omega_0$, ∇F_{opt} is positive and therefore $\Gamma_{\text{eff}} > \Gamma_{\text{m}}$. The damping of the mechanical system is therefore increased by optical forces. For a system in thermodynamical equilibrium with a bath at temperature T, the fluctuation dissipation theorem states that the energy carried by the mechanical motion is $k_B T$ (k_B is the Boltzmann constant), regardless of its damping constant Γ_{m}. However, the assumption of thermodynamical equilibrium does not hold in the presence of dynamical optomechanical effects. The optical force actually drains energy from the mechanical system so that it fluctuates with an energy $k_B T_{\text{eff}}$. The relation between T_{eff} and T can be shown to be [19] :

$$\frac{T_{\text{eff}}}{T} = \frac{\Gamma}{\Gamma_{\text{eff}}} < 1 \tag{1.13}$$

This is the regime of optomechanical cooling of motion where the motional energy contained in the mechanical mode fluctuations drops below $k_B T$. The fact that the optomechanical interaction can bring or drain energy from the mechanical system can be seen as a consequence of the delayed optical force: the force applied onto the mirror is not in phase with the mirror velocity v, so the integral of the work $\mathbf{F}_{\text{opt}} \cdot \mathbf{v}$ on an oscillation cycle is not zero. See [20, p. 66] for more details.

We see from equations 1.12 that in the limit $\Omega \gg 1/\tau$, called the good cavity limit, the delayed force model does not predict any OM effect: Γ_{eff} tends to Γ_{m} and K_{eff} tends to K. However, OM effects still exist in the good cavity limit. This discrepancy arises because the optical cavity dynamics are oversimplified in this model : the time evolution of the intra-cavity intensity cannot be reduced to a mere exponential decay, and the effect of detuning between laser frequency and cavity resonance must be taken into account. We now present a model that overcomes this flaw.

1.1.4 Coupled dynamical equations for optomechanics

In this section we present a classical (non-quantum) model that integrates the full optical and mechanical dynamics. The interesting feature of this model is that it correctly predicts OM effects in the good cavity limit. This model introduces the dynamical equation for the cavity amplitude, that will be used again in chapter 3 in order to describe the behavior of waveguide to disk coupling in our experiments.

1.1.4.1 Dynamical equation of optical amplitude

We first define a time-dependent complex amplitude $a(t)$, such that the total energy stored in the optical Fabry-Pérot cavity at time t is $|a(t)|^2$. For a given stationary mode of the electro-magnetic (EM) field in the cavity, there exists a function $\mathbf{M}(\mathbf{r})$ such that the electric field can be expressed as $\mathbf{E}(\mathbf{r}, t) = \mathbf{M}(\mathbf{r}).\text{Re}(a(t))$.

We now consider an EM mode of the Fabry-Pérot cavity with frequency ω_0. If the cavity is lossless, the mode amplitude can be written as $a(t) = a_0 e^{-i\omega_0 t}$ and therefore satisfies the equation :

$$\frac{da(t)}{dt} = -i\omega_0 a(t) \tag{1.14}$$

We now heuristically introduce a loss term and a coupling term in equation 1.14 :

$$\frac{da(t)}{dt} = -i\omega_0 a(t) - \frac{\kappa}{2} a(t) + \sqrt{\kappa_{\text{ext}}} s_+ \tag{1.15}$$

This is justified as long as the total loss rate of the optical cavity $\kappa = \kappa_{\text{int}} + \kappa_{\text{ext}}$ is small compared to ω_0. The new solution of equation 1.15 can therefore be seen as a perturbation of the solution of equation 1.14. The amplitude loss term is $\kappa/2$ implies a the decay rate of the energy $|a|^2$ is equal κ. The term $\sqrt{\kappa_{\text{ext}}}s_+$ accounts for the energy brought to the Fabry-Pérot cavity by the incident wave, and s is defined such that $|s_+|^2$ denotes the associated optical power.

1.1.4.2 Resolution of coupled dynamical equations

For simplicity, we look at the optical amplitude in a reference frame that spins as $e^{-i\omega_0 t}$. In this frame, $a_0 e^{-i\omega t}$ becomes $a_0 e^{i\Delta t}$, with $\Delta = \omega - \omega_0$. Taking into account the OM coupling shifting the cavity frequency ω_0 to $\omega_0' = \omega_0 + g_{\text{om}}x$ under a displacement x, equation 1.15 becomes:

$$\dot{a}(t) = [i(\Delta - g_{\text{om}}x(t)) - \kappa/2]a(t) + \sqrt{\kappa_{\text{ext}}}s \tag{1.16}$$

that we can complete with the equation of motion:

$$\ddot{x}(t) = -\Omega_{\text{m}}^2(x(t) - x_0) - \Gamma\dot{x}(t) + (F_{\text{opt}}(t) + F_{\text{th}}(t))/m \tag{1.17}$$

The mechanical equation 1.17 is essentially the same as equation 1.6. The optical force can be expressed as $F_{\text{opt}}(t) = g_{\text{om}}|a(t)|^2/\omega_0$. A derivation of this expression will be carried in section 1.3. We will now suppose that the OM effects induce perturbations $\delta x(t)$ and $\delta a(t)$ that can be considered small with respect to the stationary solutions $\bar{x}$ and $\bar{a}$ of equations 1.16 & 1.17 (this is the regime of linearized optomechanics). Writing $a(t)$ and $x(t)$ respectively as $\bar{x} + \delta x(t)$ and $\bar{a} + \delta a(t)$, and neglecting second order terms, one obtains the equations satisfied by small perturbations:

$$\delta\dot{a}(t) = [i\bar{\Delta} - \kappa/2]\delta a(t) - ig_{\text{om}}\bar{a}\delta x(t) \tag{1.18a}$$

$$\delta\ddot{x}(t) = -\Omega_{\text{m}}^2\delta x(t) - \Gamma_{\text{m}}\delta\dot{x}(t) - \frac{g_{\text{om}}}{m\omega_0}[\bar{a}^*\delta a(t) + \bar{a}\delta a^*(t)] + \frac{F_{\text{th}}(t)}{m} \tag{1.18b}$$

with $\bar{\Delta} = \Delta + g_{\text{om}}\bar{x}$ the detuning taking into account the static shift of the optical cavity resonance. These equations are linear, which is not the case of equations 1.16 & 1.17 because of the term F_{opt} that is quadratic in $a(t)$. It is now possible to solve this set of equations by shifting to Fourier space. Equation 1.18a yields : $\delta\tilde{a}(\omega) = ig_{\text{om}}\bar{a}\delta\tilde{x}(\omega)\chi_c(\omega)$, with $\chi_c(\omega) = (-i\omega - i\bar{\Delta} + \kappa/2)^{-1}$. Using this expression for $\delta\tilde{a}(\omega)$ in the Fourier transform of equation 1.18b, we get :

$$\delta\tilde{x}(\omega) = \frac{F_{\text{th}}}{m(\Omega_{\text{m}}^2 - \omega^2 - i\omega\Gamma_{\text{m}}) + \Sigma(\omega)} \tag{1.19a}$$

$$\text{with } \Sigma(\omega) = \frac{-ig_{\text{om}}^2|\bar{a}|^2}{\omega_0}[\chi_c(\omega) - \chi_c^*(-\omega)] \tag{1.19b}$$

If we omit the term $\Sigma(\omega)$ in equation 1.19a, we recognize the typical susceptibility function of an harmonic damped oscillator of pulsation Ω_{m} and damping factor Γ_{m}. It appears then that the real and imaginary parts of $\Sigma(\omega)$ correspond to a modification of the spring constant and damping factor of the oscillator coupled to light. This is similar to the effective constants Γ_{eff} and K_{eff} obtained in §1.1.3. We can write the additional damping factor and the resonance frequency shift as:

$$\Gamma_{\text{OM}} = \frac{\kappa|\bar{a}|^2 g_{\text{om}}^2}{2m\omega_0\Omega_{\text{m}}}\left[\frac{1}{(\Omega_{\text{m}} + \bar{\Delta})^2 + \kappa^2/4} - \frac{1}{(\Omega_{\text{m}} - \bar{\Delta})^2 + \kappa^2/4}\right] \tag{1.20a}$$

$$\Delta(\Omega_{\text{m}}^2) = \frac{|\bar{a}|^2 g_{\text{om}}^2}{m\omega_0}\left[\frac{\Omega_{\text{m}} + \bar{\Delta}}{(\Omega_{\text{m}} + \bar{\Delta})^2 + \kappa^2/4} - \frac{\Omega_{\text{m}} - \bar{\Delta}}{(\Omega_{\text{m}} - \bar{\Delta})^2 + \kappa^2/4}\right] \tag{1.20b}$$

With the notation of the delayed force model: $\Gamma_{\text{eff}} = \Gamma_{\text{m}} + \Gamma_{\text{OM}}$ and $K_{\text{eff}} = K + m\Delta(\Omega_{\text{m}}^2)$.

As can be seen on figure 1.3, for a given intra-cavity optical energy the largest values of Γ_{OM} are achieved for large values of the parameter Ω_{m}/κ. This is in strong opposition with the delayed force model developed in the previous section, which predicted no effect for $\Omega_{\text{m}}/\kappa \gg 1$. It can also be noted that as Ω_{m}/κ increases, the region of strong OM damping rate is more and more peaked around the values $\bar{\Delta} = \pm\Omega_{\text{m}}$.

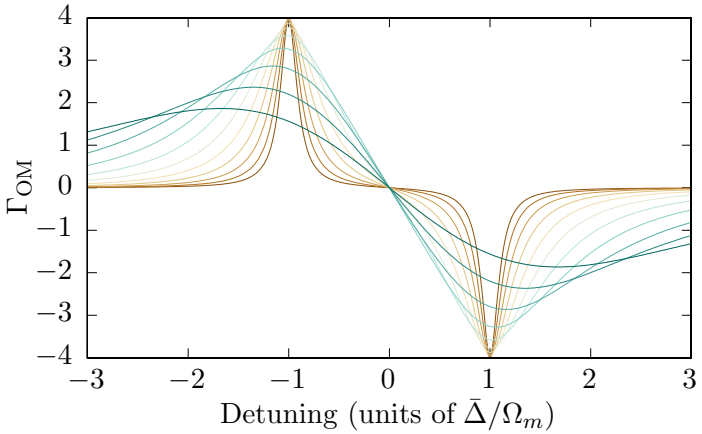

Figure 1.3 – OM damping rate Γ_{OM} as a function of the effective detuning $\bar{\Delta}$. The pre-factor in equation 1.20a is set to 1. $\Omega_{\mathrm{m}}/\kappa$ spans the range 0.2 (turquoise) to 5 (brown).

1.1.5 Quantum model

The coupled dynamical equations model presented above predicts optomechanical effects in both the bad and good cavity limit. This is a nice feature, but it predicts no limit on the amount of OM cooling: it suffices to increase the optical energy $|\bar{a}|^2$ in the cavity to obtain arbitrarily high values of Γ_{OM}. We now briefly develop a quantum theory of OM effects that shows that the amount of achievable OM cooling ($\Gamma_{\mathrm{OM}} > 0$) presents a maximum value independent of the EM energy stored in the cavity.

1.1.5.1 Quantum Hamiltonian

We derive the quantum Hamiltonian of the canonical OM system presented in figure 1.1. A more detailed derivation can be found in [21]. The idea is to derive a classical Hamiltonian of the system, and then apply a standard quantization procedure. We start by writing the equations satisfied by the electric field in a Fabry-Pérot cavity. q is the horizontal spatial coordinate. For simplicity we suppose that the mirror's dimensions are large when compared to the cavity length L, so that the field is only dependent on the q spatial coordinate. Moreover we consider one polarization of the field only, so that the electric field can be described by the scalar function $E(q,t)$. Both mirrors are supposed to be perfect reflectors. Optical losses will be considered later, as the coupling to a continuum of modes exterior to the cavity. The electric field therefore satisfies the two optical equations :

$$\frac{\partial E(q,t)}{\partial q^2} - \frac{\partial E(q,t)}{\partial t^2} = 0 \tag{1.21a}$$

$$\forall t,\ E(0,t) = E(L + x(t), t) = 0 \tag{1.21b}$$

where $x(t)$ is the time varying coordinate of the mirror around its equilibrium position L. Equation 1.21a is the propagation equation for the field, and equation 1.21b expresses the fact that tangential electric fields vanish on the surface of a perfect electric conductor.

The mechanics of the system are described by Newton's 2$^{\mathrm{nd}}$ law applied to the moving mirror. The forces exerted are the spring's response – that we model by a potential $V(x)$ – and the field's radiation pressure $(\partial E/\partial q)^2$. We therefore obtain the following equation :

$$m\ddot{q} = -\frac{\partial V(x)}{\partial x} + \left(\frac{\partial E(q,t)}{\partial q}\right)^2\Bigg|_{q=L+x} \tag{1.22}$$

We will now spatially decompose the field E at time t on a basis of sinusoidal functions supported by the Fabry Pérot cavity of length $L + x(t)$:

$$E(q,t) = \sqrt{\frac{L+x(t)}{2}} \sum_k X_k(t) \sin\left(\frac{k\pi q}{L+x(t)}\right) \tag{1.23a}$$

$$\text{with} \quad X_k(t) = \sqrt{\frac{2}{L+x(t)}} \int_0^{L+x(t)} E(q,t) \sin\left(\frac{k\pi q}{L+x(t)}\right) dq \tag{1.23b}$$

Now if we use expression 1.23a in equations 1.21 and 1.22, we get a set of differential equations satisfied by the $X_k(t)_{k\in\mathbb{N}}$ and $x(t)$, which can be found for instance in [22, p. 9]. They are called equations of motion for the generalized coordinates. The next step of our quantization procedure is to find the classical Lagrangian $L(x, \dot{x}, \{X_k(t), \dot{X}_k\}_{k\in\mathbb{N}})$ such that the set of equations $\left\{\frac{d}{dt}\left(\frac{\partial L}{\partial \dot{\alpha}}\right) = \frac{\partial L}{\partial \alpha}\right\}_{\alpha\in\{x,\{X_k\}_{k\in\mathbb{N}}\}}$ is equivalent to the equations of motion for generalized coordinates. Once the Lagrangian is found it is then possible to derive the classical Hamiltonian of the system as a function of the $\{x, X_k\}$ and their conjugate momenta $\{p, P_k\}$ [22, p. 10]. This Hamiltonian is quite complex, as it contains cross terms between the different X_k's. However it can be simplified by making two assumptions :

- The mirror displacement is sufficiently small so that the latter can be supposed to move in an harmonic potential. $V(x)$ therefore takes the form $V(x) = m\Omega_{\mathrm{m}}^2 x^2/2$.
- Instead of considering all the modes of the optical cavity, we only retain one mode, which we label ω_0. This considerably simplifies the Hamiltonian by suppressing all the cross terms. This approximation is justified if the cavity resonance shift $\Delta\omega_0 = g_{\mathrm{om}}\Delta x$ is negligible when compered to the cavity's free spectral range (FSR) $\Delta\omega_{\mathrm{FSR}} = \pi c/L$. We write X and P the generalized coordinates corresponding to the mode at ω_0.

We then "promote" $\{q, p, X, P\}$ as operators that satisfy standard commutation relations :

$$\left[\hat{x}, \hat{X}\right] = \left[\hat{x}, \hat{P}\right] = \left[\hat{p}, \hat{X}\right] = \left[\hat{p}, \hat{P}\right] = 0 \tag{1.24a}$$

$$[\hat{x}, \hat{p}] = \left[\hat{X}, \hat{P}\right] = i\hbar \tag{1.24b}$$

Finally, we define normalized annihilation and creation operators as :

$$\hat{a} = \sqrt{\frac{1}{2\hbar\omega_0}}\left(\omega_0\hat{X} + i\hat{P}\right) \quad , \quad \hat{a}^\dagger = \sqrt{\frac{1}{2\hbar\omega_0}}\left(\omega_0\hat{X} - i\hat{P}\right) \tag{1.25a}$$

$$\hat{b} = \sqrt{\frac{m\Omega_{\mathrm{m}}}{2\hbar}}\hat{x} + i\sqrt{\frac{1}{2\hbar m\Omega_{\mathrm{m}}}}\hat{p} \quad , \quad \hat{b}^\dagger = \sqrt{\frac{m\Omega_{\mathrm{m}}}{2\hbar}}\hat{x} - i\sqrt{\frac{1}{2\hbar m\Omega_{\mathrm{m}}}}\hat{p} \tag{1.25b}$$

The OM system's Hamiltonian can then be expressed as :

$$\hat{H}_0 = \underbrace{\hbar\omega_0\left(\hat{a}^\dagger\hat{a}\right)}_{\text{optical energy}} + \underbrace{\hbar\Omega_{\mathrm{m}}\left(\hat{b}^\dagger\hat{b}\right)}_{\text{mechanical energy}} + \underbrace{\hbar g_{\mathrm{om}} x_{\mathrm{ZPF}}\hat{a}^\dagger\hat{a}\left(\hat{b}^\dagger + \hat{b}\right)}_{\text{OM interaction term}} \tag{1.26}$$

with $g_{\mathrm{om}} = -\partial\omega_0/\partial x|_{x=0}$ the OM coupling and $x_{\mathrm{ZPF}} = [\hbar/(2m\Omega_{\mathrm{m}})]^{1/2}$ the RMS displacement of the mechanical oscillator when in the energy ground state. ZPF stands for "zero point fluctuation". This expression for the Hamiltonian turns out to be quite intuitive. Indeed, from equation 1.25b it can be seen that $x_{\mathrm{ZPF}}(\hat{b}^\dagger + \hat{b}) = \hat{q}$, and therefore $g_{\mathrm{om}}x_{\mathrm{ZPF}}(\hat{b}^\dagger + \hat{b})$ is the cavity frequency shift corresponding to the mirror's displacement. The optical energy in the cavity is therefore:
$\hbar[\omega_0 + g_{\mathrm{om}}x_{\mathrm{ZPF}}(\hat{b}^\dagger + \hat{b})]\hat{a}^\dagger\hat{a}$, which is obtained by combining the "optical energy" and "interaction term" of equation 1.26. In the following we use the optomechanical vacuum coupling g_0, defined as $g_0 = g_{\mathrm{om}} \cdot x_{\mathrm{ZPF}}$. This parameter is more fundamental than g_{om}, as explained in §1.3.1.

1.1.5.2 Input output formalism

The Hamiltonian from last section was derived in the case of an OM system isolated from its environment. In reality our optical cavity has intrinsic and extrinsic loss rates, which result in a temporal loss of the optical field's coherence. In this section we derive the spectral power density of the photon number operator $\hat{a}^\dagger\hat{a}$:

$$S_{NN}(\omega) = \int_{-\infty}^{+\infty} e^{-i\omega t}\langle(\hat{a}^\dagger\hat{a})(t)(\hat{a}^\dagger\hat{a})(0)\rangle dt \tag{1.27}$$

In the case of a system isolated from its environment the temporal evolution of $\hat{a}$ would be a simple exponential factor rotating at frequency ω_0, and $S_{NN}(\omega)$ would be a Dirac function. It is the coupling to the bath of modes outside the OM cavity that results in a richer $S_{NN}(\omega)$. We use the so-called input-output formalism for its derivation keeping only the main steps of the calculation in order to build some insight on the final result.

We consider the "complete" optical Hamiltonian (the mechanics are ignored in this section). It is composed of the optical part of our "closed" OM Hamiltonian (equation 1.26), of the optical bath's Hamiltonian, and of the interaction between cavity and bath:

$$\hat{H}_{\text{tot}}^{\text{opt}} = \hbar\omega_0\hat{a}^\dagger\hat{a} + H_{\text{bath}} + H_{\text{int}} \tag{1.28a}$$

$$\text{with} \quad \hat{H}_{\text{bath}} = \sum_q \hbar\omega_q\hat{\alpha}_q^\dagger\hat{\alpha}_q \tag{1.28b}$$

$$\text{and} \quad \hat{H}_{\text{int}} = -i\hbar\sum_q(f_q\hat{\alpha}_q\hat{a}^\dagger + f_q^*\hat{\alpha}_q^\dagger\hat{a}) \tag{1.28c}$$

The term $f_q\hat{a}^\dagger\hat{\alpha}_q + f_q^*\hat{\alpha}_q^\dagger\hat{a}$ accounts for the optical interaction between the cavity and the q^{th} mode of the environment. $\hat{\alpha}_q\hat{a}^\dagger$ creates an additional photon in the cavity and annihilates one in the bath, and vice versa for $\hat{\alpha}_q^\dagger\hat{a}$. Although intuitive, expression 1.28c already comes from a calculation where quadratic coupling is supposed and non resonant terms $\hat{\alpha}_q^\dagger\hat{a}^\dagger$ and $\hat{\alpha}_q\hat{a}$ are neglected (this is the rotating wave approximation)[23].

We now adopt the Heisenberg picture, where the time evolution of the system is carried by the operators with time dependence. The temporal evolution of an operator $\hat{A}$ is given by:

$$\hbar\frac{d\hat{A}(t)}{dt} = -i\left[\hat{A}(t), \hat{H}_{\text{tot}}^{\text{opt}}\right] \tag{1.29}$$

applying this formula to $\hat{A} \equiv \hat{\alpha}_q$ yields :

$$\dot{\hat{\alpha}}_q = -i\omega_q\hat{\alpha}_q + f_q^*\hat{a} \tag{1.30}$$

This equation can be integrated :

$$\hat{\alpha}_q(t) = e^{-i\omega_q(t-t_0)}\hat{\alpha}_q(t_0) + \int_{t_0}^{t} e^{-i\omega_q(t-\tau)}f_q^*\hat{a}(\tau)d\tau \tag{1.31}$$

Equation 1.29 also yields the time evolution of the cavity's field annihilation operator ($\hat{A} \equiv \hat{a}$) :

$$\dot{\hat{a}} = -i\omega_0\hat{a} - \sum_q f_q\hat{\alpha}_q \tag{1.32}$$

We then use the expression 1.31 for $\hat{\alpha}_q$ to write the sum on the right hand side of equation 1.32 :

$$\begin{aligned}\sum_q f_q\hat{\alpha}_q &= \sum_q f_q e^{-i\omega_q(t-t_0)}\hat{\alpha}_q(t_0) \\ &+ \sum_q |f_q|^2\int_{t_0}^{t} e^{-i(\omega_q-\omega_0)(t-\tau)}[e^{i\omega_0(\tau-t)}\hat{a}(\tau)]d\tau\end{aligned} \tag{1.33}$$

The second line of equation 1.33 can be simplified by the following considerations :

- If the strength of the cavity to bath coupling is weak, $\hat{a}$ can be assumed to essentially have a $\propto e^{-i\omega_0\tau}$ time dependency. The term between square brackets is therefore a slowly varying function of τ and can be taken out of the integral.

- We assume that the bath is Markovian, i.e. has no time memory. In other words, its spectral density is constant. Thus we set $f_q = \sqrt{\kappa}, \forall q$. The notation κ is chosen so that a coherence is kept with the notations of section 1.1.4. If the spacing between the modes of the bath is small enough, then we have : $\sum_q |f_q|^2 e^{-i(\omega_q-\omega_0)(t-\tau)} = \kappa\delta(t-\tau)$, with δ the Dirac distribution.

Finally by using the identity : $\int_{-\infty}^{x_0} \delta(x-x_0)dx = 1/2$, we get the following result :

$$\begin{aligned} \dot{\hat{a}} &= -i\omega_0\hat{a} - \frac{\kappa}{2}\hat{a} - \kappa\hat{\alpha}_{in}(t) \\ \text{with} \quad \hat{\alpha}_{in}(t) &= \sum_q e^{-i\omega_q(t-t_0)}\hat{\alpha}_q(t_0) \end{aligned} \tag{1.34}$$

The coupling with the environment induces a decay loss $-\frac{\kappa}{2}\hat{a}$ and an input term $-\kappa\hat{\alpha}_{in}(t)$. In a semi-classical approach $\hat{a}(t)$ can be written as the sum of a complex amplitude and a quantum part, both rotating at the laser drive's frequency, i.e. $\hat{a}(t) = e^{-i\omega_L}(\bar{a} + \delta\hat{a}(t))$. $\hat{\alpha}_{in}(t)$ is written in the same way : $\hat{\alpha}_{in}(t) = e^{-i\omega_L}(\bar{\alpha}_{in} + \hat{\xi}(t))$. A quite straightforward calculation then yields the autocorrelation function for the $\delta\hat{a}$ operator : $\langle\delta\hat{a}(t)\delta\hat{a}^\dagger(0)\rangle = e^{i\Delta t - \frac{\kappa}{2}|t|}$. The autocorrelation function for the photon number operator is therefore $\bar{N}e^{i\Delta t-\frac{\kappa}{2}|t|}$ with $\bar{N}$ the average photon number. The Wiener-Khinchin theorem then yields the desired result :

$$S_{NN}(\omega) = \int_{-\infty}^{+\infty} e^{-i\omega t}\bar{N}e^{i\Delta t-\frac{\kappa}{2}|t|}dt = \bar{N}\frac{\kappa}{(\omega+\Delta)^2 + (\kappa/2)^2} \tag{1.35}$$

where $\Delta = \omega_L - \omega_0$ an we have used the identity $\langle\delta\hat{\xi}(t)\delta\hat{\xi}(t')\rangle = \delta(t-t')$.

1.1.5.3 Fermi's golden rule for mechanical transitions

In this section we show that the transition rate from a mechanical Fock state $|l\rangle$ to neighbor states $|l-1\rangle$ and $|l+1\rangle$ is proportional to the value of the photon number spectral power density at a given frequency.

We start from the OM Hamiltonian without the bare optics: $\hat{H} = \hbar\Omega_{\mathrm{m}}\hat{b}\hat{b}^\dagger + \hbar g_0(\hat{b}+\hat{b}^\dagger)\hat{a}^\dagger\hat{a}(t)$, where $\hat{a}^\dagger\hat{a}(t)$ is the photon number operator. We will apply standard perturbation theory with the unperturbed Hamiltonian $\hat{H}_m = \hbar\Omega_{\mathrm{m}}\hat{b}\hat{b}^\dagger$ and g_0 the small perturbation parameter. We write the state of the mechanical system on the base of $\hbar\Omega_{\mathrm{m}}\hat{b}\hat{b}^\dagger$ eigenstates: $|\psi\rangle(t) = \sum_n b_n(t)|n\rangle$. One finds that the probability amplitude to find the mechanical system in state $|j\rangle$ at time t, given that it was initially in state $|i\rangle$ at time t_0, is to first order given by (see for instance [24, p. 8-9]) :

$$b_j(t) = -ig_0\Theta_{ij}\int_{t_0}^{t} e^{-i\omega_{ij}\tau}\langle\hat{a}^\dagger\hat{a}\rangle(\tau)d\tau \tag{1.36}$$

where Θ_{ij} is the matrix element $\langle i|\hat{b}+\hat{b}^\dagger|j\rangle$, $\omega_{ij} = (E_i - E_j)/\hbar$, and $\langle\hat{a}^\dagger\hat{a}\rangle(\tau)$ is the average of the photon number operator on the optical system state. The probability to find the system in state $|j\rangle$ after a time t is the square of the probability amplitude :

$$P_j(t) = g_0^2|\Theta_{ij}|^2\int_{t_0}^{t}\int_{t_0}^{t} e^{-i\omega_{ij}(\tau-\tau')}\langle\hat{a}^\dagger\hat{a}(\tau)\hat{a}^\dagger\hat{a}(\tau')\rangle d\tau d\tau' \tag{1.37}$$

If we assume that the state of the system is stationary, i.e. $\langle\hat{a}^\dagger\hat{a}(\tau)\hat{a}^\dagger\hat{a}(\tau')\rangle = \langle\hat{a}^\dagger\hat{a}(\tau-\tau')\hat{a}^\dagger\hat{a}(0)\rangle$, then we have :

$$P_j(t) = g_0^2|\Theta_{ij}|^2\int_{\omega}d\omega\int_{t_0}^{t}\int_{t_0}^{t} e^{-i(\omega_{ij}-\omega)(\tau-\tau')}S_{NN}(\omega)d\tau d\tau' \tag{1.38}$$

with $S_{NN}(\omega) = \int_{-\infty}^{+\infty} e^{-i\omega\tau}\langle(\hat{a}^\dagger\hat{a}(\tau)(\hat{a}^\dagger\hat{a}(0)\rangle d\tau$. The double time integral can be evaluated and we get :

$$P_j(t) = g_0^2|\Theta_{ij}|^2 \int_\omega d\omega S_{NN}(\omega) \left(\frac{\sin[(\omega_{ij}-\omega)(t-t_0)]}{\omega_{ij}-\omega}\right)^2 \tag{1.39}$$

Finally, by noticing that the squared factor under the integral can be approximated by $(t-t_0)\delta(\omega_{ij}-\omega)$, the transition rate from the initial mechanical state $|i\rangle$ to state $|j\rangle$ is :

$$\Gamma_{i\to j} = \frac{dP_j(t)}{dt} = g_0^2|\Theta_{ij}|^2 S_{NN}\left(\frac{E_i - E_j}{\hbar}\right) \tag{1.40}$$

$\Gamma_{i\to j}$ is proportional to the power spectral density of the photon number operator evaluated at the difference between energies of the two states. With results 1.35 and 1.40, we are now equipped for the calculation of OM cooling in the quantum mechanical framework.

1.1.5.4 Optomechanical cooling

We now consider the question of the minimum phonon number that can be achieved by OM cooling. We define the phonon decrease rate A^- by $\Gamma_{|n\rangle\to|n-1\rangle} = nA^-$. Similarly we define the increase rate A^+ such that $\Gamma_{|n\rangle\to|n+1\rangle} = (n+1)A^+$. The average phonon number in our mechanical mode is $\bar{n} = \sum_{n=0}^{\infty} nP_n$, P_n being the probability of being in the Fock state $|n\rangle$. A quick calculation leads to :

$$\dot{\bar{n}} = (\bar{n}+1)(A^+ + A_{\text{th}}^+) - \bar{n}(A^- + A_{\text{th}}^-) \tag{1.41}$$

where we have introduced the transition rates due to the exchange of phonons with the bath: $A_{\text{th}}^+ = \bar{n}_{th}\Gamma_{\text{m}}$ and $A_{\text{th}}^- = (\bar{n}_{\text{th}}+1)\Gamma_{\text{m}}$, $\bar{n}_{\text{th}}$ being the mean phonon number occupancy due to the coupling to the bath. The stationary mean phonon number $\bar{n}$ is found by solving equation 1.41 with $\dot{\bar{n}} = 0$:

$$\bar{n} = \frac{A^+ + \bar{n}_{\text{th}}\Gamma_{\text{m}}}{\Gamma_{\text{OM}} + \Gamma_{\text{m}}} \tag{1.42}$$

with $\Gamma_{\text{OM}} = A^- - A^+$ the OM damping rate. We see that even in the case of perfect mechanical isolation from the bath, the minimal phonon number attainable is not zero :

$$\bar{n}_{\min} = \frac{A^+}{A^- - A^+} \tag{1.43}$$

Now from equation 1.40 we have : $A^\pm = g_0^2 S_{NN}(\mp\Omega_{\text{m}})$, and equation 1.35 gives the expression for $S_{NN}(\omega)$. The minimal phonon number can therefore be re-expressed as :

$$\bar{n}_{\min} = \left(\frac{A^-}{A^+} - 1\right)^{-1} = \left(\frac{(\Delta+\Omega_{\text{m}})^2 + (\kappa/2)^2}{(\Delta-\Omega_{\text{m}})^2 + (\kappa/2)^2} - 1\right)^{-1} \tag{1.44}$$

In the good cavity limit, where the cavity's total damping rate κ is small compared to Ω_{m}, expression 1.44 can be simplified to :

$$\bar{n}_{\min} = \left(\frac{\kappa}{4\Omega_{\text{m}}}\right)^2 \tag{1.45}$$

The quantum model hence predicts that a final number of phonons smaller than 1 is only possible when the system operates in the good cavity limit. Indeed, in the bad cavity limit ($\Omega_{\text{m}} \ll \kappa$), expression 1.44 simplifies to $\kappa/(4\Omega_{\text{m}}) \gg 1$.

Figure 1.4 shows two quantum illustrations of the OM cooling effect. Figure 1.4a represents the spectral power density of the photon number fluctuation in the cavity, which is peaked for $\Omega = -\Delta$ (see equation 1.35). As shown earlier the transition rates $A^\pm$ are proportional to the value of S_{NN} evaluated at $\mp\Omega_{\text{m}}$. Thus we see that in the configuration of figure 1.4a the transition rate A^- is greatly enhanced compared to A^+, inducing overall cooling, although the system is not even

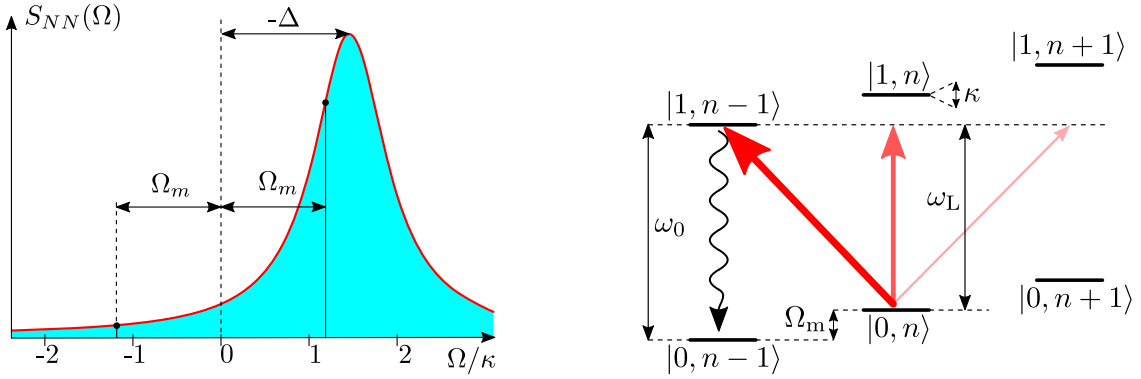

(a) Photon number spectral power

(b) OM "ladder"

Figure 1.4 – Two "quantum" illustrations of the OM cooling effect. On figure a) the laser is red detuned from the cavity resonance, so that $-\Delta > 0$. On figure b), the states $|N, n\rangle$ have a finite vertical width κ. The figure corresponds to the good cavity limit case where $\Omega\mathrm{m} \gg \kappa$.

deeply in the good cavity limit. In the case where the FWHM of $S_{NN}(\Omega)$ is far larger than Ω_m, the enhancement of A^- relative to A^+ is not so pronounced anymore and the cooling is therefore not very efficient.

Figure 1.4b shows another way to look at the cooling effect. Here the OM system's state is represented by the ket $|N, n\rangle$, with N the photon number and n the phonon number. If the system is initially in state $|0, n\rangle$ then laser radiation sent at a frequency $\omega_0 - \Omega_\mathrm{m}$ will excite preferentially the system to state $|1, n-1\rangle$ because the energy difference between the two states is better tuned to the laser frequency. The system can then decay to state $|0, n-1\rangle$ by emission of a photon. The transitions $|0, n\rangle \to |1, n\rangle$ and $|0, n\rangle \to |1, n+1\rangle$ are happening at far lower rates represented by thinner red arrows on the figure. The OM system's number of phonons therefore decreases along the path $|0, n\rangle \to |1, n-1\rangle \to |0, n-1\rangle \to |1, n-2\rangle \to |0, n-2\rangle \ldots$ until it reaches a stationary state.

1.2 Optical forces on miniature mechanical devices

The generic OM system from section 1.1.1 was presented in order to introduce concepts that are more general than the mere Fabry-Pérot case. The mechanically compliant Fabry-Pérot is sensitive to radiation pressure only, but this is not the only force that light can exert on matter. In this section we will detail the different optical forces that can be encountered in OMs. Some of these forces only take place in solids, i.e. when the EM field travels inside a material. This will be the case of our miniature OM disks, as will be discussed in the next chapter.

1.2.1 Radiation pressure

Radiation pressure is the "canonical" OM force, and most OMs theoretical papers consider it as the only force yielding OM effects. A simple way of grasping the idea of radiation pressure is to consider a photon traveling in vacuum and reflecting on a perfect (reflectivity = 1) mirror. The photon carries a momentum $\hbar k_0$, with k_0 being the photon wavenumber in free space. After reflection the photon travels in the opposite direction so that its momentum is now $-\hbar k_0$. It has therefore delivered an absolute momentum $2\hbar k_0$ to the mirror. In a realistic experimental situation, a rate of photons would impinge on the mirror, causing an amount of moment being transferred to the mirror per unit time, i.e. a force. The value of this force ca be easily calculated to be $F = 2P/c$, with P the optical power impinging on the mirror.

In order to carry accurate computations of the OM interactions in material optomechanical devices of more complex geometries, a general expression of radiation pressure for arbitrary EM

fields and dielectric distribution is needed. Such an expression can be derived from momentum conservation considerations in the framework of Maxwell's equations [25]. The idea is first to write that the Lorentz force exerted on charges within a volume V is equal to the change rate of their momentum: $d\mathbf{P}_{\text{chg}}/dt = \int_V [\rho\mathbf{E} + \mathbf{J}\times\mathbf{B}]dV$. The Lorentz force is then transformed using Maxwell's equations, and one finally gets :

$$\frac{d}{dt}\left(\mathbf{P}_{\text{chg}} + \mathbf{P}_{\text{field}}\right)_i = \oint_S \sum_j T_{ij} n_j dS \tag{1.46}$$

with S the surface enclosing volume V, $\mathbf{P}_{\text{field}}$ a term that can be identified as the momentum of the EM field within V, and $\mathbf{n}$ the unitary vector normal to S. From equation 1.46 it can be deduced that $\sum_j T_{ij} n_j$ is the force per unit surface exerted on volume V along the direction i. T is called the Maxwell Stress Tensor (its components have indeed the dimension of a mechanical stress) and its expression is given by :

$$T_{ij} = \varepsilon_0\varepsilon_r\left(E_iE_j - \frac{1}{2}\delta_{ij}|\mathbf{E}|^2\right) + \mu_0\mu_r\left(H_iH_j - \frac{1}{2}\delta_{ij}|\mathbf{H}|^2\right) \tag{1.47}$$

with ε_0 and μ_0 the permittivity and permeability of vacuum, ε_r the relative permittivity corresponding to the dielectric configuration (ε_r is therefore dependent on coordinates) and μ_r the relative permeability (for the dielectrics of interest in the following $\mu_r = 1$).

With the conventions chosen the stress exerted along direction i on an elementary surface normal to j is : $\sigma_{ij}^{rp} = -T_{ij}$. The Maxwell stress tensor thus allows to calculate normal stresses ($i = j$) but also shear stresses ($i \neq j$). This is in contrast with the example of a bouncing photon presented earlier, where the photon could only exert a force orthogonal to the mirror's surface. It should also be noted that since the EM fields oscillate at frequencies in the 10^{14}-10^{15} range, while mechanical frequencies for our systems are in the 10^8-10^9 range, we always use the time average of optical stresses in the subsequent calculations (see chapter 2).

1.2.2 Electrostriction

The derivation of the Maxwell Stress Tensor presented above was carried in the context of a material of infinite stiffness, for which the positions of the material's atoms do not move relative to one another. However most materials have some mechanical compliance, so that the stress induced under the action of light can modify the material density, or lattice configuration in a crystal. This phenomenon of optically induced strain of a compliant material is called electrostriction. In the class of materials called photoelastic, this strain eventually produces a variation of the refractive index, hinting for some intimate link between photoelasticity and electrostriction (see §1.3.2). The expression of the Maxwell Stress Tensor obtained in the last section supposed that the materials were of fixed dielectric constant. If materials were allowed to deform, the Maxwell Stress Tensor derivation would yield additional terms to be associated with electrostriction. This formal separation of radiation pressure and electrostriction may appear superficial – after all they are just two different aspects of the action of the Lorentz force on charges – but it proves useful when carrying calculations of OM coupling on our actual devices (see chapter 2).

For crystalline materials, the dipoles induced by light within matter cannot always align with the field, they are constrained to develop in a fixed direction by the crystalline structure. In this case a tensor approach is necessary in order to model electrostriction. Let us consider a solid with crystalline structure undergoing a displacement $\mathbf{u}(\mathbf{r})$: an atom that occupied position $\mathbf{r}$ before displacement then occupies position $\mathbf{r} + \mathbf{u}(\mathbf{r})$. The tensor associated to strain $\mathbf{u}$ is: $S_{ij} = \frac{1}{2}(\partial_i u_j + \partial_j u_i)$. This tensor is symmetric. The deformation induces a change in the solid's dielectric tensor given by (we use Einstein's notation $a_{ij}b_j \equiv \sum_j a_{ij}b_j$):

$$\varepsilon_{ij}^{-1}(\mathbf{u}) = \varepsilon_{ij}^{-1}(0) + p_{ijkl}S_{kl} \tag{1.48}$$

where p_{ijkl} are the coefficients of the photoelastic tensor. In the most general case this tensor has $3^4 = 81$ coefficients, because the linear contribution of all 9 components of S_{kl} must be taken into account to compute each $\varepsilon_{ij}^{-1}(\mathbf{u})$. In the case of a cubic crystal such as GaAs these 81 components reduce to only 3 independent components [26]. A derivation similar to the one found in appendix A, but this time in a tensorial framework, yields the elements of the electrostriction stress tensor as a function of the photoelastic tensor [27], pointing again at the link between these two physical phenomena:

$$\underbrace{\begin{pmatrix} \sigma_{xx}^{es} \\ \sigma_{yy}^{es} \\ \sigma_{zz}^{es} \\ \sigma_{yz}^{es} = \sigma_{zy}^{es} \\ \sigma_{xz}^{es} = \sigma_{zx}^{es} \\ \sigma_{xy}^{es} = \sigma_{yx}^{es} \end{pmatrix}}_{\text{stress tensor}} = -\frac{1}{2}\varepsilon_0\, n^4 \underbrace{\begin{pmatrix} p_{11} & p_{12} & p_{12} & 0 & 0 & 0 \\ p_{12} & p_{11} & p_{12} & 0 & 0 & 0 \\ p_{12} & p_{12} & p_{11} & 0 & 0 & 0 \\ 0 & 0 & 0 & p_{44} & 0 & 0 \\ 0 & 0 & 0 & 0 & p_{44} & 0 \\ 0 & 0 & 0 & 0 & 0 & p_{44} \end{pmatrix}}_{\text{photoelastic tensor}} \begin{pmatrix} E_x^2 \\ E_y^2 \\ E_z^2 \\ E_y\, E_z \\ E_x\, E_z \\ E_x\, E_y \end{pmatrix} \tag{1.49}$$

This stress tensor is also symmetric so that we can adopt a vectorial representation with the convention: $xx \to 1$; $yy \to 2$; $zz \to 3$; $yz = zy \to 4$; $xz = zx \to 5$; $xy = yx \to 6$. Note the dependence with the 4^{th} power of the refractive index, which is at the advantage of strongly refractive materials ($n_{\text{GaAs}} \approx 3.4$ @ 1550 nm). Expression 1.49 will be used – in a simplified version – for calculations of the photoelastic OM coupling in our devices.

1.2.3 Photothermal forces

Radiation pressure and electrostriction presented in the two last sections are two different aspects of the action of Lorentz forces acting on materials, but light can interact with matter in other ways. The material device can also absorb photons, producing heat that can displace the device by thermal expansion. Because it is linked to thermal effects this photo-thermal force is generally way slower than the Lorentz force and is hence delayed from EM field variations by a time $\tau_{\text{th}} \gg 1/\kappa$. Its strength can however be orders or magnitude larger than Lorentz forces, as the absorbed photon releases all its energy.

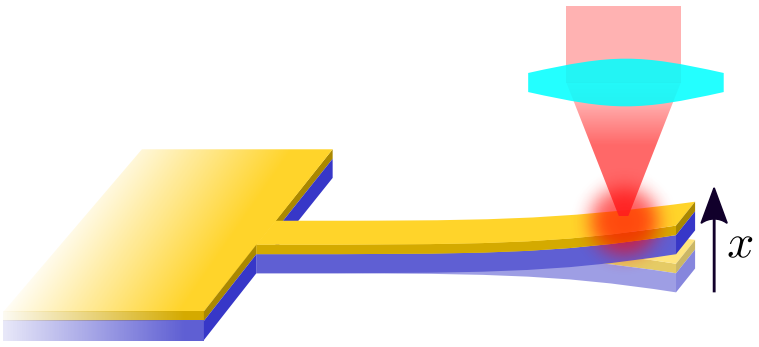

Figure 1.5 – Illustration of the photothermal force. A gold plated silicon cantilever undergoes laser illumination. The red blurry circle delimits the region of heat creation. Silicon expands more than gold as a result of its higher thermal expansion coefficient, which makes the whole cantilever bend upwards.

In a crystalline material, a local temperature increase ΔT will generate strain in the material. The two are linked by the formula : $\Delta S_{ij}^{th} = \alpha_{ij}\Delta T$, where α_{ij} is the tensorial analog to the isotropic thermal expansion coefficient. The thermally induced stress is therefore :

$$\sigma_{ij}^{\text{th}} = C_{ijkl}\alpha_{kl}\Delta T \tag{1.50}$$

with C_{ijkl} the elastic material's stiffness tensor. The "causal" chain of photo-thermal forces can be expressed as:

light absorption $\xrightarrow{fast}$ heat generation $\xrightarrow{slow}$ temperature rise $\xrightarrow{fast}$ mechanical expansion.

The thermal response of the system determines the delay of photothermal forces with respect to the moment of light exposure. It is ruled the calorific capacity C_p (in J/K) and the thermal resistance between the system and the bath R_th (in W/K). The third arrow involves thermal expansion coefficient and stiffness tensor. The retarded force model presented in section 1.1.3 can be adapted to photothermal forces, by inputting a new force proportional to the absorbed optical power in the cavity $\kappa_{abs}|a|^2$ and with a thermal delay $\tau_\mathrm{th} \equiv C_\mathrm{p}/R_\mathrm{th}$.

The coupled dynamical equations model from section 1.1.4 can be completed as well by adding a photo-thermal force term $F_\mathrm{pth}(\Delta T)$ in equation 1.17, and a third equation that describes the thermal dynamics of the system :

$$\frac{d\Delta T}{dt} = \frac{|a(t)|^2 \kappa_\mathrm{abs}}{C_p} - \frac{\Delta T R_{th}}{C_p} \tag{1.51}$$

κ_abs is the optical absorption rate, so that $|a(t)|^2\kappa_{abs}$ is the rate at which heat is generated. Dividing by the calorific capacity of the system yields a rate of temperature increase. The second term in the right hand side is the temperature relaxation, due to the heat transfer to the bath. Once equation 1.51 is added, the three coupled differential equations can be linearized and solved using Fourier analysis in a similar manner as what was developed in section 1.1.4. We will come back on photo-thermal force in chapter 2.

1.3 Optomechanical coupling constants

In section 1.2 we have introduced various forces that light can exert on materials (with an emphasis on crystalline materials): this is the action of optics on mechanics. Conversely, in optomechanics, the mechanical displacement impacts light, an aspect quantified by the frequency pull parameter $g_\mathrm{om} = -\partial\omega_0/\partial x$. This constant was already introduced in the models presented above.

The link between optical forces and g_om can be understood in the following manner : consider a cavity with perfectly reflecting mirrors. Now the movable mirror experiences a small displacement Δx such that the resonant angular frequency inside is changed by $\Delta\omega_0 = g_\mathrm{om}\Delta x$. Because no photon enters or escapes the cavity, the total optical energy in the cavity decreases by an amount $\Delta E_\mathrm{opt} = -N_\mathrm{cav}\hbar g_\mathrm{om}\Delta x$ (N_cav is the number of photons). Because of energy conservation ΔE_opt must be the opposite of the work of the optical force on the movable mirror. We therefore get : $F_\mathrm{opt} = N_\mathrm{cav}\hbar g_\mathrm{om}$. This energy argument proves useful in the following in order to compute OM couplings for arbitrary systems.

1.3.1 Reduction point $\mathbf{r_0}$ and vacuum coupling g_0

A simple mechanical system such as a translating mirror can be fully described by one single parameter: the position x of the mirror relative to its equilibrium position. However for a continuous solid undergoing an arbitrary deformation, a vectorial displacement field $\mathbf{u}(\mathbf{r})$ is necessary. Therefore when such a system starts deforming, all of its atoms do not undergo the same displacement ∂x and the definition of $g_\mathrm{om} = -\partial\omega_0/\partial x$ becomes ambiguous. In other words g_om takes a value that depends arbitrarily on the point $\mathbf{r}_0$ one focuses on. One way to overcome this difficulty is to rather employ the vacuum coupling g_0 (defined as $g_0 = g_\mathrm{om}x_\mathrm{ZPF}$). x_ZPF is also a "point dependent" quantity, so that g_0 is actually independent of the chosen point $\mathbf{r}_0$. x_ZPF can be defined in the following way : if a mechanical mode of the system undergoes a deformation $\mathbf{u}(\mathbf{r})$ such that the elastic energy corresponding to this deformation is $\hbar\Omega_\mathrm{m}/2$ (Ω_m is the mechanical mode's angular frequency), then x_ZPF chosen at point $\mathbf{r}$ is equal to $\mathbf{u}(\mathbf{r})$. Incidentally, this also defines an ($\mathbf{r}_0$ dependent) effective mass by the relation: $x_\mathrm{ZPF} = \sqrt{\hbar/(2m_\mathrm{eff}\Omega_\mathrm{m})}$. For a chosen reduction point $\mathbf{r}_0$, the value of g_om is inversely proportional to $\mathbf{u}(\mathbf{r}_0)$ whereas the value of x_ZPF is proportional to

$\mathbf{u}(\mathbf{r}_0)$. The $\mathbf{r}_0$ dependency therefore vanishes for the vacuum coupling g_0, which makes it a more fundamental parameter than the frequency pull parameter g_{om}.

1.3.2 Geometric and photoelastic g_{om}

When a solid deforms, its optical eigenmodes are modified. For instance if a parallelepipedic piece of material is "pulled" along one direction the Fabry-Pérot cavity delimited by its facets orthogonal to the elongation direction will change its resonating wavelength. At the same time, the strain resulting from the deformation also changes the lattice constant, which changes the material's optical index and shifts the resonance frequency. ω_0 is thus a function of the geometry G of the device and of the material's dielectric constant ε. The frequency-pull parameter can therefore be expressed as :

$$g_{\text{om}} = -\frac{\partial \omega_0(G,\varepsilon)}{\partial x} = \underbrace{-\frac{\partial \omega_0}{\partial G}\frac{\partial G}{\partial x}}_{\text{geometric } g_{\text{om}}^{\text{geo}}} - \underbrace{\frac{\partial \omega_0}{\partial \varepsilon}\frac{\partial \varepsilon}{\partial x}}_{\text{photoelastic } g_{\text{om}}^{\text{pe}}} \tag{1.52}$$

Starting from formula 1.1, the geometric contribution $g_{\text{om}}^{\text{geo}}$ can be derived quite simply in the case of a Fabry-Pérot cavity:

$$g_{\text{om}}^{\text{geo}} = +\omega_0/L \tag{1.53}$$

For more complex geometries where the solid of interest deforms arbitrarily, reference [28] gives a formula for the geometric frequency pull parameter :

$$g_{\text{om}}^{\text{geo}} = \frac{\omega_0}{4}\iint_S (\mathbf{q}\cdot\mathbf{n})\left[\Delta\varepsilon_{12}|\mathbf{E}_\parallel|^2 - \Delta\left(\varepsilon_{12}^{-1}\right)|\mathbf{D}_\perp|^2\right] dA \tag{1.54}$$

The integral is performed on the solid's surface S. $\mathbf{q}$ is the normalized displacement vector, $\mathbf{n}$ is the normal vector orthogonal to the solid's surface, $\mathbf{E}_\parallel$ and $\mathbf{D}_\perp$ are respectively the $\mathbf{E}$ field component tangential to the surface and the $\mathbf{D}$ field component orthogonal to the surface. $\Delta\varepsilon_{12}$ is the difference between the dielectric constant of the material and the dielectric constant of the surrounding medium. To obtain this formula the authors have applied perturbation theory to the Helmholtz equation, and they did circumvent discontinuity problems that were arising at the interfaces.

Another way to obtain $g_{\text{om}}^{\text{geo}}$ for an arbitrary mechanical displacement is to make use of the energy argument mentioned in section 1.3's introduction. First one computes the radiation pressure stress field exerted in the cavity by a single photon, $\sigma_{ij}^{\text{rp},1}$, and the work of this stress field for a displacement $\mathbf{u}(\mathbf{r})$ of the solid : $W = \iiint \sum \sigma_{ij}^{\text{rp},1} S_{ij}^{\mathbf{u}} dV$, with $S_{ij}^{\mathbf{u}}$ the strain tensor corresponding to the displacement field $\mathbf{u}$. For a given reduction point $\mathbf{r}_0$ the associated $g_{\text{om}}^{\text{geo}}$ is :

$$g_{\text{om}}^{\text{geo}} = \frac{\iiint \sum \sigma_{ij}^{\text{rp},1} S_{ij}^{\mathbf{u}} dV}{\hbar|\mathbf{u}(\mathbf{r}_0)|} \tag{1.55}$$

Formula 1.55 has the disadvantage of requiring the computation of a volume integral, when formula 1.54 only necessitates the computation of a surface integral.

Finally the geometric frequency-pull parameter can be obtained by a third, purely numerical method, which is the most simple conceptually. First an optical mode for the solid *at rest* is computed, for example by finite element method (FEM), and its frequency ω_{rest} registered. The mechanical mode of the solid is then computed, with its deformation profile $\mathbf{u}(\mathbf{r})$. Finally the optical mode is calculated again, but this time for the solid with *deformed geometry*, and the mode's frequency ω_{def} registered. The geometric frequency-pull parameter is then simply obtained by : $g_{\text{om}}^{\text{geo}} = -(\omega_{\text{def}} - \omega_{\text{rest}})/|\mathbf{u}(\mathbf{r})|$ in the limit of $|\mathbf{u}(\mathbf{r}_0)| \to 0$. Although very intuitive, this method is the most costly computationally speaking, because it requires to calculate the optical mode at least two times while the two others only require one such computation.

For the photoelastic frequency-pull $g_{\rm om}^{\rm pe}$, there is generally no simple analytic formula of the form $g_{\rm om}^{\rm geo} = \omega_0/L$. Formula 1.55 can however be adapted to the case of photoelastic coupling by changing the stress field resulting from radiation pressure by the stress field resulting from electrostriction :

$$g_{\rm om}^{\rm pe} = \frac{\iiint \sum \sigma_{ij}^{\rm es,1} S_{ij}^{\mathbf{u}} dV}{\hbar |\mathbf{u}(\mathbf{r})|} \tag{1.56}$$

The last numerical method presented for $g_{\rm om}^{\rm geo}$ calculations can also be adapted to $g_{\rm om}^{\rm pe}$. The two first steps are the same but in the final step the optical mode is calculated with the *new index profile* resulting from the mechanical strain. All these calculation methods have been implemented for numerical computation of frequency pull parameters in the case of OM disk resonators as will be seen in next chapter.

1.3.3 Thermo-optic effect

In a crystalline solid such as GaAs, a temperature increase has two consequences on EM fields oscillating within it: the solid boundaries are shifted due to the thermal expansion coefficient of the material, and the material's refractive index is also changed. Both these effects change the resonance condition of the cavity. The second effect (change of refractive index) is ∼1000 times larger in terms of cavity resonance shifting in GaAs miniature OM devices. Therefore in the following "thermo-optic effect" will only refer to the effects induced by the refractive index dependence on temperature. The thermo-optic effect contributes to the cavity resonance shift, just like geometric and photoelastic effects. In the linear limit, one can discuss a thermo-optic frequency-pull parameter proportional to $g_{\rm om}^{\rm th} = \partial\omega_0/\partial T$, but this parameter is less meaningful than the Lorentz force $g_{\rm om}$s discussed above. Indeed, in contrast to the case of Lorentz forces, the work of the photothermal force cannot be simply connected to $g_{\rm om}^{\rm th}$. The reason is that the photothermal force is not conservative, i.e. it cannot be grasped in an Hamiltonian description involving mechanical and optical degrees of freedom. Therefore, we will not use a $g_{\rm om}^{\rm th}$ to describe these forces.

This chapter provides a basic theoretical framework to understand OM effects. The concepts discussed are general to a vast diversity of experimental systems. The parameters used throughout this chapter, such as κ, $\Gamma_{\rm m}$, g_0 must be estimated accurately for the actual system under study, because they determine the amount of OM cooling achievable. Indeed, equation 1.42 can be rewritten as: $\bar{n}_{\rm cooling} = \bar{n}_{\rm th}/(1+C) + n_{\rm min}$, with C the OM cooperativity:

$$C = \frac{4 g_0^2 N_{\rm cav}}{\Gamma_{\rm m} \kappa} \tag{1.57}$$

This cooperativity should be maximized in order for OM cooling to yield a minimal phonon number. The study of OM parameters (κ, Γ_m, g_0) for GaAs disks is the subject of the next chapter.

Chapter 2

Gallium arsenide optomechanical disks

The devices we use for our OMs experiments are GaAs disks. Their radius varies from 0.5 µm to 5 µm and their thickness is on the order of 250 nm. These systems can confine light very efficiently as a consequence of the high refractive index of GaAs. They support mechanical modes of high frequency because of their small size, which is important in order to operate in the quantum regime (see section 1.1.5). Fabrication of such devices is presented in chapter 4. In this chapter we develop the physics of these OM disks, starting with the description of their optical whispering gallery modes (WGMs). We then present mechanical aspects, underlining radial breathing modes (RBMs), which are the mechanical modes of interest to us. In a last section opto-mechanical coupling constants are numerically computed for different parameters. Figure 2.1a is a schematic of a GaAs OM miniature disk. The red ellipse illustrates the optical WGM within the disk. The black arrows directed outwards represent the RBM motion. The disk "breathes", i.e. increases homogeneously its radius to occupy the volume delimited with dashes.

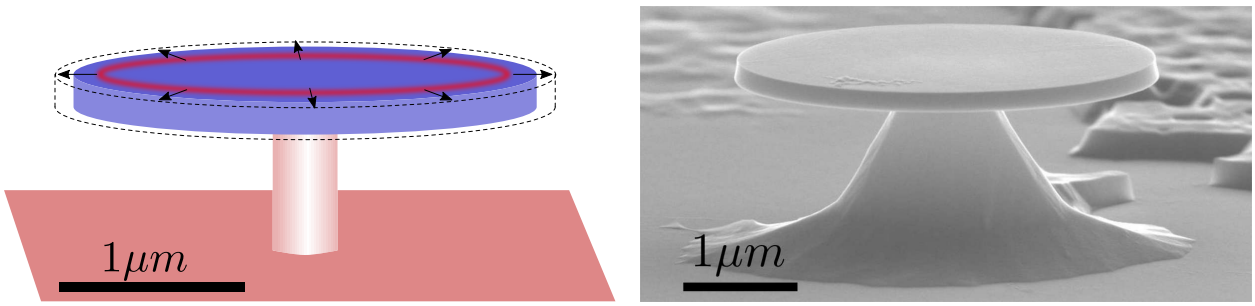

(a) Conceptual schematics (b) Experimental realization

Figure 2.1 – GaAs OM miniature disks

2.1 Optical modes of GaAs disks

2.1.1 Whispering gallery modes

This section will be dedicated to the study of optical WGMs. In semi-conductor disks surrounded by air, photons are guided along the disk's sidewall because of the refractive index mismatch. In a ray optics vision, a ray of light bounces along the disk edge by successive total internal reflections.

For a given disk geometry WGMs can be approximately described by analytic solutions of Maxwell's equations. Several assumptions for the fields have to be made, among which quasi transverse electric (TE) or transverse magnetic (TM) polarization decomposition and separation

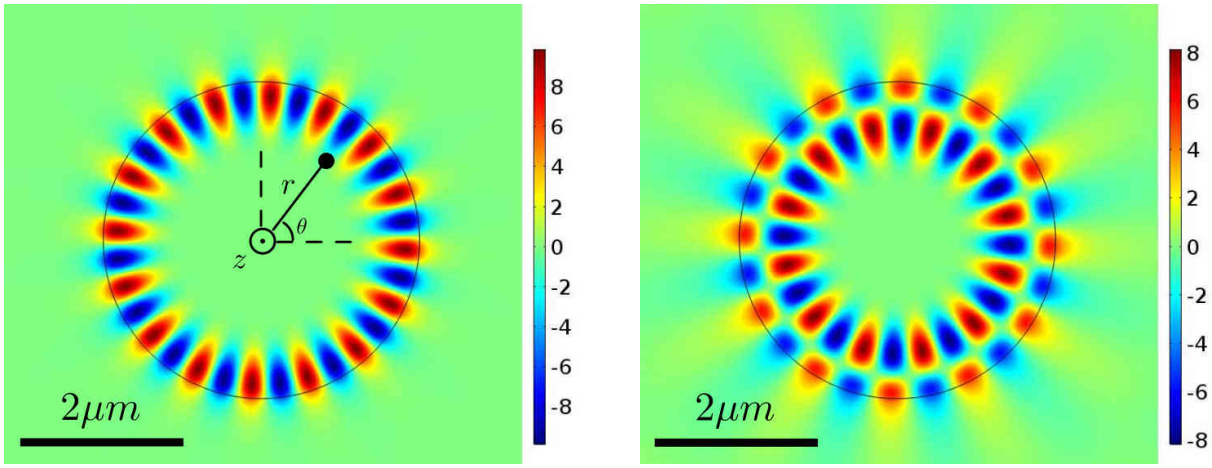

(a) $p = 1$, $m = 16$ @ 1580 nm. (b) $p = 2$, $m = 12$ @ 1620 nm.

Figure 2.2 – 2-dimensional numerical simulations of WGMs for a 2 µm-radius disk at $\lambda \approx 1600$ nm. The color scale is the component of the electric field orthogonal to the figure's plane (in arbitrary units). The $p = 2$ mode can be noticed to be more evanescent, a consequence of its smaller effective bending radius.

of variables (see [29, p. 25-31]). WGMs supported by a disk can be approximately divided in two families, i.e. TE and TM modes :

- TE modes correspond to solutions of Maxwell's equations where only the E_r, H_θ, and H_z components of the EM field are non zero.
- TM modes correspond to solutions of Maxwell's equations where only the E_θ, E_z, and H_r components are not vanishing.

One key outcome of this analytic treatment is that WGMs can be identified by 3 integer parameters p, m, and q (we use the usual (r, θ, z) cylindrical coordinate system). For both polarizations, the WGM's electric field r-component is given by:

$$E_r(r, \theta, z) = J_p(kn_\xi r)G_q(kn_\xi z)e^{-im\theta} \tag{2.1}$$

J_p is the p-th order Bessel function of the first kind, and G_q the q-th order distribution of a mode guided by an infinite slab waveguide. $p - 1$ is the number of nodes of the electric field along the r coordinate, $2m$ is the number of nodes along the azimuthal θ coordinate, and $q - 1$ is the number of nodes along z. In this work because we employ small disks ($R \sim 1$ µm) we will mostly work with $p = 1$, and $q = 1$ WGMs, and m will usually be on the order of 10.

Figure 2.2 shows WGMs numerical simulations for different values of p and m. The mode profiles are obtained by the FEM method using the Comsol software (see appendix B). In this 2D simulation, the electric field polarization in orthogonal to the disk plane. In order for these 2D simulations to be accurate, the refractive index of the domain corresponding to the disk is set to be the effective index n_{eff} of an infinite slab of same thickness (for the first order mode $q = 1$). In the limit where the WGM is localized close to the periphery ($p = 1$), an approximate formula can be written for the resonance condition (reminiscent of equation 1.1):

$$\exists m \quad | \quad 2\pi n_{eff} R = m\lambda_m \tag{2.2}$$

with R the disk radius. The effective index method, although simple to implement, sometimes lacks precision, especially when it comes to evaluate the radiation pattern of the WGM, which determines its bending quality factor (Q_{bend}). Performing a full 3D simulation yields accurate values for the resonance frequencies and Q_{bend} of WGMs, but is computationally costly. An interesting technique is to project such 3D computation in 2D by performing 2D-axisymmetric simulations of the disk.

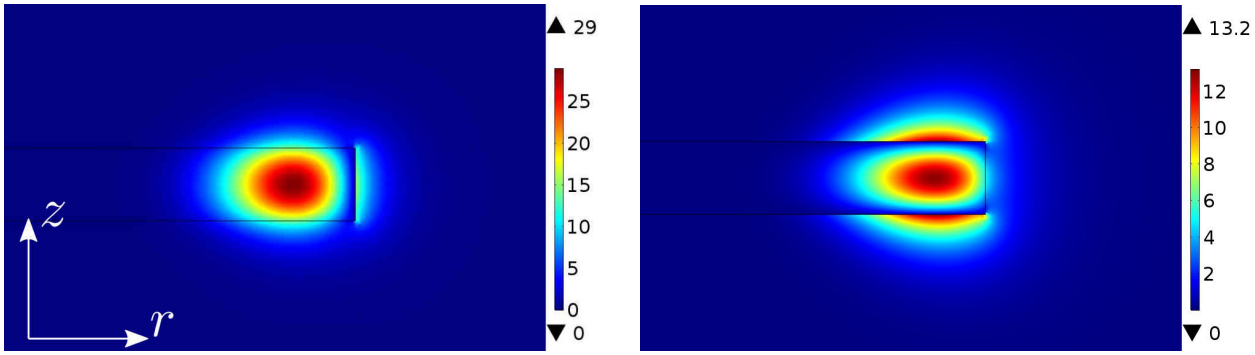

(a) E_r component of a TE mode (p=1,m=11). The field is continuous for horizontal interfaces only.

(b) E_z component of a TM mode (p=1,m=9). The field is continuous for vertical interfaces only.

Figure 2.3 – FEM simulations of WGM in the TE and TM case for $\lambda = 1550$ nm. The disk supporting the WGMs has a radius of 1 µm and a thickness of 320 nm. The field profiles are represented in a $(\mathbf{e}_r, \mathbf{e}_z)$ plane. The color scale unit is arbitrary.

In this variant Comsol performs a 2D simulation of a section of the disk in the (r, z) plane, while assuming the θ dependency of the electric and magnetic fields as $e^{im\theta}$, i.e. the field can be expressed as $\mathbf{E}(r, \theta, z) = \mathbf{E}(r, z)e^{im\theta}$. This in *not* an approximation as the problem has a perfect rotational symmetry around $\mathbf{e}_z$, provided the linear response of GaAs (which is isotropic) is considered. This method reduces importantly computational costs. However it cannot be used in the case of waveguide to disk coupling, as the straight waveguide in the disk vicinity breaks the rotational symmetry (see chapter 3).

Figure 2.3 shows (r, z) plane cuts of the electric field profile for a WGM at 1550 nm obtained by 2D axisymmetric FEM simulations. It can be seen that the TM mode (figure 2.3b) is slightly more evanescent, which is accountable for higher bending losses. A parameter of interest to us is the WGM's optical quality factor (Q_{opt}). It is defined as the energy stored in the WGM divided by the energy dissipated per cycle of the EM field oscillation: $Q_{\text{opt}} = 2\pi E_{\text{stored}}/\Delta E_{\text{cycle}}$. Q_{opt} can be linked to the loss rate κ introduced in chapter 1 : $Q_{\text{opt}} = \omega_0/\kappa$. The loss rates κ_i of all loss channels will be added to get the total loss rate of the disk. The total quality factor Q_{tot} can be obtain by: $Q_{\text{tot}} = (\sum_i 1/Q_i)^{-1}$. We now describe the different physical mechanisms that induce optical losses for WGMs.

2.1.2 Bending losses

Bending losses arises because the WGM is constrained to follow the disk's curvature. In the simple vision of a light ray reflected by successive total internal reflections on the disk sidewalls, no losses should occur. In a case where the light ray approximation is justified, as e.g. a $\lambda = 600$ nm WGM trapped inside a 50 µm water droplet, bending loss calculations yield a gigantic Q_{bend} of 10^{73}. However in our disks the concept of propagating light ray loses its validity because disk radius and wavelength become comparable. Bending losses therefore become consequent.

In the case of our miniature GaAs disks, bending losses are poorly estimated by the analytic approach, and we prefer to use Comsol FEM simulations, which are more precise. The simulation is carried out with perfectly matched layers (PMLs) in order to simulate an infinite space around the disk (more on PMLs in appendix C). It yields a complex frequency $\tilde{\omega}_0$ which imaginary part can then be used to calculate bending losses by the formula $Q_{\text{bend}} = \text{Re}(\tilde{\omega}_0)/[2\ \text{Im}(\tilde{\omega}_0)]$. Figure 2.4 displays Q_{bend} values of WGMs for different disk radiuses R. We will see in the next sections that other optical loss channels limit the quality factor of miniature GaAs disks to values in the $10^5 - 10^6$ range. The disk radius and thickness should therefore be chosen in order to have $Q_{\text{bend}} > 10^5$. This corresponds to $R \sim 1$ µm. These disks are our best candidates for quantum optomechanics.

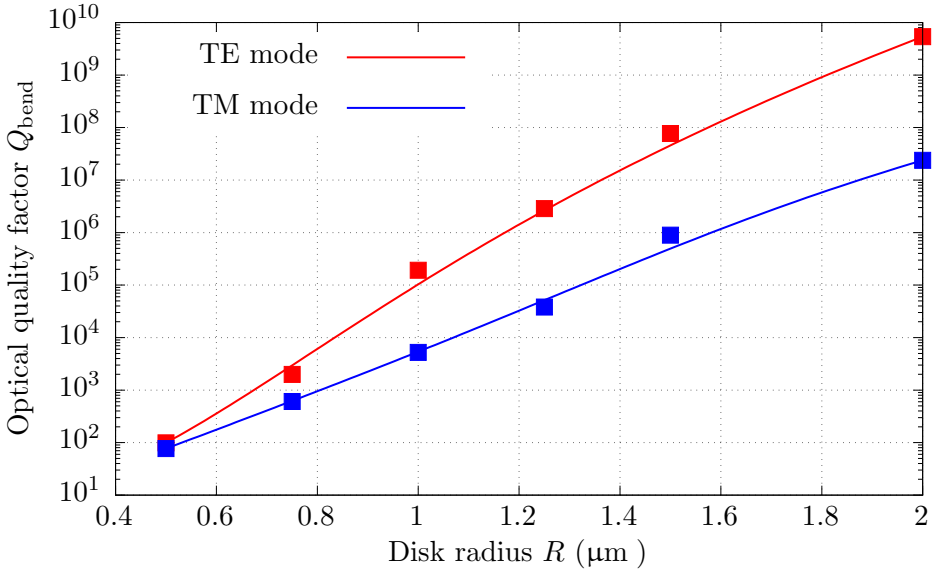

Figure 2.4 – Bending quality factors of TE and TM WGMs ($p = 1$, $q = 1$) at 1550 nm supported by disks of different radiuses and thickness 320 nm, simulated by FEM. For equal radiuses TE modes have a higher Q_{bend}. The lines are merely guides to the eye.

2.1.3 Scattering losses

Because of limitations inherent to the fabrication process, the real devices we handle cannot have a perfect geometry. An ideal miniature disk would have perfectly plane top and bottom interfaces, and an exactly circular vertical sidewall. The geometric quality of the horizontal surfaces is set by the molecular beam epitaxy (MBE) growth, it is usually very good, with a surface roughness less than one nanometer RMS. On the other hand the vertical sidewalls of our miniature disks are produced by vertical etching through a resist mask (see §4.1.3). The resist pattern irregularities are therefore transmitted to the disk during etching, yielding vertical sidewall geometric irregularity of 20 to 50 nm RMS, depending on fabrication quality, in all cases higher than for horizontal interfaces.

Such irregularities scatter light and therefore have deleterious effects on Q_{opt}. Many efforts have been engaged in order to limit the roughness of the vertical interface (horizontal surface quality is fixed by the wafer growth), but as of today it could still be the main optical loss channel of our devices. A detailed analysis made in our team [30, p. 91] on a disk of radius 2.5 µm fabricated by wet etching showed that residual irregularities were clamping the Q_{opt} of TE ($p = 1$) modes at a few 10^6 at $\lambda = 1550$ nm. However, the typical disks we fabricate for OM cooling experiments have a radius on the order of 1 µm, and result of a dry etching process. For such tiny disks, the same amount of residual irregularity is expected to have a more pronounced effect on Q_{opt}, especially for TE modes that scatter more on the vertical sidewalls. We anticipate these irregularities to clamp the Q_{opt} in the few 10^5 range for our 1 µm radius disks.

Figure 2.5 shows values of the electric field's square $|E|^2$ integrated on the disk's interface for different disk radiuses and mode polarizations. We choose to integrate the square of the electric field $|E|^2$ because this quantity is linear with the field scattered by surface polarization currents. $\int |E|^2$ is higher on the vertical interface for TE modes than for TM modes. However for the horizontal interfaces (the smoother ones) the situation is reversed, as $\int |E|^2$ is far greater for TM modes. We mentioned earlier that vertical interfaces should be expected to be more rough than horizontal ones. TE modes are therefore expected to be more sensitive to sidewall scattering.

Back-scattering and mode splitting Sidewall imperfections induce losses by scattering the light from the WGM at infinity. In other words, they couple the WGM to radiative modes of the

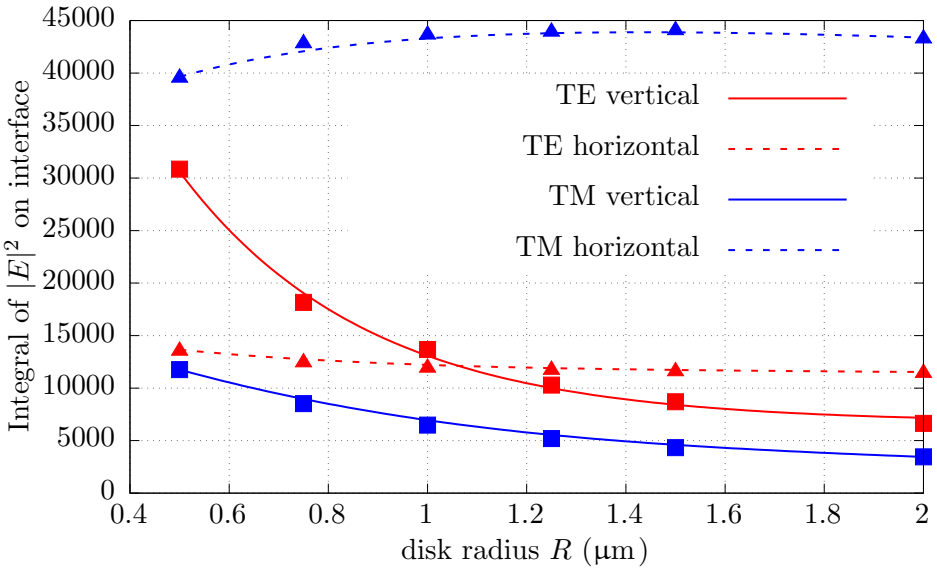

Figure 2.5 – Integral of the electric field on different interfaces (arbitrary units) for WGMs supported by disks of different radiuses. All the WGMs used for these calculations are normalized to a single photon energy. The disk thickness is 320 nm.

environment. However, sidewall imperfections can also transfer energy from one WGM to another. This coupling cannot be seen as a net loss of energy, but it has a consequence: mode splitting.

A WGM with phase evolution of the type $e^{-i\omega_0 t - m\theta}$ can spin clockwise (CW) or counter-clockwise (CCW) depending on the sign of m. Let us consider a propagating WGM turning in the CW direction. If the disk is perfectly circular, the opposite CCW WGM with identical p, m, and q parameters has exactly the same resonance frequency. In presence of imperfections, the CW and CCW modes feel slightly different boundaries (otherwise the disk boundaries would remain unchanged when flipping the disk upside down). This lifts the degeneracy: the two modes adopt slightly different frequencies, characterized by a splitting as can be seen on figure 2.6. The split Lorentzians in this figure were obtained using the same equations for the field amplitude $a(t)$ as in §1.1.4.1, but this time adding a "back scattering" coupling κ_r between CW and CCW modes:

$$\begin{cases} \frac{da_{\mathrm{cw}}(t)}{dt} & = -i\Omega_{\mathrm{m}} a_{\mathrm{cw}}(t) - \frac{\kappa}{2} a_{\mathrm{cw}}(t) + i\frac{\kappa_r}{2} a_{\mathrm{ccw}}(t) + \sqrt{\kappa_{ext}}s \\ \frac{da_{\mathrm{ccw}}(t)}{dt} & = -i\Omega_{\mathrm{m}} a_{\mathrm{ccw}}(t) - \frac{\kappa}{2} a_{\mathrm{ccw}}(t) + i\frac{\kappa_r}{2} a_{\mathrm{cw}}(t) \end{cases} \tag{2.3}$$

The detail of calculations can be found in [20, P. 215-216]. At resonance, the EM field in the disk becomes a standing-wave, corresponding to a symmetric and anti-symmetric combination of CW and CCW modes. The splitting between the symmetric and anti-symmetric peaks in the spectrum is equal to $2\kappa_r$, which allows to experimentally assess the amount of edge imperfections.

2.1.4 Absorption losses

GaAs has a gap energy of ∼1.5 eV (the value changes slightly with temperature). This means that photons satisfying the condition $\hbar\omega < 1.5$ eV should propagate without optical losses due to linear absorption. This corresponds to a minimum wavelength of $\lambda \sim 850$ nm. For our experiments we often operate at $\lambda = 1550$ nm (or $\lambda = 1320$ nm), which widely satisfies the non-absorption condition.

Surface absorption

The band structure of GaAs with gap energy equal to ∼1.5 eV is a property of the bulk, i.e. it is deduced from calculations where the GaAs crystal is supposed to have infinite extents in space.

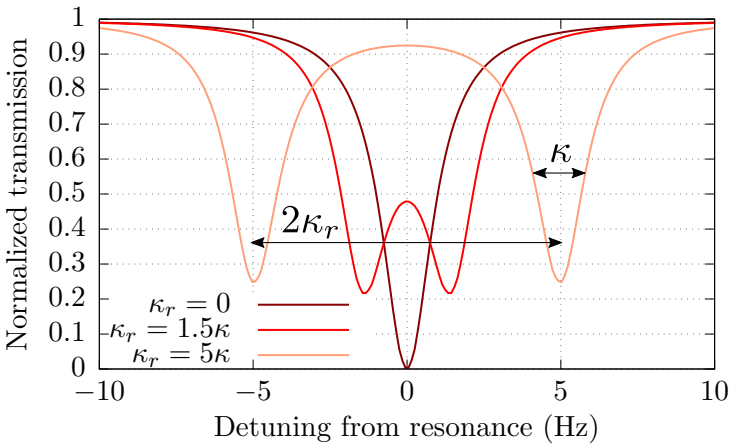

Figure 2.6 – Splitting of a WGM Lorentzian response under the influence of back scattering induced mode coupling.

However a tiny piece of crystal (like our disks) has edges. The GaAs structure re-organizes at these interfaces and the local band structure is of the environment, modified. Moreover, surfaces also interact with other chemical elements which can further modify the local band structure, by e.g. oxidizing the surfaces. These two effects are responsible for the apparition of mid-gap states, possibly "tuned" to the energy of the photons we use, therefore resulting in absorption of sub-bandgap photons. The impact of this process is double as it lowers Q_{opt}, but also generates heat in the device that causes optical instabilities (§D). In practice surface absorption is thought to be a central loss process in our devices. Together with scattering losses, it limits optical Q_{opt} to a value of roughly 10^5.

An efficient way to avoid such detrimental reorganization of the disk interfaces is to *passivate* the surface. The idea is to grow, on the *clean* GaAs surface, a layer that will not chemically react with the environment, or at least mitigate the density of unwanted mid-gap states.

First efforts in our team focused on a wet nitridation process [31] that indeed passivates and improves luminescence properties of disks, but showed no impact on Q_{opt} and absorption. A second route explored in out team has been atomic layer deposition (ALD) of aluminum oxide (Al_2O_3). This technique consists in exposing the clean GaAs surface to different chemicals in an alternative way [32]. Each precursor-reactant cycle deposits a mono-layer of the desired chemical on the surface, so that the grown Al_2O_3 thickness can be controlled with sub-angstrom precision. ALD was successful with our devices as we could measure a 2 to 3 times enhancement of Q_{opt}, as well as a clear reduction of absorption-based thermal effects [33]. This result confirms that surface absorption is an important and limiting optical loss channel in our devices, and gives us a handle to limit it.

Bulk absorptions

In spite of the high quality of the GaAs material we use for the fabrication of our devices, some amount of defects (chemical impurities, stress induced vacancy sites) remain in the bulk. As for surface reconstruction, these defects locally modify the band structure. Mid-gap states can therefore appear and can cause linear absorption. In practice this bulk sub-bandgap absorption is small compared to surface absorption, as is hinted by the 3 times Q_{opt} enhancement resulting from ALD.

Another bulk absorption to consider is two photon absorption (TPA). Although one photon at $\lambda = 1550$ nm is not energetic enough to promote an electron to the conduction band, two photons have sufficient energy (1550nm/2 < 850nm). The TPA absorption rate scales with the square of the optical intensity in our disks. This quadratic dependency is quite intuitive if one considers that

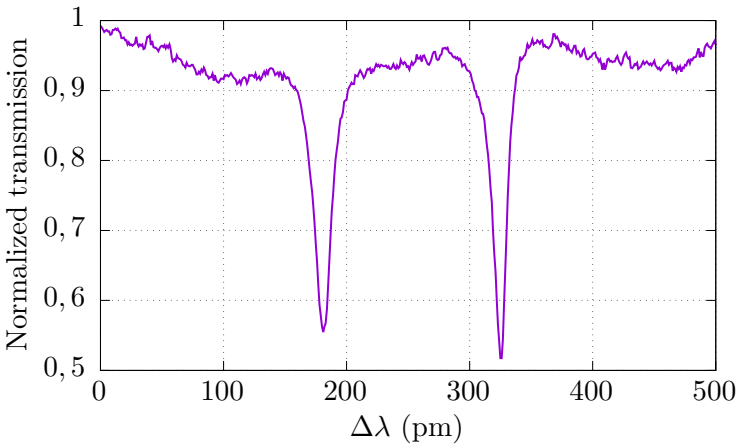

Figure 2.7 – Low power spectroscopy of a WGM near 1290 nm ($\Delta\lambda = 0$ on the graph) of a 1.3 µm disk before passivation. The splitting of the resonance can be clearly observed. The independent modes have a FWHM of ∼10 pm, which corresponds to a Q_{opt}∼130 000. After ALD passivation, Q_{opt} of ∼300 000 could be observed on such disks.

a TPA event requires two photons to coincide in time and space. Absorption in our systems can therefore be expressed as:

$$\frac{dI(z)}{dz} = -\alpha I(z) - \beta I(z)^2 \tag{2.4}$$

with I the light intensity in W/m^2 and z the position along the optical path. α is the linear absorption coefficient taking into account surface and bulk defects absorption. β is the TPA coefficient. In GaAs the β coefficient values vary between ∼ 20-30 cm/GW at 1300 nm and ∼ 10-15 cm/GW at 1500 nm [34, 35]. Because of the high Q_{opt} of our resonators the optical intensity in the cavity is large and TPA can limit Q_{opt} even when working with low laser power incident on the cavity (∼50 µW). TPA cannot be avoided with fabrication efforts. The only way to counter it is too work at large wavelengths for which the TPA coefficient β decreases or to employ other materials like AlGaAs [36].

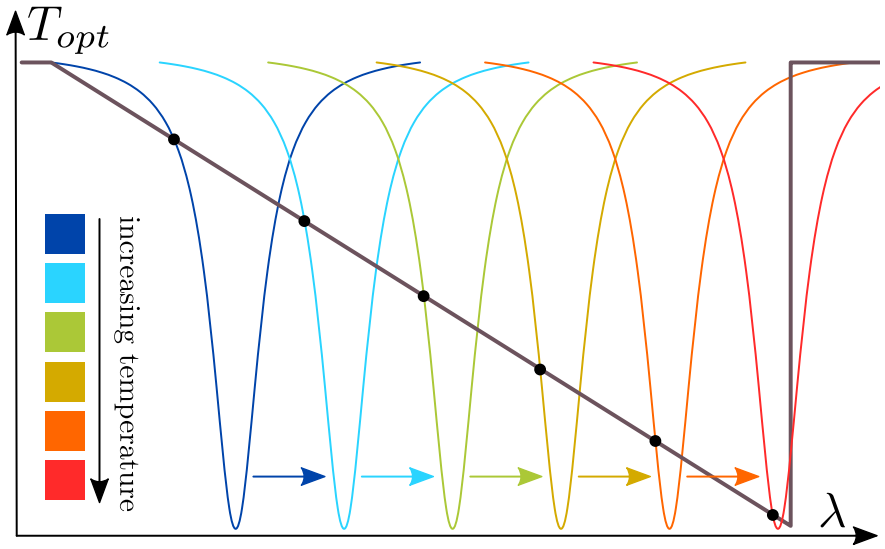

Figure 2.8 – Illustration of the resonance deformation due to thermo-optic effect

2.1.5 Thermooptic triangular envelope

A major consequence of the thermo-optic effect presented in §1.3.3 is the deformation of the Lorentzian optical response into a triangular shape. To explain this effect we will make use of figure 2.8. On this figure, λ is the scanning wavelength sent to probe the system, and T_{opt} is the optical power transmitted at the system's output. The deep blue Lorentzian curve on the left hand side corresponds to the Lorentzian response when the system is at ambient temperature. Now let's say that, starting from the low wavelength side, we scan the laser so that we enter the deep blue Lorentzian from the left. A fraction of the optical power sent in the disk is absorbed by surface or bulk absorption, which results in some generated heat and therefore in some temperature increase. The refractive index thus increases, and the new resonance wavelength of the system is shifted to the right (light blue Lorentzian). If the scanning wavelength is increased again, more power is sent into the cavity, so the resonance is shifted more to the right, etc. The cavity resonance therefore seems to be "running away" from the laser scanning. This phenomenon is shown in discrete steps on figure 2.8 but it is actually continuous. When the cavity resonance is finally reached (red curve), no additional power can be used to heat the system and shift the mode even more, the cavity therefore "unhooks" and swiftly comes back to its starting position. The transmission therefore "hops" to 100%. This whole process results in an effective response given by the triangular brown curve. When a higher laser power is used, the cavity is heated more so that the triangular brown curve extends to larger wavelengths.

2.2 Mechanical modes of GaAs disks

GaAs disks are also *mechanical* resonators. They support many vibrational modes, which are more complex than the canonical harmonic motion of a spring loaded mirror presented in chapter 1. We will see that some of these modes couple to the optical degree of freedom (the photons in the cavity), while some others do not, and are therefore of little interest to us. For instance, in the case of the Fabry-Pérot cavity with a spring loaded mirror, a mechanical mode consisting in a mirror displacement orthogonal to the light propagation direction would not couple at all to the optics. We start with an analytic and numerical description of the mechanical modes of disks. Then we present the different types of mechanical losses than can be encountered and solutions to limit them.

2.2.1 Modes of thin disks: analytic approach

A mechanical mode is characterized by a frequency Ω_{m} and a profile function $\mathbf{u}(\mathbf{r})$. The motion of the mechanical system can then be described by its displacement field: $\mathbf{u}(\mathbf{r},t) = \mathbf{u}(\mathbf{r})\cos(\Omega_{\text{m}}t)$. This description of motion is actually an approximation, that holds as long as $|\mathbf{u}(\mathbf{r})|$ is small compared to the size of the mechanical system (mechanical non-linearities can be neglected and the notion of eigenmodes remains relevant). This condition is largely satisfied for quantum optomechanics. The analytic results presented in this section apply to a mechanically isotropic material for which the Young modulus E and Poisson ratio σ can be defined. In the case of a mechanically anisotropic material (which is actually the case for GaAs), numerical simulations are better employed.

We focus on the family of *in plane* modes of disks, which is of highest interest for OM experiments. These modes are characterized by a displacement vector $\mathbf{u}(\mathbf{r})$ that lies in the plane of the disk. Three categories of in plane modes can be distinguished (figure 2.9). Tangential modes (a) are mostly "compression-dilatation" modes in the azimuthal direction, with no displacement of the disk's boundary. In the case of wineglass modes (b) the boundary is displaced, but in an ellipse shape so that the disk's boundary length remains the same at first order. Only in the case of radial modes (c) is the boundary length greatly modified. Those are the modes that couple efficiently with photons. In the following these radial modes are referred to as radial *breathing* modes (RBM),

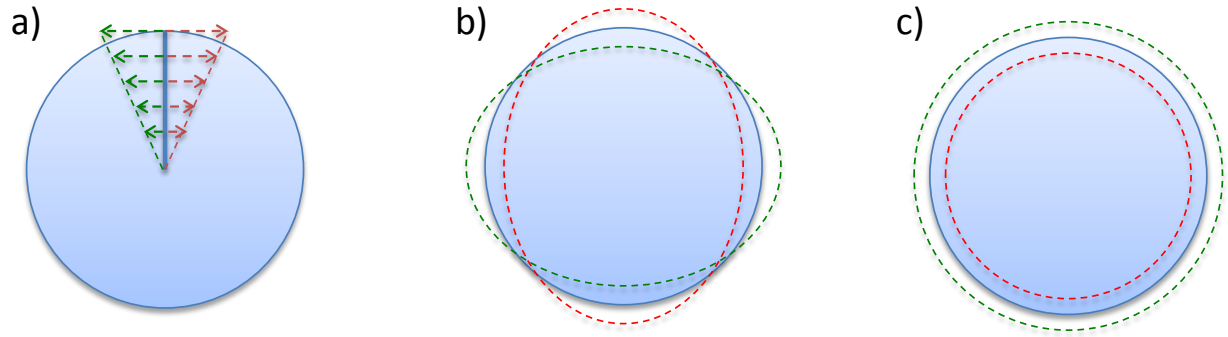

Figure 2.9 – The three categories of in plane modes. a) Tangential modes: the displacement is purely tangential. b) Wineglass modes: the displacement of the disk periphery is elliptic. c) Radial modes: the displacement $\mathbf{u}(\mathbf{r})$ is purely radial.

to image the fact that the disk radially expands and contracts during the mechanical motion, i.e. the disk is "breathing".

Analytic solutions for RBMs of successive order can be found [37, 38]. The displacement of the p-th order RBM is a function of r only and can be expressed as :

$$\mathbf{u}(r,\theta) = \mathrm{u}(r)\mathbf{e}_r = C\alpha_p J_1(\alpha_p r)\mathbf{e}_r \tag{2.5}$$

with C a normalization constant and J_1 the Bessel function of the first kind of order 1. α_p is a parameter depending on the material's density, Young modulus E, Poisson ratio σ, and on the RBM's eigenfrequency Ω_m. Ω_m takes different values for the successive RBMs of order p, and α_p hence depends on the RBM order considered. The successive eigenfrequencies for the RBMs of increasing radial order p can be found by solving the following equation :

$$\frac{\zeta}{\xi}\frac{J_0(\zeta/\xi)}{J_1(\zeta/\xi)} = 1-\sigma \quad \text{with} \quad \begin{aligned} \zeta &= \Omega_\mathrm{m} R\sqrt{\tfrac{\rho(2+2\sigma)}{E}} \\ \xi &= \sqrt{\tfrac{2}{1-\sigma}} \end{aligned} \tag{2.6}$$

The term "$\Omega_\mathrm{m}R$" in the expression of ζ hints that RBM frequencies scale as $1/R$.

2.2.2 Numerical simulations of disk mechanical modes

The analytic discussion presented above is useful as it provides some insight on the mechanics of such disks, but it is only approximate. The two main approximations made by the analytic model for RBMs are the following :

- the radial component of the displacement u_r does not depend on z. Although quite correct for the first order RBM, this approximation (2D plate approximation) does not hold well for higher order RBMs (see figure 2.10).
- the material is supposed to be isotropic, and hence uniform Young modulus E and Poisson ratio σ can be defined. This is actually not true for GaAs (and most materials with crystalline structure), and the full elasticity tensor should in principle be taken into account. This isotropic approximation yields acceptable eigenfrequency values, but can cause errors for g_om and mechanical quality factor (Q_m) calculations.

In order to be more predictive on the eigenfrquency values, but also on g_om parameters and Q_m, numerical simulations are required. The 2D plate approximation can be overcame by performing 3D calculations in the form of 2D axisymmetric FEM in the (r,z) plane. The material is supposed isotropic so that the problem respects a perfect rotation symmetry. The displacement is now solved as a function of r and z. 2D-axisymmetric simulation results are shown on figure 2.10.

Calculation type	f_{RBM1}	f_{RBM2}	f_{RBM3}	f_{RBM4}
Analytic (formula 2.6)	1.071 GHz	2.803 GHz	4.456 GHz	6.098 GHz
2D-axisymmetric	1.068 GHz	2.748 GHz	4.184 GHz	5.224 GHz
3D anisotropic	1.074 GHz	2.947 GHz	4.541 GHz	5.542 GHz

Table 2.1 – RBM eigenfrequencies determined by different means. The material parameters used for GaAs are taken from [39]

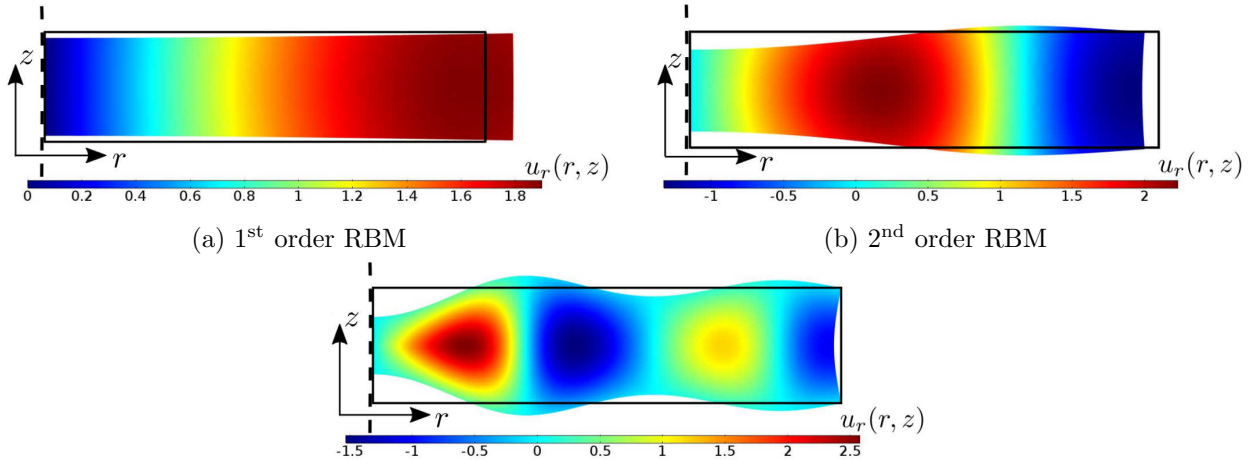

(a) 1st order RBM

(b) 2nd order RBM

(c) 4th order RBM

Figure 2.10 – RBM displacement $u_r(r,z)$ calculated with 2D-axisymmetric FEM. The black rectangle symbolizes the position of the disk's outer edges at rest. The displacement unit is arbitrary.

If one wants to push the simulation precision one step further, and this is necessary for some Q_{m} and g_{om} estimations, then a complete 3D FEM simulation must be performed. Indeed, the GaAs elasticity tensor C is not constant with orientation θ. These simulations are way more costly computationally. Thanks to the face-centered cubic lattice of GaAs the 36 components of the tensor can be reduced to the three components c_{11}, c_{12}, c_{44}. The conventions on index are the same as those used for equation 1.49. In a cubic crystal like GaAs a rotation around the z-axis by an amount θ is equivalent to a rotation by $\theta' \in [0, \pi/4]$. Therefore it is sufficient to perform the 3D FEM simulation in a "piece of cake" corresponding to $1/8^{th}$ of the complete disk (see figure 6.6). This divides computational costs by a factor 8 or more[1].

Table 2.1 summarizes frequency values for RBM of different orders. Note that analytic and 2D-axisymmetric methods agree well for the RBM1 but depart from another for RBMs of higher order. The reason is that the 2D plane approximation does not hold for high order RBMs as mentioned earlier. This can be seen on figure 2.10, where the color scale accounts for the radial displacement $\mathrm{u}_r(r,z)$, and where a z dependence is clearly visible.

Figure 2.11 displays mode profiles of RBMs of orders 1 and 2 for 2D-axisymmetric and 3D anisotropic simulations. The 2nd order RBM's profile is more distorted when going from 2D to 3D simulation. This corroborates the higher relative error found on the eigenfrequency (table 2.1).

[1]Computation time is supposed to scale linearly with the number of nodes, but in practice the dependency is overlinear, supposedly because of memory management complications.

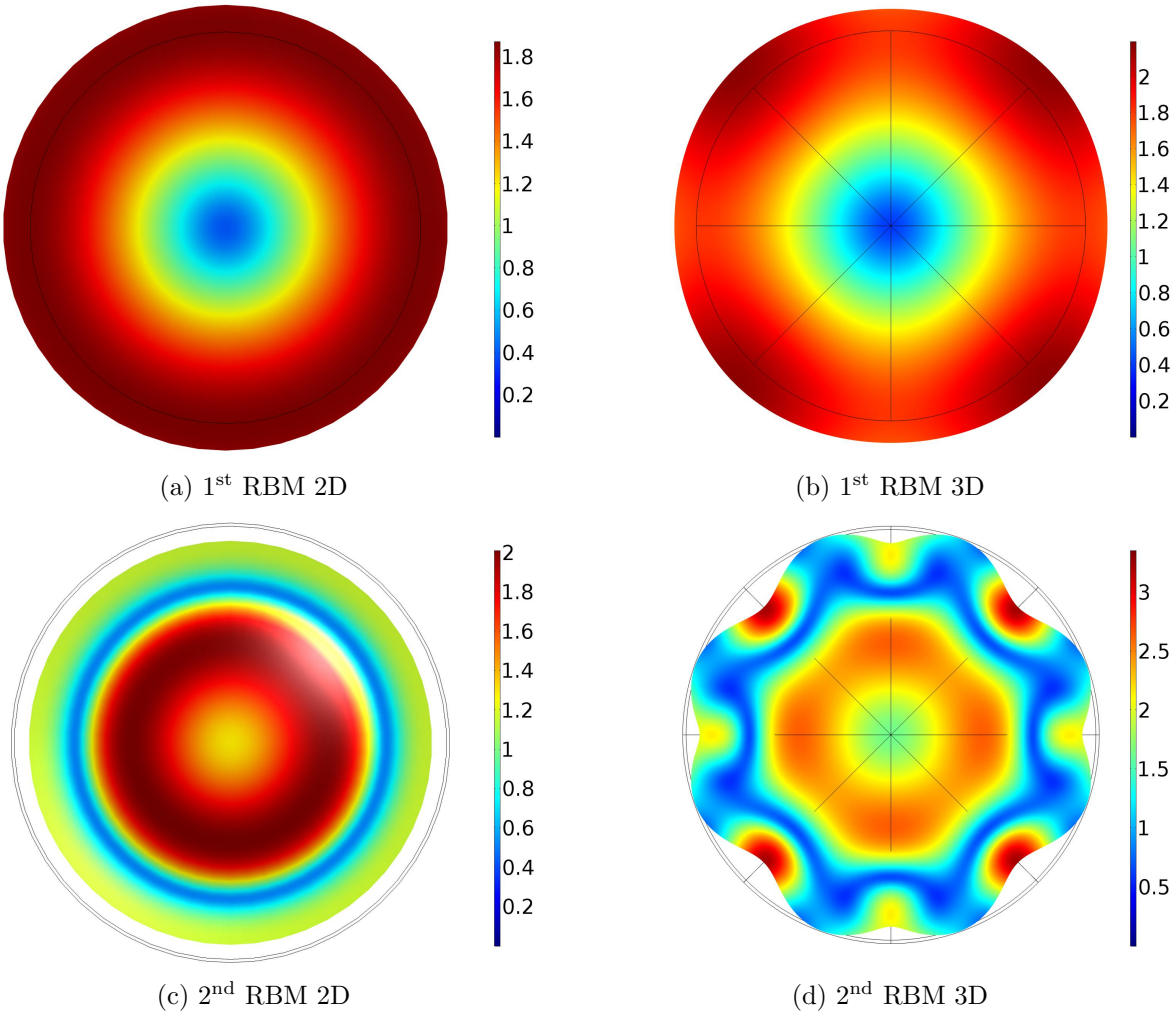

(a) 1st RBM 2D

(b) 1st RBM 3D

(c) 2nd RBM 2D

(d) 2nd RBM 3D

Figure 2.11 – Comparison of RBM displacement profiles obtained by either 2D-axisymmetric or 3D anisotropic FEM simulations. Disks are seen from the top. The black line accounts for the disk's position at rest. The displacement $|\mathbf{u}(r,\theta)|$ is shown in an arbitrary unit. The effect of anisotropy is limited for the RBM1, but is important for the RBM2, with a strongly distorted mode profile.

2.2.3 Mechanical losses in GaAs disks

The Q_m of our devices is a parameter of great interest to us. Indeed, in the context of OM cooling, the amount of cooling scales linearly with Q_m. Alternatively, the product of the mechanical quality factor with the mechanical frequency, $Q_\mathrm{m} \cdot f_\mathrm{m}$, is a figure of merit which has been extensively employed in the micro electro-mechanical systems (MEMS) community. In quantum optomechanics experiments, it is also of paramount importance [40] as it sets the number of coherent quantum operations that can be performed on the mechanical device. In this section we will present the various physical mechanisms that are responsible for mechanical dissipation in our devices, and discuss associated values of Q_m and $Q_\mathrm{m} \cdot f_\mathrm{m}$.

2.2.3.1 Thermo-elastic damping

Thermo-elastic damping occurs in a material subject to strain gradients, as is the case for our miniature disks. During the deformation, regions subject to tensile strain cool down while regions subject to compressive strain heat up, as a result of the material's thermal expansion coefficient α_{th}. This results in a heat flow from the hot source to the cold one, thus generating entropy. Mechanical energy is therefore lost. Two remarks :

- It is not necessary for the mechanical structure to undergo simultaneous compressive and tensile strains in order to obtain such loss: if a gradient of compressive strain exists in the structure, then infinitesimal sources at different temperature are generated, causing some heat flow.
- An essential parameter for thermo-elastic damping is the thermal expansion coefficient α_{th}, which links strain to temperature. For GaAs this coefficient goes to zero twice, for temperature of 56 K and 12 K [39]. Therefore at these temperatures virtually no thermo-elastic damping should take place.

For our mechanical resonators[2], FEM simulations of thermo-elastic damping yielded Q_{m} values of 10^5 at 300K and 10^9 at 3K [20, p. 58]. Thermo-elastic damping is therefore not a concern for cryogenic experiments.

2.2.3.2 Air damping

In some experiments, dissipation due to the surrounding fluid can occur. The disk's outer boundaries move and produce some work on the surrounding gas or liquid. The moving fluid dissipates this energy through viscosity (viscous loss regime). These losses can be simulated with the Stokes spheres method. Simply put, analytic solutions for the motion of a sphere undergoing linear oscillations in a viscous fluid are known [41]. The idea is then to "cover" our structures with Stokes spheres and impose to these spheres a motion equal to the motion of the mechanical mode of interest. In the case of out of plane flexural motion of disks this technique gave satisfying results with Q_{m} in the few hundreds [42], matching experimental measurements. The disk boundary displacement is smaller for RBMs, and therefore lower air damping is expected. Recently, a model was developed in our team that allowed to express analytically the Q_{m} of RBMs when limited by viscosity of the surrounding fluid [43]:

$$Q_{\mathrm{viscous}} = \frac{3.34 \cdot 10^5/\sqrt{\rho\mu}}{3.18/\sqrt{R} + \sqrt{R}/H} \tag{2.7}$$

yielding a value Q_{viscous}=11000 for small disks of radius R=1 μm and thickness H=320 nm in air (ρ_{air}=1.2 kg/m^3, μ_{air}=18.6 μPa·s). Experimentally, for small disks not limited by clamping losses (see next section) we measure a Q_{m} around 1500 in air at ambient pressure, increasing to ∼2000 in vacuum (10^{-3} mbar). This value of 2000 is supposed to be attributable material induced losses (see §2.2.3.4). The air limited quality factor can therefore be found:

$$(\underbrace{Q^{-1}_{\text{free carriers}}}_{=1/2000} + Q^{-1}_{\mathrm{air}})^{-1} = 1500 \Rightarrow Q_{\mathrm{air}} = 6000 \tag{2.8}$$

The disagreement between Q_{air} and Q_{viscous} could be explained by a lack of precision for formula 2.7, or by the fact that viscosity is not the only phenomenon creating losses in the case of air. In the case of cryogenic operation, the resonator environment is vacuum (pressure levels are around 10^{-4} mbar) so that air damping is not a concern anyways.

2.2.3.3 Clamping losses

Clamping losses correspond to the dissipation of energy into the substrate through the anchoring point of the mechanical system. They are determined by the system's geometry (anchor included) and the material's acoustic properties. These parameters do not change much with temperature (GaAs acoustic properties change by a few percent between 300 K and 0 K), so that clamping losses remain at first order constant over the full temperature range accessible in our experiments.

[2] disks of 1 μm radius, 320 nm thick, 1$^{\mathrm{st}}$ order RBM @ 1.4 GHz

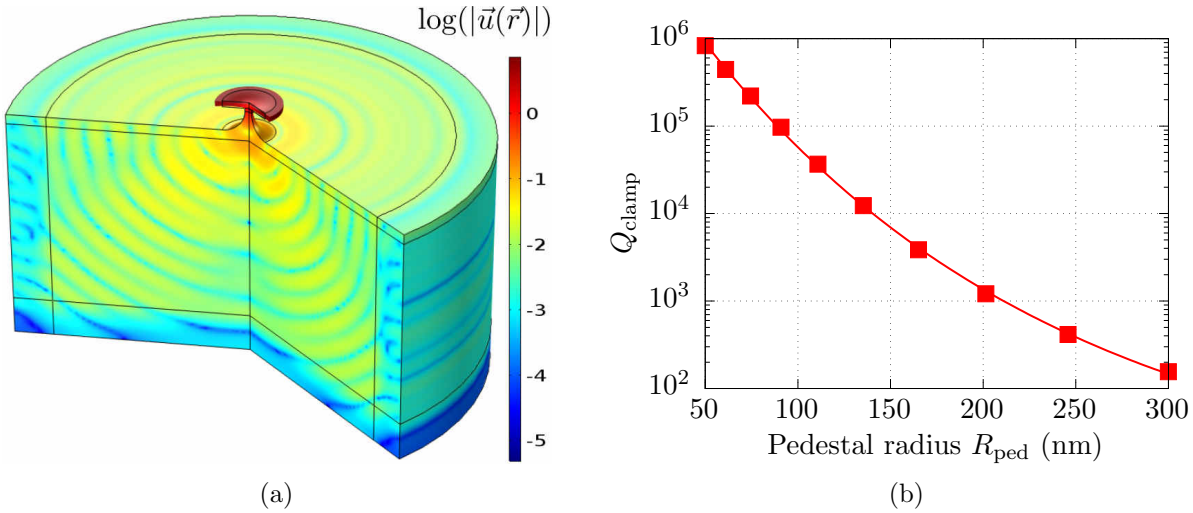

(a) (b)

Figure 2.12 – Clamping losses numerical simulations. (a): 2D-axisymmetric FEM simulation of clamping losses. The waves leaking in the substrate can clearly be seen, as well as their absorption by PMLs. (b): Q_{clamp} vs. R_{ped} (in nanometers) for a disk of radius 1.3 µm and thickness 300 nm. A strong dependance with R_{ped} can be seen.

As can be seen in figures 2.1 and 2.12a our disk is supported by a centered pedestal. The dissipation mechanism involves the Poisson ratio ν of GaAs. When the disk undergoes a positive radial extension ΔR, its thickness will decrease by an amount $\nu\Delta R$. This can be intuited as a "conservation of volume" law. The radial oscillation of the disk therefore induces vertical compression/expansion cycles of the disk plate, hence the disk sends compression waves to the pedestal that are transmitted to the substrate in the fashion of a "miniature jackhammer". This mechanism was investigated analytically in [44], but we preferred to rely on FEM simulations, because the analytic model developed in [44] supposes that the disk is an ideal plate which displacement is confined within the disk plane. This assumption does not hold well for our disks with high thickness to radius ratio. Two numerical simulation approaches have been employed during this PhD work:

- The frequency sweep method consists in exciting the disk on its vertical boundaries with oscillating forces of constant amplitude but of varying frequencies. For each frequency the response of the system – more precisely the displacement amplitude of the disk's boundary – is calculated. The amplitude response as a function of frequency is a Lorentzian-like curve peaked at the mechanical mode's eigenfrequency Ω_{m}. The mechanical quality factor can then be extracted as Ω_{m} divided by the FWHM of the curve. These simulations are carried with PMLs at the external boundaries of the computation volume (see figure 2.12a) to absorb waves and avoid back-reflexions.

- Another method consists in finding the complex eigenfrequencies $\tilde{\Omega}_{\mathrm{m}}$ of the system. They are complex because of PMLs that absorb outgoing waves. The clamping loss quality factor (Q_{clamp}) can then be obtained as $\mathrm{Re}(\tilde{\Omega}_{\mathrm{m}})/[2\ \mathrm{Im}(\tilde{\Omega}_{\mathrm{m}})]$.

The complex eigenfrequency method is less costly computationally, because one simulation only needs to be performed to obtain a Q_{clamp}, whereas the frequency sweep technique requires one simulation by point, and typically 50 points are needed to reconstruct the Lorentzian response curve. Figure 2.12b shows the final result of such simulations. The Q_{clamp} of a GaAs disk of radius R =1.3 µm and thickness T =300 nm oscillating at f_{m}=1 GHz can reach 10^5-10^6 for a pedestal radius between 90 and 50 nm, corresponding to a $Q_{\mathrm{m}} \cdot f_{\mathrm{m}}$ value of 10^{14}-10^{15}. Experimentally, the control of pedestal radius below 100 nm is a real challenge, and alternatives will be discussed in chapter 6.

2.2.3.4 Material induced losses

Material induced loss has been reported as the limiting loss factor in some micromechanical systems [45, 46]. These losses are supposedly caused by the relaxation of defect states in the bulk or surface of the device. Figure 2.13 displays the experimentally measured Q_{m} of one of our device vs. temperature. The Q_{m} drops by a factor 5 from 3 K to 300 K. According to simulations, this drop cannot be attributed to any of the mechanical dissipation phenomena listed previously. We therefore think than the decrease of Q_{m} on figure 2.13 is due to dissipative interaction between phonons and thermally activated 2-level systems.

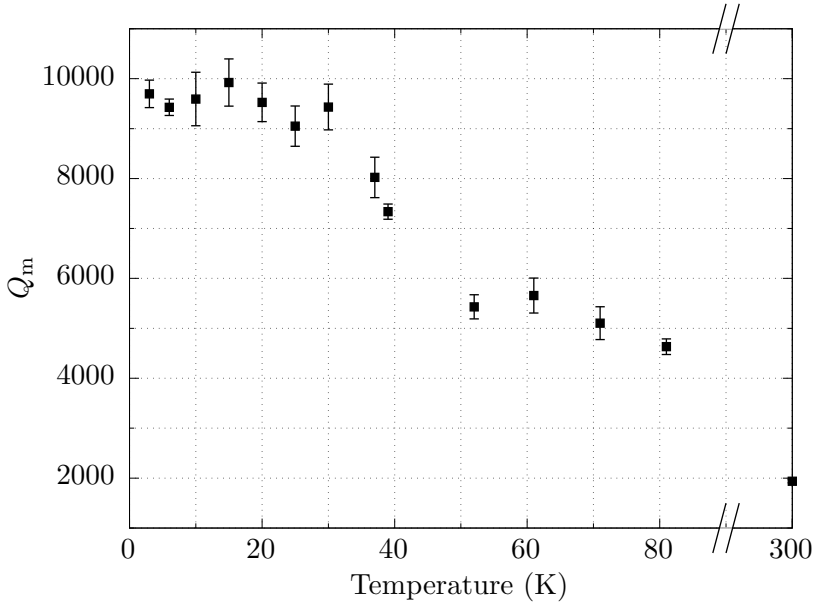

Figure 2.13 – Mechanical quality factor measured as a function of sample temperature. A plateau can be observed from 0 to 30 kelvin, followed by a quick decay

2.3 Optomechanical coupling in GaAs disks

We now focus on the estimation of OM coupling constants in GaAs disks. The different processes inducing OM coupling were presented in chapter 1. The case of geometric OM coupling for a disk supporting a WGM is similar to the Fabry-Pérot case: when the disk mechanically "breathes", its radius becomes greater and the optical round trip path around the disk becomes longer, increasing the resonance wavelength. The geometric frequency pull parameter for disks can be shown to be [20]: $g_{\mathrm{om}}^{\mathrm{geo}} = \omega_0/R_{\mathrm{disk}}$, quite similarly to equation 1.53. Accurate g_0 calculations as a function of the geometry are crucial in order to choose the best disk design. This section will be organized in two parts. In a first part 2D-axisymmetric g_0 estimates are shown for different mechanical modes, light polarizations and disk radiuses. In a second part g_0 calculations incorporating 3D anisotropic mechanical simulations are introduced.

2.3.1 2D-axisymmetric g_0 calculations

Figure 2.14 displays g_0 values computed with 2D-axisymmetric FEM simulations. The g_0 parameters are obtained by adding the geometric and photo-elastic contributions (i.e. $g_{\mathrm{om}}^{\mathrm{geo}}$ and $g_{\mathrm{om}}^{\mathrm{pe}}$) and multiplying the sum by x_{ZPF}. The calculation method used is the one based on energy considerations (see §1.3.2). Both WGMs and mechanical modes are calculated using 2D-axisymmetric simulations. EM field polarization has a strong impact on the g_0 values obtained. This reveals the importance of such simulations, as the analytic formula $g_{\mathrm{om}}^{\mathrm{geo}} = \omega_0/R_{\mathrm{disk}}$ does not take polarization

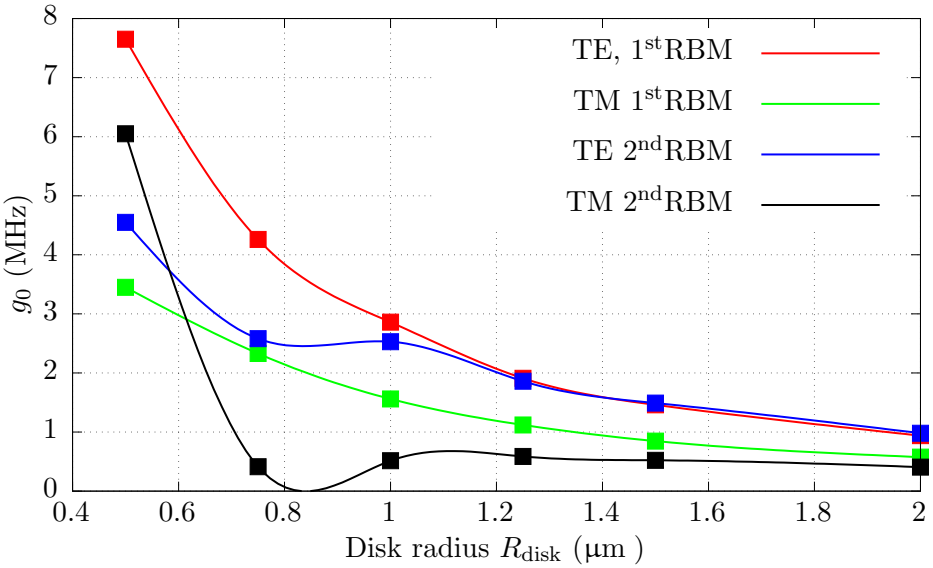

Figure 2.14 – 2D-axisymmetric simulations of the OM coupling constant g_0 for different disk radiuses, RBM order and EM field polarization. The disk thickness is T_{disk}=320 nm, and the wavelength of the RBM coupling to the mechanics is ∼1550 nm. The general tendency is a decrease of g_0 with the disk radius. The optical mode polarization, as well as the RBM order, have a strong influence on g_0.

into account. The reader can remark that for TM optical modes coupled to the 2$^{\text{nd}}$ order RBM, g_0 falls quickly from 6 MHz for a 0.5 μm disk to 0.4 MHz for 0.75 μm. In this range of radius $g_{\text{om}}^{\text{geo}}$ and $g_{\text{om}}^{\text{pe}}$ take similar absolute values but opposite signs. Such situation should obviously be avoided when choosing disk radius and thickness.

Let us illustrate that $g_{\text{om}}^{\text{geo}}$ varies in a more complex manner with geometry than what is predicted with the analytic formula $g_{\text{om}}^{\text{geo}} = \omega_0/R_{\text{disk}}$. As the disk expands radially, it also gets thinner because of the positive Poisson ratio of GaAs. A thinner disk corresponds to a smaller effective index for the WGM circulating inside the disk, so that from this effect alone the resonating optical wavelength should decrease, while it increases because of radial expansion. In the case of a 0.5 μm radius disk, the ratio of thinning over radial stretching is 6 times more than for a 2 μm disk. For this reason the outer boundary $g_{\text{om}}^{\text{geo}}$ calculated by FEM in the case of a TM mode and 1$^{\text{st}}$ RBM is 0.06 THz/nm for a 0.5 μm radius disk and 0.17 THz/nm for a 2 μm radius disk. This in in strong disagreement with the analytic formula, showing the importance of precise simulations.

2.3.2 3D g_0 calculations

A was mentioned is §2.2.2, GaAs mechanical properties are not isotropic, and 3D simulations are needed in order to solve for the mechanics precisely. On the other hand GaAs is optically isotropic, (at least in the linear regime), so 2D-axisymmetric simulations of optical modes are in principle exact. In order to go a step further in precision, the mechanical modes are therefore computed with 3D simulations. A 3D map of the optical WGM is generated from the optical 2D-axisymmetric simulation and the stress-strain integrals of formulas 1.55 and 1.56 are then calculated. Calculation results are shown on figure 2.15.

g_0 values follow the same trends as in the 2D-axisymmetric case, although in some cases the two techniques strongly disagree, as is the case for a disk of radius 0.75 μm, with a TE WGM and the 2$^{\text{nd}}$ RBM (blue line). The average disagreement between the two models in on the order of 20%, with stronger disagreements for g_0's calculated with 2$^{\text{nd}}$ RBMs. This can be intuitively understood from figure 2.11: the isotropic approximation does not work that well in the 2$^{\text{nd}}$ RBMs case. For 1$^{\text{st}}$RBMs, the 2D axisymmetric approach seems satisfactory.

In the case where the optical mode of interest is a standing wave consisting of a combination of

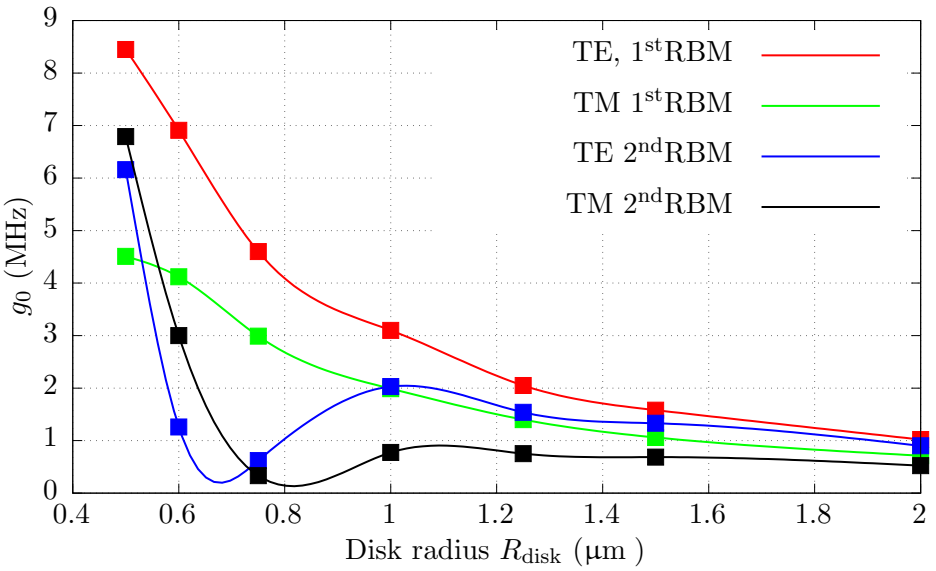

Figure 2.15 – 3D simulations of the OM coupling constant g_0 for different disk radiuses, RBM order and EM field polarization. Disk thickness and wavelength are the same as in figure 2.14. The values obtained are generally close to the 2D axisymmetric simulations case, except for some cases like (R_{disk}=0.7, RBM2, TE).

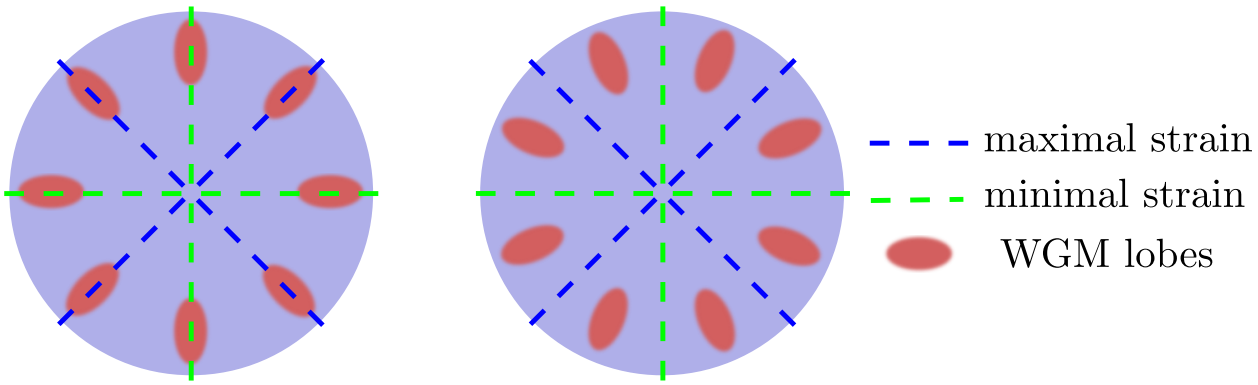

Figure 2.16 – Different possible angles for a stationary WGM supported by a GaAs disk. The green and blue dashed lines represent the axes of minimal and maximal strain, respectively. As the EM energy is confined within the lobes, situations a) ans b) correspond to different g_0 values.

CW and CCW WGMs (see §2.1.3), one could wonder about if the angular position of optical lobes is of some importance. Indeed, a disk has no azimuthal boundary to fix this angle, and the standing wave can *a priori* take any azimuthal orientation. Because of GaAs mechanical anisotropy, WGMs with different orientations will therefore "feel" different strains and this could result in different g_0's (see figure 2.16). This effect is anticipated to have moderate consequences because the WGMs we usually work with have an azimuthal order number m on the order of 10. If m was equal to 4, then on figure 2.16 the lobes could be aligned on the green dashed curve or on the blue one, yielding 2 substantially different g_0 values. However in the case $m = 8$ as shown on the figure, the lobes can be aligned with axes or between axes. By continuity the amount of strain between the green and blue axes is an intermediate value, so that configurations a) and b) in figure 2.16 must correspond to close g_0 values.

2.3.3 Photothermal forces

This section aims at quantifying the value of photothermal forces in out optomechanical system, and comparing them to radiation pressure and electrostrictive forces. We remind to the reader (§1.3.3)

that, in opposition with radiation pressure and electrostrictive forces, an optomechanical coupling constant cannot be defined for photothermal effects, a consequence of their non-conservative nature. In an isotropic approach, the normal stress induced by a temperature increase ΔT can be expressed as:

$$\sigma_{ii} = \frac{E\alpha}{1-2\nu}\Delta T \quad i \in \{x, y, z\} \tag{2.9}$$

with E the material's Young modulus and α its thermal expansion coefficient. This stress, integrated on the disk outer boundary yields a force. We consider the case of a disk of dimensions R_{disk}=1.3 µm, T_{disk}=320 nm. We could estimate, from experimental measurements at 3 K a typical temperature increase of $\Delta T_{1\text{ph}} = 7.7 \cdot 10^{-4}$ K/photon. This result can be obtained in two ways:

- The optical absorption coefficient κ_{abs} (see equation 1.51) is estimated, as well as the disk's anchoring point thermal resistance R_{th}. Then equation 1.51 is solved in stationary state.
- The temperature increase resulting from photon injection is directly deduced by measuring resonance shifts induced by the thermo-optic effect.

We chose the second way, because of its higher accuracy (κ_{abs} and R_{th} cannot be independently precisely estimated). Then we can estimate the photothermal force exerted on the disk boundary for 1 photon circulating in the cavity:

$$F_{\text{pt1}} = \frac{E\alpha}{1-2\nu}\Delta T_{1\text{ph}} 2\pi R_{\text{disk}} T_{\text{disk}} = 1.84 \cdot 10^{-13}\ \text{N} \tag{2.10}$$

This value is to be compared with the radiation pressure force per photon: $F_{\text{rp1}} = \hbar g_{\text{om}}^{\text{geo}} = \hbar g_{\text{om}}^{\text{pe}} = 6.3 \cdot 10^{-14}$ N. The photothermal force therefore dominates by a factor ~ 2 at 3 K. However, the optomechanical work produced by the photothermal force is impacted by the its large delay with respect to optical intensity. While Lorentz force (radiation pressure and electrostriction) have a delay set by the optical loss rate κ, photothermal forces are delayed by the optomechanical system thermal response time, which can be orders of magnitude larger than κ. Thermal response time numerical calculations carried by FEM yield a value τ_{th}=100 ns for 1.3 µm disks ($1/\kappa$ =1 ns). In the framework of the time delayed force model, hotothermal OM effects are found to be weaker than Lorentz force OM effects by a factor 50 for 1.3 µm disks operated at 3 K. The time delayed force model should still be valid for our systems where $\kappa \sim \Omega_{\text{m}}$. For systems operating more deeply in the good cavity limit, the resolution of the coupled differential equations {1.51, 1.16, 1.17}, is necessary. This work is being carried presently in our team. Two last remarks:

- photothermal forces can exert cooling work just as Lorentz forces, and a recent study has shown that they can be used to reach the quantum ground state [18]. Obviously the cooling rate resulting from photothermal forces should be higher that the heat rate generating the force itself.
- the measurements that lead to the estimation of $\Delta T_{1\text{ph}}$ were carried with disks that were not passivated by ALD. A reduction of surface absorption by a factor 5 to 10 has been measured in our team on ALD passivated disks, so the photothermal force should be of lesser impact in those disks.

This chapter provided the tools to estimate key optomechanical parameters in miniature GaAs disks systems. In this chapter the disks were considered isolated, far away from any other optical structure. However, in order to carry experiments, light has to be injected inside the disk. This requires the presence of a waveguide structure in the vicinity of the disk. The design and optimization of this waveguide structure, which impacts the overall optomechanical system design in several ways, is the subject of the next chapter.

Chapter 3

Design of "on chip" coupling to GaAs disks

The physics of EM modes supported by GaAs disks was presented in §2.1. Although these WGMs are solutions of Maxwell's equations, they cannot be used in our experiments if they are not excited by a light source, which must match the WGM's spatial and temporal evolution. Consider for instance the WGM of figure 3.1. A laser beam sent at incidence normal to the disk plane and focused on a very narrow area in the center of the disk would not excite the WGM as there is no EM field density at the center. A perhaps better scheme would be to "de-focus" the laser beam so that its transverse spatial extent matches the disk size. But this would not work either. Indeed, two consecutive WGM lobes have opposite electric field directions – this cannot be seen on figure 3.1 as the color scale is the electric field's square, but it can be seen on figure 2.2. The overlap integral with a plane wave incident on the disk is therefore zero, and no excitation of the mode happens.

One solution to efficiently couple light into the WGM is to bring a waveguide in the disk's vicinity. If the propagation constant β of the wave traveling in the straight guide matches the azimuthal propagation constant of the WGM defined as $2\pi R/m$, some coupling between the waveguide and the disk can be expected. This chapter deals with various aspects and problems of optical waveguide to disk coupling.

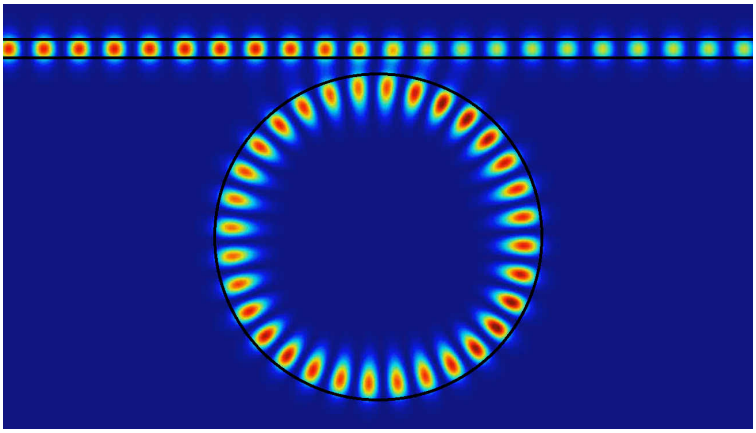

Figure 3.1 – Snapshot of the excitation of a WGM by a directional waveguide. The color scale represents electric field intensity. The laser light comes from the left. The power carried in the waveguide decreases with propagation, hinting that some EM energy is *dropped* in the disk.

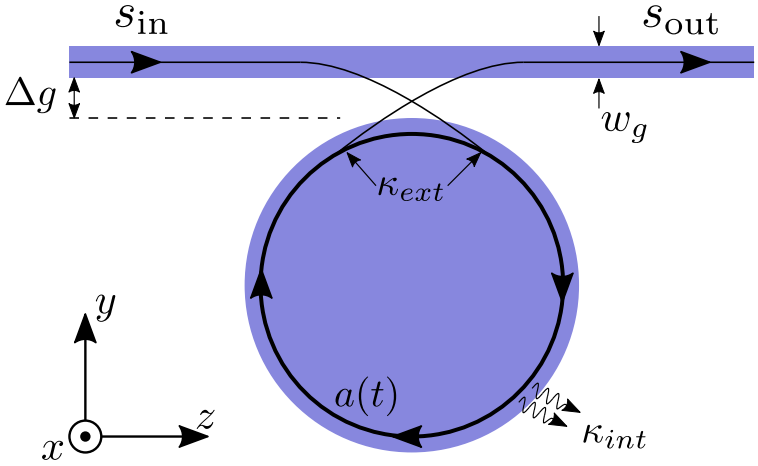

Figure 3.2 – Schematic of waveguide to disk coupling described by CMT. The incident and outgoing field amplitudes are respectively s_{in} and s_{out}.

3.1 Coupled mode theory

We will now review the coupled mode theory (CMT) of waveguide to disk coupling. In this formalism, both eigenmodes supported by an *isolated* disk and an *isolated* waveguide are calculated. The total EM field when bringing disk and waveguide close to each other is then computed within a perturbation of Maxwell's equations, and expressed in a basis consisting of the individual sum of the eigenmodes. The two individual modes interact : the waveguide mode will have some evanescent spatial extent in the disk, it will therefore excite dipoles within the disk which will input some energy into the WGM. The reverse is also true (the WGM feeds energy to the waveguide mode). CMT yield accurate results as long as the perturbative approach holds. This is not always the case as we will see in the following.

We start from the formalism of ref. [47], which was already used in §'s 1.1.4.1 and 2.1.3. The dynamic evolution for the WGM's energy amplitude $a(t)$ and the outgoing field power amplitude $s_{\text{out}}(t)$ is given by :

$$\frac{da(t)}{dt} = -i\omega_0 a(t) - \left(\frac{\kappa_{\text{int}}}{2} + \frac{\kappa_{\text{ext}}}{2}\right) a(t) + \sqrt{\kappa_{\text{ext}}} s_{\text{in}}(t) \tag{3.1a}$$

$$s_{\text{out}}(t) = s_{\text{in}}(t) + \sqrt{\kappa_{\text{ext}}} a(t) \tag{3.1b}$$

κ_{int} represents the intrinsic losses rate of the cavity, which various contributions were presented in §2.1. κ_{ext} is the extrinsic mode loss due to the waveguide presence. ω_0 is the cavity mode's resonance frequency. κ_{ext} can be tuned by changing the gap g between the disk and the waveguide. If the cavity has no intrinsic losses and the input field s_{in} is turned off, then equation 3.1a gives the evolution of the energy $|a(t)|^2$ stored inside the disk : $d|a(t)|^2/dt = -\kappa_{\text{ext}}|a(t)|^2$. This corresponds to the energy that the "charged" disk feeds into the waveguide. This energy decay rate is therefore equal to the outgoing waveguide power $|s_{\text{out}}(t)|^2$. This justifies the term $\sqrt{\kappa_{\text{ext}}}$ in both equations.

Now assume that the s_{in} port is excited with a $\propto e^{i\omega t}$ dependency. The system being excited in a linear regime, the cavity amplitude $a(t)$ will respond at the same frequency, only with dephasing and attenuation, so that it can be expressed as $a_0 e^{i\omega t}$, with $a_0 \in \mathbb{C}$. Replacing the aforementioned expressions in 3.1a yields the following amplitude :

$$a_0 = \frac{\sqrt{\kappa_{\text{ext}}} s_{\text{in}}}{-i\Delta + \left(\frac{\kappa_{\text{int}}}{2} + \frac{\kappa_{\text{ext}}}{2}\right)} \tag{3.2}$$

With $\Delta = \omega - \omega_0$. The amplitude for s_{out} can then be obtained from equations 3.1b and 3.2, and

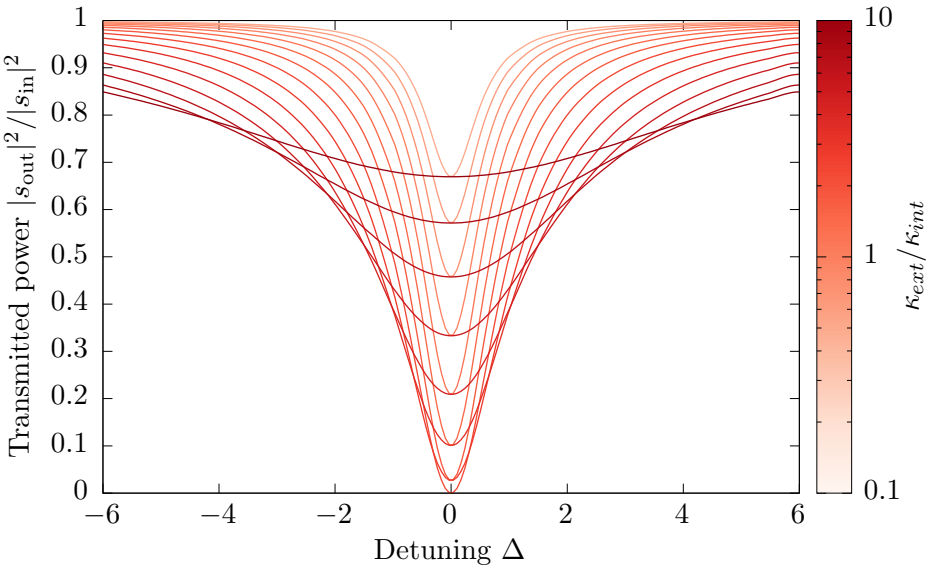

Figure 3.3 – Transmitted power vs. detuning for different values of the parameter $\kappa_{\text{ext}}/\kappa_{\text{int}}$. The plots are generated with formula 3.3

finally transmission T through the waveguide can be found to be :

$$T = \frac{|s_{\text{out}}|^2}{|s_{\text{in}}|^2} = \frac{\Delta^2 + \left(\frac{\kappa_{\text{int}}}{2} - \frac{\kappa_{\text{ext}}}{2}\right)}{\Delta^2 + \left(\frac{\kappa_{\text{int}}}{2} + \frac{\kappa_{\text{ext}}}{2}\right)} \tag{3.3}$$

Figure 3.3 represents the normalized transmission spectrum, a function of Δ, for values of $\kappa_{\text{ext}}/\kappa_{\text{int}}$ going from 0.1 to 10. Two regimes can be identified : the under-coupled regime where $\kappa_{\text{ext}} < \kappa_{\text{int}}$, and the over-coupled regime where $\kappa_{\text{ext}} > \kappa_{\text{int}}$. When $\kappa_{\text{ext}} = \kappa_{\text{int}}$ the coupling is called *critical*. This corresponds to a contrast of 100% of the resonance observed in the transmission spectrum. In the under-coupled regime the contrast is smaller than 100% and the linewidth resonance is narrower than at critical coupling. In the over coupled regime the contrast is also smaller that 100%, but this time the linewidth becomes broader. The over-coupled regime can seem disadvantageous in terms of linewidth and WGM power injection, but this is not always true : because $\kappa_{\text{ext}} > \kappa_{\text{int}}$, the photons will preferentially escape the cavity through the waveguide than be absorbed or scattered by intrinsic physical processes, which can be advantageous to protect the fidelity of some operations. Indeed, photons that escape the disk through the waveguide can be measured, so the over-coupled regime allows precise and efficient detection. Measurement limitations are discussed in chapters 5 and 7.

The external coupling term κ_{ext}

In the CMT vision, the power transfer from waveguide to disk (and vice-versa) is enabled by the overlap of the waveguide and disk individual modes. The following formula can be obtained [48]:

$$\sqrt{\kappa_{\text{ext}}} = -i\varepsilon_0 \frac{\omega}{4} \int_{-z_1}^{z_1} dz \iint_{x,y} dxdy(n^2 - 1)\mathbf{e}^*_{\text{wgm}}\mathbf{e}_+ e^{-i\beta z} \tag{3.4}$$

The coordinates x, y, z match the definitions on figure 3.2. $\mathbf{e}_{\text{wgm}}(x, y, z)$ is the normalized field corresponding to the disk's WGM, and $\mathbf{e}_+(x, y)e^{-i\beta z}$ is the normalized field supported by the waveguide. $n(x, y, z)$ is the refractive index. This formula is obtain by applying Poynting's theorem on $z = constant$ slices. The z integration interval must be large enough so that it encompasses the full interaction zone of the disk and waveguide modes. An interval length equal to the disk diameter is in practice sufficient. The term $n^2 - 1$ underlines the fact that the two modes do not

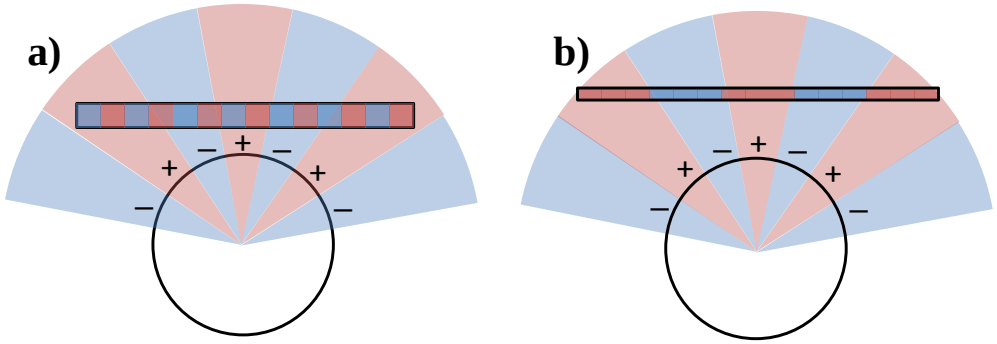

Figure 3.4 – Schematic of electric field overlap in different coupling configurations. Colors account for the electric field direction. Case b) correspond to a better overlap.

interact in vacuum. The normalized fields used in formula 3.4 can be computed analytically using an approximate effective index approach, or by 2D or 3D numerical simulations.

Figure 3.4 represents 2 different coupling configurations. In the case a), the waveguide is wide and positioned close to the disk. It can be seen that the longitudinal electric field oscillations in the waveguide are 2 times shorter than the azimuthal oscillations of the WGM. In other words upward and downward field orientation areas do not match. The integral in formula 3.4 will hence be very small. Areas of same sign have a better overlap in case b) and will yield a higher coupling constant. For a given WGM, the extrinsic coupling constant κ_{ext} depends on the waveguide width w_{g} – because it impacts the longitudinal propagation constant β – and on the gap distance Δg – because it modifies the azimuthal oscillation period seen by the waveguide.

We often want to work close to critical coupling, as it provides efficient optomechanical detection (see §1.1.2). The waveguide width w_{g} and gap distance Δg must therefore be chosen so that κ_{ext} is equal to the intrinsic losses of the disk. Many $(w_{\text{g}}, \Delta g)$ configurations can yield $\kappa_{\text{ext}} = \kappa_{\text{int}}$. The one retained should correspond to the largest values for w_{g} and Δg. Indeed, a wider waveguide has less longitudinal losses (the mode is more confined inside the waveguide so that surface roughness scatters less energy). Large gap distance values are also desirable because the waveguide + disk pattern is less sensitive to technilogical proximity effects (see §4.1.2.2).

3.2 Straight and bent waveguides

We will now discuss the various practical solutions used in our laboratory to couple light from an external laser source to a GaAs disk's WGM. The first approach in our group has been to use fiber tapers. The tapered region of a fiber is positioned with a nano-positioning stage in the vicinity of the disk to excite its WGMs. The advantages and drawbacks of this technique are :

- (+) The gap distance can be adjusted continuously by moving the fiber relatively to the disk. This allows to tune the extrinsic coupling constant κ_{ext}.
- (+) Propagation losses within the tapered fiber are low. The best tapered fibers can attain a transmission superior to 99%.
- (−) Tapered fibers are very fragile and complicated to handle. Being very soft, they suffer from mechanical noises. They must be operated in a low humidity environment to prevent optical degradation.
- (−) For small disks ($\varnothing 2$ µm), the tapered fiber propagating mode does not respect the geometry of the WGM. In order to get sufficient κ_{ext} the fiber must be brought very close to the disks, which perturbs the WGM. CMT is not valid anymore and Q_{opt} are strongly degraded by parasitic coupling effects.

An other approach is to define disk and waveguide on the same piece of material (see figure 4.1). The waveguide is therefore made of GaAs instead of glass. Very narrow waveguides ($\sim$ 100 nm) of various geometries can be achieved. The advantages and drawbacks of this approach are the exact opposite of the tapered fiber case :

- (−) The gap distance cannot be adjusted in situ, it is fixed during the fabrication of the sample. It is nevertheless possible to fabricate many *disk* & *waveguide* ensembles with varying gap distance and waveguide width on a single chip.
- (−) Propagation losses within the waveguide tend to be higher, and also the input/output coupling of light in the waveguide with external optical elements is more involved. The best overall transmissions attained are around 25% in our experiments, corresponding to 50% (3dB) matching efficiency at input and output waveguide ports.
- (+) Integrated GaAs waveguides are very robust and their performance do not degrade with time. The stability is excellent and measurements of several hours can be performed without any transmission fluctuation.
- (+) Disk and waveguide are made of the same material, and therefore their refraction index are the same. The waveguide mode thus matches more naturally the WGM's geometry. Efficient coupling configurations can therefore be attained on small disks, without degrading Q_{opt}.

Because quantum optomechanics require to work with small radius disks (large g_0, high frequency), we chose to use the integrated waveguide approach. The enhanced stability is also a major advantage, especially when working in a cryogenic environment.

3.2.1 GaAs waveguide design

We will now discuss the design of the central part of the GaAs waveguide (the one in the disk's vicinity). The problematic of efficiently linking this central part to the sample's edges will be discussed in the next section. The requirements for this central part are the following :

- It must be single mode. Although higher-order modes could in theory couple to the WGM, this would render experimental monitoring more difficult. Indeed, the disk could couple to the distinct waveguide mode and make our CMT understanding invalid.
- Its presence must induce negligible perturbations of the WGM. Single mode narrow waveguides tend to induce less parasitic Q_{opt} degradation.
- The waveguide linear losses must be small. Although the central part of the waveguide is rather short ($\sim$ 5 µm), the field circulating within it is sensitive to sidewall roughness, so that linear loss coefficients may be high. Specific efforts should therefore be engaged to limit sidewall irregularity during fabrication.

Consider a infinite GaAs slab waveguide of thickness s_t. Simple ray optics considerations predict that this slab is single mode if the following condition is respected [49]:

$$s_t < \frac{\lambda}{2\sqrt{n_{\text{GaAs}}^2 - n_{\text{air}}^2}} \tag{3.5}$$

where λ is the wavelength in vacuum of the monochromatic EM radiation considered. This formula is valid for an *infinite* slab. Note that the TE/TM polarization distinction is not made here. Using more precise calculations based on Maxwell's equations allow to get the second mode cutoff for both polarizations.

mode polarization	slab - ray optics	slab - Maxwell	rectangular guide
TE	240 nm	270 nm	450 nm
TM	240 nm	410 nm	380 nm

Table 3.1 – 2nd mode cutoff dimension for different configurations. In the rectangular waveguide case, the other dimension is fixed at 320 nm.

The case of a waveguide with rectangular section is more complex. There is no analytic solution for Maxwell's equations, and numerical methods must be used. The cutoff values are given in table 3.1. There is quite a disagreement between the slab and waveguide predictions, without much surprise. Another difference between infinite slab and rectangular waveguide is that the waveguide has a cutoff for the fundamental mode also (a slab theoretically supports a fundamental mode for arbitrarily small thicknesses). For a waveguide of thickness 320 nm, the minimal width that supports the fundamental mode is 230 nm in the TE (chip-plane E polarized) case and 140 nm in the TM case. Note that the TE/TM approximation is not perfectly correct in the rectangular waveguide case, where eigenmodes are hybrid TE/TM. This is not an issue for the FEM method that solves the Helmholtz equation in a full vectorial way. The modes found by the FEM method have in general a TE or TM dominant character.

3.2.2 Bent waveguides

The integrated waveguide scheme also allows to fabricate curved waveguides that better respect the geometry of the WGM. Because their propagation mode naturally overlaps with the WGM's EM field, these waveguides can be placed at bigger gap distances, and hence induce less perturbation on the WGM. Figure 3.5 schematizes different waveguide designs that have been tried experimentally during this PhD work.

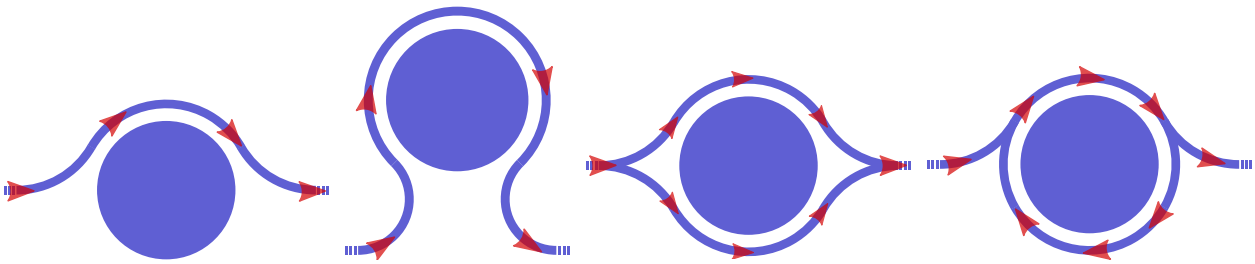

(a) "120°" (b) "omega" (c) "eye" (d) "ring"

Figure 3.5 – Different designs for the waveguide that passes in the vicinity of the GaAs disk. The red arrows represent the light propagation direction.

- The 120° is the simplest bent waveguide, but showed some interesting results : the best loaded quality factors for R =1.3 µm disks where obtained which these waveguides, with a value of 300 000 at λ =1.5 µm.

- The *omega* is conceptually similar to the 120° , but is wraps around a larger angular sector. The gap distance can thus be made bigger than in the 120° case for a constant κ_{ext}. This should allow for a coupling behavior with minimal parasitic coupling and departure from CMT. One of its drawbacks is its increased fragility and sensitivity to deleterious stiction effects (see §4.3.4).

- The *eye* is conceptually different from the above designs because the incident wave is split in two and then recombined. Two WGMs propagating in opposite directions are thus excited, and a stationary wave is formed. The *eye* has the advantage of covering a big angular section

as the *omega*, while being slightly more robust mechanically. Its drawback is that dry etching reactants cannot escape the trench between disk and waveguide laterally as is the case for 120° and *omega*. This results in increased roughness and lateral etch during the ICP etch (§4.3.2.1).

- The *ring* wraps completely around the disk, and would therefore allow for the optimal coupling. In practice though, it is not viable as the ring itself will have its own resonances. They have poor optical quality factors due to the high losses in bent waveguides. These broad resonances perturb the transmission spectrum of the disk itself, which is very inconvenient experimentally.

The two designs retained are the 120° and the *eye*. Very good experimental quality factors were observed on both designs, with a 50% enhancement compared to straight waveguides. The fact that *eyes* waveguides completely wrap around the disk also allows to fabricate disks with a better symmetry.

3.2.3 Coupling simulations

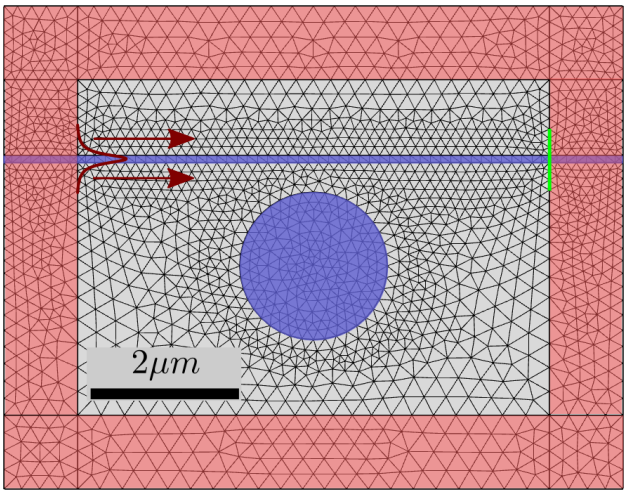

Figure 3.6 – Typical configuration for a 2D FEM simulation. The triangular meshing of the simulation domain can be seen. GaAs is blue, air is grey, and PMLs are pink. The waveguide eigenmode (dark red) is excited from the left input port and the guided optical power remaining after interaction with the disk is integrated on the green line.

As mentioned before, CMT holds as long as a perturbative approach suffices to describe the evanescent coupling on the basis of individual disk and waveguide eigenmodes. The smaller the gap distance, the bigger the perturbation induced by the waveguide on the disk. 2D FEM simulations were performed in order to quantify the advantage conveyed by bent waveguides compared to straight ones. In both cases the simulations cannot be carried by 2D axisymmetric methods, because the full waveguide does not have azimuthal symmetry, in contrast to the disk. Complete 3D simulations are too computer consuming, hence 2D simulations with the effective index approximation are used. This means that the refractive index of the *2-dimensional* disk and waveguide is taken to be the effective index of an infinite plane of same thickness.

The simulation procedure is then the following: first, the eigenmode of the waveguide is calculated for a frequency ω_0 close to the WGM resonance frequency (see dark red curve on figure 3.6). Then the waveguide is excited with this eigenmode profile at several frequencies in the range $\omega_0 \pm \Delta\omega$ [1] and COMSOL computes the response of the whole simulation domain to this excitation. The power transmitted through the waveguide after interaction with the disk is calculated and a

[1] the shape of the eigenmode is dependent on ω, but as $\Delta\omega \ll \omega_0$, this effect is negligible

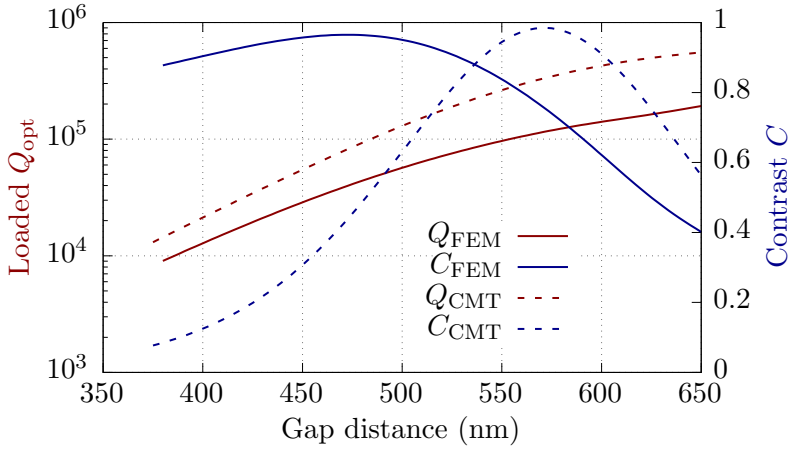

Figure 3.7 – 2D FEM simulations of coupling efficiency for a straight waveguide. The CMT values for an identical system are also displayed. The best FEM $Q \cdot C$ value is lower than its CMT counterpart by a factor of 4.

transmission spectrum $T(\omega)$ can be constructed. From such a curve the loaded Q_{opt} and contrast $C = 1 - T(\omega_0)$ of the resonance spectrum can be extracted by fitting to Lorentzian functions. These data are calculated for different gap distances. Figure 3.7 represents the Q_{opt} and contrast C derived from FEM simulations for different gap distances in the case of a straight waveguide. The maximum QC product is attained for a gap distance of 575 nm, with a value of 100 000. It can be seen quite easily that the FEM curves disagree with CMT. Indeed, the maximum contrast value ($C \sim 0.95$) corresponds to a quality factor of 50 000, which is a factor 4 smaller than the intrinsic Q_{opt} of 200 000 observed at large gap distance. In CMT, at a difference, the maximum intrinsic Q_{opt} is divided by 2 at critical coupling ($C = 1$). The same simulations have been carried for an *eye* waveguide this time. The Q and C vs. *gap distance* trends are the same as in figure 3.7, but the maximum QC product is attained for a gap distance of 820 nm, with a value of 250 000. This is a 2.5 times enhancement compared the to straight waveguide design, which is appreciable given that the optomechanical cooperativity scales for example linearly with the Q_{opt}.

3.3 Global waveguide design

In the previous sections we have discussed the physics of waveguide to disk coupling. The part of the waveguide in the immediate disk vicinity – which is a few microns long – was hence of interest. However the chip must have a size of several millimeters so it can be produced and handled correctly. It is therefore necessary to link the edges of the chip to the central part where the waveguide to disk coupling happens. This section will be divided in two parts. In the first part we will describe the long waveguide (LW) coupling scheme developed before I started this PhD work. In a second part the fully suspended waveguide (FSW) design will be presented, which I developed during my PhD. Note that the epitaxial structure from which the devices are fabricated consists in a 320 nm GaAs layer (refractive index ∼3.4) on top of a 1.8 µm AlGaAs layer (index ∼3).

3.3.1 Long waveguides devices

The first idea to couple light in and out from the sample was to define LWs whose extremities are delimited by sample cleaving. Cleaved facets can indeed be very smooth, which limits roughness scattering. A schematic of the LW design is found on figure 3.8. The waveguide width is 200 nm in the disk vicinity. It is then progressively increased up to a value of 8 µm in a region called *taper*, and then kept constant for ∼1 mm until the end of the sample is attained on each side. The reason for tapers is that the EM field in the narrow waveguide zone is highly evanescent. This

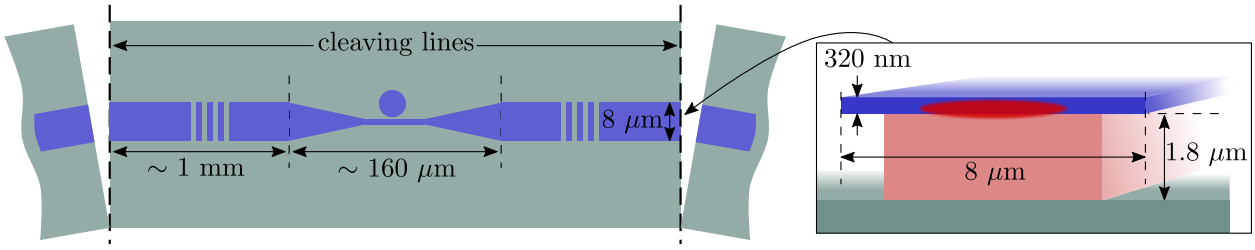

Figure 3.8 – LW design. The sample is cleaved on both sides to define clean and straight end facets for the waveguide. The waveguide length is $\sim$ 2 mm, with a central part (tapers+evanescent guide) 160 µm long. The top GaAs layer is blue, AlGaAs is pink and the bottom GaAs substrate is grey.

is necessary in the disk vicinity in order to couple efficiently to the WGM, but it induces large propagation losses as the waveguide sidewall roughness is sensed by a strong electric field. If this narrow width was kept through the whole sample, the total light transmission would be very low. With a larger waveguide (8 µm), the EM field is well confined within the GaAs (see inset in figure 3.8). An $Al_{0.8}Ga_{0.2}As$ ($n \approx 3$) bottom layer of thickness 1.8 µm is however necessary to avoid leakage of the guided mode down to the substrate. In the inset of figure 3.8 the lateral undercut of the AlGaAs layer is a consequence of the hydrofluoric acid (HF) under-etching carried in the fabrication process. Although this etching has not much impact on the mode guiding in the wide waveguide section, it has a crucial importance in the central narrow waveguide area as it allows to completely release the guide from its AlGaAs supporting layer (see figure 4.1). If it was not the case the mode would be strongly localized in the AlGaAs layer and it would couple poorly to the disk's WGM.

In the tapered sections the optical mode undergoes an adiabatic transformation from a well confined to a highly evanescent profile. The main requirement for tapered sections is to minimize losses. Reference [50] gives a criterion to limit losses in adiabatic tapers. Simply put, the taper length must be greater than the beating length $z_b = 2\pi/(\beta_1 - \beta_2)$ between the fundamental and the 2^{nd} order guided modes. This condition is well respected for a taper length of 80 µm. LW samples are simple to fabricate but they accumulate a few problems :

- The index contrast is important at the cleaved facets, resulting in a 40% reflectivity at the sample edges. The waveguide therefore behaves as a low finesse Fabry-Pérot cavity, with a FSR equal to $\sim$200 pm. This generates oscillations in the optical spectra (see figure 3.11) that superimpose with WGM optical resonances, and disturb measurements.

- The fundamental mode guided in the 8 µm wide waveguide has a strongly anisotropic profile. It has a $\sim$4 µm horizontal FWHM and a $\sim$400 nm vertical FWHM. At the output facet this mode will radiate an anisotropic beam in far field (vertical divergence 6 times bigger than horizontal divergence according to simulations). This makes light collection complex and quite inefficient. In the best case some 20% of the light exiting the cleaved facet could be collected. Similar difficulties appear with injection at the input port, but are less of a concern as it is often possible to compensate input losses by increasing the laser power.

- Because the total waveguide is rather long ($\sim$2 mm), it has a high probability to be on the path of some impurities or wafer defects, which will scatter light and lower the overall transmission.

- As was mentioned before the efficient guiding of the fundamental mode in the 8 µm wide waveguide sections necessitates an AlGaAs layer of at least 1.8 µm between the guiding GaAs layer and the GaAs substrate. This is because of the low index difference between GaAs and $Al_{0.8}Ga_{0.2}As$. This precludes the fabrication of compact mechanically shielded (MS) structures as will be seen in chapter 2.

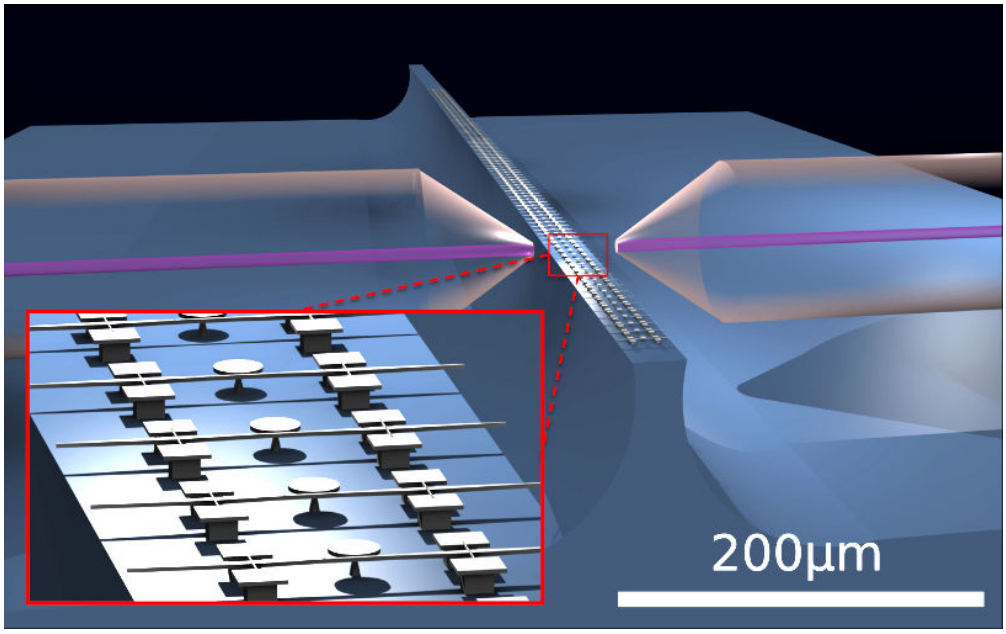

Figure 3.9 – Fully-suspended waveguides. The micro-lensed fibers come above the sample and focus light into the fully suspended waveguides. These waveguides are 50 times shorter than the sample itself. The "plateau" on which the FSWs are positioned is called a *mesa*. Image is roughly to scale.

3.3.2 Fully suspended waveguide devices

The impossibility to conciliate compact MS devices and LWs, along with the other drawbacks mentioned above, encouraged us to look for a new waveguide configuration. Many of the drawbacks came from the fact that the waveguide needed to be as long a the sample width, i.e. at least 2 mm. We therefore tried to find a way to make the waveguides way shorter, while keeping the same sample size for obvious handling purposes. The idea we had was to elevate the optomechanical structures and waveguides on a pedestal, called a *mesa*. Micro-lensed fibers would then come above the sample and couple light into the waveguide. The idea is certainly best explained with a picture (see figure 3.9).

Figure 3.10 shows a close-up on one single FSW. The waveguide is completely surrounded by air, which allows efficient optical confinement of the propagating mode. The overall length of the waveguide is 40 µm, which makes it 50 times shorter than the LWs used in the previous design. Below are listed FSWs advantages over LWs:

- The waveguide ends can be tapered. As the width decreases, the effective index of the guided mode is reduced progressively. The mode hence never "feels" a strong index mismatch, and the reflection coefficient at the waveguide tip is small. 3D Finite Differences - Time Domain (FDTD) simulations show that the reflection coefficient goes from ∼40% to ∼1% when using proper inverted tapers instead of cleaved facets. This greatly reduces the amplitude of Fabry-Pérot oscillations (see figure 3.11). Moreover, the oscillation period goes from 200 pm to 10 nm because the waveguide is 50 times shorter. Hence Fabry-Pérot oscillations do not pollute the transmission spectrum at the scale of the typical width of a WGM. We will call these tapered ends *inverted tapers* in the following

- The effective index decreases along the inverted taper as light propagates, and the propagating mode becomes more symmetric as well (the guide section supporting the mode is highly sub-wavelength and cannot impose a strong transverse anisotropy to the mode). Moreover, the width of the inverted taper's end can be adjusted so that the mode's transverse profile at this point matches the focused Gaussian mode of the micro-lensed fiber. The matching can be adjusted to provide up to ∼70% injection (collection) efficiency.

- FSWs are short, hence they are less likely to be disrupted by an impurity or dust present on the sample. The transmission efficiency is therefore more homogeneous for all the waveguides on a given sample.

- Because the waveguide is now entirely surrounded by air, the mode propagating can be efficiently guided without the need for a large optical cladding. For instance, a FSW with 1 µm×320 nm cross section suspended 500 nm above the GaAs substrate would guide the mode without leaks to the substrate. This feature is particularly interesting in the context of MS devices. As will be shown in chapters 4 and 6, it is much easier to fabricate MS devices for which the distance between the GaAs disk and shield is small ($\sim$ 500 nm). This could not have been carried with LWs as an AlGaAs layer of at least 1.8 µm is necessary to guide the light without substrate leaks.

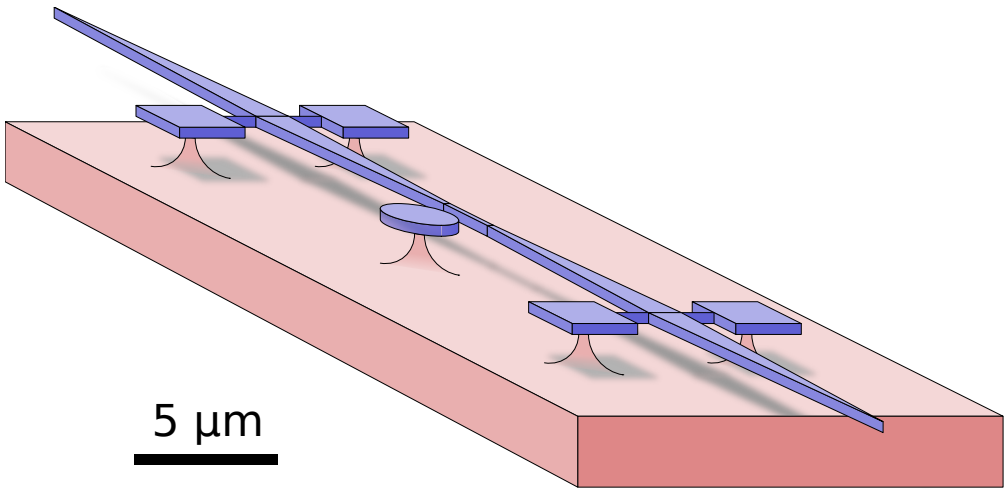

Figure 3.10 – Close-up on a FSW device. The waveguide is fully under-etched, so that it is completely surrounded by air. It is 1 µm wide at its largest, where it is held by threads. These threads are very thin (∼100 nm wide), so that they do not perturb the propagating wave. We will call them anchoring points in the following. Both ends of the FSW are also tapered, in order to suppress reflections and optimize coupling with the micro-lensed fibers.

Inverted tapers design

For LW devices, tapering the waveguide from 8 µm wide to 200 nm wide over a length of 80 µm shows good results. This corresponds to a slope of ∼1/10, which we decided to keep for the FSW tapers and inverted tapers. In order to maximize the inverted taper coupling to a micro-lensed fiber at each port, 3D FDTD simulations were carried for different widths of the inverted taper's end. The simulation principle is the following : the plane at the inverted taper's end in excited with a source. Spatially, this source is a 2 µm diameter Gaussian mode. Spectrally it is a pulse of spectral width 100 nm, centered at 1550 nm. Propagation is then simulated by FDTD, and the energy flowing at the end of the inverted taper (when the latter is 1 µm wide) is computed[2]. Figure 3.12 shows the transmission efficiency for *one* inverted taper / micro-lensed fiber interface. Neglecting all other losses, the total transmission of a device will be the square of this transmission, because there are two inverted tapers on each waveguide.

[2]More precisely, the field is projected on the fundamental mode of the 1 µm wide guide. This is the mode of interest to us, as higher order modes are filtered by the narrow guide section in the disk vicinity.

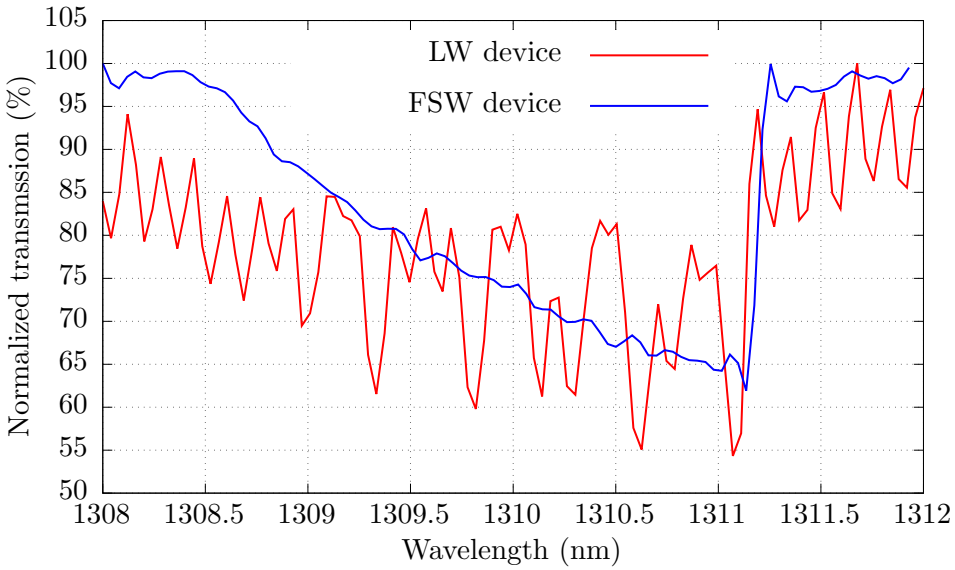

Figure 3.11 – Wavelength scans of an optical resonance with LW and FSW devices. The resonances show strong thermo-optic effect (see §1.3.3). A strong Fabry-Pérot oscillation can be observed in the LW device case. Note also that in the FSW case, the Fabry-Pérot oscillation period is actually larger than the wavelength span.

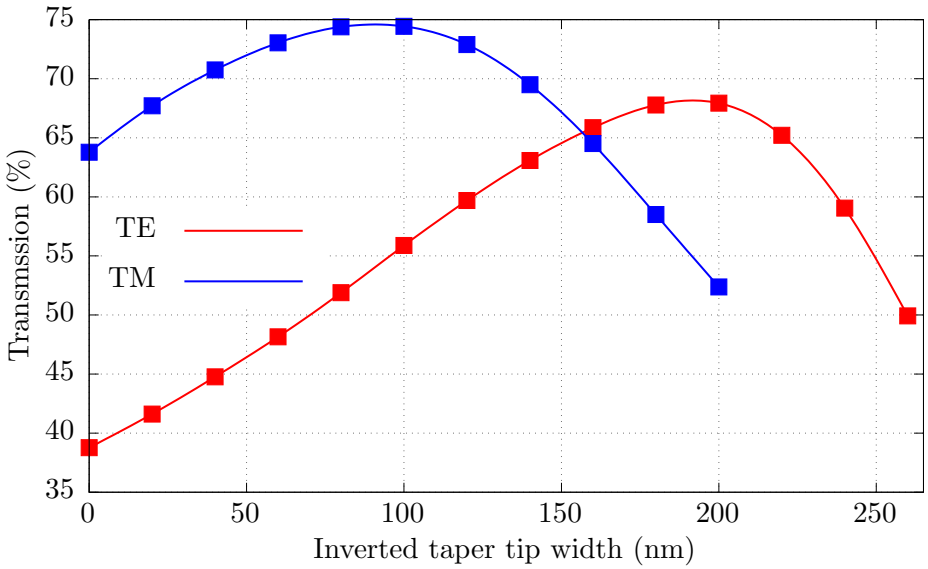

Figure 3.12 – Power transmission at 1550 nm from an inverted taper to a micro-lensed fiber (and vice-versa) for different widths of the inverted taper's tip. The GaAs layer thickness is 320 nm. Very good coupling efficiency of almost 75 % can be obtained in the TM case.

Anchoring points design

The anchoring points holding the waveguide must be designed so that they do not induce too strong losses, otherwise all the advantages of FSW mentioned earlier would be pointless. 3D FDTD simulations very similar to the ones used for inverted tapers design were carried. A source corresponding to the waveguide's eigenmode was positioned on the left of the anchoring point (see figure 3.13) and a collector was placed on the right.

For 100 nm wide anchors holding the guide (figure 3.13), transmissions above 98% were obtained for waveguides larger than 600 nm in the TE case, and waveguides larger than 300 nm in the TM case. We chose to position the anchoring points at a position where the waveguide is 1 µm wide.

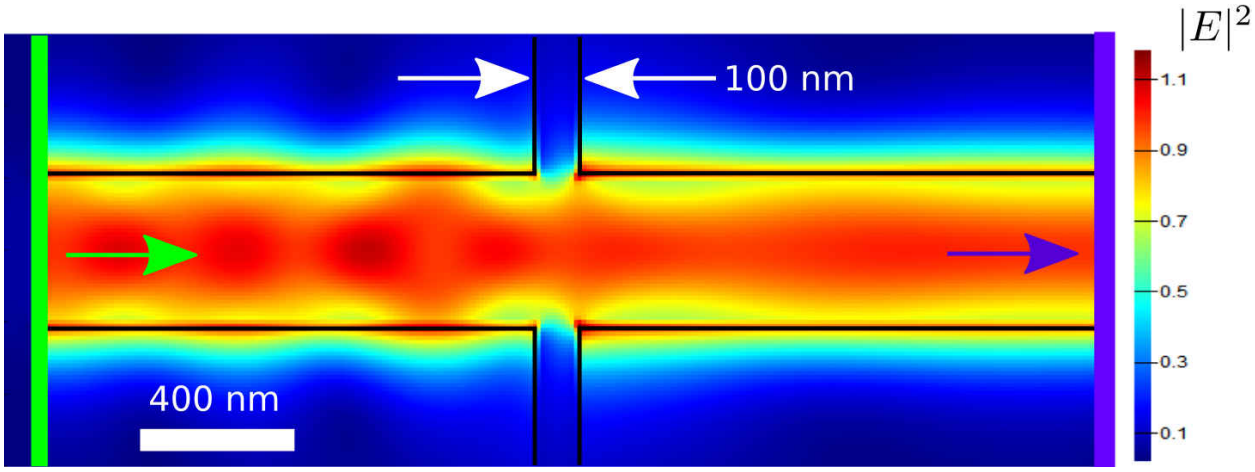

Figure 3.13 – 3D FDTD simulations of anchoring point losses. The waveguide is 400 nm wide and the anchoring points are 100 nm wide. An EM field distribution corresponding to the waveguide fundamental mode in injected on the left side (green line). The fraction of energy passing through is then collected on the purple line and projected on the same fundamental mode. The transmission is 90% in this case.

Anchoring points losses are therefore negligible.

A few remarks

In practice the transition to FSW along this PhD work allowed to multiply the overall waveguide transmission by a factor 3, with Fabry-Pérot oscillations quasi-suppression (see figure 3.11). They also allowed fabrication of compact MS devices, which was impossible before.

A few words now on injection/collection. The FSW are symmetric, so that the injection efficiency – i.e. the the fraction of light transmitted from the micro-lensed fiber to the central waveguide – must be equal to the collection efficiency. However the injection and collection ports do not play a symmetric role in our experiments. In practice the optical power that we wish to drop in our disks for quantum optomechanics experiments is rather small (a few tens of μW). The reason is that dropping too much power induces thermal instabilities that prevent stable operation. The laser sources available to us can deliver much more power (∼10mW). A high injection efficiency is therefore not crucial, an injection efficiency of 1% would be sufficient to drop 100 μW in the disk. Collection is more critical, because it sets a limit to the sensitivity of mechanical motion detection. For a given optical power circulating in the optomechanical disk resonator, the power gathered on the photo-diode will depend linearly on the collection efficiency. The signal to noise ratio (SNR) of motion sensing therefore depends on collection performance. For future experiments where quantum states of light will be imprinted onto the mechanical resonator, injection and collection will both be equally important to protect the fidelity of operations.

Chapter 4

Device fabrication

This chapter aims at showing the various tools and techniques involved in the fabrication of on-chip GaAs miniature OM systems, as well as the developments carried to improve their performance. This fabrication work was mainly accomplished in the *Matériaux et Phénomènes Quantiques* laboratory's clean room at Université Paris Diderot, except for the electron beam (e-beam) lithography step that was partly performed in the clean room of the physics department at *École Normale Supérieure*.

For the fabricated sample to show the expected performance, great care and preciseness must be brought into each fabrication step, as the most minute detail neglected can yield dramatic effects in the next fabrication step. I will therefore try to conciliate precision with conciseness in describing the technological process.

This chapter will be divided in three main parts. In the first part I will expose the fabrication steps developed by Christopher Baker during his PhD thesis for the fabrication of LW devices. Emphasis will be put on the anisotropic etch step description, in anticipation of later discussions. In the second part I will present the developments that I carried in order to fabricate FSW devices. In the third part technological issues related to MS devices developed during this PhD work devices will be presented.

4.1 Fabrication steps of long waveguide devices

Figure 4.1 summarizes the main steps of the fabrication process. It shows the central part of the LW structures (see §3.3.1), where only the tapered section close to the disk resonator is suspended. We will now describe these steps in a sequential fashion.

4.1.1 Epitaxial structure

The semi-conductor epitaxial growth used for our fabrications consists typically in a 320 nm GaAs layer on top of a 1.8 µm AlGaAs ($Al_{0.8}Ga_{0.2}As$) layer, both grown on a 600 µm thick GaAs substrate. The wafer is grown at the *Laboratoire de Photonique et Nanostructures* in Marcoussis, by Aristide Lemaître and Carmen Gomez.

The top GaAs layer can be considered as the "active" one: the OM disk will be defined in this layer, see figure 4.1. Very high purity and lattice uniformity are therefore required for this layer, in order to minimize bulk optical and mechanical losses. Our growth is typically specified at a level of residual p-doping in the few 10^{14} /cm^3, regularly checked by the growers in their chamber.

Figure 4.2 shows GaAs's unit cell. GaAs is a face-centered cubic crystal (brown atoms), with 50% occupation of tetrahedric sites (purple atoms). Gallium and Arsenide atoms exist in equal proportions within the crystal. AlGaAs has basically the same structure, with some fraction of Gallium atoms replaced by Aluminum ones. The lattice constant is very close to the GaAs one, and AlGaAs can therefore be easily grown on a GaAs substrate with minimal stress.

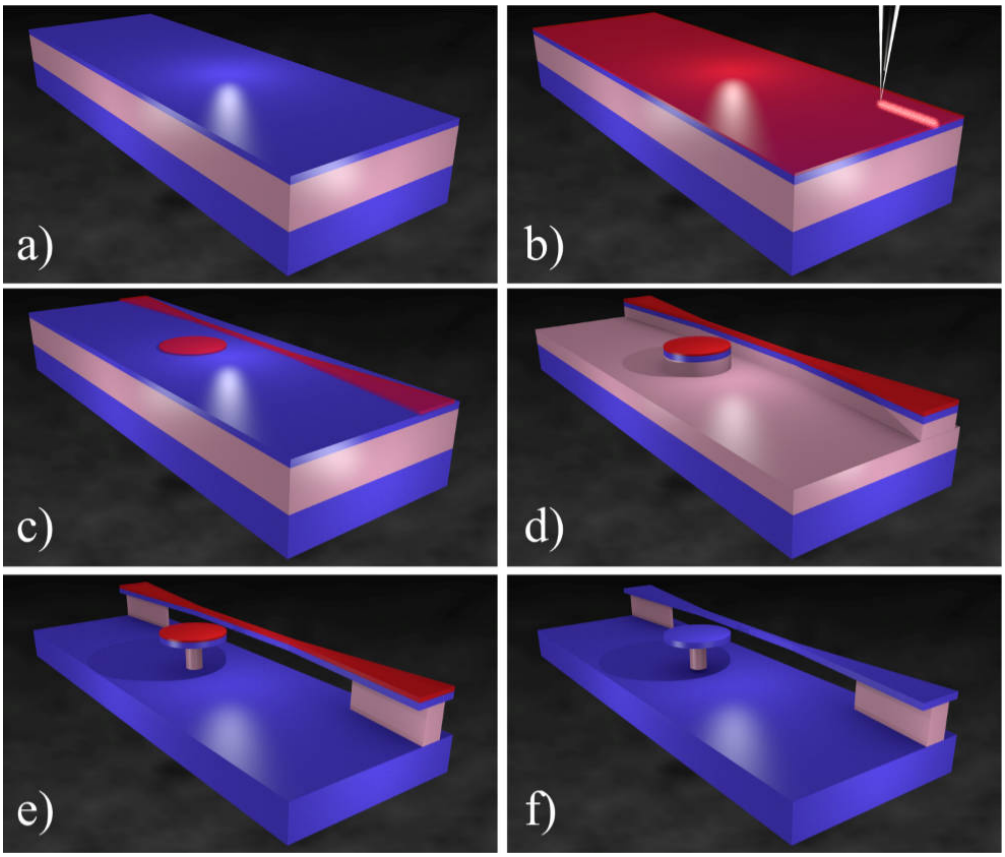

Figure 4.1 – **Fabrication steps - a)** The epitaxial structure consists in a 320 nm GaAs layer (blue) on top of a 1.8 µm $Al_{0.8}Ga_{0.2}As$ layer (pink), both grown on a GaAs substrate. **b)** E-beam sensitive resist (red) is spun on the surface and exposed. **c)** The exposed pattern is developed in an alkaline solution. **d)** Anisotropic dry etch. **e)** Selective HF under-etching. **f)** Resist stripping.

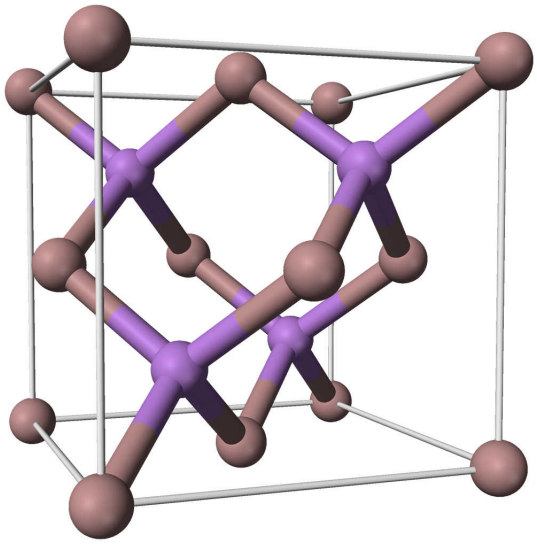

Figure 4.2 – GaAs unit cell

The $Al_{0.8}Ga_{0.2}As$ layer in our epitaxial structure is the "sacrificial" one. Its purpose is to be selectively under-etched in HF, in order to be shaped into a thin pedestal on which the GaAs OM disk will stand. The 80% AlGaAs molar fraction was chosen for the three following reasons :

- HF etching selectivity is high : $Al_{0.8}Ga_{0.2}As$ is etched $\sim 10^7$ faster than GaAs [51].
- Optical index difference between $Al_{0.8}Ga_{0.2}As$ and GaAs is high, which allows for efficient confinement of light in LW devices.
- Oxidation in air is limited [52]. At aluminum concentrations above 80%, AlGaAs starts to oxidize heavily in air which can result in crumbliness and overall fragility.

4.1.2 Definition of the resist mask

The e-beam sensitive resist used for the definition of our OM devices is the ma-N 2400. It is a negative tone resist, i.e. the exposed patterns stay on the sample after development. It comes in several dilutions for different nominal thicknesses after spin coating. It consists in the mixture or a polymeric bonding agent (novolak) and a photo-active compound (PAC). The PAC was originally designed for deep ultra violet applications, but ma-N 2400 shows good performance with e-beam. Upon exposure of electrons the polymer chains in the PAC are going to cross-link with each other to form bigger chains, which will locally decrease the resist tendency to dissolve in aqueous alkaline solutions, thus allowing development of the patterns exposed.

4.1.2.1 Spin coating

A wafer piece of typical size 1 cm^2 – referred in the following simply as the "chip" – is first cleaved from a 2 inch (5 cm) diameter wafer using a diamond tip, and is then cleaned from organic and other surface contaminants by a 10 minutes dip in acetone, followed by a 5 minutes dip in isopropanol. Ultrasound pulses are sent through the beaker to accelerate the cleaning.

After cleaning the chip is dehydrated for 5 minutes at 200°C on a hotplate, for the purpose of desorbing water on the surface. Immediately after an adhesion promoter (Ti-Prime) is spin coated on the surface (for 30 s at 6000 rpm)[1] and makes it hydrophobic, as remaining water can lead to poor resist adhesion.

A few drops of ma-N 2401 (nominal thickness 100 nm) are deposited on the chip, which is then spun 30 s at 3000 rpm. Most of the deposited resist is ejected from the chip, and a layer 100 nm thick remains. The resulting layer thickness has two main impacts on the subsequent fabrication steps :

- The thinner the layer, the higher the resolution of written patterns, as the electrons impinging on the resist have a lesser thickness to diffuse in.
- The ticker the layer, the deeper the anisotropic dry etch step can be. Indeed, the dry etch step wears the resist (see §4.1.3).

Because of surface tension, resist tends to accumulate – and therefore be thicker – on the sides of the chip, so a sufficiently large wafer piece must be used in order to obtain a large enough working area in the middle. Within this constant thickness area, some thickness variations can also occur. They are usually caused by pre-existing defects on the wafer surface – usually inherent to the epitaxy – which perturb the resist flow during the spin coating.

After spin coating the chip undergoes a "soft bake" step : 65 s on a hotplate at 95°C. The purpose is to evaporate the solvent still contained in the resist film, which enhances adhesion to the substrate and avoids resist popping during exposure by formation of nitrogen bubbles. 95°C is a compromise between efficient solvent evaporation and limitation of thermally induced cross-linking.

[1] rpm: rotations per minute

4.1.2.2 Exposure

The e-beam exposure is performed with a Raith eLINE e-beam lithography system. An acceleration voltage of 20 kV is used, which is a good compromise between resolution and ease of use. Indeed, increasing furthermore the acceleration voltage of the e-beam would result in enhanced resolution, but the adjustment of beam parameters would be more fastidious, and proximity effects would increase.

The typical dose used for exposure is 120 $\mu C/cm^2$. Again, a compromise is found between smoothness of the developed pattern and limitation of proximity effects. Indeed, a higher dose results in more regularity (by statistical averaging) in the frontier between exposed and non exposed areas, but the number of electrons scattered away from the beam spot will also increase, resulting in "non exposed" areas being actually exposed, i.e. proximity effects. This optimal value was found by experimental trials, and is subject to slight variations depending on the chosen geometry.

Two exposure modes exist, normal mode and fixed beam moving stage (FBMS) mode. The idea is that the e-beam should not be deflected by more than 100 µm in order to limit aberrations in the spot shape. The normal mode works in the following way: the e-beam is deflected in order to expose patterns in a 100 µm side square centered on the un-deflected e-beam position. Then the beam is shut off and the stage is moved so that the next adjacent square is centered under the un-deflected beam, and exposure by beam deflection resumes. In FBMS mode, the e-beam is fixed, and the stage is homogeneously translated in one direction. This mode is well suited for the exposure of long waveguides. FBMS was used in LW devices fabrication, where several millimeter waveguides were needed [20]. With FSW devices (see §3.3.2), the waveguide and disk are fully contained within a 100 µm writing field so that FBMS mode is not needed. Only the normal mode is used, which simplifies the configuration of the lithography machine.

4.1.2.3 Development

After exposure the chip is developed in AZ 726 MIF, a strong, metal ion free alkali solution with added surfactants for homogeneous wetting. The development is performed in small steps (typically 10 s) to improve chip cleanliness. Although most of the resist is removed after a few seconds, a complete development time of typically 50 s is needed in order to resolve the narrow regions, like the gap between disk and waveguide or the anchoring rods region (see §3.3.2). The development should not be too long as it can increase resist edge roughness. The chip is very gently agitated in the developer (one vertical up and down motion in 10 s) in order to avoid strong currents that could bend or even tear off some resist patterns.

4.1.2.4 Resist reflow

In spite of exposure and development process optimization, developed resist sidewalls still exhibit significant roughness, which is then directly transmitted to the GaAs disk by the subsequent etch step. This roughness can be responsible for a decrease of the device's Q_{opt} (see §2.1.3). An efficient way to reduce sidewall roughness is to reflow the resist after development [53].

The chip is heated at 145°C for 5 minutes on a hotplate. At this temperature the resist softens, subsides under its own weight, but is held in shape because of surface tension. In this equilibrium position the surface is perfectly smooth. However, in our case, the part of the resist in contact with the substrate does not move during the reflow, and therefore some amount of roughness persists.

Using a reflow step can lead to two significant drawbacks :

- Because of the relatively high temperature – 50°C above the soft bake step – the resist cross-links strongly which makes its subsequent stripping more difficult.
- The resist takes a "water droplet" shape – thinner on the sides of the pattern, thicker inside. The resist on the sides is too thin and does not protect the semi-conductor material throughout the whole subsequent etch step (see §4.1.3).

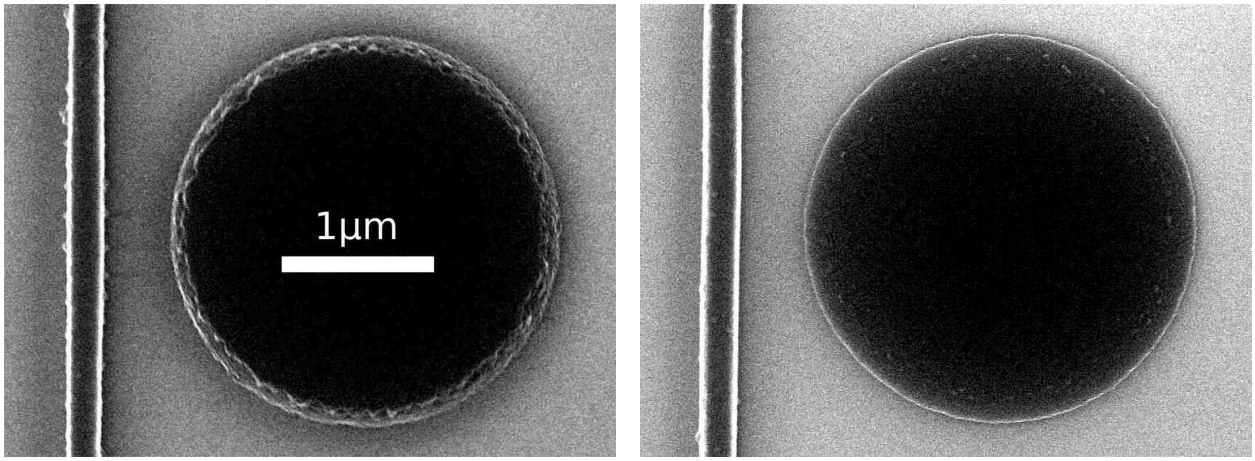

(a) Without reflow (b) With reflow

Figure 4.3 – Effect of reflow on Ma-N 2403 resist edge roughness. The two disks have a 2.6 µm diameter.

4.1.3 ICP anisotropic etch

4.1.3.1 ICP working principle

The first non-selective etch that defines the GaAs disk and waveguide is performed using an Inductively Coupled Plasma - Reactive Ion Etching (ICP-RIE) machine, that we will call ICP from now for simplicity. In an ICP machine, the sample is placed in a vacuum chamber and gaseous species are introduced within the chamber. The *ICP source* sends a radio frequency (RF) signal in a inductor (coil) in order to create a high density plasma. This plasma is then submitted to a RF electric field created by the *RF source*, which is connected to the sample holder. Electrons have a higher mobility than ions and strike the sample, which therefore charges negatively to a value called *self bias*. Ions follow in a second time and strike the sample, inducing some mechanical sputtering because of their high mass. The ability to tune independently plasma density and self bias allows to perform very gentle etches, which are of great interest to us.

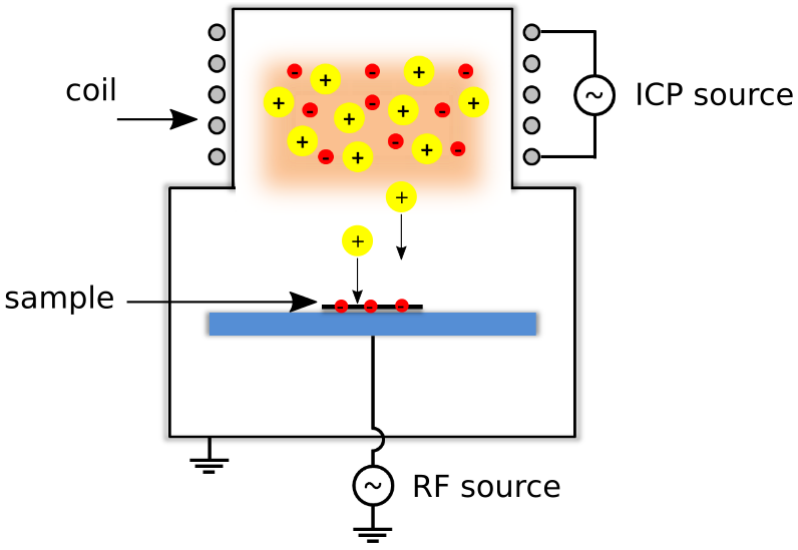

Figure 4.4 – ICP-RIE schematic

Ar (sccm)	$SiCl_4$ (sccm)	ICP power (W)	RF power (W)	Temp (°C)	Pressure (Pa)	Self bias (V)
9	3	25	17	10	0.1	-100

Table 4.1 – ICP etch parameters used for the fabrication of the disk resonators shown in Figure 4.5. The self bias is not set but depends on the other parameters value. The MaN-2401 resist mask thickness is 100 nm.

4.1.3.2 ICP Etching mechanism

It could be thought that the anisotropic etching is solely due to mechanical sputtering by accelerated ions that impact the semi-conductor surface. The etching mechanism is actually more complicated, and the following explanations, although given to the best of my knowledge, might be incomplete and inaccurate. The gases used in our standard recipe are argon (Ar) and silicon tetrachloride ($SiCl_4$). When the RF power is applied, Ar is ionized as Ar^+. Collisions between $SiCl_4$ and other particles in the plasma create $SiCl_x$ free radicals and $SiCl_x{}^+$ ions. The free radicals are neutral but can react chemically with GaAs and AlGaAs.

The key point is that the chemical reaction of these radicals with GaAs is not active at 10 °C, which is the temperature at which our sample is thermalized during the etch. The ions – Ar^+ and $SiCl_x$ based ions – play a crucial role, as they will increase the local temperature of the GaAs surface through collisions and therefore thermally activate the chemical reaction with $SiCl_x$ radicals. This etching process can be seen as an "ion assisted chemical etching". Although chemical in nature, the etch is anisotropic as ions, which are accelerated vertically, will have a significant mechanical impact for horizontal surfaces only. However, because of collisions in the plasma and on the GaAs surface, some ions can acquire non-vertical trajectories and the etching can become partly isotropic (see §4.3.2).

It could also be possible [54] that the reaction products are not volatile enough to leave the surface and allow a "second wave" to react. So if there was no accelerated ions, no etching would occur, only a chlorinated layer would form on the sample's surface. Ions induce desorption of reactants by mechanical collisions, allowing for a new "wave" of $SiCl_x$ radicals to react, and so on. The role of accelerated ions is therefore double in the etching process.

Although in principle it is possible to rely only on the mechanical sputtering of ions to perform the etching (we could achieve it by having Ar only in the chamber during the etch), this is not an efficient way, as mechanical sputtering etches GaAs and resist mask at the same rates. Therefore if only Ar is used, a resist mask as thick as the desired ICP etch depth is necessary. This not optimal as too thick resist layers induce proximity effects during the e-beam exposure (see §4.1.2.2). On the contrary, Ma-N 2400 resist does not react with $SiCl_x$ radicals – or at least not in the same way as GaAs/AlGaAs, and is thus etched much more slowly by our $Ar/SiCl_4$ recipe. Selectivities – defined as the ratio of GaAs etching rate over resist mask etching rate – on the order of 10 can therefore be achieved in the presence of $SiCl_x$ radicals.

4.1.3.3 Optimal ICP parameters

Starting from standard recipe parameters provided by the ICP manufacturer (Sentech Instruments GmbH), an optimization campaign [20, p. 108-109] was carried. The desired outcome is vertical sidewalls and a smooth etching. A fast etching rate is not really important, as the total etching length required is of the order of a few hundred nanometers. Table 4.1 resumes the optimal parameters found for the fabrication of the first generation of devices, using Ma-N 2401 for the resist mask. Below are some comments on these parameters:

- The chamber pressure is quite low if compared to other standard ICP recipes. The aim is to limit collisions in the plasma that would result in non-vertical trajectories of ions, which would collide with sidewalls and activate their chemical etching.

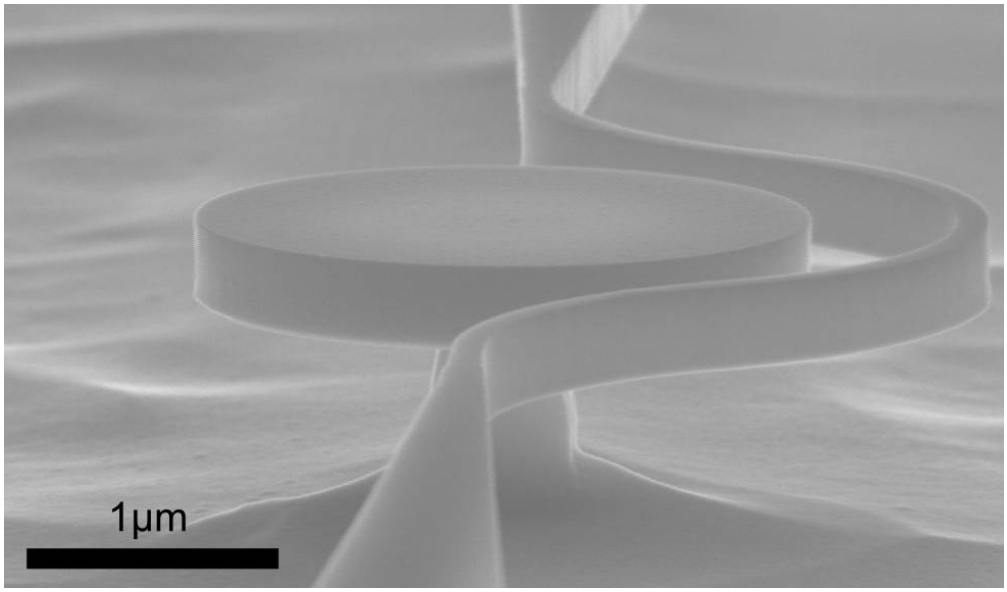

Figure 4.5 – SEM micrograph of an OM disk and integrated "bent" coupling waveguide.

- A low temperature – relative to plasma etching standards – is used to enhance the anisotropic aspect of etching as radicals have lesser probability to undergo temperature induced desorption and the etch is therefore exclusively activated by ions.
- The RF and ICP powers are quite low in order to obtain a self bias in the optimal range (~ -100 V). A too low absolute value would be insufficient to initiate etching, while a too high value would induce etching of vertical sidewalls because boucing ions would still have enough energy to activate the reaction.

Figure 4.5 shows a SEM image of an OM disk obtained with the ICP recipe of table 4.1. An experimental "loaded" Q_{opt} of $\sim$ 300 000 is obtained with such a disk (radius 1.3 µm, thickness 370 nm, 10 nm Al_2O_3 passivation layer deposited by ALD).

4.1.4 Hydrofluoric acid under-etching

Once the disk and coupling waveguide are defined by the ICP etching, a selective wet under-etching is performed in order to shape the AlGaAs layer underneath the disk into a thin pedestal, and get a "free standing" coupling waveguide (see figure 4.1). A HF aqueous solution is chosen for this purpose. It combines two advantages :

- HF etching selectivity is high (see §4.1.1). This is important as the GaAs disk and waveguide dimensions must not be affected by the etch.
- When used at low concentration and temperature, HF tends to produce smooth and isotropic etching under proper agitation conditions.

Right after the ICP etching step, the sample is immersed in isopropanol to limit oxidation of the $Al_{0.8}Ga_{0.2}As$ layer, as this creates an oxide "sheet" than will re-deposit on the sample during etching. The presence of this sheet degrades sample cleanliness and adds uncertainty on the etching rate. The sample is then etched in a diluted aqueous HF solution (1% in volume) stabilized at 4 °C. The sample is stirred gently in the solution as this helps with the etch isotropy. Indeed, we want the pedestal to respect the rotational symmetry of the disk. The etch time is $\sim$ 1 minute, which allows for good control of the under-etching depth. The sample is then dipped in water to stop the etching.

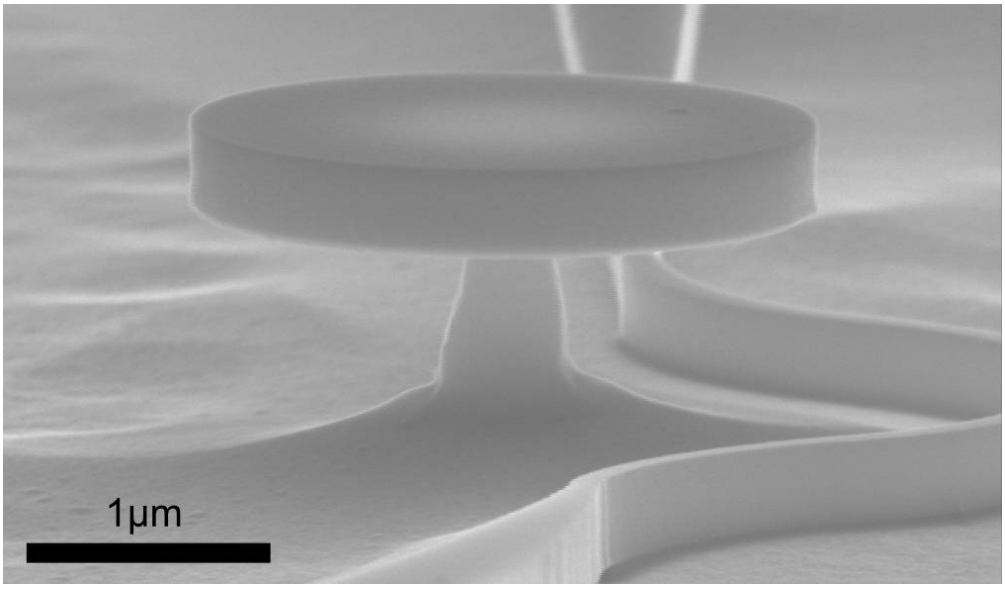

Figure 4.6 – SEM micrograph of an OM disk standing on its AlGaAs pedestal.

The low temperature (4 °C) is chosen because it yields smoother and more regular pedestals. At too low concentrations (0.1% in volume), AlGaAs close to the GaAs/AlGaAs interface is not removed, which is highly undesirable. Figure 4.6 shows a disk with its supporting pedestal. The latter is made clearly visible by the collapsing of the coupling waveguide (see §4.3.4).

Potassium hydroxide cleaning. As reaction products of HF with AlGaAs are poorly soluble in dilute HF, they can re-deposit as "flakes" on the sample, which can be troublesome especially if they land on GaAs disks. It has been reported [55] that a 2 minutes dip in concentrated potassium hydroxide (KOH) (10g/100mL) aqueous solution can dissolve these reaction products. If the ICP etch goes through the entire AlGaAs layer, very small quantities of AlGaAs remain on the sample – only what is left under the resist patterns – and practically no troublesome "flakes" are found. On the contrary, when the ICP etch is not carried through the entire AlGaAs layer, as shown for instance in figure 4.1, large amount of AlGaAs are etched by HF – indeed resist patterns represent less than 1% of the total sample surface – and a KOH cleaning in necessary.

4.1.5 E-beam resist removal

Although remaining e-beam resist on disks does not seem to affect optical properties – we measured Q_{opt} above 100 000 on R=1 µm, T=320 nm disks with a 100 nm thick resist layer on top – its effect on mechanical properties is supposedly deleterious. Indeed, resist is composed of long organic chains and friction will occur during mechanical motion of the resist which could dissipate energy. It is therefore crucial to efficiently strip the resist layer remaining on top of the disk.

MaN-2400 resist is usually stripped quite easily by dipping the sample in acetone or in strong alkali solutions. In our process, this is not sufficient to remove completely the resist film. The reason is that resist reflow and ICP etching both heat the resist mask, which makes it harder (or at least less soluble in chemicals) by increasing cross-linking. We therefore have to use an oxygen (O_2) plasma cleaning oven. In such an apparatus oxygen is ionized but ions are not accelerated like in a RIE etcher. Ultra violet (UV) light emitted by electronic relaxation in the plasma breaks the resist's high molecular weight organic chains into smaller ones, which then react chemically with oxygen species created in the plasma (O_2^+, O_2^-, O_3, etc.). Products like H_2O, CO, or CO_2 are formed, which desorb easily from the surface and are thus efficiently evacuated.

The O_2 plasma cleaning is performed for 15 minutes in a O_2 pressure of 0.5 mbar and a RF power of 160 W. Such a procedure removes the resist film very efficiently – no resist is seen remaining

(a) LW device coupling scheme : the waveguide (dark blue) is as long as the sample

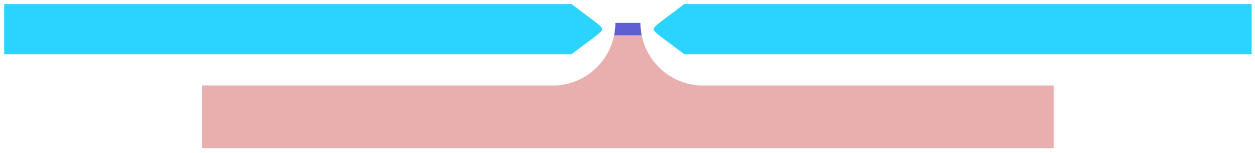

(b) FSW device coupling scheme : micro-lensed fibers come above the sample and the waveguide can therefore be arbitrarily short.

Figure 4.7 – Schematics representing LW device and FSW device coupling schemes. Waveguide is purple, micro-lensed fibers are blue and substrate is pink.

with SEM observation – but devices undergoing O_2 plasma tend to have lower Q_{opt}. We speculate that this Q_{opt} drop is due to heavy oxidation of the GaAs surface, which does not happen when the sample is just exposed to air. See §2.1.4 for more information.

4.2 Fully suspended waveguide devices

Although operational, LW devices have low optical transmission and show strong Fabry-Pérot effect. Improvement on these two points was achieved by the fabrication of FSW devices. A full description of the electromagnetic design of such devices can be found in §3.3.2. After presenting the general idea underlying the design of such devices, we will develop the additional technological steps required for their fabrication.

4.2.1 General idea

LW devices are designed in such a way that the physical extremities of the waveguide are the limits of the sample itself (see §3.3.1). In theory this does not put any constraint on the minimal waveguide length, but in practice it obviously does, as the cleaving and subsequent handling of a 50 µm wide sample is impossible with conventional tools at our disposal. Typical waveguide lengths in LW devices were therefore of a few millimeters. However, simple electromagnetic considerations show that it is of great interest to reduce significantly the length of the coupling waveguide. Indeed, the latter plays no active role – in contrary with nonlinear optics oriented devices where wavelength conversion intensity increases with waveguide length – and a long waveguide will only accumulate losses.

We therefore had to come up with a design where sample and waveguide length were not correlated anymore. The idea we had was to position the disk and waveguides on an elevated plateau – referred to as the “mesa” – so that the element bringing light to the waveguide would come above the sample. We could therefore achieve waveguides of very short length while maintaining a normal sample size, as can be seen on figure 4.7.

The fabrication steps described in §4.1 still apply for FSW devices and are partly unchanged. The e-beam resist spin coating, exposure and development procedure is exactly identical, only the patterns exposed by the e-beam machine are different: in LW devices FBMS exposure mode was needed to efficiently expose millimeter long waveguides, which is not the case anymore as the waveguides have a length of 40 µm in FSW devices. ICP and HF steps are also unchanged.

Figure 4.8 shows the fabrication steps performed subsequently to the HF selective under-etching. Ideally, the inverted tapers tips should go past the mesa edge for optimal optical access, otherwise

part of the light is lost (as seen in figure 4.9), but the mesa etching should obviously stop before the anchoring pillars of the waveguide structure is reached (see §3.3.2 for a description of FSW geometry). The etching amount and mesa flank straightness must therefore be controlled precisely. Otherwise, only some of the structures will be accessible.

The fibers have a radius of 65 µm, so the depth of the mesa shall be on the order of 100 µm. Indeed, some margin is necessary to avoid tilt complications when the sample is not well aligned with the micro-lensed fibers.

4.2.2 Photosensitive resist mask definition for the mesa

We start by spin coating photosensitive resist (Microposit S1800 series) on the sample (figure 4.8b). The mask exposition is performed with an optical lithography mask aligner (SÜSS MicroTec MJB4). Optical lithography is well adapted for such a mask for the following reasons :

- The mask, as can be seen on figure 4.8c is merely a big rectangle and does not have to be defined with the same resolution as the e-beam mask used for the disks and waveguides. Optical lithography has lower resolution than e-beam lithography, but it enough in this case.
- In optical lithography, UV light is sent on the whole sample, and some part of the light is blocked by a metal-on-glass mask. This allows for efficient exposition of large areas, as the full area is exposed in a few seconds typically. Exposing a mask of this size (~ 100 µm $\times$ 5 mm) with an electron beam would take several hours, if not days ...
- Microposit S1800 series photo-resist has the advantage of being transparent in the visible spectrum, which is crucial for the in-situ control of the mesa etch.

The photo-resist mask must cover entirely the optomechanical structures in the center. Otherwise they will be etched away while etching the mesa. The mask must therefore be at least 2 µm thick – the height of the disk standing on its pedestal is ≈ 1 µm – to protect the structures efficiently.

Once the resist is exposed we develop it in an alkali solution (Microposit MF-319). The aim is to control the distance between the inverted tapers tip and the mask edge to achieve the desired mesa depth. The mesa etching is not perfectly isotropic – contrary to what is shown (for simplicity) on figure 4.8d. The vertical etching rate is between two and three times faster than the horizontal one. Therefore, in order to get a 100 µm high mesa, a distance of 40 µm between the tip of inverted tapers and the mask edge is sufficient. The total mask width is therefore ~ 120 µm. Its length is ~ 10 mm, which is the sample length. Note that figure 4.8 is not to scale, the sample is actually 50 times wider than the FSWs.

Because of surface tension, resist accumulates at the edges of the sample and is significantly thicker there. These "bumps" of resist have to be exposed and developed several times to be removed completely. Indeed if resist remains at the sample edges the underlying GaAs substrate will not be etched and it will prevent fibers from accessing the OM structures.

Back surface protection. While we etch the sample's top surface in an isotropic etchant, the back surface of the sample gets etched too. For a 100 µm deep mesa, the sample thickness goes from 600 µm to 400 µm. This makes the sample fragile, and it can then break if handled to roughly. In order to limit sample thinning, we protect the back surface with the same S1800 photo-resist. The resist deposition is not possible via standard spin coating, as it would damage the optomechanical structures and their covering mask, which are now downwards. We proceed by depositing a drop of resist on the back surface and then evacuating the excess in a clean room grade cloth by capillarity.

Another advantage of back surface protection is that after resist mask removal the back surface is perfectly flat, which is typically not the case when it is etched. This facilitates handling and positioning of the sample in our measurement apparatus.

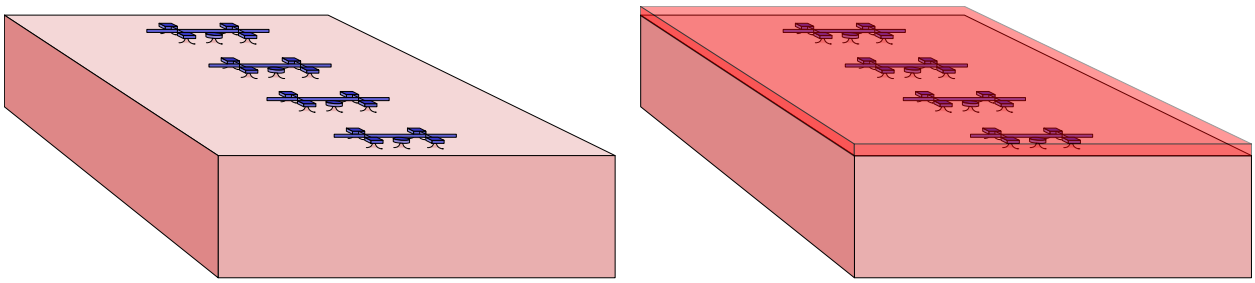

(a) Sample after HF under-etching step

(b) Optical resist spin coating

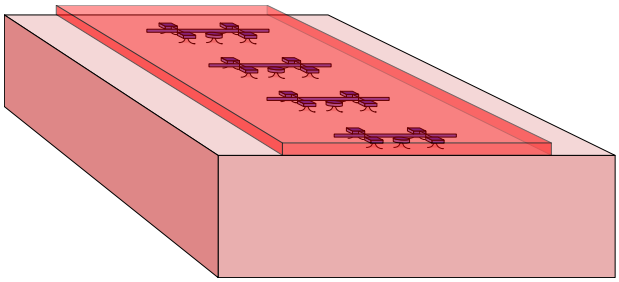

(c) Resist after development

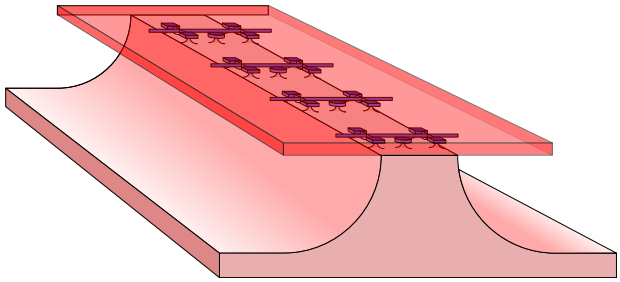

(d) BCK wet chemical etch

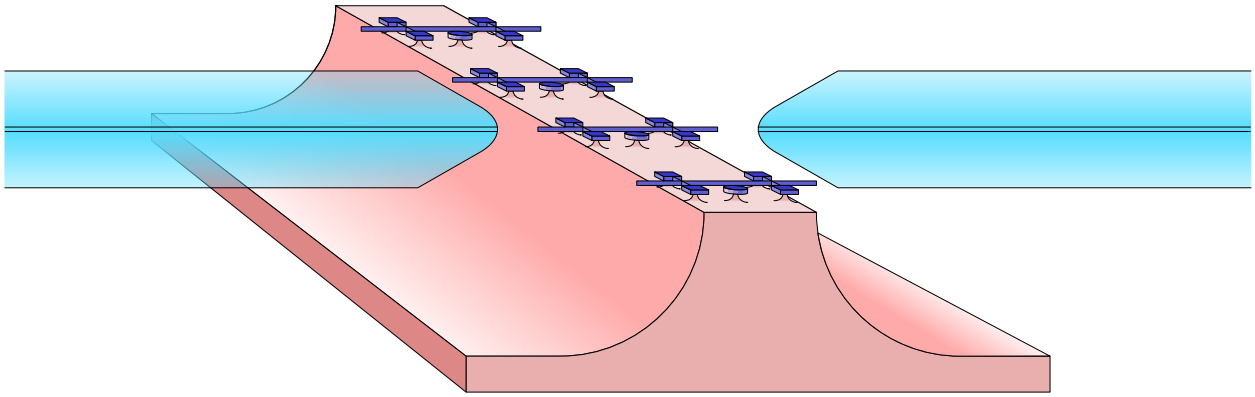

(e) Mask dissolution and fiber positioning

Figure 4.8 – Additional fabrication steps necessary for the fabrication of FSW devices. Optomechanical structures are shown in dark blue, substrate is pink, resist mask is red and micro-lensed fibers are blue. Figure is not to scale.

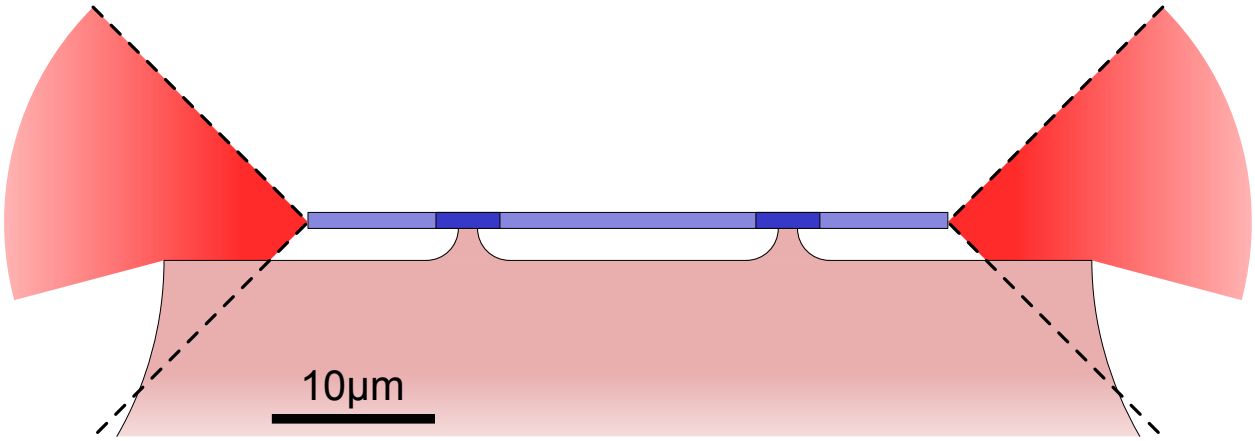

Figure 4.9 – Clipping effect happens if the mesa etching is not advanced enough. The dashed cones represent the inverted taper's numerical aperture (NA).

4.2.3 Mesa etching

The simplest way to transfer the mask pattern to the semi-conductor material is to perform a "wet" etching, i.e. immerse the sample in a chemical solution. For the GaAs/AlGaAs hetero-structure, several chemical solutions exist. Most of them consist in the mixture of an acid with an oxidizer and work on the following principle : the oxidizer first oxidizes the semi-conductor surface, and the oxide layer is then dissolved by the acid. This iteration repeats until the desired etching depth is reached. Once the mask is defined we proceed with the mesa etching. As can be seen in figure 4.8 the mesa edge must go past the inverted taper tips but stop before the pillars anchoring the waveguides. If the mesa edge stops before the inverted tapers tips, clipping occurs (see figure 4.9) and a significant fraction of light is lost. Precise control of the etching advancement must therefore be achieved, as well as straight mesa edges. Indeed, only 4 disk+waveguide devices are shown on figure 4.8, but a real sample packs several hundreds of devices, which will obviously not be all accessible if the mesa edge is not kept straight along the whole sample length. For these reasons the chemical solution and etching procedure must be chosen carefully.

4.2.3.1 Etchant choice

The ideal etching solution would have the following properties :

- fast etching rate, because the mesa etching is deep.
- same etching rates for GaAs and AlGaAs
- isotropic etching
- smoothness of etched sidewalls

Several solutions are potential etchants for the GaAs/AlGaAs hetero-structure. They all rely on the oxidation/etching cycle. The ones we tried are HF/H_2O_2, HCl/H_2O_2, H_2SO_4/H_2O_2, H_3PO_4/H_2O_2, and BCK. BCK has been reported to produce smooth and isotropic surfaces [56]. It is prepared by mixing aqueous solutions of hydrobromic acid (H**B**r), acetic acid (**C**H_3COOH) and potassium dichromate ($\mathbf{K}_2Cr_2O_7$) in equal volume proportions. The results for the different etchants are the following:

- HF/H_2O_2 completely dissolved the resist mask and the structures underneath.
- HCl/H_2O_2 strongly damaged the resist mask and produced irregular flanks.
- H_2SO_4/H_2O_2 yielded something that we were not able to interpret under optical microscope observation...

BCK and H_3PO_4/H_2O_2 yielded good results. The mask was not damaged, etching was smooth and seemed isotropic. At first, we decided to retain $H_3PO_4 + H_2O_2$, as it is less toxic than BCK, transparent (BCK is completely opaque), and *seemed* to produce straighter flanks. This was a mistake for reasons that I will develop later, and the etchant used is now BCK.

4.2.3.2 Agitation conditions

The determination of the best etchant was done without any agitation of the sample into the beaker. Although the H_3PO_4/H_2O_2 result was smooth, the mesa edges were not straight, and thus only a fraction of the sample's waveguides could be addressed with the micro-lensed fibers. In order to improve mesa edges straightness we tried to agitate the sample in the solution.

Figure 4.10 shows the setup used for agitation of the sample in the etchant solution. We use a stirring device that drives the rotation of a magnetic rod located inside the etchant beaker.

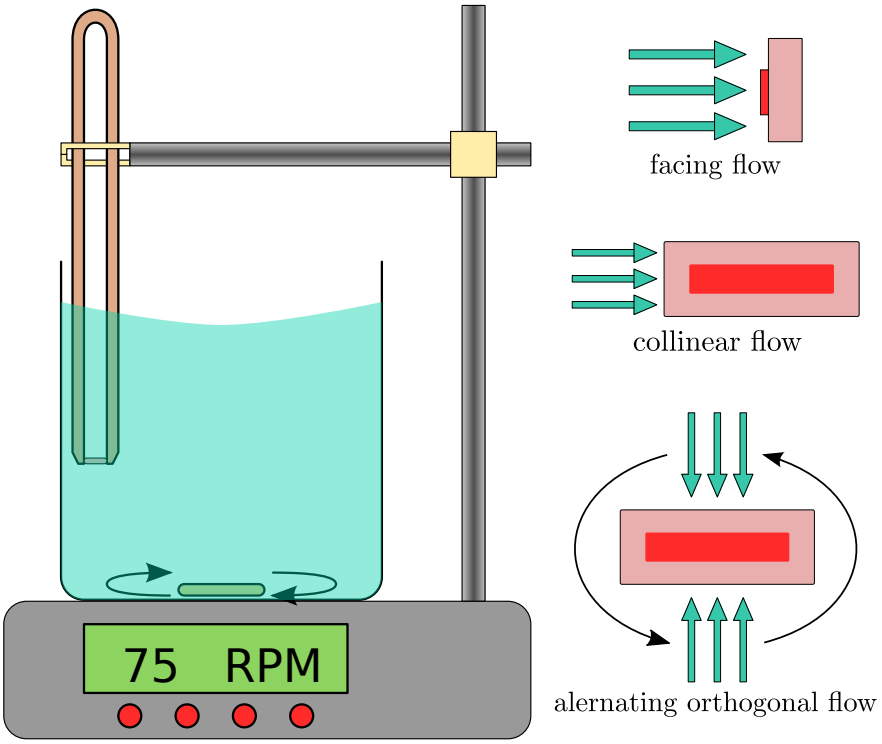

Figure 4.10 – Agitation of the sample in the etching solution. Depending on sample orientation and magnetic rod programming, different agitation conditions can be achieved.

The sample is held by an acid-proof polytetrafluoroethylene (PTFE) tweezer. We tried three different agitation conditions. A facing flow yielded straighter flanks than without agitation, but still insufficiently straight to access all structures. A flow collinear to the mesa edge gave sometimes good results, but sometimes poor results as well. We believe that it was quite sensitive to the sample tilting with respect to the etchant flow. It did not yield reproducible results. The last agitation condition we tried was to alternate flows perpendicular to the mesa edge – alternating is necessary otherwise the etching would by intrinsically asymmetric. For this mode the stirring device must be programmed to alternate clockwise and counter-clockwise rotation of the magnetic rod. This mode gives very straight and reproducible results. We've therefore been using it since.

4.2.3.3 Etching progression control

The etching rate of H_3PO_4/H_2O_2 is $\sim$ 3 µm/min. It is not known precisely, and depends on the solution temperature, aging of the chemical products used, and exact positioning and tilting of the sample. Furthermore, the etching rate seems to be increasing at the end of the etching process. Therefore it is not possible to predict the etching time, as the tolerance for the mesa etch stopping point is only a few microns.

Fortunately, the resist mask that we use is transparent in the visible spectrum (see figure 4.11). We can therefore etch a first "safe step" (we are sure to etch less than the desired amount), then take the sample out of the chemical solution, dry it, and observe the mesa etching progress under an optical microscope. A calibration of the etching speed can be done and the etching can be continued in shorter – and thus more precise – steps until the desired etching advancement is obtained. Once the etching is finished the mask is dissolved using acetone and the sample is then dried. Optical resist is removed very easily in acetone because it is not cross-linked by any heat during the process.

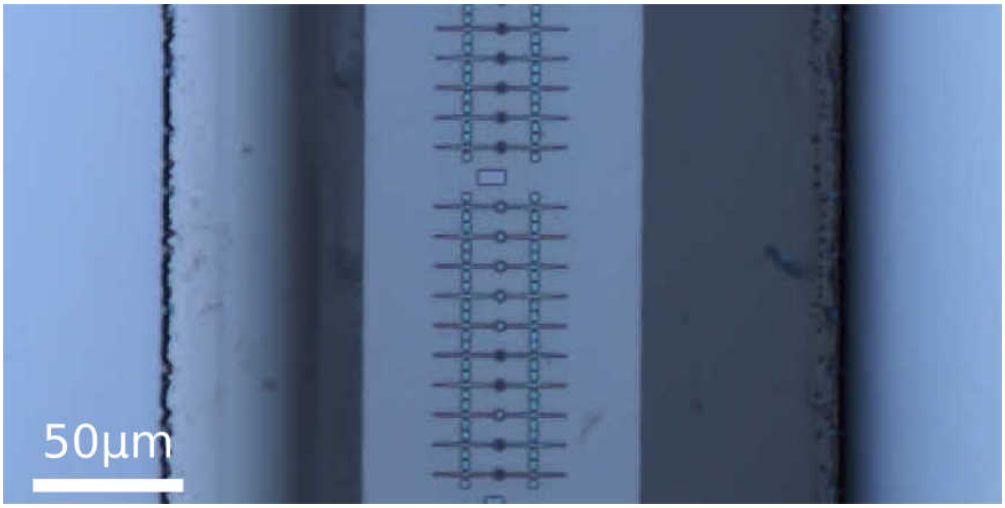

Figure 4.11 – Optical microscope image of a sample after 55 minutes of etching in BCK. The mesa edges can be seen through the resist mask by transparency. Etching is straight and symmetric.

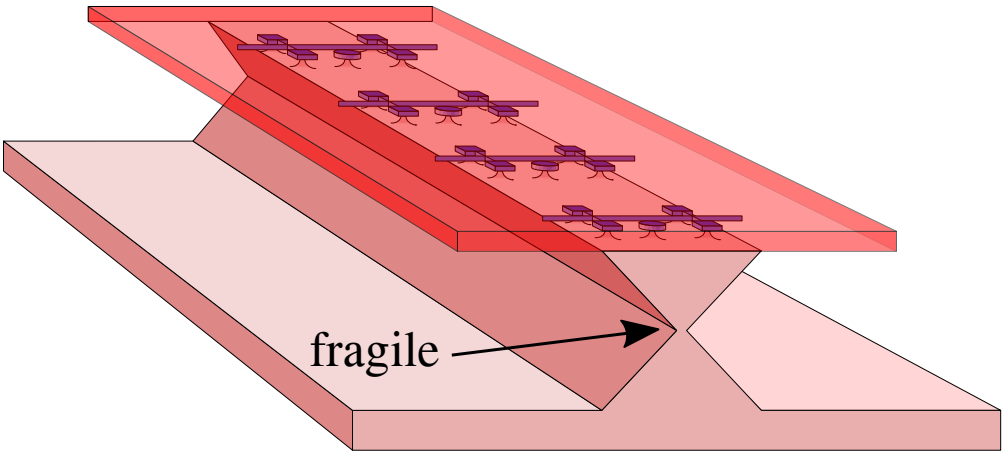

Figure 4.12 – "Hourglass" shaped mesa resulting from a H_3PO_4/H_2O_2 non-isotropic etch

4.2.3.4 Switch to BCK as the mesa chemical etchant

Although it did not always happen, some of the H_3PO_4/H_2O_2 etches finished in a catastrophic way, i.e. the mesa broke shortly before reaching the desired etching advancement. The reason is that in some stirring conditions, the H_3PO_4/H_2O_2 etch is not isotropic but strongly follows some specific planes of the GaAs crystal lattice. This results in a significant undercut of the mesa (see figure 4.12), which sometimes break apart from the sample's main body...

As we could not prevent this from happening, we came back to the BCK solution. We could obtain the same mesa edge regularity, without any crystalline oriented etch. We also realized another advantage : the ratio of vertical to horizontal etching is ~ 2.5. This is convenient as only 40 µm of horizontal etching is necessary in order to dig a 100 µm deep mesa. This gives less time to "build up" irregularities during the etch.

One disadvantage of the BCK-etched mesa is that the mesa flanks are very steep. Because of this it is quite difficult to image the micro-lensed fiber in our cryogenic apparatus (see §5.2.2), which can make alignment protocols extremely tedious, but we found ways to overcome this.

One could wonder why we do not use an ICP step to etch the mesa, as this would certainly enhance the regularity of the mesa edge. The reason is that our ICP recipe has an etching rate of ~ 40 nm/min, so the etching of a 100 µm mesa would take up to 40 hours... We could increase the etch rate by augmenting the RF and ICP power, but then the resist mask would undergo some

increased damage, and a very thick mask should be processed, which is not convenient.

Figure 4.13 shows SEM micrographs of a finished device. On the top picture the waveguide inverted taper tips can be seen extending beyond the mesa edge. The devices have Ω-shaped waveguides for optimized disk-waveguide evanescent coupling (see §3.2).

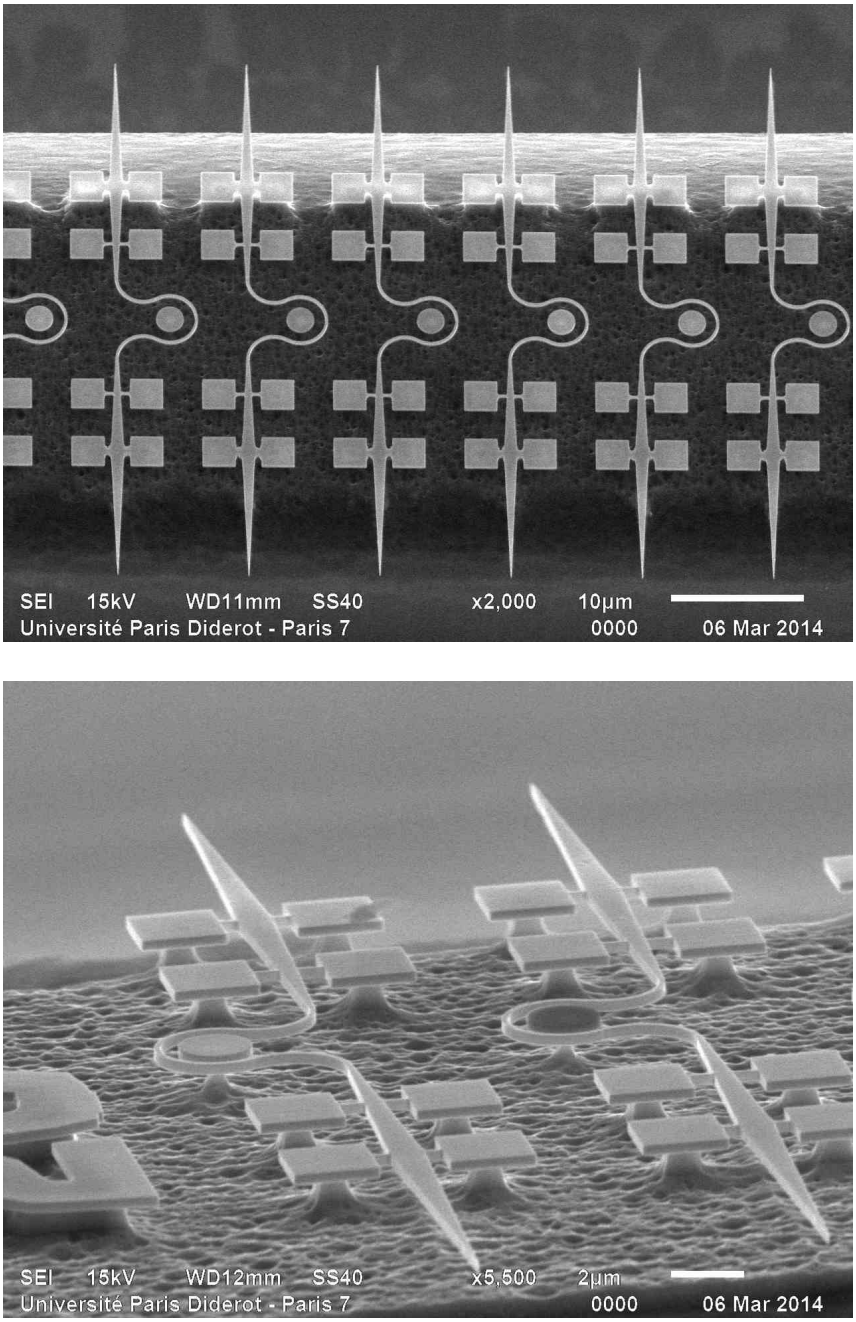

Figure 4.13 – SEM micrographs of finished FSW devices. The waveguide is patterned in the *omega* shape discussed in §3.2. The rough floor is AlGaAs wet etched by HF, it does not impact the optomechanical system's performance.

4.3 Mechanically shielded devices

In order to boost the Q_m of our disks, we decided to adopt a design with a mechanical "shield" located under the disk. To achieve this the wafer epitaxial structure has to be modified. Instead of one GaAs layer (the disk) on top of one AlGaAs layer (the pedestal), the wafer is now composed of four layers : two GaAs/AlGaAs alternations (see figure 4.14). Because disks and waveguides are integrated on the same chip and result from the same process, the coupling waveguide will also have a vertical replica (see figure 4.19). This is not desired and can actually cause problems as we will show in the following. This transition to shielded disks did not require any additional step in the fabrication process, but almost every existing step had to be re-optimized in order to avoid deleterious effects.

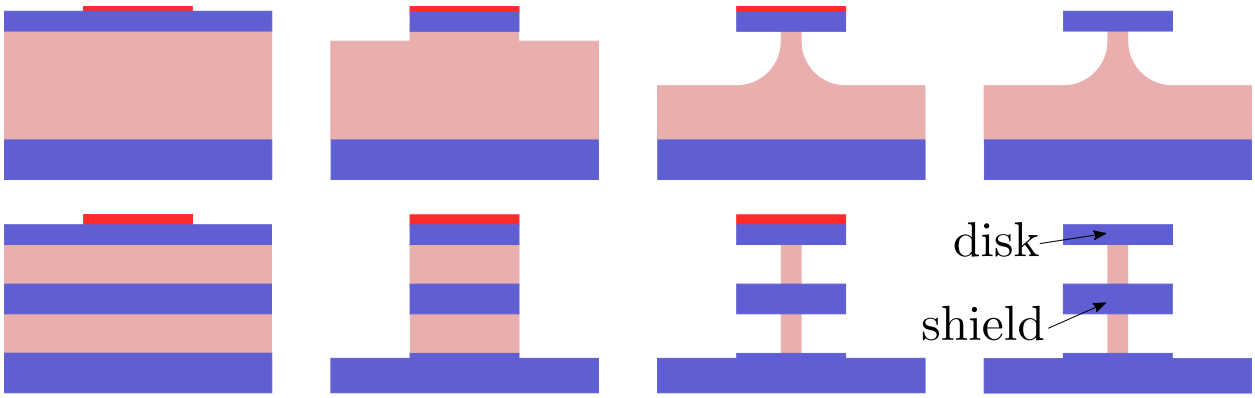

Figure 4.14 – disk fabrication steps with the two different wafer structures. Steps are, from left to right : **1:** resist mask definition, **2:** ICP anisotropic etch, **3:** HF selective under-etch, **4:** resist removal.

4.3.1 Change in the e-beam resist thickness.

In the single disk fabrication process the ICP etch depth only needs to go through the top GaAs layer (see figure 4.14). This corresponds to a depth of ~ 400 nm. For shielded resonators fabrication the ICP etch has to go through four layers, which corresponds to a depth of ~ 2 µm. Because the resist mask we use has a finite selectivity (see §4.1.3.2), it must be made thicker to endure a 2 µm deep ICP. We therefore change the mask thickness from 100 nm to 250 nm. This is achieved by spin coating a more viscous variant of the ma-N 2400 resist. The optimal exposure dose is barely changed, but development times are longer.

The amount of proximity effects increases because electrons have a thicker layer to diffuse in. Figure 4.15a shows the consequences of proximity effects. The area between the disk and waveguide receives a significant amount of exposure because of the "spread function" of the e-beam spot. When developed, some of the resist in this zone is sufficiently cross-linked to not dissolve in the developer solution. We did not find a final solution to this problem, but we noticed that a longer development time (~ 60 s) was enough to prevent proximity effects, although it tends to increase the amount of edge roughness...

Another disadvantage of using a thicker resist layer is reflow complications. Figure 4.15b shows the resist pattern equivalent to the one in figure 4.15a, but after a reflow step – 3 minutes at 160 °C. Instead of keeping a cylindrical shape, the resist takes a "water drop" shape with very thin edges. Those edges undergo quick wearing during the ICP etch step. The disk rims are no longer protected and become rough. We therefore cannot afford a resist reflow, which impacts the Q_{opt} of fabricated MS resonators. Although it has not been tried yet, a possible workaround would be a "plasma assisted reflow" using nitrogen [57]. This may change the contact angle between resist and substrate and produce a very smooth mask without thin edges. It must be noted that this "water drop" effect must also exist when reflowing 100 nm thick resist. It must however be less important

because we never observed degradation of disks quality in this case (also the ICP etch is 5 times shorter in this case).

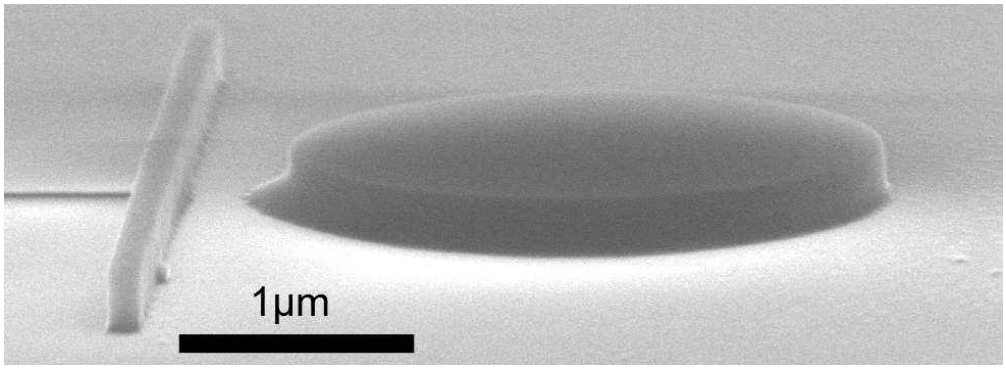

(a) Proximity effect

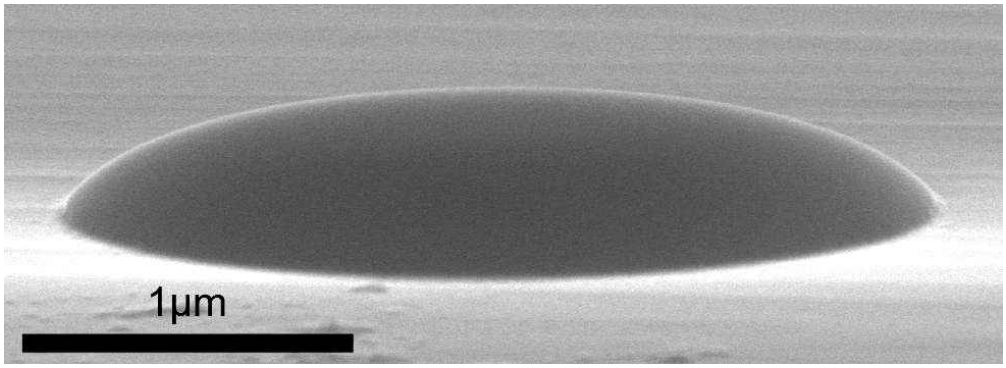

(b) Too thin edges after reflow

Figure 4.15 – SEM micrographs showing problems occuring with 250 nm thick resist masks.

4.3.2 ICP optimization

Obtaining a smooth and vertical plasma etch is quite challenging, especially if the etch is deep [54, 58]. Additionally, MS disks dimensions must be controlled very precisely, as for instance a 10 nm difference between disk and shield radius can have a drastic impact on the anchoring Q_{m} (see §6.3.2). ICP optimization has therefore been a demanding and challenging work, and a satisfactory recipes were found only recently.

4.3.2.1 Horizontal etching

In the first MS disks fabrication trials, we used the ICP recipe optimized for single disks (see table 4.1). It gave good results for "test" disks that did not have a coupling waveguide in their vicinity (see figure 4.16a), but for complete structures with integrated coupling waveguide, we noticed two unwanted effects (see figure 4.16b):

- some asymmetry in the disk flanks slope
- significant weathering of the shield's upper rim on the waveguide side

These unwanted effects are both a consequence of horizontal etching. Although it can obviously be attributed to the waveguide vicinity, the physical mechanisms at play are not clearly identified. One possibility is that ions are "trapped" in the trench that is being dug between the disk and

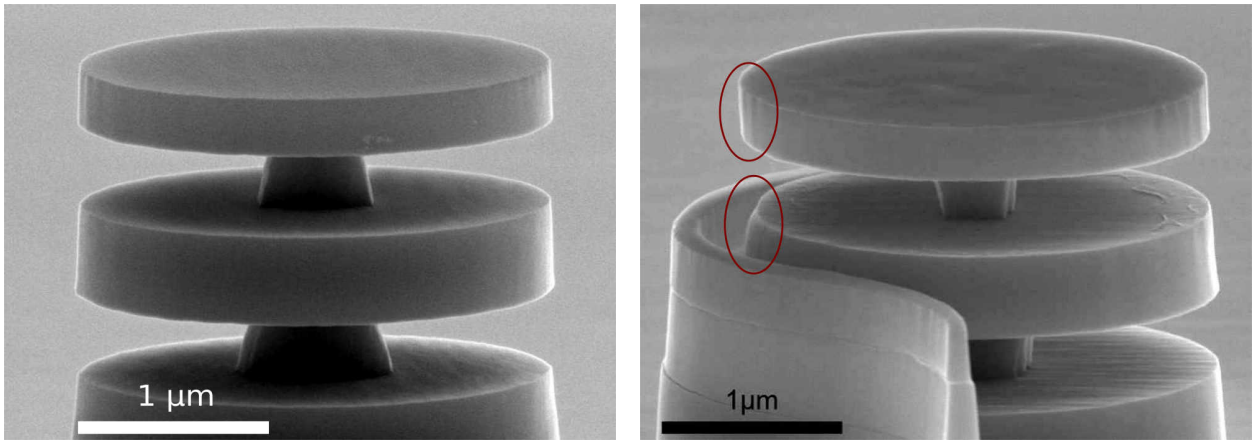

(a) Isolated disk (b) Disk with waveguide

Figure 4.16 – SEM micrographs of MS disks after ICP ad HF selective etch step

the waveguide. They could bounce many times between the trench walls and therefore thermally activate the walls etching. A close inspection of figure 4.16b reveals that the horizontal etching rate is not equal for GaAs and $Al_{0.8}Ga_{0.2}As$. Indeed, the slope between the upper and lower rims of the disk is more vertical than the one between disk lower rim and shield upper rim. Moreover, it can be seen that the shield recovers a radius equal to the disk's radius as the etching goes (we are still considering the side facing the waveguide), because the disk plays the "mask" role now for vertically impacting ions.

Of course this asymmetric weathering of disk and shield had a deleterious impact in Q_m. We tried different approaches to limit the horizontal etching. The first one was to reduce the relative concentration of $SiCl_4$ in the ICP chamber. The idea was to increase the etching fraction by mechanical sputtering. This improved slightly the situation, but not sufficiently. Another idea was to reduce the self bias just above the etching threshold, so that ions, after bouncing on the horizontal surface, do not have enough energy to activate the etching of vertical walls. Again this seemed to bring some improvement, but the ICP etch quality was not steady from day to day, and it was difficult to see a clear correlation between a change in etching parameters and a diminution of horizontal etching. After some exchanges with the ICP manufacturer, we came to understand that the ICP and RF sources power used were not high enough to guarantee a good plasma stability. Nonetheless these low powers are required as more powerful ICP recipes yield inferior results.

This asymmetry can be mitigated by the use of *eye* waveguides that completely surround the disk. The drawback is that the only way out for reaction products is now upwards, whereas with straight waveguides products could be evacuated laterally. This modifies the etching equilibrium and yields rough disks (not shown here).

Two possibilities that have not been tried yet are ICP temperature reduction and lower aluminum fraction in the AlGaAs layer.

- The wafer temperature used for all ICP etches during my PhD thesis was 10 °C (see table 4.1). It could be decreased to ~ -10 °C, but cryogenic temperatures are not attainable with the current ICP setup in our clean room. Anyways, low temperature is reported to enhance the anisotropic aspect of plasma etching [54], seemingly because ions bouncing on sidewalls need more energy to activate chemical etching.

- As mentioned above, $Al_{0.8}Ga_{0.2}As$ is more prone to horizontal etching than is GaAs. This suggests that aluminum reacts more with $SiCl_x$ radicals than gallium or arsenic, and therefore a decrease of the aluminum fraction would make AlGaAs closer to GaAs in terms of behavior during the ICP etch. This would help to reduce AlGaAs horizontal etching, and therefore shield weathering.

4.3.2.2 Oxygen addition

As we couldn't find a way to avoid horizontal etching with the $Ar/SiCl_4$ chemistry, we tried to add O_2 in the chamber during the etch. The idea was to passivate the GaAs/AlGaAs surface with a silicon oxide (SiO_x) layer. Silicon necessary for the SiO_x formation comes from sputtering of the silicon wafer on which the sample is placed during the etch. This passivation layer has been reported [59] to mitigate the effects of lateral undercut. We did a few trials, with essentially the same parameters as those shown in table 4.1, but with different gas flows. We set equal flows for Ar and $SiCl_4$, and the O_2 flow was set to be 2.5% and 5% of the total gas flow in two different trials we made.

The etch with 2.5% O_2 did not give good results. The optomechanical structures surfaces were irregular, and some "grass" [60] formed on the rest of the sample. The recipe with 5% O_2 gave better results. A passivation layer could be observed on the surfaces (we could measure an increase of the disks radiuses), which prevented horizontal undercut.

Figure 4.17a shows a disk observed after 5% O_2-ICP and HF under-etching steps. The disk is very smooth, but the whole structure has a pronounced "A" shape, and the shield size is therefore out of the tolerance range for efficient mechanical shielding effect. Observations of disks with a waveguide in the vicinity did not show horizontal etching, which we attribute to the formation of an SiO_x passivation layer. Additionally, the resist mask is intact, although it is usually damaged with standard processes. This suggests that the resist has been passivated too. Achieving such resist passivation in a reproducible way would allow to perform deep ICP etches, with a very thin resist mask, with all advantages associated to thin masks (see §4.3.1).

Figure 4.17b is a wider view of the same 5% O_2-ICP sample. It can be see that the ICP etching only occurred in the vicinity of the resist mask, resist-free areas have been completely passivated. The role of the resist in these passivation fluctuations is not understood. Because of their strong "A" shape, mechanical shielding does not work with these O_2-ICP structures, so we did not carry on with O_2 trials. It would however be interesting to pursue, indeed only few gas flow parameters were explored, there are many more configurations to try.

Another ICP chemistry is being investigated in our team more recently, consisting of Ar - $SiCl_4$ - nitrogen (N_2). The addition of nitrogen has been reported to lessen lateral undercutting effects [59]. The first observations are quite positive as they show a better "tuned" passivation process: it is sufficient to prevent lateral undercutting, without inducing the deleterious "A" shape seen in figure 4.17a.

4.3.3 Pedestal under-etch control

Typical mechanical simulations of MS optomechanical structures allow a tolerance of $\pm$ 20 nm on the pedestal radius for the Q_{clamp} to stay above 10^5 (see chapter 6 and more specifically figure 6.9). Given that the etching speed of 1% HF solution at 4 °C is $\sim$ 10 nm/s, the etching time must be controlled within $\pm$ 2 s. This precision can be achieved experimentally thanks to the quick dipping in isopropanol after the ICP step, which prevents oxide formation. Additionally, we define disks of variable radii on a single sample. This results in pedestals of different radii and therefore the desired pedestal size can always be obtained.

However we lack control on pedestal geometry. The ideal situation would be a perfect cylindrical shape for both pedestals of the MS device, and equal radiuses in both layers, as can be seen on the bottom-right sketch of figure 4.14. In reality the upper and lower pedestals tend to have different radiuses, and their shape is not cylindrical. These effects can be seen in figure 4.16a. In the following we will detail our efforts to address these problems.

4.3.3.1 Radius difference

The AlGaAs layers in the hetero-structure we use have a typical thickness of several hundred nanometers. As the AlGaAs under-etching progresses, this narrow thickness enhances diffusion

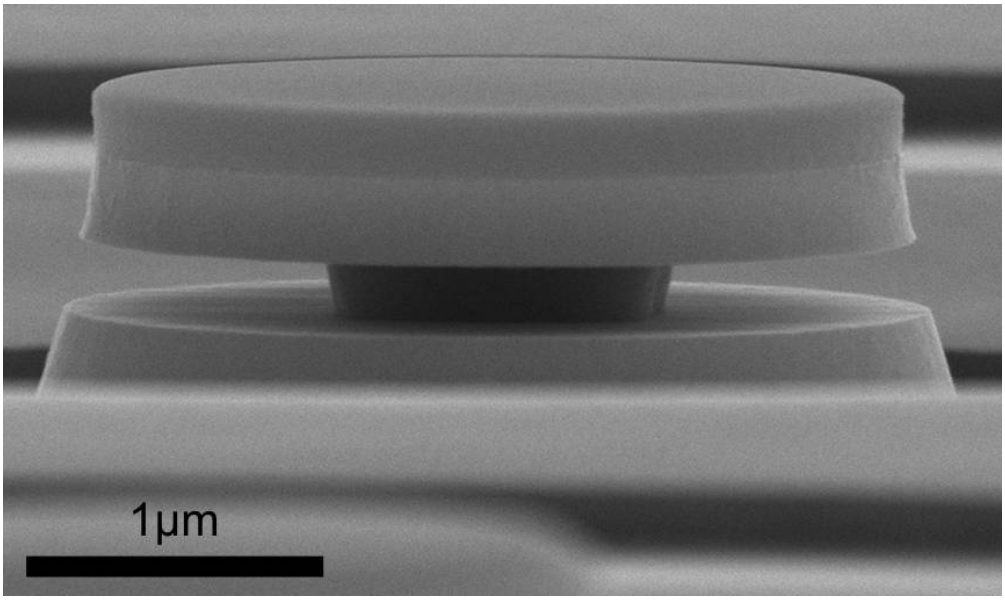

(a) Disk produced with 5% O_2

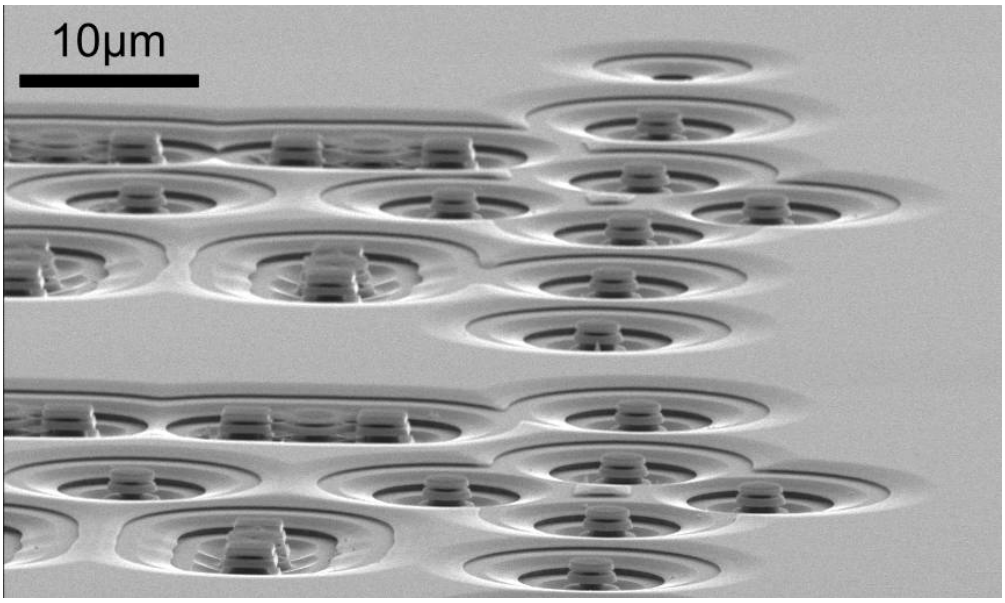

(b) Complex passivation effects

Figure 4.17 – SEM micrographs of MS structures fabricated with a 5% O_2 ICP

effects that hinder the travel of "fresh" HF towards the etching front, as well as the evacuation of reaction products. The etching rate is therefore slowed down. It could be expected that if one of the AlGaAs layers is significantly thinner than the other, then diffusion effects will be stronger and etching rate will decrease.

The hetero-structure grown for our first generation of MS devices had different AlGaAs layer thicknesses. This could be exploited in order to control the relative radius of one pedestal with respect to the other, by variations of stirring conditions: when the sample is immersed in the HF solution, the etching – or "digging" – of both AlGaAs layers start simultaneously. The digging rate is slower for the thinner AlGaAs layer so when the sample is removed from the HF solution, its associated pedestal radius is greater. The sample is then dipped in water to stop the etching process, but this does not take effect immediately, as the HF must diffuse out of the narrow space between the GaAs layers. HF will take a longer time to evacuate the thinner trench, and therefore this layer will be etched more during this water rinsing step.

Diffusion effects tend to have less impact when the stirring in the solution is strong. Therefore the pedestal radius difference between thin and thick AlGaAs layers at the end of the HF dip will be more pronounced if the sample is kept still in the HF than if it is strongly agitated. The following rules can be applied :

- if a bigger radius is desired for the thick AlGaAs layer, then the sample should be strongly stirred during the HF dip, and then kept still during the water dip.
- if a bigger radius is desired for the thin AlGaAs layer, then the sample should be kept still during the HF dip, and then strongly agitated during the water dip.

If pedestals of equal dimensions are desired, the right amount of agitation must be found. In practice, we could control the radius difference to a good level on a wafer with AlGaAs layers of 500 nm and 300 nm : it was reduced from 100 nm to less than 10 nm when paying attention to agitation effects. The wafer growth we ordered for the second generation of MS devices had the two AlGaAs layers thickness of almost equal size – 460 nm and 455 nm. It was therefore not possible to take advantage of diffusion effects, and the bottom layer systematically had a larger pedestal (see figure 4.16a), for a reason that was never clearly understood.

4.3.3.2 Non-cylindrical shape

Another unwanted effect that occurs is the non cylindrical shape of pedestals. Pedestal have an "A" shape as in figure 4.16a, or a "V" shape as in figure 4.16b, depending on the angle of SEM observation. The reason is that HF under-etching is not isotropic, but can follow crystalline planes. The result is a complex pedestal shape than gives either an "A" or "V" profile depending on the direction it is projected on. We tried to change HF under-etching conditions – temperature, concentration, strength of agitation – in order to induce a more isotropic etching regime, but this had only little impact and pedestals stayed essentially non-cylindrical. Two routes could be followed in the future in order to enhance etching isotropy:

- The use of gaseous HF. Gaseous HF etching of silicon dioxide (SiO_2) has been reported to be very isotropic [61]. However it is not sure that gaseous HF would efficiently etch AlGaAs.
- A diminution of the aluminum fraction in the AlGaAs layer might also change the wet HF etching dynamics...

4.3.3.3 Off-centered pedestals

For a single isolated disk (i.e. no other structures exist in the vicinity), the HF under-etching front progresses in a symmetric fashion and the pedestal is therefore centered under the disk. However, the vicinity of the waveguide structure on one side of the disk can make HF diffusion asymmetric,

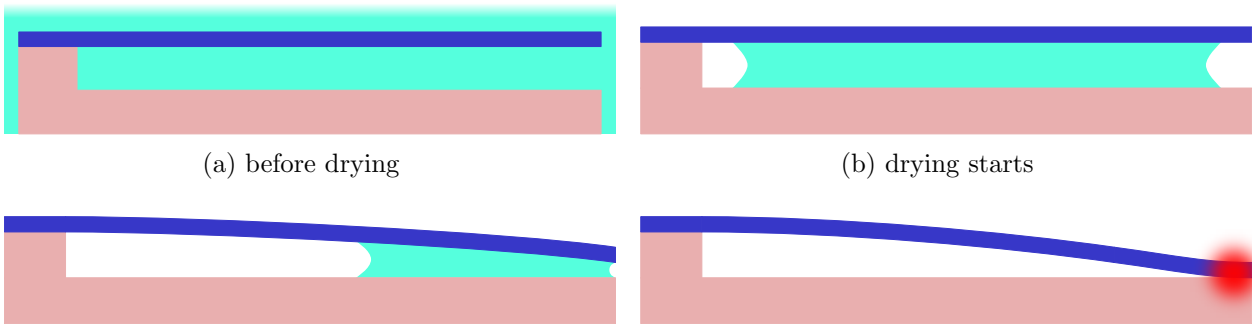

(a) before drying (b) drying starts

(c) capillary forces bend the cantilever (d) cantilever is pinned to substrate

Figure 4.18 – Stiction mechanism schematics. The red area represent strong Van der Vaals forces.

which can result in pedestal off-centering. Again diffusion effects are at stake here and we noticed that a strong agitation in HF and subsequent water tends to decrease the off-centering effects. Unfortunately this systematic strong agitation is not compatible with the techniques detailed in §4.3.3.1.

A way to get intrinsically rid of this off-centering effect is to adopt an *eye* waveguide geometry that respects the azimuthal disk symmetry (see §3.2). However the quality of long ICP processes – necessary to fabricate MS devices – seems to be degraded when applied on structures with an *eye* waveguide. This is supposedly due to the deleterious confinement of reactants by the *eye*. It is important to limit pedestal off-centering effects as they strongly affect the Q_{m} (see §6.3.2). On figure 4.16b, a slight pedestal off-centering of ∼30 nm exists, although hard to see with the bare eye. Simulations showed that this off-centering is enough to impact by two orders of magnitude the clamping loss quality factor of our devices.

4.3.4 Stiction problems

4.3.4.1 Phenomenon description

Stiction problems were already occurring with the first generations of devices [20, p. 118], but they became a major difficulty during the development of MS devices. Stiction has been known to be a cause of fabrication failure for a long time in the MEMS industry, and different methods have been used to deal with it [62]. The general idea of the stiction mechanism for a suspended cantilever is schematized in figure 4.18. During the drying subsequent to a wet under-etching step, a thinning liquid film will bring cantilever and substrate in contact by capillary forces. Once the liquid is evaporated, the two surfaces stay in contact because of Van der Waals surface forces – and possibly some remaining liquid.

Van der Waals forces can be modeled by the following formula, which gives the interaction energy per unit area for two surfaces separated by a distance d [62] :

$$E_{vdW} = -\frac{A}{12\pi d^2} \tag{4.1}$$

A is the Hamaker constant, which depends on the properties of both surfaces interacting. Formula 4.1 is actually only valid when the two surfaces are separated by less than a few tenths of nanometers. For larger separations, Van der Waals forces decay even faster. Therefore when the cantilever is not bent (figure 4.18a), Van der Waal forces are too weak to collapse the cantilever on the substrate. However, once the cantilever in brought in contact to the substrate by the drying liquid, Van der Waals forces can pin the cantilever to the substrate. A small contact surface is sufficient, we observed 10 µm long tapered waveguides pinned by a 50×50 nm contact surface. Van der Waals force per unit surface depends on the nature of surface dipoles and therefore specific surface coatings

can reduce its strength. Electrostatic forces could also be at play in the stiction process, although it is difficult to quantify their effect.

4.3.4.2 Waveguide sticking

Stiction mainly affects the waveguides of our structures. Waveguides behave similarly to the cantilever shown in figure 4.18, but are doubly clamped (see figure 4.1). This provides more rigidity, but capillary forces can still be strong enough to bring waveguides in contact to the substrate. One important parameter is the height between suspended waveguide and substrate. The larger this height, the larger the capillary force needed to pull the waveguide in contact with the substrate. Therefore choosing a large height between active layer and substrate is an efficient way of avoiding stiction effects. Such a choice is however not always possible.

For devices without mechanical shield the height between waveguide and substrate was $\sim$1 µm, which resulted from the HF under-etching of a 1 µm radius disk. This height was sufficient to prevent a waveguide of 10 µm length and 200×320 nm cross section from collapsing to the substrate with normal drying conditions, i.e. evaporating isopropanol with a N_2 blower.

For MS devices, stiction becomes a major problem. The reason is that the coupling waveguide now has a vertical replica located typically 500 nm below. Capillary forces can easily bring the two waveguides in contact, because they are close (500 nm compared to 1 µm in the case of non-MS devices), but also because both waveguides can deform, whereas in the former case the substrate had "infinite" rigidity.

Figure 4.19 shows a SEM micrograph of a finished MS device. It can be seen that many inverted taper tips are stuck together, which prevents efficient coupling of light in the top inverted taper. All inverted tapers are not stuck together, three inverted taper pairs are unstuck on the right side. Although stiction effects are subject to some randomness, stiction events must remain exceptional; the sample showed in figure 4.19 is unusable (the disks are also collapsed but this is because of a too long HF under-etch here). The central part of the waveguide – the one that provides evanescent coupling to the disk – can also collapse, as can be seen on the third structure from the top on figure 4.19. Waveguides that include curved parts have a higher probability of collapsing due to their increased length. It should also be noted that capillary forces are also responsible for collapsing of disks when the pedestal that supports them is too thin. Indeed, we noticed that for small pedestal radii, the disk had a higher chance of not collapsing when using techniques that reduced capillary forces. Techniques such as critical point drying (see §4.3.4.3), which virtually suppresses capillary forces, would therefore allow the fabrication of disks with extremely thin pedestals, yielding high Q_{m}.

4.3.4.3 Solutions to stiction

Different approaches were tried in order to prevent stiction. Some of them worked better than others, and some can be combined in order to increase efficiency.

Surface treatment Surface treatment can lower the Van der Waals binding energy per unit surface and therefore prevent stiction effects, as the restoring force of the deformed pinned waveguide takes over. Surface treatment can also increase the liquid/solid interface surface tension, therefore resulting in a decrease strength of capillary forces. These two effects often go together in solids with small polarizability, such as PTFE. The Al_2O_3 ALD process used in order to decrease surface optical absorption (see §2.1.4) also yielded improvements in terms of stiction (a lower fraction of our waveguides collapsed).

Drying fluid The fluid chosen for the final drying stage also impacts the liquid/solid interface surface tension. Water molecules have a strong dipole force which results in strong surface tension with air (75 mN/m). The liquid we use for drying is isopropanol. It is a standard and safe chemical,

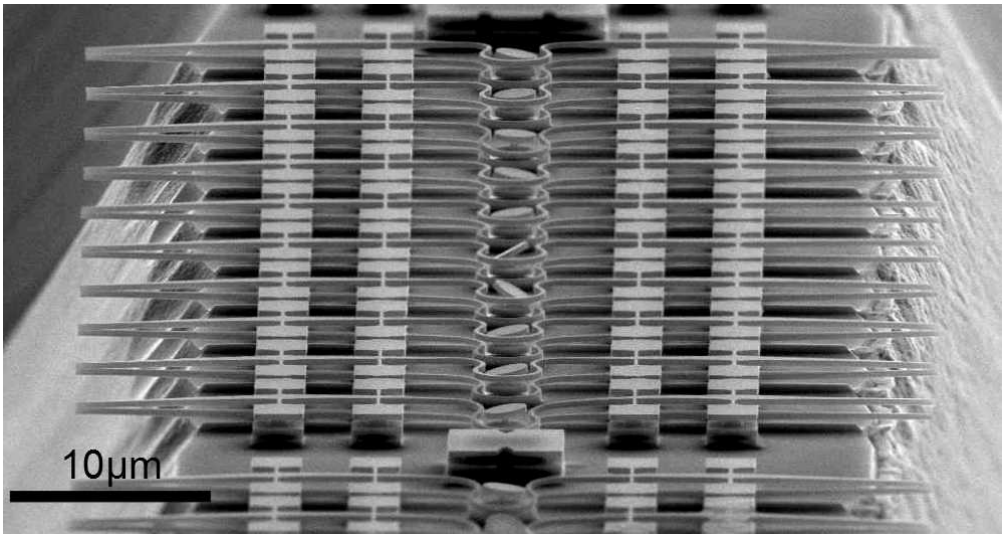

Figure 4.19 – Stiction phenomenon : inverted tapers tips are stuck together.

and its surface tension is quite low (21 mN/m). Some fluorinated liquids have an even lower surface tension but are also more hazardous. They have not been tried yet.

High temperature drying The standard method used to dry isopropanol is to blow N_2 on the sample. This was insufficient to avoid stiction with MS devices. In order to reduce capillary forces, we tried to evaporate isopropanol by heating the sample on a hotplate at 250 °C. This temperature does not harm the GaAs (arsenic desorption happens around 500 °C). The effect of high temperature drying is double: first the surface tension decreases, secondly the liquid may start to boil locally which will further decrease the capillary pressure. In practice this method gave good results, and stiction effect could be avoided on MS structures.

Reinforced anchoring Another way to limit stiction effects is to increase the stiffness of suspended waveguides. This can be achieved by increasing the number of waveguide anchoring rods. The initial FSW structure included two pairs of anchoring points (see figure 3.10), which provided enough stiffness to avoid stiction for non-MS devices. However in some cases two pairs of anchoring rods were insufficient and four pairs gave better results (see figure 4.13). Adding too many anchoring rods will result in optical losses so a compromise must be found.

Lower waveguide etch A very efficient way of avoiding stiction of top and bottom waveguides with each other is to etch away the bottom waveguide. This can "naturally" happen during the mesa etching, without the need to add any additional fabrication step. Figure 4.20 shows the mechanism that allows the bottom waveguide to be etched. The crucial point is that the hetero-structure design must be such that the distance between substrate and bottom waveguide $d_{\text{s-bw}}$ is significantly smaller than the distance between bottom and top waveguide $d_{\text{bw-tw}}$. This will increase the probability that the bottom waveguide sticks to the substrate instead of sticking to the top waveguide. On an hetero-structure that respected the aforementioned condition ($d_{\text{s-bw}} = 300$ nm, $d_{\text{bw-tw}} = 500$ nm), we could obtain clean and reproducible lower waveguide etch. Another advantage of this technique is that only one inverted taper tip exists in the focus plane of the micro-lensed fiber in our experiments, which is the ideal coupling case. Coupling in the top waveguide when two inverted taper tips are tangent to the focus plane is less efficient. Unfortunately, the last generation of MS devices for the 2nd order mechanical RBM did not respect the criterion $d_{\text{s-bw}} < d_{\text{bw-tw}}$, and this technique could not be used.

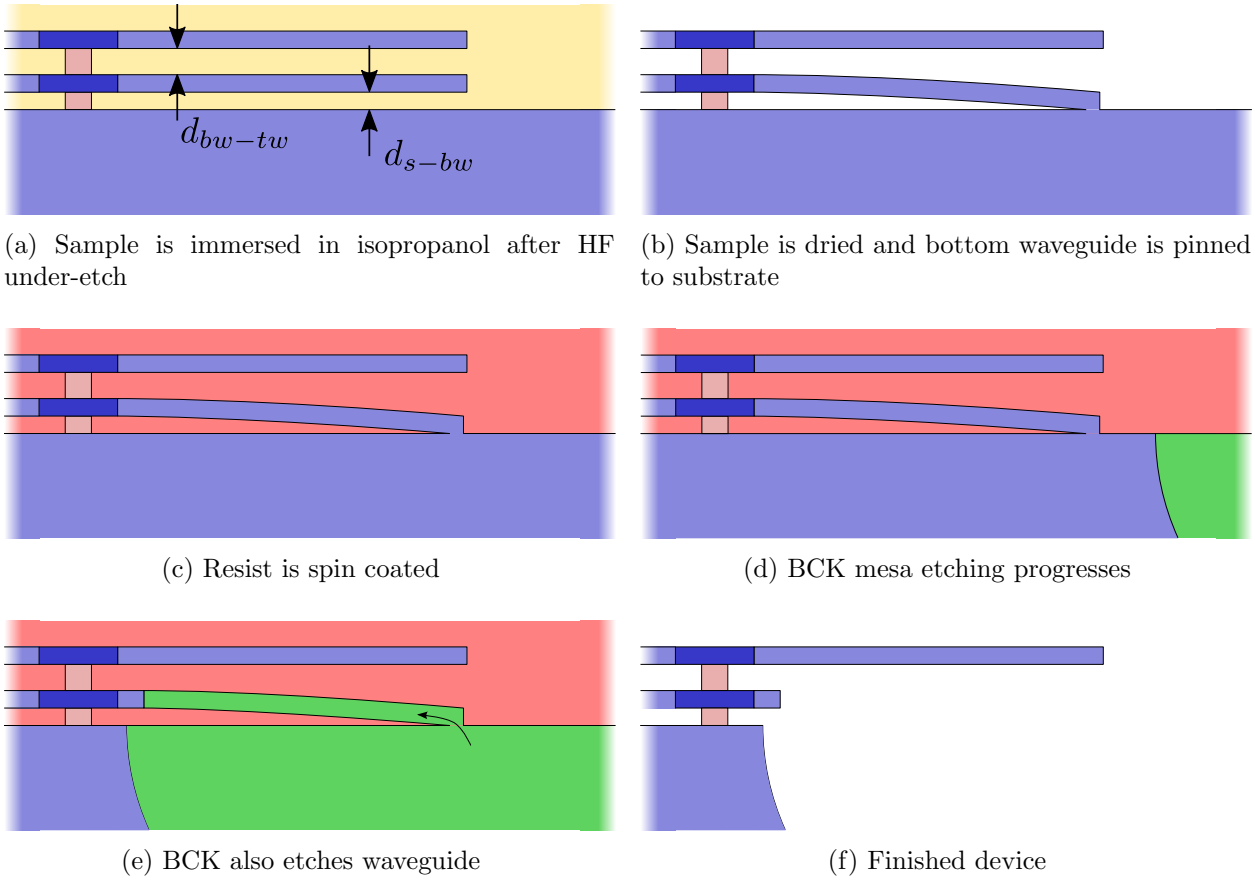

(a) Sample is immersed in isopropanol after HF under-etch

(b) Sample is dried and bottom waveguide is pinned to substrate

(c) Resist is spin coated

(d) BCK mesa etching progresses

(e) BCK also etches waveguide

(f) Finished device

Figure 4.20 – Schematics showing how the lower waveguide can be etched during the mesa etching step depicted on figure 4.8

Critical point drying Stiction happens because of surface tension effects, which are inherent to the interface between the drying liquid and its vapor. Critical point drying avoids the liquid phase during drying by imposing temperature and pressure conditions in order to get around the thermodynamic critical point. The drying procedure is the following :

- The sample to be dried is deposited in the critical point dryer's chamber with an acetone droplet on top of it.
- High pressure carbon dioxide (CO_2) is then injected in the chamber. The CO_2 liquidizes and rinses the acetone away – in practice the chamber is filled with CO_2 then partially flushed several times in order to rinse acetone efficiently.
- Once the chamber is filled with liquid CO_2, the temperature is increased slightly above 31 °C, which allows the CO_2 phase to enter the supercritical state.
- Pressure is then released to atmospheric level. During this pressure release no liquid/gas transition occurs, therefore capillary forces are avoided and stiction does not happen.

Although very efficient, this method is time consuming as a single dry can take several hours, during which the user must stay close to the apparatus to monitor the partial flushes. For this reason we have not used this method extensively.

4.3.5 E-beam resist removal (bis)

ICP etch is known to induce e-beam resist cross linking. The physical processes involved are the mechanical action of ions, which heat the resist, and UV emission by the plasma (Ma-N is actually

designed to be cross linked by deep UV). A consequence of the longer ICP processes used for MS devices is therefore an increased amount of cross linking. This makes the resist harder to remove. The standard technique used is O_2 plasma, but we noticed a drop in Q_{opt} for devices undergoing such a removal step, because of O_2 plasma induced oxidation. Dipping the sample in ammonium hydroxide (NH_4-OH) to remove the O_2 plasma oxide layer allowed to increase Q_{opt} but not to the amount obtained without O_2 plasma. This might be due to additional roughness induced by NH_4-OH, as it is known to slowly etch GaAs.

We tried to use several resist strippers – heated to 60 °C with agitation – but they do not completely remove the resist. We could not come up with a procedure that performs efficient resist stripping without degrading the optical properties. The best Q_{opt} obtained during this PhD thesis work were measured on devices that first underwent a O_2 plasma resist stripping, followed by an Al_2O_3 ALD. Indeed, preliminary steps in the ALD clean the surface thoroughly, and therefore remove the oxidation resulting from O_2 plasma cleaning. These steps might remove the oxide more efficiently than NH_4-OH, or induce less roughness.

This chapter reviewed the tools and techniques used for fabrication of devices aimed at cryogenic optomechanical experiments. The quality of yielded devices is of great importance, as their figures of merit set the limit of what can be achieved in terms of OM cooling. The developments carried during this PhD work allowed to increase the efficiency of coupling to and from the miniature disk resonator (with fully suspended waveguides), as well as the mechanical quality factors (with mechanical shields). The optical quality factors were also enhanced, due to a better control on resist development and ICP etch, and to the works on ALD passivation carried in our team by Biswarup Guha. Once a sample is produced, its properties have to be measured. The description of the experimental setup that allows these measurements, as well as further, mode sophisticated, optomechanical experiments is the object of the next chapter.

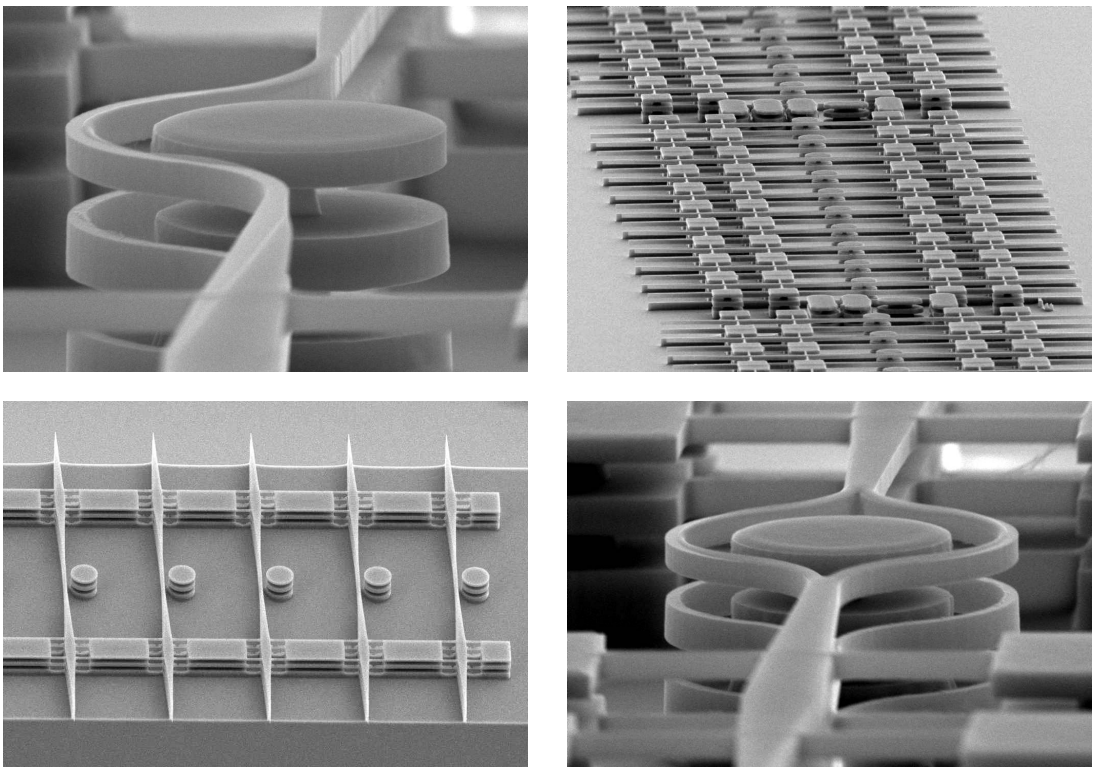

Figure 4.21 – SEM micrograph compilation of fabricated structures.

Chapter 5

Experimental setup

This chapter presents the experimental setup used for device characterization and implementation of optomechanics experiments. The characteristics of apparatus used (lasers, positioning stages, amplifiers, fibers) have a crucial importance and determine, along with the optomechanical device, the efficiency of optomechanical experiments. After presenting the general setup, a description of the various apparatus used will be carried.

5.1 The setup in general

Figure 5.1 is a schematic of the typical setup used in this doctoral work. A continuous wave laser source is used to generate monochromatic light in the telecom band (1.3 μm to 1.6 μm). This light then goes through a fiber polarization controller (FPC), which allows to select between TE and TM WGMs. Light is then brought into a cold environment (cryostat) where the device sits, and is then injected into the device's waveguide, which guides light to the OM resonator. At the device's optical output a 90%/10% fiber beam splitter is used to divide the optical power into two paths. The main path (90%) is the OM readout. The readout principle was explained in section 1.1.2. The optical signal carried by the fiber is first optically amplified, and then directed on a fast (5 GHz) photo-diode. The photo-diode bandwidth must be larger than the mechanical motion frequency. The current at the photo-diode output is then loaded on a spectrum analyzer, and the spectral properties of the OM device's motion can be extracted. The other path (10%) is used to perform DC optical measurements, like for instance broad scans of the laser wavelength in order to find WGM resonances. A standard trans-impedance amplified photodiode with typical 10 kHz bandwidth is enough for these DC measurements. The setup presented is schematic and subject to changes depending on the OM experiment performed. Optomechanically induced transparency (OMIT) experiments, which will be presented in chapter 7, necessitate an electro-optic modulator (EOM) before the device input, which is not shown on figure 5.1.

5.2 Cryostats

Operation at cryogenic temperatures is important for quantum OM experiments. Indeed, even though OM effects generate an optical "cooling power" that extracts some mechanical phonons from the system, it is advantageous to start the cooling in an thermodynamic equilibrium with few phonons in the OM resonator. The two cryostats employed in this PhD can stabilize the sample temperature at a few K, dividing the number of phonons by a factor about 100 compared to room temperature operation (300 K). Another benefit of low temperature is that it can enhance some of the properties of the OM device. In our case the Q_{m} is enhanced by a factor 10 to 100 by operating at a few K instead of 300 K. Another advantageous feature is that the derivative of the refractive index with temperature dn/dT is lowered by a factor 100 when compared to 300 K values. This reduces the impact of thermo-optic instabilities which are of paramount importance in our

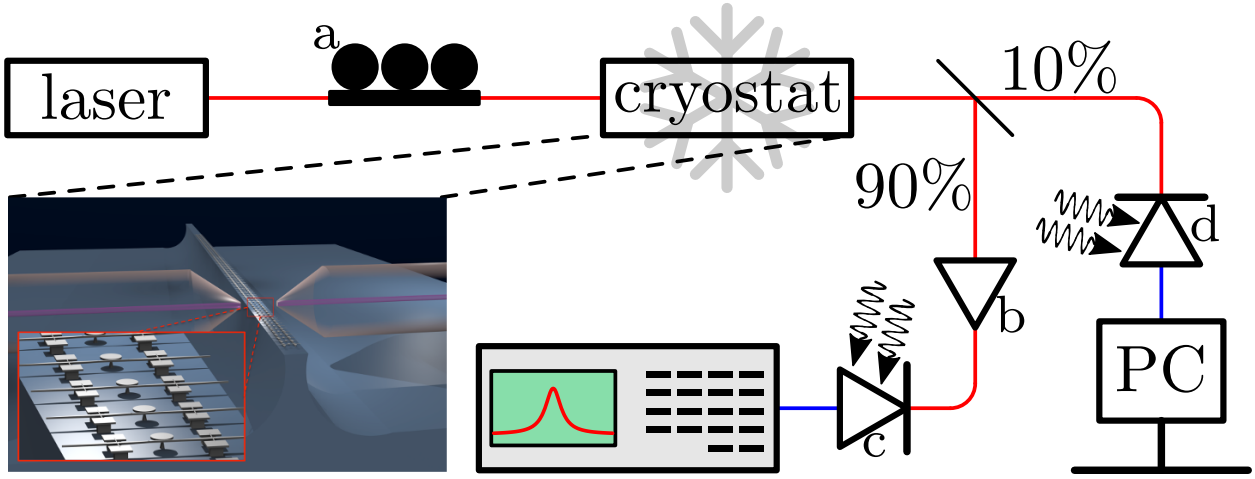

Figure 5.1 – Experimental setup schematic. **a**: FPC. **b**: optical amplifier. **c**: fast-photo-diode. **d**: slow photo-diode. The red lines represent telecom range optical fibers (1300-1600 nm). The blue lines represent electronic co-axial cables.

experiments. Unfortunately no enhancement was observed concerning Q_{opt} at low temperature. In this section the two cryostats used during this doctoral work will be presented. Experiments started with a Janis ST-300, a liquid helium apparatus. This cryostat allowed first cryogenic operations but raised some difficulties, and a closed-cycle, gaseous helium cryostat was then developed in a collaboration with Attocube company and acquired.

5.2.1 Janis ST-300 cryostat

The Janis ST-300 is a standard liquid helium cryostat (see figure 5.2). The liquid helium is brought by a pipe linking the cryostat to a helium tank (not shown on figure). This pipe is inserted in the tube at the top of the cryostat. We customized the cryostat with windows in order to address the OM device optically. A schematic in the insert of figure 5.2 shows the optical coupling configuration. Because the waveguide propagation mode is well confined within the waveguide, the outgoing beam at the cleaved facets has a high NA (typically close to 1). High NA optics must therefore be used in order to collect light efficiently. An additional difficulty comes from the fact that the optics cannot be brought arbitrarily close to the sample because of the cryostat windows. The optics used must therefore have a relatively long working distance. At such high apertures the cryostat windows introduce significant abberations, which hinders perfect mode-matching when injecting and collecting light to and from the sample. A lens with very high NA is used in collection in order to maximize light gathering. The light collected by this lens is then re-focused by a fiber collimator and sent to a telecom fiber for optical amplification. After proper optimization, this collection and re-injection in a telecom fiber reached at best 10% for a single-mode fiber, and 20% for a multimode fiber.

A major inconvenient of this cryostat is that it does not form a single mechanical body with the optical elements that perform light injection and collection. Indeed, these optical elements are mounted on independent micro-positioning platforms. The ensemble is not mechanically steady, and since injection and collection mode matching require a few hundred nanometer precision on the alignment, appreciable variations of the detected signal occur. At room temperature, these transmission variations consist in an oscillation at ∼100 Hz with 30-40% contrast – which correspond to the fundamental vibrating mode of the long (70 cm) copper finger holding the sample – and a slow "irreversible" drift which takes transmission down by 50% in a few minutes. When operating at low temperature the situations complicates. The irregular flow of liquid helium through the cryostat induces temperature gradients that give rise to mechanical displacements within the cryostat via thermal expansion coefficients. "Irreversible" drifts become way stronger, and the coupling of light

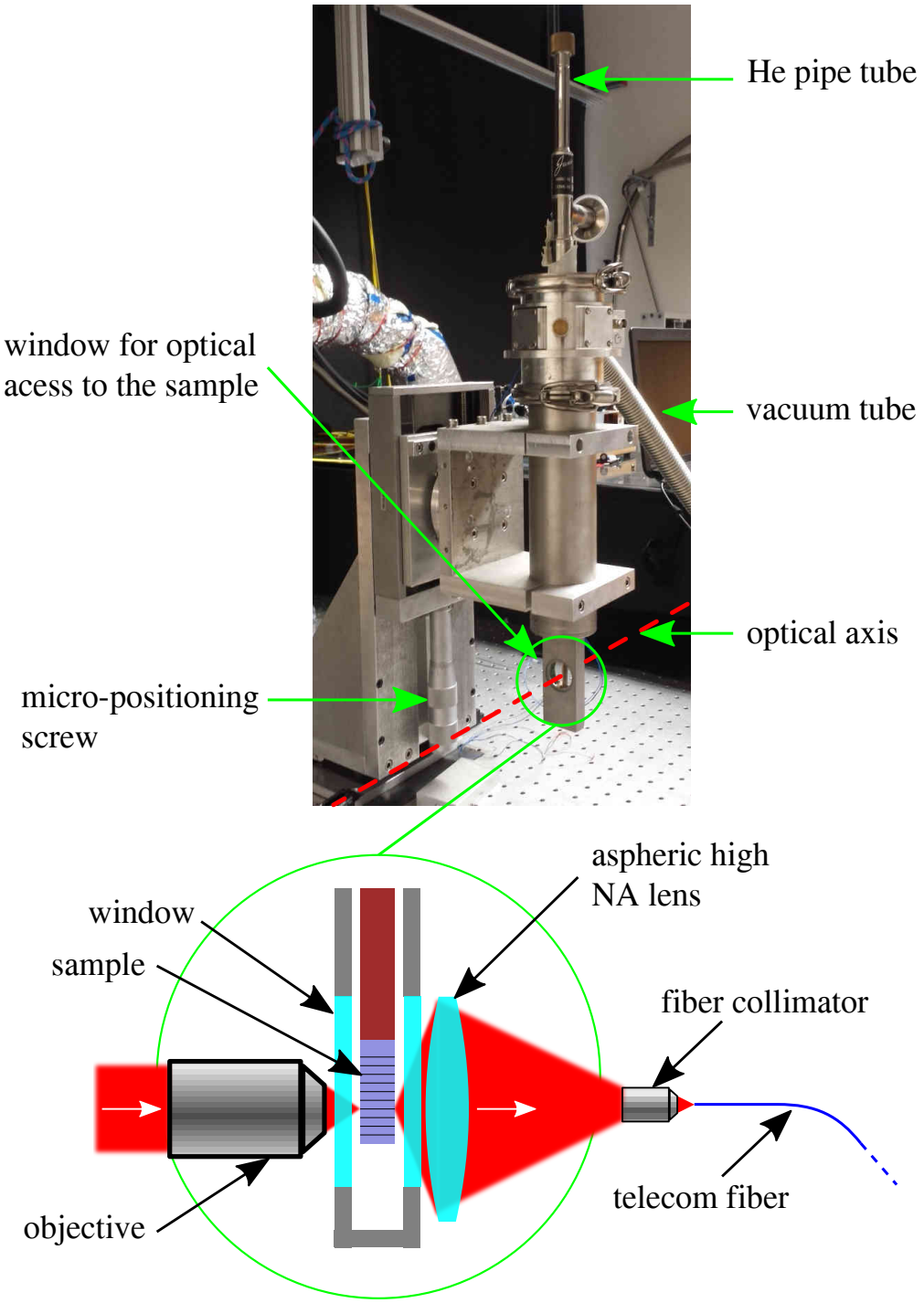

Figure 5.2 – Janis ST-300 cryostat. Optical elements cannot be brought arbitrarily close to the sample because of the cryostat windows, so high working distance elements must be used. The collected light is injected in a telecom fiber for subsequent optical amplification.

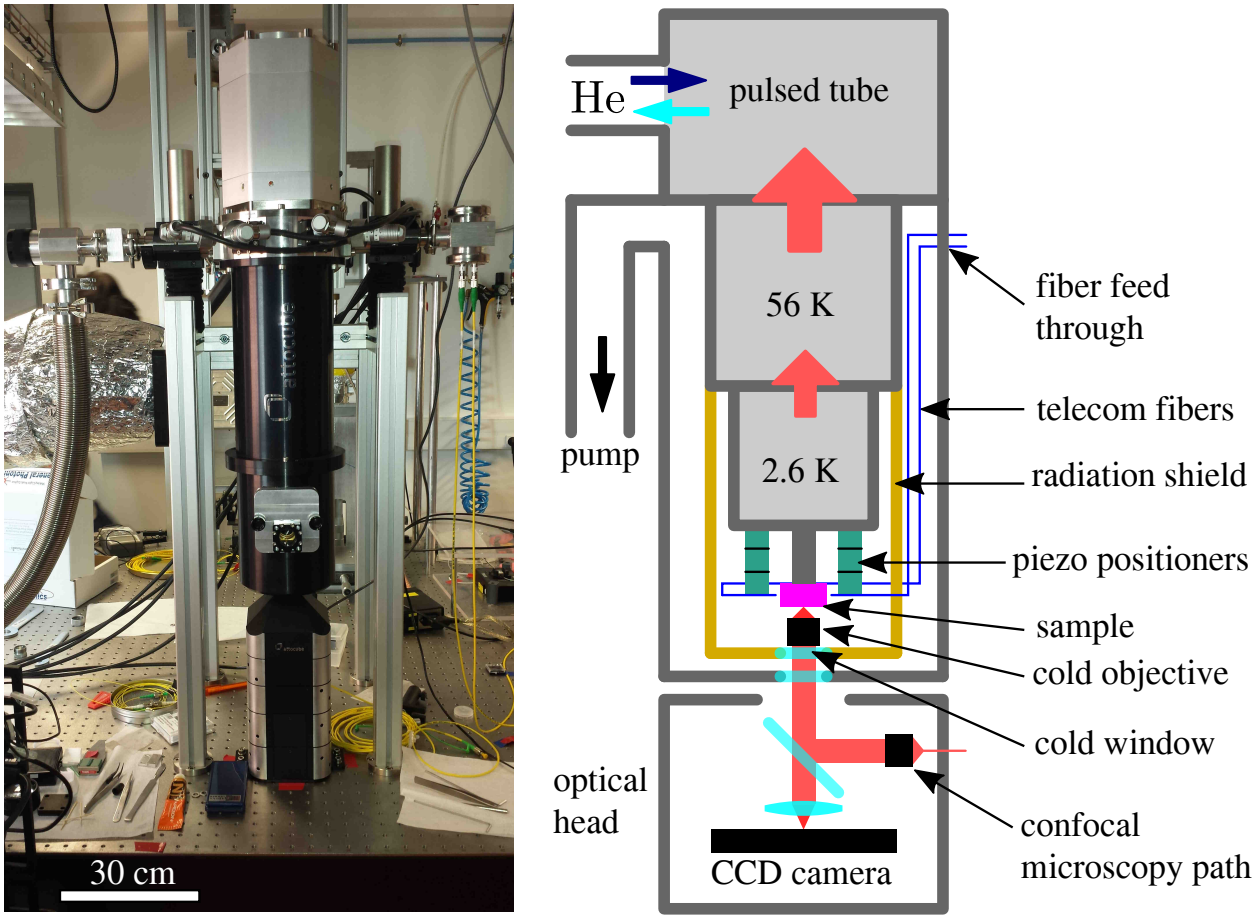

Figure 5.3 – Attocube cryogenic probe station. The pressured helium for the pulsed tube is pumped with a compressor located under the optical tabletop.

in the sample can be lost in a few seconds. In order to stabilize the setup a heating element was wrapped around the cryostat body, and regulated by a proportional integral derivative (PID) controller. This improved the situation but optical coupling stability could not be maintained for more than a few minutes at best, which is incompatible with advanced experiments.

As can be seen on figure 5.2, the sample is held between two large windows and is thus much exposed to external light. This external light, as well as black body radiation from the cryostat's outer walls, heats the sample which cannot thermalize at the liquid helium temperature (4 kelvin). In practice the sample temperature is around 20 kelvin. To overcome this we engineered a radiation shield (not shown on figure 5.2) which protects the sample from light emission, and allowed to reach a sample temperature of 8 K.

5.2.2 Attocube cryostat

Towards the end of the first year of this doctoral work, we started using another cryostat with greatly enhanced mechanical properties. The device is a cryogenic probe station developed by *Attocube systems AG* at our request, and which design was elaborated in collaboration with our research group. The apparatus is now part of the Attocube's catalog under the name "Photonic Probe Station". The cooling power comes from a pulsed-tube refrigerator [63]. This type of refrigerators have two main advantages over liquid helium cooling. They use gaseous helium in close loop so there is no need for expensive liquid helium supplies, and they can achieve temperatures below 4 K [1]. In our case a temperature of 2.6 K can be obtained in the best case.

[1] low pressure helium remains gaseous below 4 K

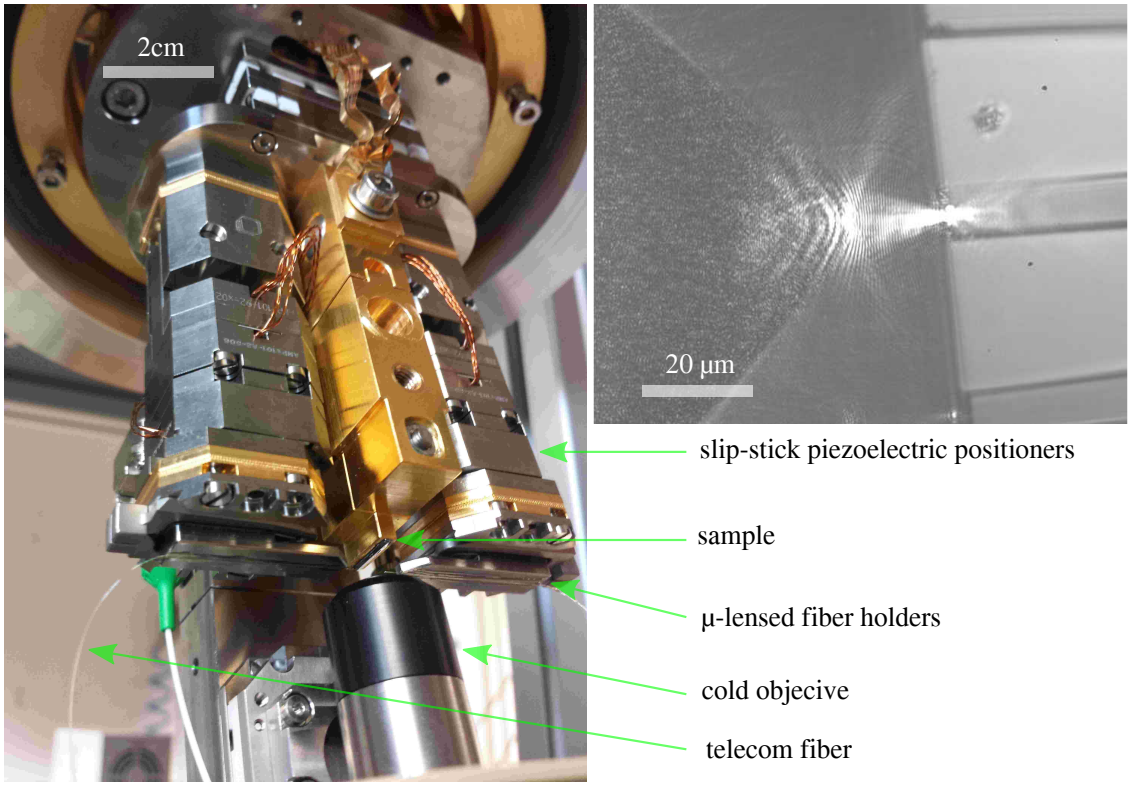

Figure 5.4 – Attocube cryostat 2.6 K stage (left) and image produced by the objective (right). The contour of the micro-lensed fiber, as well as the beam focused on the waveguide facet can be seen.

Figure 5.3 shows the Attocube cryostat used for OMs experiments. High and low pressure gaseous helium flow through the pulsed-tube element which starts to cool down two temperature stages, at 56 K and 2.6 K. The red arrows represent the heat flow. The interior of the cryostat is pumped to $\sim 10^{-3}$ mbar so that heat transfer with the outer walls at 300 K is avoided. Attached to the 2.6 K stage is the sample and two piezo-electric stepper positioners [64] that hold the micro-lensed fibers. These stepper positioners work with the "slip-stick" effect, and they combine a high traveling course (few mm) with nanometer range position resolution. The whole 2.6 K stage is surrounded by a radiation shield at 56 K. An image of the sample is formed by a 100× objective located within the 2.6 K stage. The objective output is then fed to an external module at room temperature and focused on a CCD camera. The beam from the 2.6 K objective is actually split in two, another channel couples the beam to a fiber in order to perform confocal microscopy[2]. One first and central advantage of this design when compared to the Janis ST-300 is its exceptional stability. The fiber positioners are mounted on the same 2.6 K platform as the sample holder. The ensemble is mechanically compact and robust, and the motion of the micro-lensed fibers relative to the sample is very low. Transmission variations at ∼1 Hz due to the pulse tube vibrations are below the percent, and long term drift is so small that it cannot be measured after 24 hours.

Thanks to the high magnification objective located in the 2.6 K chamber, the positioning of fibers in order to couple light in the optomechanical system can be done very quickly and easily. The shift from a given chip waveguide to the next adjacent one only requires a few piezo actuator slip-stick steps. Additionally, the swapping of one chip to another is considerably easier than it was with the Janis cryostat. The sample holder can be removed from the 2.6 K stage, which allows to position the chip on it in optimal conditions.

[2]for instance the 2.6 K objective could be used to focus light from an external source on a disk resonator.

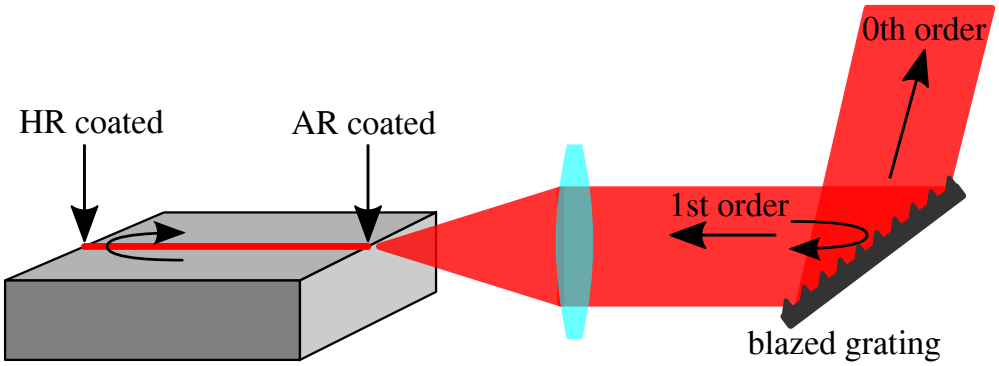

Figure 5.5 – External cavity diode laser in the so-called "Littrow" configuration. The beam at the chip output is collimated and sent on a blazed grating. In such a grating the 1^{st} order reflection is maximized, so that the cavity defined by the High Reflectivity coated end of the chip and the grating has a high finesse. The 0^{th} order of the grating is the diode laser's output. By adjusting the grating's tilt it is possible to tune the lasing wavelength.

5.3 Laser sources

Our OMs experiments require the laser sources used to have low noise (more on this later) and broad tuning capabilities. The gap of GaAs being at 870 nm, wavelengths from this value and above can in principle be used for OMs experiments. Three different laser sources corresponding to three different wavelength ranges were used for this doctoral work :

- $1500 - 1600$ nm, with a Yenista Tunics T100-S
- $1260 - 1370$ nm , with a (different) Yenista Tunics T100-S
- $870 - 1000$ nm, with a M-squared SolsTi:S

The two first ranges are provided by external cavity diode lasers (ECDLs). The last range is provided by a titanium sapphire (Ti:S) laser. This laser can actually be tuned from 690 to 1000 nm. Each wavelength range has its advantages and drawbacks. For a given disk size, the $1500 - 1600$ nm range corresponds to more evanescent fields of WGMs, which causes more bending losses. Operation of small disks ($\varnothing < 2$ µm) in this range is not interesting as bending losses are too high. On the other hand, TPA is reduced in this range and an erbium doped fiber amplifier (EDFA), which is a very low noise optical amplifier, can be used for fine detection. The range $1260 - 1370$ nm is more advantageous in terms of bending losses but amplifiers as efficient as EDFAs do not exist in this wavelength range: we employed a Thorlabs BOA 1132S semiconductor optical amplifier (see §5.4.3). The $870 - 1000$ nm range corresponds to more confined modes in the disks, but its closeness to the GaAs gap makes it more susceptible to residual linear absorption and TPA. One advantage is that photoelastic constants rise quickly near the gap, so that high OM coupling constants can be expected when working in this range. Additionally, high Q_{opt} ($> 10^5$) WGMs can in theory be obtained for disks with a radius as small as 500 nm.

5.3.1 External cavity diode lasers

We start by briefly describing ECDLs. The two diode lasers used during this doctoral work are very similar, the two models used merely correspond to optimizations for different wavelength ranges. Diode lasers are PIN diodes with a central intrinsic (I) region made of direct bandgap semi-conductor. The intrinsic region can include quantum wells in order to choose the wavelength range of emission. The laser cavity is defined by cleaving both ends of the semi-conductor chip, optimizing reflection on one end of the chip, and optimizing transmission with an anti reflection (AR) coating on the other end so that it can be interfaced with an external cavity (see figure 5.5). Such a design has the following advantages:

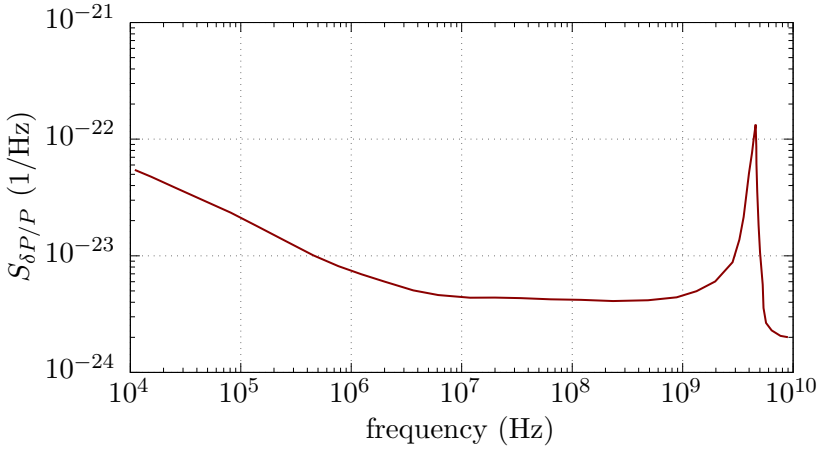

Figure 5.6 – Relative power spectral density of an typical ECDL, reproduced from [67]. The so-called "$1/f$" noise, as well as the relaxation oscillation peak can be observed. For this laser in particular, the relaxation oscillation peak is centered at 4 GHz, close to the mechanical frequency of our OM resonators, hence it may cause perturbations.

- The additional cavity length increases cavity damping time which reduces phase noise [65].
- Wavelength tuning is made possible by the grating element in the cavity.

ECDLs like the Tunics model can be tuned in single mode operation on a range of typically 100 nm[3]. This range can be scanned in a few seconds, which makes these lasers very convenient for long span spectroscopy of our devices. They have a typical linewidth of 400 kHz, which is sufficient to resolve WGMs of typical linewidth $1 - 100$ GHz. One problem is that their phase noise spectral density can be quite high in the GHz range, which typically corresponds to the mechanical oscillation of our devices. This is due to the laser's relaxation oscillations [66] (see figure 5.6). A nice feature of these lasers is the possibility to modulate their output intensity at high frequencies (∼200 MHz). This allows for stabilization schemes (see appendix D) as well as sideband creation. However, the creation of sidebands in the GHz range necessitates the use of an EOM (see §5.5).

5.3.2 Titanium sapphire laser

Ti:S laser sources typically operate in the $700 - 1000$ nm range, thanks to the broad optical gain of the Ti:S crystal. The laser we work with operates in continuous wave. It is the model SolsTi:S–SRX, developed by M-Sqaured. Ti:S lasers can also work in pulsed scheme, where many longitudinal modes of the laser oscillate at the same time, which results in the emission of very intense and very short ($<$ ps) pulses of light when modes are locked in the proper phase relations.

Figure 5.7 is a schematic of the SolsTi:S–SRX. The Ti:S gain medium is pumped by a green (532 nm) diode pumped solid state laser (DPSSL). The cavity path is of the "bow-tie" type, which allows, in conjunction with an optical diode, to have light propagating in one direction only. This avoids the creation of a standing wave which would deplete the Ti:S gain medium at the anti-nodes only. In order to select the longitudinal oscillating mode a bi-refringent filter (BRF) is placed in the optical path. Depending on its orientation, it will induce a wavelength dependent loss in the cavity, selecting one mode for lasing. However this selection is not very narrow, and given the small FSR of the bow-tie cavity (∼1 pm), it is possible that several consecutive modes oscillate at the same time. To avoid this problem an etalon is inserted in the cavity. The etalon is a Fabry Pérot resonator with a short distance between the two mirrors (∼1 mm). This results in a FSR of ∼0.5 nm, 500 times lager than the main cavity's FSR. If the etalon has a sufficient finesse, it prevents two consecutive longitudinal modes from lasing together, and therefore enhances stability. Actually, although this

[3]such a broad tuning range is actually quite remarkable, and is the result proprietary, patented techniques.

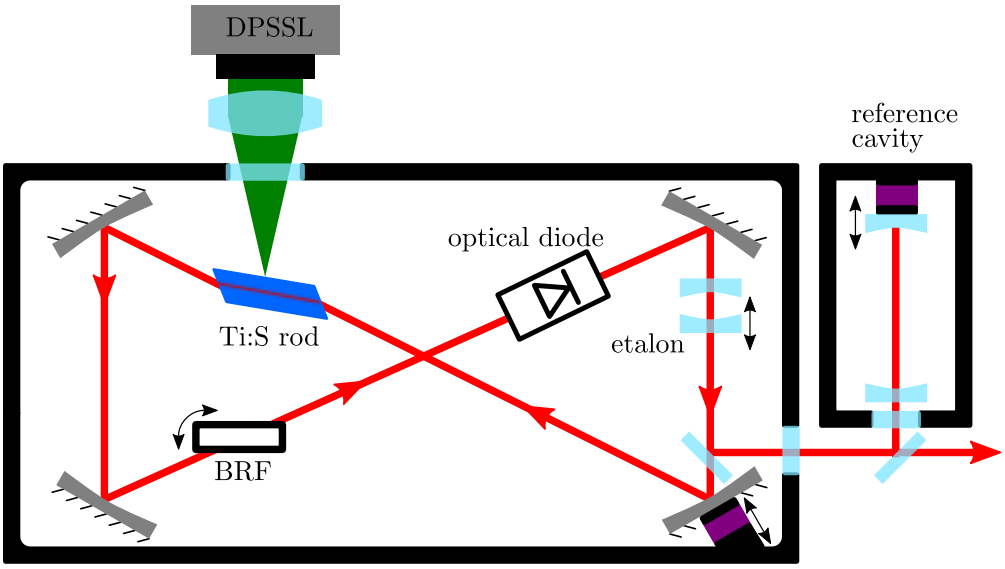

Figure 5.7 – M-squared SolsTi:S laser system schematic. The gain medium is the titanium-sapphire rod. Several optical elements are inserted in the bow-tie cavity path to guarantee single mode operation and wavelength control. Some mirrors are mounted on piezo-electric actuators (purple).

is in general sufficient to guarantee single mode operation, mechanical vibrations and temperature changes can lead to oscillations on more than one frequency, and an active locking of the etalon is necessary to guarantee single mode operation.

Although quite good already, the spectral stability of the SolsTi:S laser can be enhanced further by the use of an active Pond-Drever-Hall stabilization technique [68]. The idea is that the laser's phase variations are detected by a high finesse, temperature stabilized reference Fabry-Pérot cavity. An error signal is generated, which is then applied on one of the laser cavity's mirrors[4]. With such stabilization active, linewidths as small as 25 kHz are achieved. An external wave-meter is also used (not shown on figure). This device uses a Fizeau interferometer that measures optical wavelengths with an absolute precision better than 2 MHz (16 fm @ 1550 nm). It is possible to lock the laser on this wave-meter. The lasing wavelength can therefore be chosen with an excellent absolute precision, and undergoes virtually no drift.

Solsti:S Scanning modes

When the BRF is rotated, the laser's output is tuned in steps (mode hops) equal to the etalon's FSR (0.5 nm). This resolution is insufficient as the spectral linewidths of the optical modes we wish to find is typically 1 to 100 pm. A *stitching* scheme is implemented in the system to perform more continuous scans (see figure 5.8a). In such a scheme the wavelength is *continuously* scanned by changing the spacing of the etalon. At some point the lasing mode hops: the etalon is set back to its original position, and the BRF is moved to retrieve the wavelength just before the mode hop. The etalon is set in motion again, etc. This technique allows to perform large (> 100 nm) continuous scans although the wavelength range accessible by a single etalon sweep is (~ 1 nm). Two options are actually possible for the continuous scan parts. One is to change the etalon spacing, the other one is to move one of the bow-tie cavity's mirrors. The advantage of the second option is that while the cavity's mirror is moved, the etalon can be locked on the longitudinal mode that is being tuned, thus guaranteeing single mode operation during the scan.

One inconvenient of the stitching mode is that it is slow. Each stitching procedure takes at least 10 s, which results in a 100 nm wavelength scan taking 1 hour at least, to be compared with the 3

[4]One of the bow-tie cavity's mirrors is actually mounted on a stack composed of a long range slow piezo-electric element for wavelength tuning, and a fast, short range one for the phase stabilization technique.

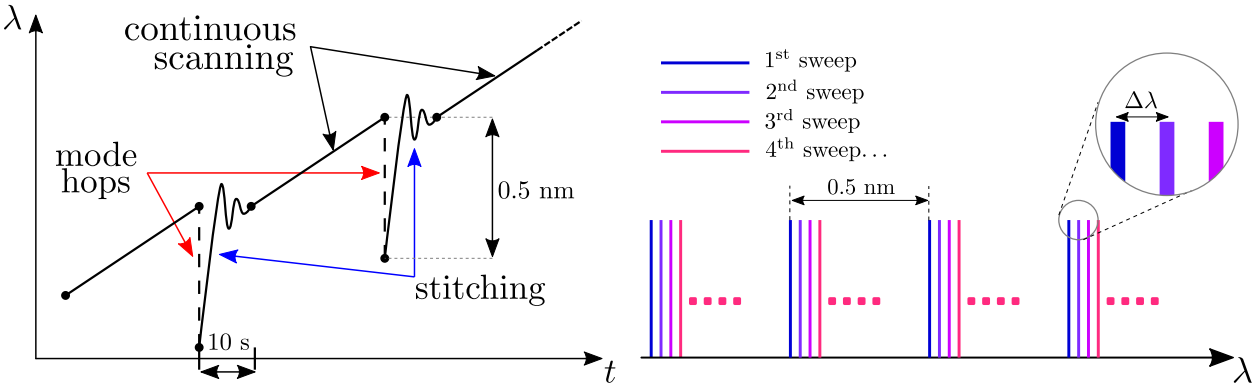

(a) Scanning in *stitch* mode

(b) Scanning in *BRF sweeps* mode.

Figure 5.8 – Different scanning modes for the SolsTi:S laser. Increased scanning speed could be achieved with the *BRF sweeps* mode, but at the cost of a reduced stability.

seconds taken by our ECDL. We tried to increase the scanning speed with a technique consisting of several BRF sweeps, each of them shifted by a small wavelength amount by the means of the etalon spacing (see figure 5.8b). The resulting wavelength sampling consists in a series of combs of spacing 0.5 nm, shifted from one another by an amount $\Delta\lambda \ll 0.5$ nm chosen by the user. This amount $\Delta\lambda$ is also the resolution of the scan. This technique is faster than the *stitching* one. For instance a 10 pm resolution requires the launch of 50 BRF sweeps. Each sweep takes 5 s, so that the full scan can be accomplished in 4 min. Unfortunately, the lasing stability is not very good when operating in this mode, so that the scans quality is barely sufficient for us. An additional problem is that because the scan is not continuous, triangular thermo-optic resonances are not detectable (see §2.1.5 for thermo-optic resonances).

The best compromise between scan quality and speed was found by modifying slightly the *stitch* scan mode. The stitching step induces some redundancy in the wavelengths acquired, which is by default filtered out in real time during the scan. This requires the laser and the scanning program to communicate constantly, which slows down the scan. Breaking this communication link and taking care of the redundancy in post treatment allowed to enhance the scanning speed by a factor 4.

5.3.3 Laser noise

Aside from tuning capabilities, an important parameter of laser sources is their noise. There is actually two types of noise: intensity noise and phase noise. The most fundamental limit to laser intensity noise is the shot noise. It is due to the random nature of photon emission and absorption events in the laser cavity. Photon emission follows a Poisson law of mean N, meaning that if N photons are in average emitted per unit time, then the RMS of the number of photons emitted in this time interval is $\sqrt{N}$. The signal to noise ratio of the optical intensity emitted by the laser therefore goes like $\sqrt{N}$. The single sided power spectral density of the optical intensity I emitted by a shot noise limited laser is:

$$S_{II}(\omega) = 2\hbar\omega_{\mathrm{L}}\bar{I} \tag{5.1}$$

with ω_{L} the pulsation of the emitted photons.

In terms of phase noise, a spontaneous emission event will add a small phase $\Delta\phi$ to the coherent cavity oscillating wave's phase ϕ. The evolution of the laser signal's phase is therefore that of a random walk with step $\Delta\phi$. The study of this random walk allowed Schawlow and Townes [65] to derive a formula for the fundamental limit of attainable laser linewidth :

$$\Delta\nu = \frac{\pi h\nu(\Delta\nu_{\mathrm{c}})^2}{P_{out}} \tag{5.2}$$

with ν the laser frequency, and $\Delta\nu_c$ the **passive** cavity's linewidth, which in the case of a standard solid state laser can be derived from gain medium absorption and cavity losses. This fundamental limit is usually very low, in the case of our Ti:S laser it amounts to no more than a few mHz! The main contribution in the linewidth is due to technical limitations, like mechanical instabilities, power to phase coupling in diode lasers, etc. Linewidth is typically 25 kHz for the SolsTi:S laser and 400 kHz for the diode lasers. Characterizing phase noise by a single real number is sometimes insufficient, and the complete power spectral density of the phase noise $S_{\phi\phi}(\omega)$ would be preferable.

There are two reasons for which the spectral linewidth of the laser should be kept small. The first reason is that a laser linewidth smaller that our OM devices optical linewidth is necessary to realize their spectroscopy. The best OM systems we work with have a κ of 1 GHz. Both Ti:S and diode laser have a $\Delta\nu$ below 1 MHz, and the condition is therefore respected. The second reason is that laser phase noise can perturb OM cooling and noise spectral density readout. Reference [69] shows that the minimal attainable number of photons $\bar{n}_\phi$ in presence of phase noise is given by:

$$\bar{n}_{\min} = \sqrt{\frac{\bar{n}_{\mathrm{th}}\Gamma_{\mathrm{m}}}{g_0^2}\Omega_{\mathrm{m}}^2 S_{\phi\phi}(\Omega_{\mathrm{m}})} \tag{5.3}$$

where n_{th} is the number of thermal phonons, and Γ_{m} is the intrinsic mechanical dissipation. Laser phase noise is hence potentially deleterious for optomechanical cooling, especially if the peak frequency of relaxation oscillations coincides with the optomechanical system's mechanical frequency. Careful measurements have however shown that phase noise did not necessarily prevent ground state cooling with ECDLs, even when the relaxation oscillation peak is close to the mechanical frequency [70]. Phase noise can also be responsible for noise squashing. This effect arises from the interference of:

- the laser light that does not interact with the OM system, but carries a given phase noise
- the laser light that has interacted with the OM system. Phase fluctuations are transduced to intensity fluctuations within the cavity via the cavity's optical response. This intensity fluctuations are equivalent to a force fluctuation, which excite the OM system. The excited OM system then modulates back the light phase at its output.

These two signals, that are obviously correlated, interfere constructively (or destructively) and provoke an increase (or decrease) of the local noise floor near the mechanical frequency. This noise is subtracted (or added) to the mechanical power spectral density and can cause phonon estimation errors. However it was also shown in [70] that for diode lasers this effect, if carefully considered, can be corrected.

5.4 Amplification and detection

The mechanical motion of the OM system is transduced to optical fluctuations via the OM coupling. These optical fluctuations must then be detected as efficiently as possible. Indeed, when performing OM cooling the mechanical motion is artificially damped, so that the signal to detect is weak. This section will cover the standard detection scheme used in our setup, as well as a few variants.

5.4.1 Transduced signal and fluctuation-dissipation theorem

We derive the general expression for the OM system transmission. We start from the coupled dynamical equations model (§1.1.4). In equation 1.16, we suppose an harmonic motion for $x(t)$: $x_0\cos(\Omega_{\mathrm{m}}t)$. We re-write the equation for the reader's convenience:

$$\dot{a}(t) = [i(\Delta + g_{\mathrm{om}}x_0\cos(\Omega_{\mathrm{m}}t)) - \kappa/2]a(t) - \sqrt{\kappa_{\mathrm{ext}}}s \tag{5.4}$$

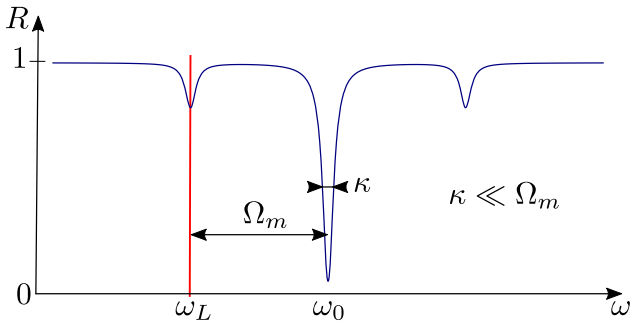

Figure 5.9 – Reflection spectrum of an OM system in the good cavity limit ($\Omega_{\rm m} \gg \kappa$).

The mechanical motion is therefore imposed, and we wish to find a general expression for $a(t)$. To do so we expand the "slowly" varying part of $a(t)$ in Fourier series :

$$a(t) = e^{-i\omega t} \underbrace{\sum_{p\in\mathbb{Z}} a_p e^{-ip\Omega_{\rm m} t}}_{\text{slowly varying part}} \tag{5.5}$$

Now this ansatz for $a(t)$ is re-injected in equation 5.4, which yields a system of equations for the $\{a_p\}$. For the purpose of OM cooling and detection, only the first order sidebands ($p = \pm 1$) are significant. One finds :

$$a_0 = \frac{-s\sqrt{\kappa_{\rm ext}/2}}{i\Delta + \kappa/2} \quad , \quad a_{\pm 1} = \frac{-ig_{\rm om}x_0 a_0}{i(\Delta \mp \Omega_{\rm m}) + \kappa/2} \tag{5.6}$$

Notice that the sideband amplitudes depend on the mechanical motion amplitude x_0, as well as the OM coupling constant $g_{\rm om}$. Figure 5.9 represents the reflection spectrum of the OM system with first order sidebands included. Because of the OM coupling, laser light tuned at $\omega_0 - \Omega_{\rm m}$ can be absorbed significantly.

Now that we have the amplitudes for a_0 (at frequency ω) and $a_{\pm 1}$ (at frequency $\omega \mp \Omega_{\rm m}$) we can calculate the beating between these components, which is responsible for intensity modulation measured by the photodetector. We obtain the optical single sided power spectral density carried by a beam at detuning Δ as a function of Ω [7]:

$$S_{PP}(\Delta,\Omega) = \hbar^2\omega_0^2 \frac{g_{\rm om}^2\kappa_{\rm ext}^2 s^4}{[\Delta^2 + (\kappa/2)^2][(\Delta - \Omega_{\rm m})^2 + (\kappa/2)^2]} x_0^2 \delta(\Omega - \Omega_{\rm m}) \tag{5.7}$$

with $\Delta = \omega_{\rm L} - \omega_0$. The term $\delta(\Omega - \Omega_{\rm m})$ comes from the purely sinusoidal mechanical motion that was assumed in equation 5.4. In practice the mechanical motion is Brownian and the Dirac distribution must be replaced by a Lorentzian function.

Fluctuation-dissipation and spectral density of motion

Given an harmonic mechanical system with trajectory $x(t)$, – the whole system's motion $\mathbf{U}(\mathbf{r},\ t)$ can be written as $\mathbf{U}(\mathbf{r},\ t) = \mathbf{u}(\mathbf{r}).x(t)$ – we define the gated Fourier transform on a finite time interval τ as:

$$\tilde{x}(\Omega) = \frac{1}{\sqrt{\tau}} \int_0^\tau x(t) e^{-i\Omega t} dt \tag{5.8}$$

Averaging over several experimental runs (several realizations of $x(t)$) in the limit $\tau \to \infty$), one gets the spectral density of the random process $x(t)$, which we write $\langle|\tilde{x}(\Omega)|^2\rangle$. The Wiener-Khinchin theorem states that $\langle|\tilde{x}(\Omega)|^2\rangle = S_{xx}(\Omega)$, with $S_{xx}(\Omega)$ defined as:

$$S_{xx}(\Omega) \equiv \int_{-\infty}^{+\infty} \langle x(0)x(t)\rangle e^{-i\Omega t} dt \tag{5.9}$$

Now let's consider a mechanical system with susceptibility $\chi_{xx}(\Omega)$, which means that its frequency response $\tilde{x}(\Omega)$ to a force $\tilde{F}(\Omega)$ is $\tilde{x}(\Omega) = \chi_{xx}(\Omega)\tilde{F}(\Omega)$. The fluctuation-dissipation theorem states that the single sided displacement spectral density at thermal equilibrium is:

$$S_{xx}(\Omega) = 2\frac{k_B T}{\Omega}\mathrm{Im}[\chi_{xx}(\Omega)] \tag{5.10}$$

A typical harmonic damped oscillator has a mechanical susceptibility of the form:

$$\chi_{xx}(\Omega) = \frac{1}{m_{\mathrm{eff}}[(\Omega_{\mathrm{m}}^2 - \Omega^2) - i\Gamma_{\mathrm{m}}\Omega]} \tag{5.11}$$

If the oscillator's mechanical quality factor is high (i.e. $\Omega_{\mathrm{m}} \gg \Gamma_{\mathrm{m}}$) then it ca be shown that $S_{xx}(\Omega)$ is a Lorentzian function of FWHM Γ_{m} and area $\langle x^2 \rangle = k_B T/m_{\mathrm{eff}}\Omega_{\mathrm{m}}^2$. In equation 5.7, the Dirac distribution $x_0^2\delta(\Omega - \Omega_{\mathrm{m}})$ must be replaced by $S_{xx}(\Omega)$ in order to get the real power spectral density carried by the optical signal.

5.4.2 Electronic spectrum analyzer

The device we use to perform the signal analysis is a swept-tuned electronic spectrum analyzer. We describe this apparatus before the photo-diode and amplification devices because it is the spectrum analyzer's performance that determine the choice of the other detection components, as we will see later. The spectrum analyzer performs a real time power spectral density measurement of the electric signal generated by the photo-diode. The essential idea underlying the spectrum analyzer's operation is that the multiplication of a signal $x(t)$ by a sinusoidal signal at frequency ω_{ref} shifts the Fourier transform of $x(t)$ by $\pm\omega_{\mathrm{ref}}$: $\tilde{x}(\omega) \xrightarrow{\times\cos(\omega_{\mathrm{ref}}t)} \tilde{x}(\omega + \omega_{\mathrm{ref}})/2 + \tilde{x}(\omega - \omega_{\mathrm{ref}})/2$. By using a tunable reference oscillator by which the signal is multiplied (in time domain), it is therefore possible to shift the signal's spectrum by the desired amount. This shifting allows to place a given portion of the signal within the bandwidth of an electronic filter. The filter's center frequency does not need to be changed, only its bandwidth needs to be adjusted to choose the spectral analysis resolution. The higher the desired resolution, the longer the scan will be.

The advantage of swept-tuned analyzers is that they do not need high speed analogic to numeric conversion, which is a process that can generate important noise. The mixing and filtering are performed on the input analogic signal, and the power-meter output is then digitalized, but the required speed is merely fixed by the time spent on each frequency step of the scan. This allows these devices to combine high frequency operation with low added noise. The apparatus used in our team is a Rhode & Schwartz FSP 3. It can measure spectral densities from 9 kHz to 3 GHz, with a noise floor (or entrance noise) of -150 dBm/Hz. This value is to be compared with the noise power of -168 dBm/Hz resulting from Johnson noise in a electronic resistor. We thus see that the performance of the FSP 3 is not far from this fundamental limit. To be detected, the electronic signal being input in the spectrum analyzer must be above this limit of -150 dBm/Hz. It is for this purpose of raising the signal spectral density above the noise floor of the FSP that we use amplifiers.

5.4.3 Amplifiers

We use two types of amplifiers: electronic and optical ones. An optical amplifier will be inserted between the OM system's optical output and the photo-diode, whereas an electronic amplifier will be inserted between the photo-diode and the electronic spectrum analyzer. An amplifier is essentially described by its gain, bandwidth, noise equivalent power (NEP), and noise figure.

- The NEP is defined, for a given bandwidth, as the amplifier's output noise power divided by the gain, when the input is not excited. Therefore an input signal with power smaller than the NEP will correspond to an output SNR below 1 (the signal will be "drowned" in the noise).

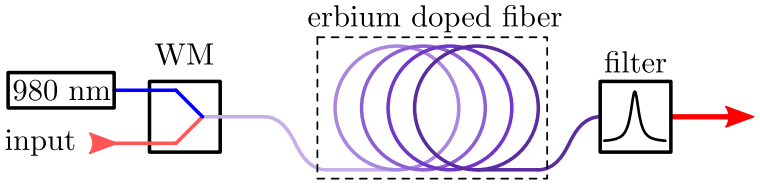

Figure 5.10 – Working principle of an EDFA amplifier. A 980 nm pump is mixed with the signal at ∼1550 nm by a wavelength multiplexer (WM) and then injected in an erbium ion doped optical fiber. The signal is amplified by stimulated emission and the 980 nm is filtered out at the end of the doped fiber.

- The noise figure (NF) is the noise added by the amplification stage itself. Electronic amplifiers have a finite entrance equivalent resistance that is subject to Johnson noise. This noise is fed at the amplifier's input. If the amplification was perfect, the noise level at the output would be the Johnson noise multiplied by the gain. Because it is not perfect, the output noise level is higher, and the noise figure is defined as : $output\ noise/(gain \times Johnson\ noise)$. It is usually expressed in decibels. This definition can also be applied to optical amplifiers, but this time with a reference noise source (shot noise if possible) used at the input.

Optical amplifiers

Optical amplifiers generally show better performance than electronic amplifiers. This is, among other reasons, due to the absence of Johnson noise. An optical amplifier of interest to us is the EDFA. This amplifier has very low NEP and noise figure, and works in the band $1520 - 1570$ nm. The input signal is injected in an erbium doped fiber along with a pump beam at 980 nm. The pump excites the erbium ions within the fiber, which can then amplify the signal at 1550 nm by stimulated emission (see figure 5.10). The main source of noise in EDFAs is amplified spontaneous emission (ASE), which has the same spectrum as the gain medium.

Another amplifier that we use to amplify light at 1.3 µm is a so-called "optical booster". The model used is a BOA 1132S from Thorlabs. The general principle of operation is the same as for the EDFA, except that the population inversion is created by electrical instead of optical pumping. The active medium is an InP/InGaAsP quantum well layer structure. These devices exhibit higher noise than EDFAs.

Electronic amplifiers

EDFA's outstanding performance is only available in the $1520 - 1570$ nm range. When working at other wavelengths (980 nm for instance), substitute amplification schemes must be used. Electronic amplifiers are convenient because they obviously do not show any optical bandwidth. They are placed after the photo-diode, so only the latter must be compliant with the optical wavelength used in experiments. Electronic amplifiers must however have a bandwidth comprising the mechanical frequency. Amplifiers that exhibit low noise and GHz bandwidth are readily available at a reasonable price (few thousand dollars). One additional advantage of electronic amplifiers is that, because they perform amplification after the photo-diode, the optical intensity impinging on the photo-diode is usually very low, so that the photo-diode is not saturated and works in its linear regime. When using an optical amplifier the optical signal is amplified before the photo-diode so that the intensity falling on it can be quite high and saturate it.

Gain requirements

The purpose of the amplifier (electrical or optical) is tho amplify the light imprinted with the mechanical frequency to a level above the input noise of the spectrum analyzer. If the amplifier was perfect (zero input noise and zero noise figure) increasing the gain would increase the SNR between the signal and the spectrum analyzer's input noise, so a gain value as high as possible

would be desirable. However, the amplifier also has its own entrance noise. This noise will be amplified too so that for a fixed signal level, the SNR exiting the amplifier will be independent of the gain. The amplifier's gain is therefore sufficient when the spectrum analyzer's input noise contribution to the SNR is negligible. The gain of the EDFA can be adjusted by varying the 980 nm pump power, but many electronic amplifiers are packaged with a fixed gain that must therefore be chosen wisely.

	EDFA	Optical booster	Electrnonic amp
Optical bandwidth	1530–1560 nm	1280-1330 nm	900-1600 nm*
Mechanical bandwidth	0-10 GHz	0-10 GHz	1.2-1.4 GHz
Gain	40 dB	30 dB	40 dB
NEP	-	-	Johnson noise
NF	3.5 dB	7 dB	0.5 dB**

Table 5.1 – Parameters of different amplifiers. Precise values for the NEPs of optical amplifiers cuold not be obtained. They should anyways be lower that the Johnson Noise, especially in the case of the EDFA.
(*) with an electrical amplifier the full bandwidth of the InGaAs photodetector can be used.
(**) the noise figure for electronic amplifiers is defined relative to the Johnson noise of an electrical resistor, whereas it is defined relatively to the photon shot noise for optical amplifiers. This latter source of noise is usually way smaller, hence smaller values for electrical amplifiers do not mean higher overall performance.

5.5 Electro-optic modulators

As will be seen in §7.5, some OM experiments require to modulate the light intensity (or phase) at the mechanical frequency. Our diode lasers are equipped with an input for fast current modulation, but the bandwidth is limited to 200 MHz, an order of magnitude below the mechanical frequency of our systems (GHz typically). Electro-optic modulators (EOMs) allow to modulate the intensity (or phase) of the laser light at very high speed. They generally rely on the Pockels effect in lithium niobate ($LiNbO_3$): an electric field applied on the crystal changes its refractive index, therefore the output light has a shifted phase. Intensity modulators can be achieved by the use of a Mach-Zehnder configuration (see figure 5.11). In this configuration the output intensity is a function of the phase delay $\Delta\phi$ introduced in one of the arms : $I_{out} = I_0 \cos^2(\Delta\phi/2)$. The phase delay $\Delta\phi$ is a linear function of the applied voltage on the parallel plates.

If one wants to obtain a sinusoidal modulation of the intensity with a sinusoidal voltage, the response $I_{out}(V)$ must be linear. This is only the case for small voltage variations around one of the inflexion points of $I_{out}(V)$. To achieve modulation the voltage applied on the EOM must therefore be the sum of a constant voltage V_{avg} plus an oscillating voltage. The Mach-Zehnder is quite sensitive to temperature variations, so a feedback loop on V_{avg} is used in this work in order to keep the EOM operation on its inflexion point.

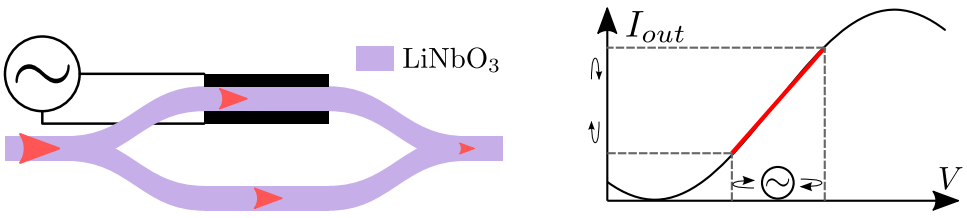

(a) Schematic. (b) Operation point

Figure 5.11 – Electro-optic intensity modulator used in our experiments. The refractive index of one of the arms is changed by applying a voltage by the means of parallel plates around the waveguide, inducing a phase delay. The intensity of the recombined light depends on the delay, and is therefore modulated via the applied voltage.

Chapter 6

Mechanically shielded disk resonators

This chapter exposes the efforts developed during this doctoral work to increase the Q_{clamp} of our devices. Indeed, in vacuum environment and at a few K, clamping losses are a central dissipation channel. The concept presented in this chapter is that of a mechanical shield (MS) that is situated just under the disk, and whose motion interferes destructively with the disk so that the anchoring point to the substrate remains still. In consequence, the amount of mechanical energy radiated into the substrate is diminished and Q_{clamp} increases. The fabrication problems arising in MS devices are exposed in chapter 4. In this chapter we will deal with the design, optimization, and characterization of MS structures.

6.1 Clamping losses of disk resonators

6.1.1 Analytic formula

The first generation of OM structures fabricated in our team consisted in single disks supported by an AlGaAs pedestal (see figure 4.6 & 2.1). The mechanism that leads to clamping losses of RBM modes was introduced in chapter 2.2.3.3. The main idea is that the disk oscillates in its thickness during its radial mechanical motion because of the Poisson ratio. This oscillation leads to the emission of compression waves through the pedestal, which are then scattered in the substrate. Reference [44] derives an analytic formula for the Q_{clamp} of the RBM of a disk resonator supported by a pedestal. The idea of the derivation in the following :

- Following Love's theory of circular plates [37], the displacement of the disk is calculated. The movement is assumed to follow the 2D plane approximation (see §2.2.2), and the mechanical link to the pedestal is ignored.
- The pedestal's displacement is then derived analytically. It is modeled as a cylinder with boundary conditions set by the disk's displacement on the top surface and the semi infinite substrate on the bottom.
- Q_{clamp} is then calculated as the total elastic energy W stored in the RBM divided by the integral over a mechanical period of the $stress \times strain$ at the surface S_{int} interfacing the pedestal and the substrate :

$$Q_{\text{clamp}} = 2\pi \frac{W}{\iint_{S_{int}} S_{ij}\sigma_{ij} dA} \tag{6.1}$$

The complete analytic formula obtained in [44] is cumbersome, so we give it in a simplified version :

$$Q_{\text{clamp}} = A \left(\frac{R_{\text{disk}}}{R_{\text{ped}}}\right)^4 \frac{R_{\text{disk}}}{T_{\text{disk}}} \sin\left(\frac{2\pi T_{\text{ped}}}{\lambda_s}\right)^2 \tag{6.2}$$

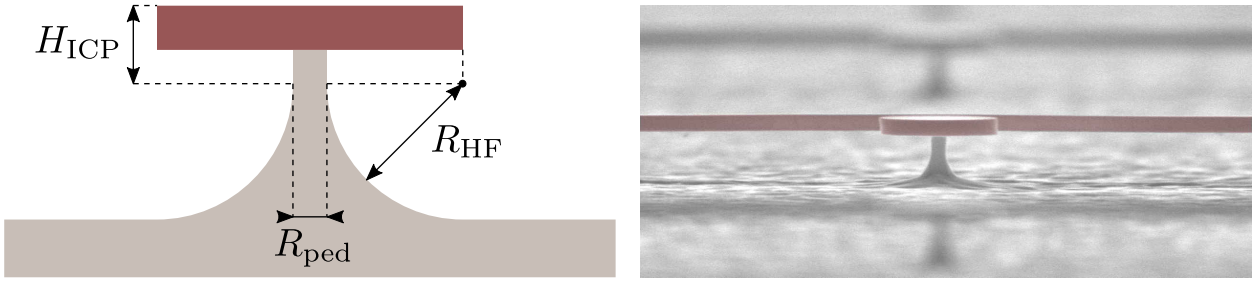

(a) Dimensions

(b) SEM micrograph of fabricated disk.

Figure 6.1 – First generation of disks. The pedestal cannot be cylindrical because of the isotropic wet HF under-etching step used in the fabrication process.

A is a constant depending on the mechanical properties of the materials used, and also on the RBM of interest. R and T are radii and thicknesses, respectively. λ_s is the speed of sound in the pedestal material. We see that Q_{clamp} depends strongly on the $R_{\mathrm{disk}}/R_{\mathrm{ped}}$ ratio. The $(R_{\mathrm{disk}}/T_{\mathrm{disk}})$ dependency comes from the fact that larger disk thicknesses correspond to a larger vertical displacement through the Poisson's ratio. The sinusoidal dependence in square brackets is a consequence of the acoustic impedance mismatch between the pedestal and the substrate. The acoustic compression wave excited in the pedestal by the disk reflects at the pedestal-substrate or pedestal-disk interfaces. A stationary wave thus forms in the pedestal. If the pedestal height is such that the contact point with the substrate is a node of this stationary wave, then virtually no displacement is transferred to the substrate and Q_{clamp} goes to infinity. In practice, the acoustic compression waves travelling through the pedestal are only partially reflected at those interfaces, so that Q_{clamp} remains finite.

6.1.2 Experimental measurements

The theoretical model described above assumes that the pedestal is a cylinder. In practice this is not the case, because of the isotropic nature of the HF under-etching step (see figure 6.1). The pedestal remains cylindrical on a height equal to the ICP etching depth within the AlGaAs layer, and then takes a "trumpet nozzle" shape until it reaches the substrate. This modifies the pedestal acoustic dynamics, which is a reason why we prefer to rely on FEM simulations rather than analytic formulas for Q_{clamp} predictions, on top of the fact that the above analytical model relies on some assumptions.

In order to boost experimental Q_{clamp} it appears quite clearly from formula 6.2 that the pedestal radius R_{ped} should be made as small as possible. R_{disk} and T_{disk} are fixed by other constraints (respectively g_0 and Q_{bend}). Figure 6.2 shows experimentally measured Q_{m} as a function of the pedestal radius, for a disk radius of 1 µm. We observe a plateau for pedestal radii smaller than 150 nm at 300 K. This indicates that clamping losses are not the limiting dissipation phenomenon to the overall Q_{m} at room temperature and for small radius disks. At 8 K, in contrast, the measurements are in accordance with clamping losses simulations again.

We see that, even on such small radius disks, Q_{clamp} of several 10^5 could in theory be obtained for pedestal radii smaller than 50 nm. Unfortunately such ultra-small pedestals lead to several problems :

- The disk standing on a very narrow pedestal is a fragile structure. When the sample is dried after HF under-etching, capillary forces tend to bring the disk down. Drying with a N_2 gun breaks the disks that have a pedestal radius smaller than 50 nm. Some techniques can however reduce the effects of capillary forces (see §4.3.4.3), allowing to produce even thinner pedestals.

- In spite of the possibilities offered by sophisticated drying techniques, a somewhat more

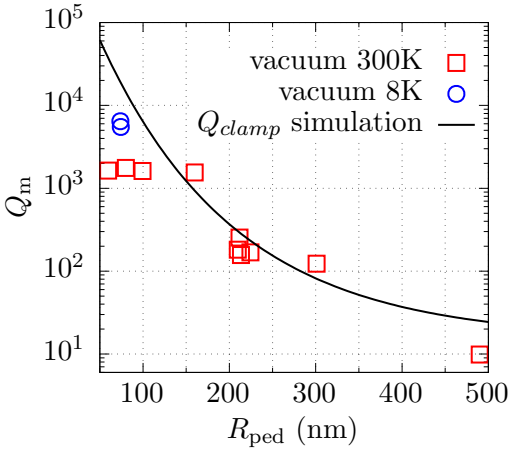

Figure 6.2 – Experimentally measured mechanical quality factors as a function of the pedestal radius R_{ped} (see figure 6.1a). $R_{disk} = 1$ μm and $T_{disk} = 0.32$ μm.

fundamental limitation of very thin pedestals is their poor thermal conduction (heat is generated in the disk by surface absorption of photons). In theory, the thermal conductance of a pedestal of given height is proportional to R_{ped}^2. Thus we see that, for instance, a 50 nm radius pedestal evacuates heat ∼10 times less efficiently than a 150 nm radius pedestal. This is important for two reasons:

- To perform successful cooling of mechanical motion we must start from a low thermodynamic temperature. If the disk heats too much because of thermal effects and poor thermal anchoring then the cooling capabilities of the cryostat are wasted.
- Thermal instabilities tend to kick in at very lower optical power (few μW) when the thermal anchoring is poor (see §7.2.2).

For these reasons disks with ultra narrow pedestals are questionable candidates for OM cooling. But how to increase the mechanical quality factor while maintaining a good thermal dissipation to the substrate ? This seems contradictory: we want to isolate the mechanical mode from the substrate, while at the same time set the disk in good thermal contact with the substrate. These two requirements can be conciliated because in our case heat is transferred by a collection of incoherent phonons. An ultra narrow pedestal stops phonons at all frequencies: it therefore provides efficient mechanical isolation for the GHz mechanical modes of interest, but also for all other phonons, i.e. it blocks the heat within the disk too. The ideal solution would be a structure that would block phonons at the mechanical mode's frequency and let pass all phonons at other frequencies. This can be achieved by using Bragg reflectors.

6.1.3 Acoustic Bragg reflectors

Bragg reflectors consist in the stacking of alternating layers of different impedance, be it in the optical or acoustic domain. Figure 6.3 shows the electric field penetration inside an optical Bragg mirror. An interference phonemenon arises that prevents the EM field from penetrating deep inside the Bragg structure. The Bragg reflector will work efficiently for a given wavelength range only.

The concept of Bragg reflector is valid in the case of acoustic waves as well, and can be used to confine phonons. The first geometry we considered consisted in a Bragg mirror located just under the pedestal. Alternating layers of GaAs/AlGaAs were used, two materials that have different acoustic impedance. The layers thicknesses were chosen to reflect acoustic waves at the disk's RBM frequency, and hence block mechanical dissipation to the substrate. Numerical simulations showed however that this design was rather inefficient. The reason in that standard Bragg reflectors work efficiently only for waves with propagation direction orthogonal to the Bragg layers. The pedestal

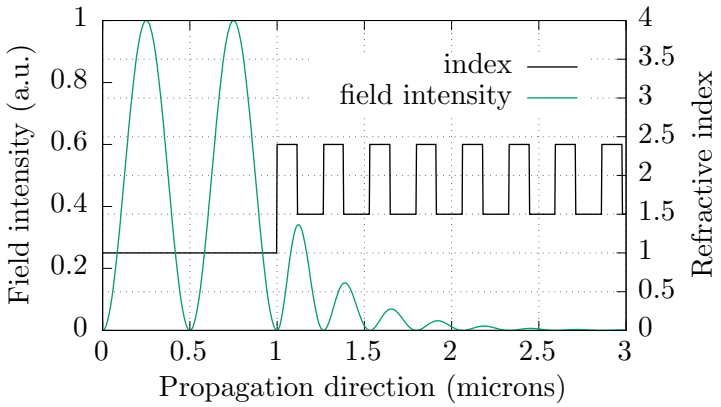

Figure 6.3 – Field profile of a plane wave of wavelength 1 µm sent on a Bragg reflector. The field has a short penetrating distance within the Bragg reflector, and is therefore largely reflected.

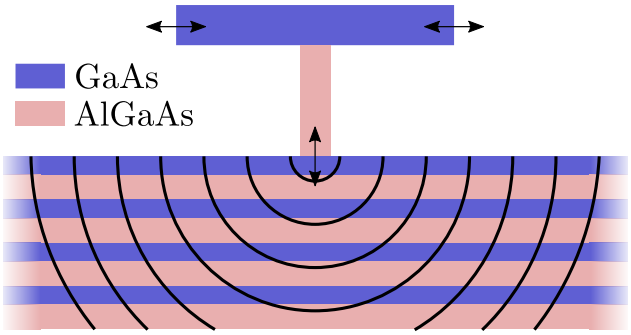

Figure 6.4 – OM disk resonator positioned above a Bragg reflector in the substrate. The pedestal acts as a "point source" emitting spherical waves (black lines) into the substrate, which pass through the Bragg structure.

however, at its anchoring point, acts as a point source that emits (half) spherical waves in the substrate. The Bragg mirror can only reflect efficiently the portion of these spherical waves that propagate vertically, and not the rest. This design was hence abandoned.

6.2 Disks with mechanical shields

6.2.1 Principle

The idea underlying MS structures could be resumed as "bringing the Bragg reflector inside the OM structure, directly within the pedestal". The MS consists in one or several additional masses positioned below the OM disk and held by a common pedestal (see figure 4.16a). Although partly incorrect, figure 6.5 allow easy understanding of the physical mechanism underlying mechanical shields. When the OM disk undergoes radial extension, the additional disk mass (the shield) moves in phase opposition and radially contracts. The disk, when extending, gets thinner because of the Poisson ratio of GaAs, while the shield gets thicker. The thickness of the overall structure therefore remains constant, and no compression waves are emitted through the bottom pedestal (the interface between the shield and the bottom pedestal, represented by the dashed line in figure 6.5, does not move). The clamping quality factor of the structure is in consequence greatly enhanced. The described physics is that of two pendula, (the disk and the shield) coupled together though a strong mechanical link (the pedestal). The mechanical mode shown in figure 6.5 is an asymmetric mode: disk and shield move with a dephasing of π. A symmetric mode of (almost) same frequency also exists, but with poor Q_{clamp} this time.

The explanation given above is however a simplification. Because of the large thickness over

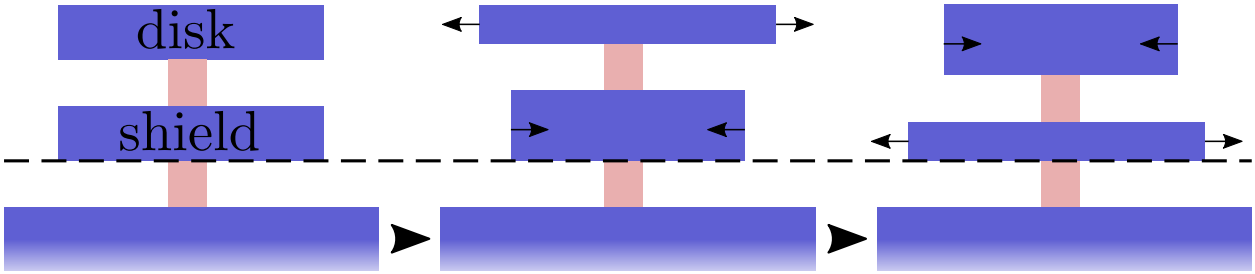

Figure 6.5 – MS working principle. Disk and shield undergo RBM motion in phase opposition.

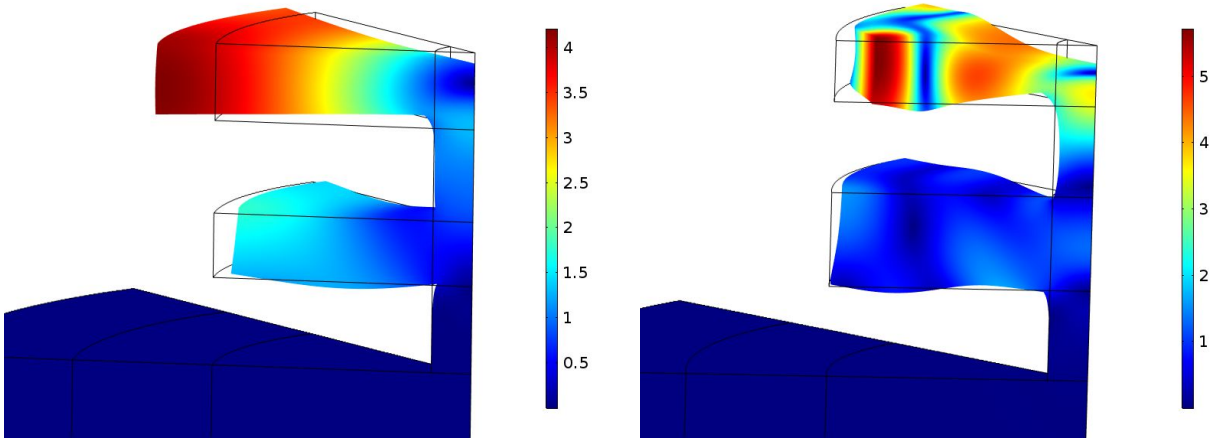

(a) MS optimized for the 1st RBM

(b) MS optimized for the 2st RBM

Figure 6.6 – FEM simulations of MS structures. The color scale is the total displacement in arbitrary units. The black lines delimit the disk at rest. In both cases Q_{clamp} is above one million. In fig. (6.6a) the phase opposition between the disk and shield can be seen. However on fig. (6.6b) disk and shield seem to have their motion in phase. In this case the mechanical compensation mechanism is more complex and cannot be intuited easily. In both cases the bottom pedestal and substrate displacement is close to zero, hinting that no mechanical waves are sent in the substrate.

radius ratio of the disks we use, the mechanical motion is complex and the pedestal does not only carry vertical compression waves. The thickness compensation mechanism described above thus does not suppress all the displacement transmitted to the substrate via the bottom pedestal. However, as we will see in the next section, FEM simulations show that it is possible to attain extremely high ($> 10^6$) Q_{clamp}'s with a MS.

6.2.2 Numerical simulations

We now describe how we numerically find the proper structure dimensions to achieve a high Q_{clamp}. Figure 6.6 shows FEM simulations of MS structures. These simulations are carried in 3D, with a fully anisotropic model for GaAs and AlGaAs. For symmetry reasons only one eighth of the total structure needs to be simulated. The estimation of Q_{clamp} with 3D simulations is necessary, as we observed that it can differ by one order of magnitude (or more) from the value obtained by 2D axisymmetric simulations. Because the disk and the shield are meant to be fabricated out of the same ICP vertical etch and HF under-etching step the disk/shield and top/bottom pedestal respectively share (in the ideal case) a common radius. The parameters that shall be explored in numerical simulations are therefore:

The elastic properties of AlGaAs can be varied by changing the fraction of aluminum in the stoichiometry. The goal of our numerical simulations is to find the largest *volume* in the parameter space within which Q_{clamp} is above 10^5 (this value is quite arbitrary, although such a quality factor,

– disk and shield radius R_{disk}	– disk thickness T_{disk}
– top and bottom pedestal radius R_{ped}	– top pedestal thickness T_{ped1}
	– shield thickness T_{shield}
	– bottom pedestal thickness T_{ped2}

corresponding for our GHz RBMs to $Q \cdot f$ factors above 10^{14}, should allow us to reach the ground state in OM cooling). A large volume in parameter space means big tolerances for the structure's dimensions, which is desirable because of fabrication imperfections. In the following the *tolerance* on a given parameter will be defined as the length of the interval on which the given parameter can evolve while keeping the overall structure's Q_{clamp} above 10^5. Not all parameters have the same tolerance requirements. The thicknesses are defined during the wafer epitaxy, and can be obtained with a precision on the order of a few nanometers the best case (relative precision of $\sim$1%). The disk radius can be defined with a precision of a $\sim$10 nm from the e-beam exposure, and the ICP etch does not add significant additional uncertainty. Finally, for the pedestal radius, a larger tolerance is necessary, because the HF under-etching step cannot be controlled with similar precision. There are two reasons to this:

- The HF under-etching conditions (temperature, concentration) as well as the etching time are subject to fluctuations. Thus the pedestal radius cannot be controlled with a precision better than $\sim$25 nm. However, the disks radiuses can be varied in, e.g., 10 nm steps on a given sample undergoing homogeneous HF under-etching so that the targeted pedestal under-etch can always be achieved[1].
- The HF under-etch is not fully isotropic, which results in a non-cylindrical pedestal shape (§4.3.3.2). Intuitively, a large pedestal radius tolerance in simulations should induce a better Q_{clamp} resilience to non-cylindrical shapes. For this reason a tolerance of several hundred nanometers would be ideally desirable on R_{ped}.

The search of Q_{clamp} tolerant zones is restrained to a given volume because of several considerations involving optics, mechanics, and microfabrication aspects. The constraints are the following:

- The disk radius determines to first order the frequency of operation for a given RBM, hence it cannot be varied too much. In the study reported here, we decided to work with the second RBM of a 1.3 μm disk, whose frequency is at 2.8 GHz.
- The disk thickness in also confined to a quite limited range. If the disk thickness is too small, the Q_{bend} drops to a level where is becomes the limiting factor for Q_{opt}. If T_{disk} is too thick, the disk mechanical motion distorts from the ideal RBM motion, and we know from simulations that the shield does not work well in this case. In practice for a 1.3 μm radius disk, T_{disk} is limited between 250 and 400 nm.
- The pedestal thicknesses (T_{ped1} and T_{ped2}) cannot be too small, otherwise some optical energy might leak from the disk to the shield. Because the waveguides are also duplicated (see figure 4.19), optical energy might also leak from the top waveguide, where the light is injected, to the second waveguide. Numerical simulations show that T_{ped1} and T_{ped2} should be larger than 250 nm to preclude this. T_{ped1} and T_{ped2} should not exceed $\sim$1 μm, otherwise the ICP etching step is too long and deleterious effects might occur, like resist wearing or asymmetries induced by waveguide vicinity (see §4.3.2).
- The shield thickness can be adjusted with more freedom. The thickness can be as small as needed (as long as the shield stays mechanically resilient), and the maximum limit is again set by the deleterious effects occurring with too long ICP etching.

[1] Actually the disk radii also change so that this trick does not allow for a sweep of pedestal radii with other parameters fixed constant, but this is not critical since the Q_{clamp} tolerance with the disk radius is quite high.

	R_{disk}	T_{disk}	$T_{\text{ped1\&2}}$	T_{shield}	R_{ped}
min	1200	250	250	0	150
max	1400	400	800	800	300

Table 6.1 – Parameter ranges for MS devices dimensioning simulations. Values are in nanometers. The maximum value of 800 nm for $T_{\text{ped1\&2}}$ and T_{shield} is somewhat arbitrary, the idea being to not exceed $\sim$2.5 µm for the sum of all thicknesses.

- The pedestals radiuses must be if possible large, in order to enhance thermal anchoring to the substrate.

Table 6.1 summarizes the different ranges that are explored for simulations, in the case of disks with 1.3 µm radius. Even with algorithm optimization, one mechanical simulation (i.e. a value of Q_{clamp} for a given set of parameters) requires a time on the order of 5 min. Computing Q_{clamp} for the whole parameter space would take too much time: even a quite modest resolution of 10 points per parameter would lead to 10^6 Q_{clamp} estimations, which would represent a computation time of 10 years! It is therefore a necessity to find a more efficient way of finding areas yielding high Q_{clamp} in the parameter space.

6.2.3 Optimization with the genetic algorithm

The systematic search for high Q_{clamp} areas in the parameter space being too costly, clever optimization techniques are required. One possibility would be the search of maxima with a "gradient-like" technique, but these algorithms work well when the function explored does not have local maxima, which is not true in our case. We chose to use the genetic algorithm [71], which is a heuristic search, meaning that there are no solid mathematical foundations to its design and probability of success. It is inspired by laws of natural evolution: in a given generation, the most fit individuals survive, others are evinced. Figure 6.7 schematizes the algorithm.

One nice feature of the genetic algorithm is its ability to find *tolerant* areas. Indeed, as the parameter space is explored heuristically, the algorithm has a higher chance to find a large hence tolerant zone than a narrow one (see figure 6.8). However the genetic algorithm does not provide a measure of the tolerance for each point found. It merely outputs a collection of points in the parameter space. Tolerances must then be calculated in a systematic way for each of those points. Two approaches can be adopted :

- The *hyper-cube* approach. In this approach the full 6D (we have 6 parameters to vary) volume around the point of interest is computed. This approach is rigorous, but is quite costly computationally. If for instance 4 steps are tried to estimate tolerances on each parameter (e.g. $R_0 \pm 5$ nm and $R \pm 10$ nm), the total number of points that must be evaluated to compute the hyper-cube is $4^6 = 4096$, which takes 24 hours with our most powerful computer. In practice we did not use this approach too much.

- The *sequential* approach. Here the tolerance of each parameter is explored sequentially with all other parameters kept constant at their central value (the one that was determined first by the genetic algorithm). In other words this technique consists in computing only the lines of the hyper-cube linking the center of a given facet to the center of the opposite facet. With this technique the exploration of 10 variation steps for each parameter requires only 60 computations, which is more reasonable computationally speaking. However this technique is an approximation, and nothing guarantees that the $Q_{\text{clamp}} > 10^5$ volume computed with the hyper-cube approach equals to the product of the $Q_{\text{clamp}} > 10^5$ lines computed with the sequential approach.

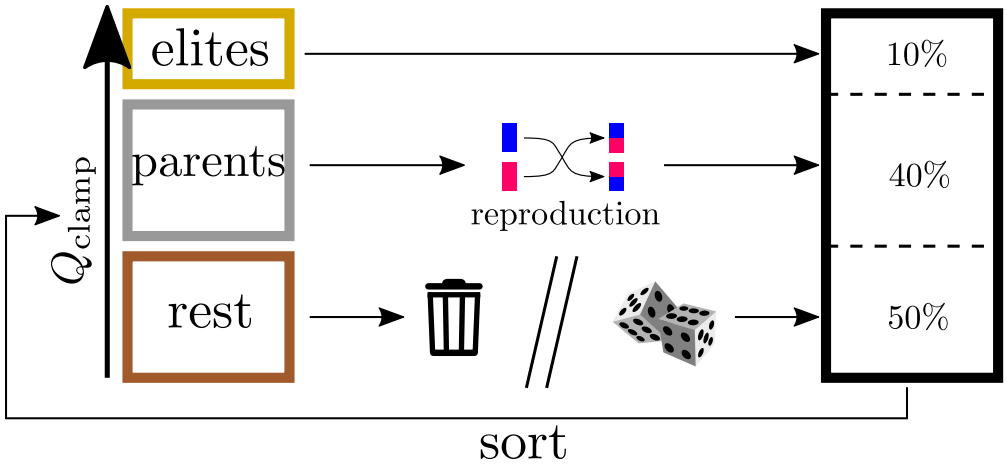

Figure 6.7 – Genetic algorithm. The "individuals" of a given generation are first sorted in terms of performance (Q_{clamp} in our case). The top 10%, the *elites*, are transmitted to the next generation without change. The next 40%, the *parents*, breed and their children are transmitted to the next generation. The remaining 50% is evinced and re-generated randomly. The algorithm can be stopped after a fixed number of generations, or when a sufficient population has attained a given score of Q_{clamp} in a given generation.

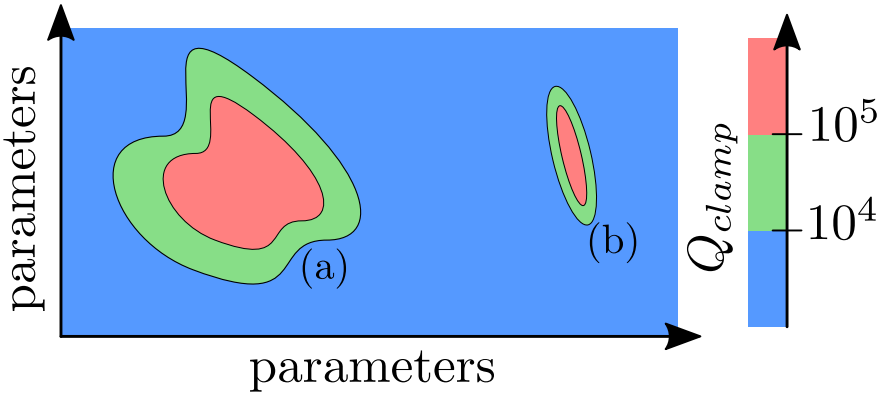

Figure 6.8 – Schematic of a map displaying Q_{clamp} as a function of the devices parameters. The map shown here is 2D, although the parameter space is 6-dimensional in our case. Zone (a) on the left is quite tolerant whereas zone (b) on the right is not.

The *sequential* approach, although less rigorous, was therefore implemented to find tolerant points. Experience gained by performing several simulations showed that some parameters are more tolerant than others. R_{disk}, T_{disk}, and $T_{\text{ped1\&2}}$ are usually rather tolerant (>100 nm), while T_{shield} and R_{ped} are more sensitive (tolerance <30 nm typically). This allowed to speed up the tolerance check by, e.g., using coarser variation steps for the more tolerant parameters.

The genetic algorithm allowed for example to find the two designs displayed in figure 6.6, for the 1$^{\text{st}}$ and 2$^{\text{nd}}$ RBM of a disk of radius 1.3 µm. These designs were selected on the basis of their tolerance and respect of the constraints listed in table 6.1. Their tolerance is greatly superior to the tolerance of a high Q_{clamp} point obtained randomly.

Figure 6.9 displays a 6D *sequential approach* calculation of tolerances for the RBM2 design displayed on figure 6.6b. As was hinted earlier, the least tolerant parameters are T_{shield} and R_{ped}, with respective tolerances of ∼30 nm and ∼60 nm in this case. The reader can notice the huge tolerance of T_{ped2}. This can be understood from the explanation given in figure 6.5: the shield *compensates* the disk's motion so that the bottom pedestal is barely excited mechanically. The latter plays little or no role in the motion compensation and its height is therefore not a crucial parameter.

R_{ped} and T_{shield} being the two most sensitive parameters, a 2D hypercube approach can be

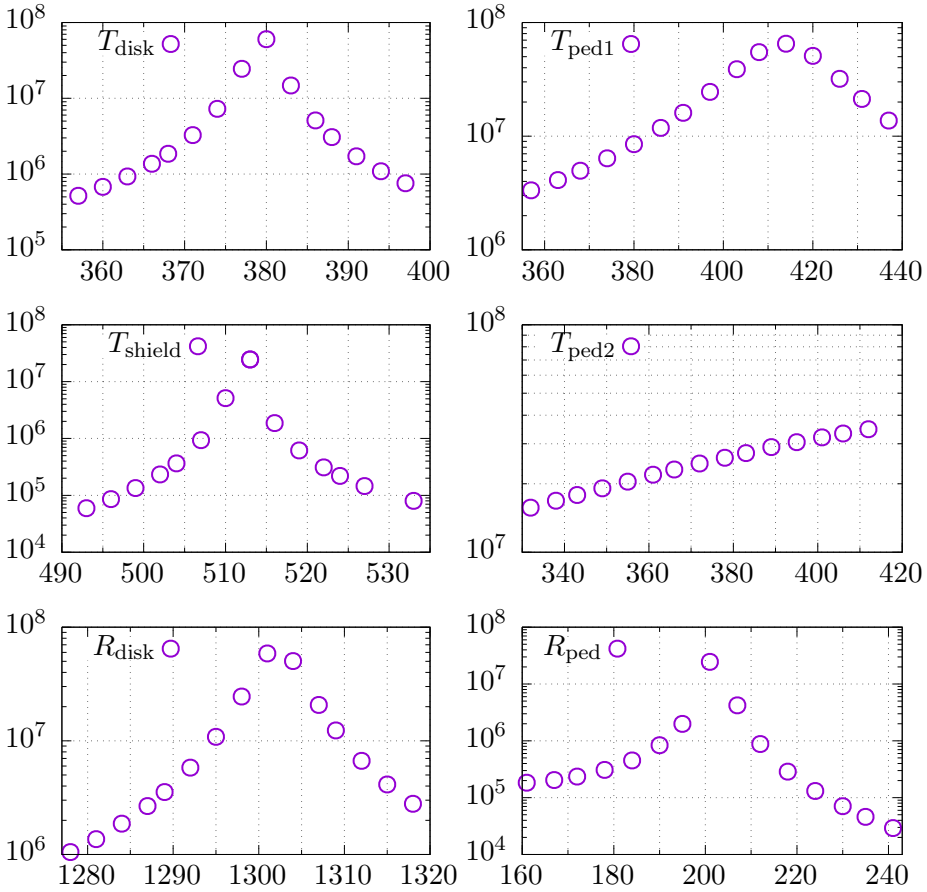

Figure 6.9 – Q_{clamp} vs. structure's dimensions in nm for the optimized, RBM2 design. The values were obtained by 3D FEM.

instructive. Figure 6.10 shows that the Q_{clamp} patterns are complex, and that the *sequential* approach is only a simplification. The design for the 1$^{\text{st}}$ RBM is more tolerant to variations in these two parameters than the design for the 2$^{\text{nd}}$ RBM. Although a simple and rigorous explanation to this fact is out of reach, it can be intuitively understood as a consequence of the greater vertical displacement of the 2$^{\text{nd}}$ order RBM (see figure 6.6). The shield therefore has to compensate a greater displacement in the upper pedestal, and this difficult task cannot be fulfilled on wide intervals for the 2$^{\text{nd}}$ order RBM.

	R_{disk}	R_{ped}	T_{disk}	T_{ped1}	T_{shield}	T_{ped2}
RBM1	1300	250	390	469	320	443
RBM2	1300	200	380	513	415	380

Table 6.2 – Dimensions of the RBM1 and RBM2 genetic algorithm designs.

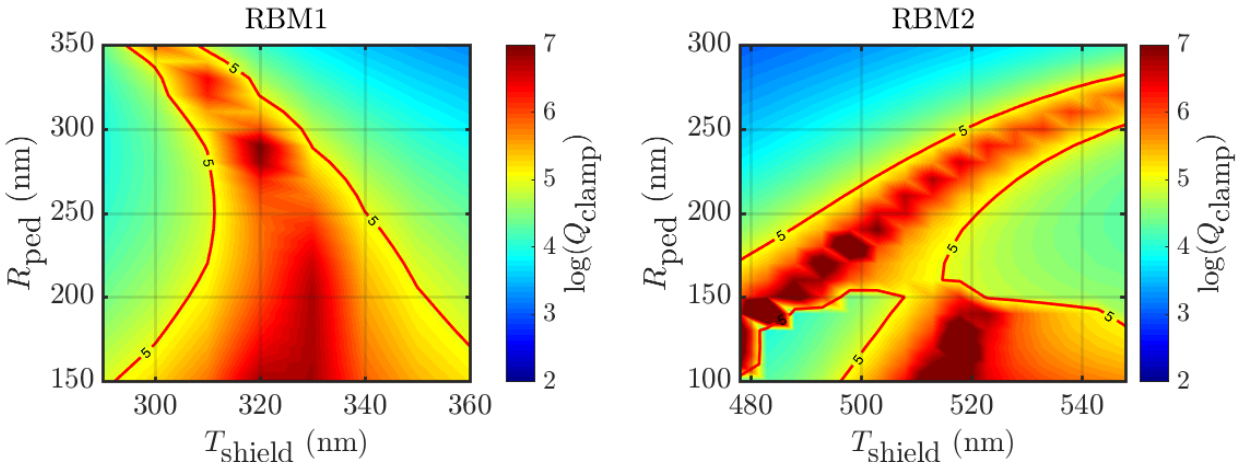

Figure 6.10 – Q_{clamp} vs. (T_{shield} vs. R_{ped}). The Q_{clamp}= 10^5 limit is drawn as a red line. Dimensions for RBM1 and RBM2 designs are given in table 6.2.

6.3 Realization of MS devices

A discussion of the technological problems arising with MS devices fabrication was already carried in §4.3. In this section we present the different milestones of the MS devices evolution. We will also describe fabrication imperfections and their consequences in further detail.

6.3.1 First generation of MS devices

As was already mentioned in §3.3.2, an interesting feature of FSW devices is the possibility to bring disk and shield close together. However FSW developments were carried almost one year after we started to develop MS devices. The first generations of MSs were therefore realized on LW devices (see §3.3.1). The main constraint arising from this waveguide design is that disk and shield must be separated by a least 1.8 µm, to preclude leakage from the waveguide into the substrate.

R_{disk}	T_{disk}	T_{ped1}	T_{ped2}	T_{shield}	R_{ped}
1000	320	2000	500	1500	200

Table 6.3 – Dimensions of the first generation of MS devices (in nanometers).

Numerical simulations were carried (back then full 3D simulations were not implemented yet). Tolerances of ∼100 nm on R_{ped} and ∼200 nm T_{shield} could be obtained [72], which was considered sufficient to account for fabrication imperfections. Table 6.3 gathers the dimensions of these devices of first generation. The overall structure's height was slightly above 4 µm, which imposed a long ICP etching step. This was causing asymmetry due to the presence of the waveguide in the vicinity (see figure 6.11a). A Q_{m} enhancement could already be experimentally measured with those devices *for a given pedestal radius* (figure 6.11b). Still the maximum Q_{m} obtained with shields was inferior to the maximum Q_{m} obtained with non-MS disks that have very narrow pedestals. This was because of the large T_{ped1} value: the pedestal was quite fragile so it was very difficult to achieve R_{ped} below 200 nm in this shielded structure of first generation [73].

6.3.2 Compact MS structure (2nd generation)

The development of FSW allowed us to bring the shield closer to the disk, thus reducing the overall height of structures. Figure 6.12 shows a compact MS structure. The better control of dimensions can be observed. It stems from the shorter ICP depth, which diminishes undesirable effects like

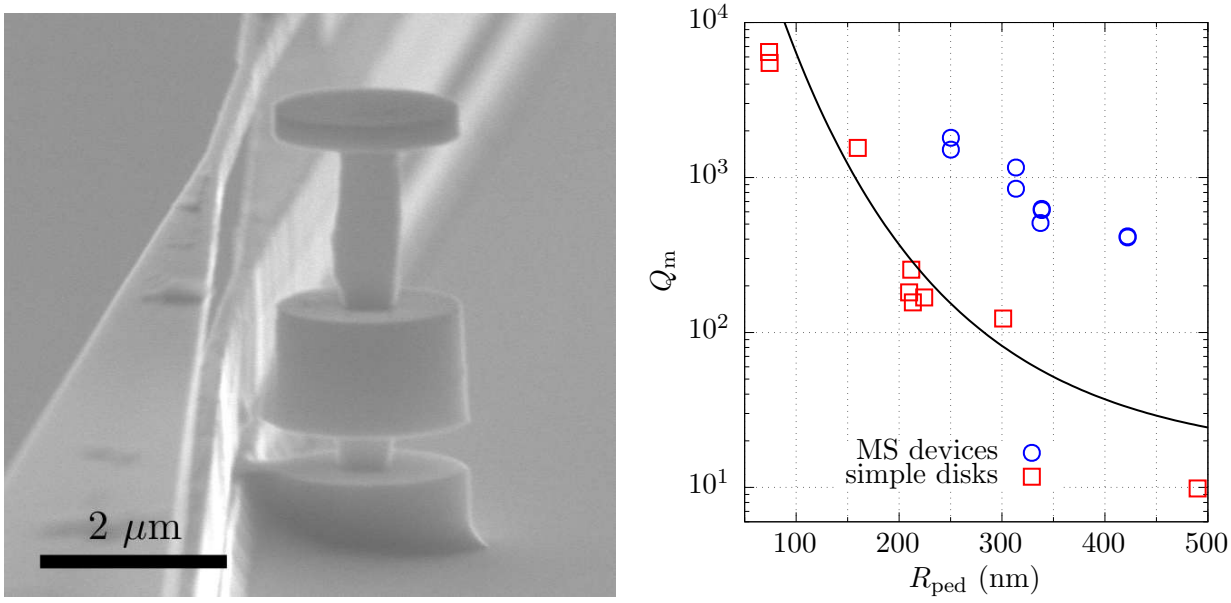

(a) (b)

Figure 6.11 – First generation of MS devices. **(a)**: SEM picture revealing fabrication imperfections. The upper pedestal radius is not homogeneous, and the shield is not symmetric. Its bottom left corner is almost touching the waveguide bottom duplicate. **(b)**: Q_{clamp} enhancement achieved with these shielded structures. For a given pedestal radius, Q_{clamp} in enhanced by a factor of ∼10. Numerical simulations for single disks is shown as a black line.

lateral etching or ICP lag, and from the pedestal's smaller height, which allows for a better HF under-etching homogeneity. The disk's edge on the waveguide side seems sloped in figure 6.12 but this was shown to be an measurement bias of the SEM: both sides of the disk are actually quite straight. Although the control on the dimensions was enhanced, some fabrication imperfections persist:

- The disk and shield are still residually sloped, i.e. the upper and lower rims of the disk (or shield) have slightly different diameters. This small slope is usually positive (lower rim larger than the upper one), but can be negative as well in some cases, e.g. when an *eye* waveguide surrounds the disk. This slope can also be asymmetric when a *straight* or 120° waveguide is used (see §3.2).
- The average shield diameter is larger than the average disk diameter. This effect is reversed when *eye* waveguides are employed.
- The pedestals can be off-centered with respect to the disks.
- The pedestal shape is not cylindrical.
- Both pedestals may have different radius.

The effect of these imperfections on the Q_{clamp} was investigated in numerical simulations. It appeared that some amount of slope on the disk and shield is acceptable as long as they have the same average radius. Indeed, if all other parameters are kept constant, a difference as small as 20 nm in the average radius can bring a 10^5 Q_{clamp} down to 10^3. Pedestal off-centering is acceptable in the case of the 1st RBM design, but not for the 2nd RBM. Strong stirring in HF, or waveguides that respect the disk symmetry, must be used in this case. The non-cylindrical aspect of pedestals is also anticipated to be deleterious, although it was not estimated precisely yet.

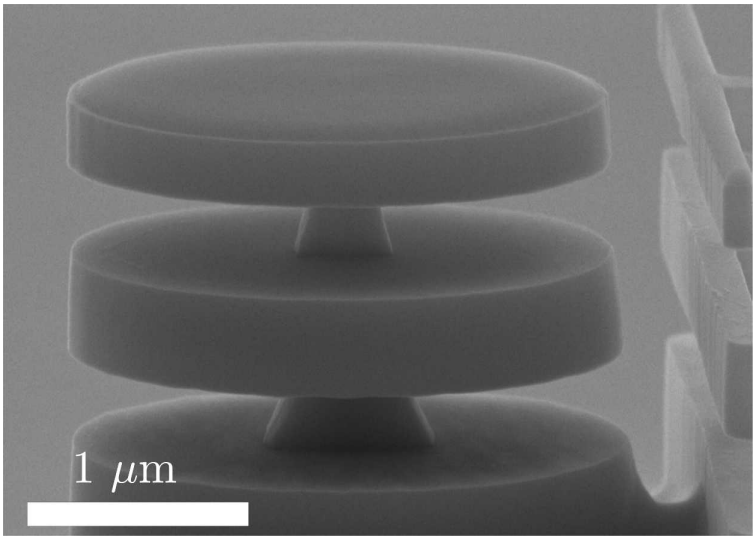

Figure 6.12 – SEM micrograph of a compact MS structure with the waveguide in the disk's vicinity.

Fabricating a MS device with perfect, straight and symmetric interfaces is not an absolute necessity: if a deviation from ideality is reproduced steadily over several fabrications, then it can be simulated, and one can compensate this imperfection by changing another parameter, like the disk radius for instance. We found that, by adjusting disk and pedestal radius, structures with non-idealities could still yield Q_{clamp}'s above 10^5. We could therefore fabricate MS devices whose dimensions (measured in the SEM) yielded $Q_{\mathrm{clamp}} > 10^5$ in simulations. Q_{clamp} over 10^5 were however not observed experimentally. The reason for this discrepancy might be a wrong estimation of the exact pedestal shape, or surface effects. These aspects are still under investigation in our laboratory.

Q_{m} measurement on shielded structures

The mechanical quality factor Q_{m} can be experimentally deduced by fitting the width of the mechanical motion's spectral power density, provided that great care is taken in order to avoid optomechanical modification of this width in the dynamical back action regime. The optomechanical damping rate Γ_{OM} evolves linearly with the optical power, so a linear extrapolation at low power allows to extract the intrinsic mechanical linewidth Γ_{m}. This extrapolation technique is actually quite general, and can be used in cases where the damping rate is modified by other physical effects than optomechanical interactions.

Figure 6.13 shows measurements of Q_{m} as a function of the optical power sent to the disk P_{drop}[2], at 3 K. The curve displays a linear behavior for P_{drop} under 20 µW, so the linear fit was performed on this section only. Interestingly, Γ_{eff} is an increasing function of P_{drop}, although OM models predict that it should decrease when measured on the blue flank ($\Delta < 0$), as is the case here. The reason for this unexpected feature is a degradation of the system's Q_{m} due to light injection in the disk. None of the mechanical loss phenomenon listed in §2.2.3 (i.e. thermoelastic damping, viscous damping and clamping losses) depend on the intensity of light circulating in the cavity. However, the free carriers (electrons and holes) generated at the surface by light absorption could interact with the phonons and degrade the mechanical properties. This phenomenon seems to take over on the Q_{m} enhancement associated with the OM dynamical back-action.

An extrapolation can still be carried, and yields a intrinsic Γ_m of 387 ± 5 kHz, corresponding to a Q_{m} of 7600 ± 100. This value is to be compared with the simulated Q_{m} of 50 obtained for the RBM2 of a non-MS disk with same R_{ped}=200 nm. Our measurements indicate then a Q_{m}

[2]More precisely, P_{drop} is the power *dissipated* by the disk. In experiments, it is determined by recording the drop of the transmitted signal, hence its name.

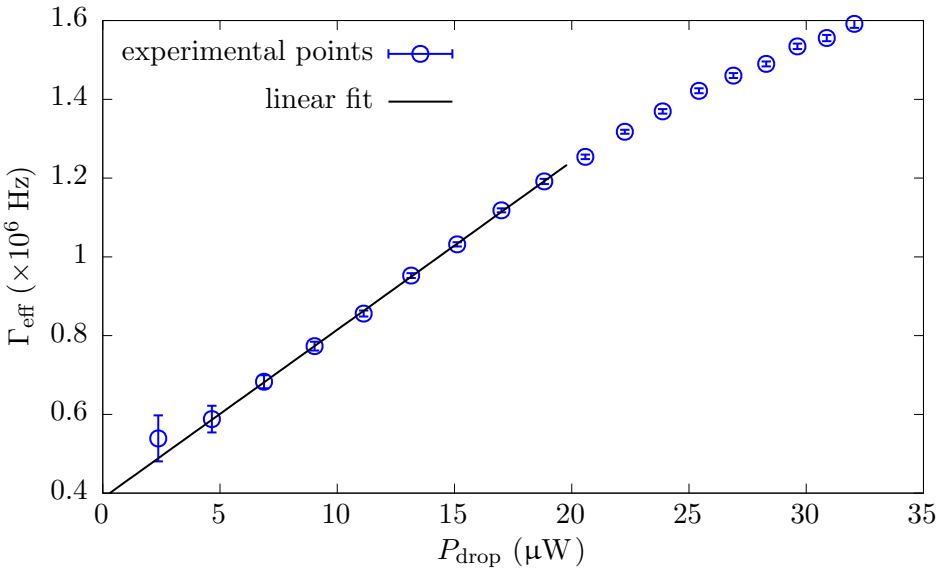

Figure 6.13 – Mechanical linewidth $\Gamma_{\text{eff}} = \Gamma_{\text{m}} + \Gamma_{\text{OM}}$ as a function of the optical power dropped into the disk P_{drop}, measured at 3 K for a RBM2 mode at 2.95 GHz. The extrapolation yields an effective linewidth of 387 ± 5 kHz.

enhancement over 100. This is significantly better than the enhancements obtained with the first generation of MS structures, and results from the better control on the structure's dimensions that arose from compact MS devices. The attained $Q_{\text{m}} \cdot f_{\text{m}}$ factor for this RBM2 is $2.25 \cdot 10^{13}$, which together with our results on non-MS disks RBM1[72] currently sets the state of the art on GaAs mechanical oscillators.

6.3.3 Sub micrometer radius shielded disks

The disk radius is an important parameter that impacts the device's figures of merit in many ways. Ultimately small disks are desirable because of the enhanced mechanical frequency and OM coupling constant g_0. For disks of 600 nm radius, g_0 is multiplied by a factor 10, from $g_0 \sim 1.5$ to $g_0 \sim 15$. Optomechanical cooling scales as g_0^2, so that enhancements by two order of magnitude are expected. However, attaining high optical and mechanical quality factors on ultra-small nano disks is more challenging. We fabricated non-MS disks of radius 500 nm and thickness 320 nm. For such a radius, the bending losses for 1550 nm radiation are large and lead to a bending losses quality factor $Q_{\text{bend}} \sim 1000$. In order to keep a high optical quality factor, we switched to a shorter wavelength of ~ 950 nm provided by the M-squared SolsTi:S laser (see §5.3.2). At this wavelength $Q_{\text{bend}} \sim 100\,000$, which sets us back to values similar to those obtained with 1.3 µm radius disks at λ=1.5 µm. Figure 6.14 shows a SEM picture of a fabricated 500 nm disk.

500 nm disks without MS show low simulated Q_{clamp}: ~ 100 for the RBM1. The addition of a mechanical shield is therefore necessary. A point in the geometric parameter space showing high Q_{clamp} ($> 10^5$) with large tolerances was found. The tolerances are given in figure 6.15. They follow the same general trends as for 1.3 µm radius disks, except for R_{disk} which is here more sensitive. This can be dealt with by varying the disk radius in small steps in the fabrication.

R_{disk}	R_{ped}	T_{disk}	T_{ped1}	T_{ped2}	T_{shield}
600	160	270	200	870	200

Table 6.4 – Dimensions of the ultra-small shielded disks.

Up to now, the optical quality factors measured experimentally were of the order of 1000. One cause of this degradation is the higher surface/volume ratio of these small disks: the energy lost at

the surfaces because of contour irregularities and mid-gap states absorption corresponds to a larger fraction of the total EM energy comprised in the disk volume. Another cause is the increased disk irregularity due to fabrication. It appeared indeed to be more difficult to fabricate smooth disks of radius 500 nm. Some further trials should be carried: with an optimized fabrication process, as well as ALD, better Q_{opt} could certainly be achieved.

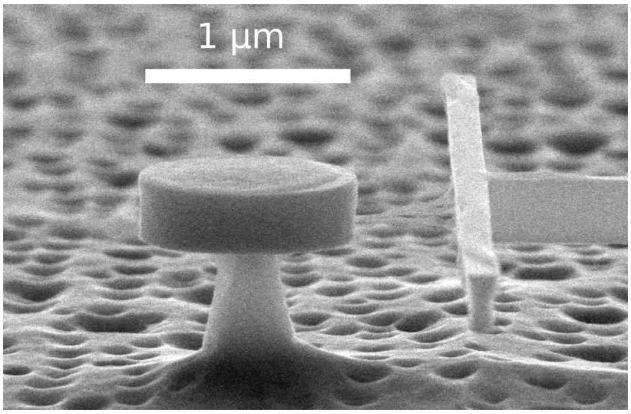

Figure 6.14 – SEM micrograph of an ultra-small, 500 nm radius disk with a test waveguide in the vicinity. The resist on top of the disk has not been removed yet.

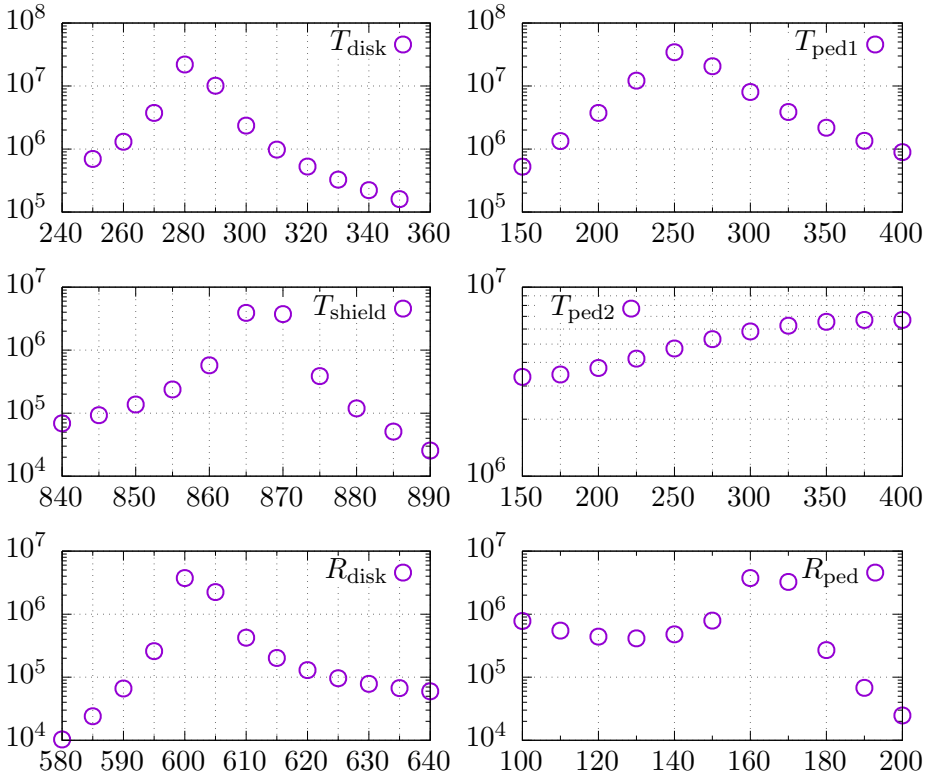

Figure 6.15 – Q_{clamp} vs. structure's dimensions for the RBM1 mechanical mode on an ultra small shielded disk. The values were obtained by 3D FEM.

Chapter 7

Optomechanical measurements in cryogenic environment

The main goal of this doctoral work is to achieve optomechanical cooling of a mechanical mode, if possible below the symbolic limit of *one phonon* average occupancy. Chapter 2, 3, 4 & 6 mainly dealt with considerations on the OM device itself. Once a sample is produced, it is placed in cryogenic environment and the figures of merit of its devices are measured. The best devices are then used to try different experiments, among which is cooling. The results of these experiments are presented in this chapter, as well as a discussion of limiting effects, such as the thermo-optic instability.

7.1 Brownian motion measurement at 3 K

The fluctuation-dissipation theorem states that the mechanical motion energy *of a given mechanical mode* is proportional to $k_B T$, given that the mechanical system is at thermodynamical equilibrium with a bath of temperature T (see §5.4.1). In the low optical power limit, where the optomechanical enhancement Γ_{OM} is negligible compared to Γ_{m}, the Brownian (thermal) motion of the mechanical mode of interest can be measured. See explanations in §1.1.2 for more detail on the mechanical spectrum readout.

Figure 7.1 shows the calibrated mechanical spectrum readout for a 1 µm radius disk at 3 K. The scale on the left y-axis is the power read by the spectrum analyzer. The power displayed by the spectrum analyzer is in W/Hz, which can be converted to a value in m^2/Hz after calibration. The calibration can be summarized with the following steps:

$$\mathrm{W/Hz} \xrightarrow{\mathrm{R}=50\Omega} \mathrm{A}^2/\mathrm{Hz} \xrightarrow{\text{A/W responsivity}} \mathrm{W}_{\mathrm{opt}}^2/\mathrm{Hz} \xrightarrow{g_{\mathrm{om}},Q_{\mathrm{opt}}} \mathrm{m}^2/\mathrm{Hz}$$

The spectrum analyzer detects the power (or equivalently the variance) of the electronic current loaded on its 50 Ω entrance impedance within a certain frequency range, determined by the apparatus resolution bandwidth. This current can then be translated to the optical intensity impinging on the photo-diode via its responsivity, in A/W. The optical intensity can be converted in a mechanical displacement, via g_{om} and Q_{opt}. The higher these two parameters, the more the optical signal reacts to a given mechanical displacement.

By measuring all these parameters, such as photo-diode responsivity, g_{om}, Q_{opt}, but also amplifier gains and optical losses through the setup, it is possible to convert the value in W/Hz of the electrical power measured by the spectrum analyzer into a value in m^2/Hz corresponding to the mechanical system's displacement at its reduction point (the choice of the reduction point impacts the value of g_{om}, see §1.3.1). Such a calibration was performed for the trace displayed in figure 7.1. Instead of the variance in m^2/Hz, the root mean square of the Brownian motion in

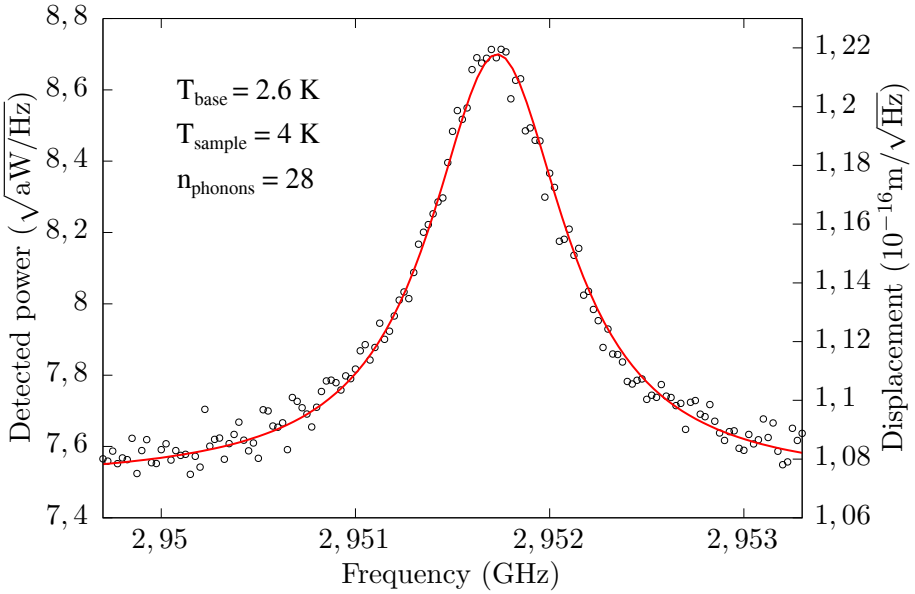

Figure 7.1 – Mechanical spectrum readout performed with a sample temperature of 4 K. The system is a 1.3 µm radius disk, measured at λ=1550 nm. The optical signal is amplifier with an EDFA before it is sent on the photo-diode. At this temperature the number occupancy of the 2.95 GHz 2$^{\text{nd}}$ order RBM is 28.

$\text{m}/\sqrt{\text{Hz}}$ is displayed. There is another way to calibrate the trace from figure 7.1. It involves the fluctuation-dissipation relation. This relation implies that the energy carried by the mechanical mode of interest's motion $\frac{1}{2}K\langle x^2\rangle$ is equal to k_BT. Here $\langle x^2\rangle = \int x(\omega)^2 d\omega$ and K is the effective spring constant of the mechanical mode. The area under the curve[1] can therefore be known, in m^2, which allows then calibrate the data.

The displacement sensitivity can be seen to be $\sim 1.08 \cdot 10^{-16}\text{m}/\sqrt{\text{Hz}}$. Lower values (corresponding to a better sensitivity) of $\sim 10^{-17}\text{m}/\sqrt{\text{Hz}}$ have been achieved on systems with higher Q_{opt}.

7.2 Intra-cavity power limitations

All optomechanical models presented in chapter 1 predict that the optomechanical damping rate Γ_{OM} is linear with the optical power circulating within the cavity. The average number of phonons obtained with cooling, $\bar{n} \approx \bar{n}_{\text{th}}\Gamma_{\text{int}}/\Gamma_{\text{OM}}$, therefore goes as an inverse function of the intra-cavity power, all other parameters left equal. In this section we will see that the maximum power that can be sent within the optical cavity is unfortunately limited by two effects: TPA and thermo-optic instability.

7.2.1 Power limitation induced by TPA

Linear loss phenomena like mid-gap states surface absorption or diffusion induced by contour irregularities are characterized by a loss rate κ. This loss rate connects the instantaneous power absorbed in the cavity with the energy E_{cav} stored within it: $dE_{\text{cav}}/dt = -\kappa E_{\text{cav}}$. TPA, on the other hand, is a nonlinear absorption process; the instantaneous absorbed power is a quadratic function of the intra-cavity energy: $dE_{\text{cav}}/dt = -\kappa_{\text{TPA}}E_{\text{cav}}^2$. In this way, $\kappa_{\text{TPA}}E_{\text{cav}}$ is an absorption rate like κ. In the literature (as in §2.1.4), TPA is characterized by a coefficient β, expressed in cm/GW, which relates to the spatial derivative of the light intensity: $\frac{dI(z)}{dz} = -\alpha I(z) - \beta I(z)^2$. β and κ_{TPA} can be related by:

$$\kappa_{\text{TPA}} = \frac{\beta c}{n_{\text{eff}}\tau_{\text{rt}}\sigma_{\text{opt}}} \tag{7.1}$$

[1] the constant noise floor must be substracted

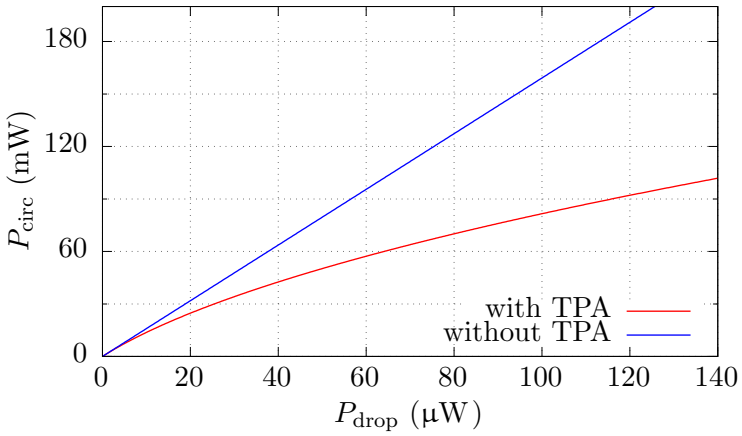

Figure 7.2 – Circulating power in the optical cavity vs. dropped laser power calculated from equation 7.3. The disk parameters are $Q_{\mathrm{opt}} = 100\ 000$, $R_{\mathrm{disk}} = 1$ µm, and a TPA absorption coefficient $\kappa_{\mathrm{TPA}} = 6.8 \cdot 10^{30}\ \mathrm{MJ}^{-1}\mathrm{s}^{-1}$. For a dropped power as low as 110 µW, TPA can be seen to reduce the circulating power within the cavity by a factor 2.

with n_{eff} the effective index of the circulating WGM, τ_{rt} the round trip time of the WGM, and σ_{opt} the WGM power flow cross section[2].

We wish to establish the relation between the optical power *dissipated* by the disk P_{drop} and the optical power circulating within it P_{circ}. In the linear regime, the circulating power and dropped power in the disk are related by: $P_{\mathrm{circ}} = \frac{F}{2\pi} P_{\mathrm{drop}} = \frac{Q_{\mathrm{opt}}}{2\pi m} P_{\mathrm{drop}}$, with m the azimuthal number of the WGM, and the quality factor can be expressed as $Q_{\mathrm{opt}} = \omega_0/\kappa$. Now, adding TPA, the new expression for the quality factor is $Q_{\mathrm{opt}} = \omega_0/(\kappa + \kappa_{\mathrm{TPA}} E_{\mathrm{cav}})$. We can thus write :

$$P_{\mathrm{circ}} = E_{\mathrm{cav}}/\tau_{\mathrm{rt}} = \frac{F}{2\pi} P_{\mathrm{drop}} = \frac{1}{2\pi m} \frac{\omega_0}{\kappa + \kappa_{\mathrm{TPA}} E_{\mathrm{cav}}} P_{\mathrm{drop}} \tag{7.2}$$

With τ_{rt} the intra-cavity round trip time. P_{circ} therefore satisfies the following equation:

$$\kappa P_{\mathrm{circ}} + \tau_{\mathrm{rt}} \kappa_{\mathrm{TPA}} P_{\mathrm{circ}}^2 = \frac{\omega_0}{2\pi m} P_{\mathrm{drop}} \tag{7.3}$$

This second degree equation can be solved to get P_{circ} as a function of P_{drop}. Of interest to us is the behavior for high circulating powers. For such high powers, we have $\tau_{\mathrm{rt}} \kappa_{\mathrm{TPA}} P_{\mathrm{circ}}^2 >> \kappa P_{\mathrm{circ}}$, and therefore:

$$P_{\mathrm{circ}} \approx \sqrt{\frac{\omega_0}{2\pi m \tau_{\mathrm{rt}} \kappa_{\mathrm{TPA}}} P_{\mathrm{drop}}} \tag{7.4}$$

We thus see that the intra-cavity circulating power goes only as the square root of the power dissipated by the disk (which is equal in the critical coupling case to the power sent to the cavity by the laser). Attempting to increase the intra-cavity photon number by using large laser powers therefore appears to be fairly inefficient for power ranges dominated by TPA.

Additionally to the limit it sets to the maximum power that can be sent within the cavity, TPA has another deleterious effect on optomechanical cooling: as for the linear absorption processes, the optical energy absorbed is converted to heat that increases the disk's temperature. The starting number of phonons before cooling $\bar{n}_{\mathrm{th}}$ is therefore increased, which has repercussions on the final number of phonons attained when optomechanical cooling is "turned on".

[2] In a given section orthogonal to the disk plane (as in figure 2.3), σ_{opt} is defined as the ratio of the total power flow across this section (in W) divided by the maximum of the power flow density (in $\mathrm{W/m^2}$) in this section.

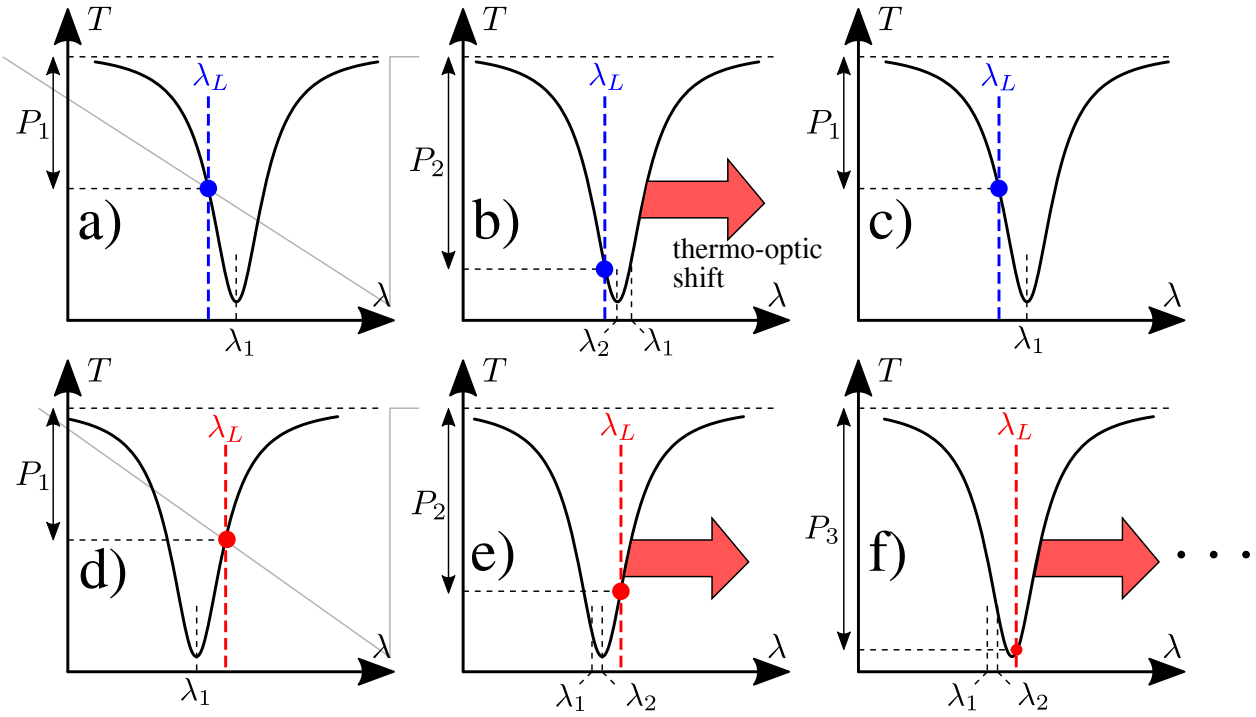

Figure 7.3 – Thermo-optic instability. The first row corresponds to the blue-detuned case (the laser wavelength is inferior to the cavity resonance wavelength). Figure **a)** corresponds to the system at *equilibrium* at a certain resonance wavelength λ_1, somewhere on the triangular thermo-optic shape (in light grey in the background). λ_1 is larger than the cavity's resonance wavelength at room temperature. Now let's assume that the cavity undergoes a small perturbation that shifts its resonance wavelength to a *lower* value λ_2 **(b)**. Because the laser wavelength is fixed, the amount of power injected in the cavity increases: $P_2 > P_1$. This results in more absorption within the cavity, which induces a temperature increase, and the mode resonance in therefore shifted to a *larger* wavelength via the thermo-optic coefficient dn/dT. The system therefore comes back to its original position **(c)**. This configuration is hence stable. If the perturbation is a positive resonance wavelength shift, or even a fluctuation of the laser's wavelength or power, the result is the same: the cavity comes back to its original position.
Now in figure **d)** we consider the red detuned configuration. If the cavity undergoes a small shift to a *larger* wavelength λ_2 **(e)**, the power injected increases, which shifts the cavity to an even higher wavelength, which increases even more the injected power, and so on... This configuration is therefore unstable. A negative resonance wavelength shift or a fluctuation of the laser's wavelength or power leads to the same unstable behavior.

7.2.2 Power limitation induced by thermo-optic instability

We describe another physical process that sets a limit on the maximal intra-cavity optical power. In the current state of our devices development, it sets a more drastic limit than TPA. The thermo-optic effect was presented in §1.3.3, with an emphasis on triangular mode shapes. Here we discuss the instability that can be triggered by this effect (see figure 7.3). The key message is that the blue-detuned[3] configuration is thermo-optically stable (resilient to perturbations), whereas the red-detuned configuration is unstable. Unfortunately, it is the latter configuration that is of interest to us, because the optomechanical cooling is achieved for red detuning.

The red flank is actually unstable for dropped powers above a given threshold only. In order to derive this threshold for our systems, we start from the square equation of 3.2 that gives the intra-cavity energy:

$$|a_0|^2 = \frac{\kappa_{\text{ext}}|s_+|}{(\omega_L - \omega_0)^2 + (\kappa/2)^2} \tag{7.5}$$

Now because of the thermo-optic effect the resonance frequency of the cavity is a function of

[3]laser blue-detuned from the optical cavity

temperature:

$$\omega_0 \equiv \omega_0(T) = \omega_0(T_{\text{amb}}) \left[1 + \frac{1}{n}\frac{dn}{dT}(T - T_{\text{amb}})\right] \tag{7.6}$$

with T_{amb} the ambient temperature and n the optical index of GaAs. The temperature increase $(T - T_{\text{amb}})$ due to absorption can be expressed as:

$$\Delta T = T - T_{\text{amb}} = \frac{|a_0|^2 \kappa_{\text{abs}}}{\sigma_{\text{th}}} \tag{7.7}$$

with σ_{th} the pedestal thermal conductivity in W/K, and κ_{abs} the absorption rate. $|a|^2$ therefore satisfies the following equation:

$$|a_0|^2 = \frac{\kappa_{\text{ext}}|s_+|^2}{\left(\omega_L - \omega_0(T_{\text{amb}})\left[1 + \frac{1}{n}\frac{dn}{dT}\frac{|a_0|^2\kappa_{\text{abs}}}{\sigma_{\text{th}}}\right]\right)^2 + (\kappa/2)^2} \tag{7.8}$$

Equation 7.8 is cubic in $|a|^2$ and has therefore 1 or 3 solutions. The threshold between the 1 and 3 solutions regime corresponds to:

$$P_{\text{thresh}} = |s_+|^2_{\text{thresh}} = \frac{\kappa^3 \sigma_{\text{th}}/(\kappa_{\text{abs}}\kappa_{\text{ext}})}{3\sqrt{3}\frac{1}{n}\frac{dn}{dT}\omega_0(T_{\text{amb}})} \tag{7.9}$$

A numerical application for our typical system gives a threshold laser power of 0.5 µW. This corresponds to $\sim$ 800 photons stored in the optical cavity. Figure 7.4 shows the equilibrium positions for different laser powers. The existence of several equilibrium points for laser powers above 0.5 µW can clearly be seen. A quick remark on the numerical value found for P_{thresh}: although κ, κ_{ext} and dn/dT can be known with a satisfying accuracy, κ_{abs} and σ_{th} are more difficult to estimate. Methods to calculate bending and scattering losses were introduced in §2.1, but some degree of uncertainty remains for the estimation of scattering losses. Absorption loss rates could therefore be deduced by substraction : $\kappa_{\text{abs}} = \kappa - \kappa_{\text{ext}} - \kappa_{\text{bend}} - \kappa_{\text{scatt}}$, but with a substantial error... σ_{th} can also be computed with FEM tools, but the thermal transport in materials and at interfaces is strongly modified in the nanoscale [74], thus making Fourier thermal transport theory imprecise. The ratio $\kappa_{\text{abs}}/\sigma_{\text{th}}$ was therefore extracted in another way. We know from experimental measurements that dropping 500 µW of laser power in a typical optomechanical system such as the one considered in figure 7.4 results in a resonance shift of 20 nm. From this a value can be extracted for $\kappa_{\text{abs}}/\sigma_{\text{th}}$ and P_{thresh} can be calculated. Howver this technique does not allow to yield independant values for κ_{abs} and σ_{th}.

The thermo-optic instability sets the lower limit on the maximum number of photons than can be sent within the optical cavity. The effects of TPA for laser power below 1 µW are indeed negligible, for this reason heat induced by TPA was not taken into account in the calculation of the thermo-optic threshold.

In order attain large cooling efficiency, the value of P_{thresh} should be increased as much as possible. We do not wish to temper with κ ans κ_{ext}, which values should stay as low as possible in order to operate in the good cavity limit. The parameters left to play with are therefore κ_{abs}, dn/dT, and σ_{th}:

- κ_{abs} should be made as small as possible. Its value was decreased by a factor 10 by ALD techniques (see §2.1.4).
- dn/dT is an intrinsic property of GaAs and therefore cannot be changed. However it is dependent on the temperature: its value is divided by a factor $\sim$100 (value derived from our own measurements) when operating at 3 K, which is of highly profitable in our case.
- σ_{th} should by as high as possible. For this purpose we designed mechanically shielded resonators (see chapter 2), which allow to increase the pedestal radius (therefore yielding a high σ_{th}), while keeping high Q_{m}.

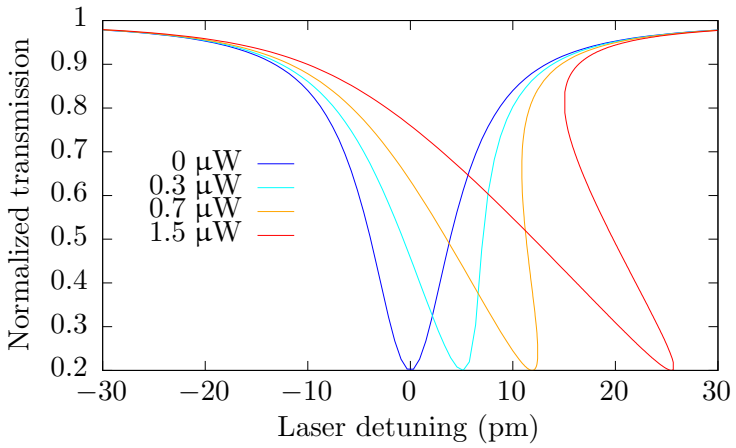

Figure 7.4 – Curves of equilibrium positions for different laser powers. The optical resonance linewidth is 10 pm, the disk has a 1 μm radius, and stands on a 100 nm radius pedestal. For laser powers above 0.5 μW the curves exhibit areas where 3 different stable configurations exist for a given laser detuning.

Another approach to increase the number of photons sent to the cavity is active stabilization. This approach does not aim at changing P_{thresh}, but rather at making the red flank *artificially* stable. The idea is to set up a feedback loop that detects a shift in the cavity's resonance frequency, and compensates it by changing the laser wavelength. This way a constant detuning can be kept. This technique was tried without success until now, because of the very large bandwidth (∼GHz) of the required feedback loop (see appendix D for more details).

7.3 Mechanical mode thermalization

As was mentioned in §5.2, cryogenic operation is necessary in order to reach a low phonon occupancy number by optomechanical cooling, as it allows to start with a phonon number ∼100 times lower than that of room temperature. The Attocube cryostat specifications guarantee a sample holder temperature under 4 K. A calibrated silicon diode thermal sensor is placed near the sample holder, and we can measure temperatures as low as 2.65 K during operation. However, this silicon sensor is not placed on the sample, hence the sample (and disk) temperature will be higher than what measured by the sensor if heated by e.g. black body radiation of the 56 K shield. The thermal links of interest are:

- Between the sample and the sample holder. The thermal contact is provided by Apiezon-N vacuum grease.
- Between the optomechanical disk and sample. The thermal contact is provided by the AlGaAs pedestal.

Estimations were carried by assuming isotropic 56 K black body emission on the structures respective cross sections, and a simple model for the thermal conductivities of the AlGaAs pedestal and Apiezon-N vacuum grease. The values obtained are a sample temperature elevation of 370 μK with respect to the 3 K sample holder, and a disk temperature elevation of 1.7 μK with respect to the sample temperature. These values are very small if compared to the cryostat base temperature and can therefore be neglected. However, the estimations for the thermal conductivities are not precise, and thermalization measurements can be used to confirm that the mechanical mode temperature is indeed 3 K. The idea underlying thermalization measurements is that a single mode spectral trace area, $\int S_{xx}(\Omega)d\Omega$, is proportional to $k_B T$. This area can be measured when the mechanical mode temperature is known for sure, e.g. when the cryostat operation is shut down (the whole cryostat is at an homogeneous temperature of 300K). The spectral trace is measured again when the sample

is cooled down. The ratio of the two traces areas is equal to the ratio of temperatures, hence the sample's temperature when cooled down can be deduced. We performed such thermalization measurements: for several temperatures the mechanical displacement spectral density was measured. The results can be seen on the left panel of figure 7.5. The mechanical mode seems to thermalize well, as the area $\int S_{xx}(\Omega)d\Omega$ is proportional to T.

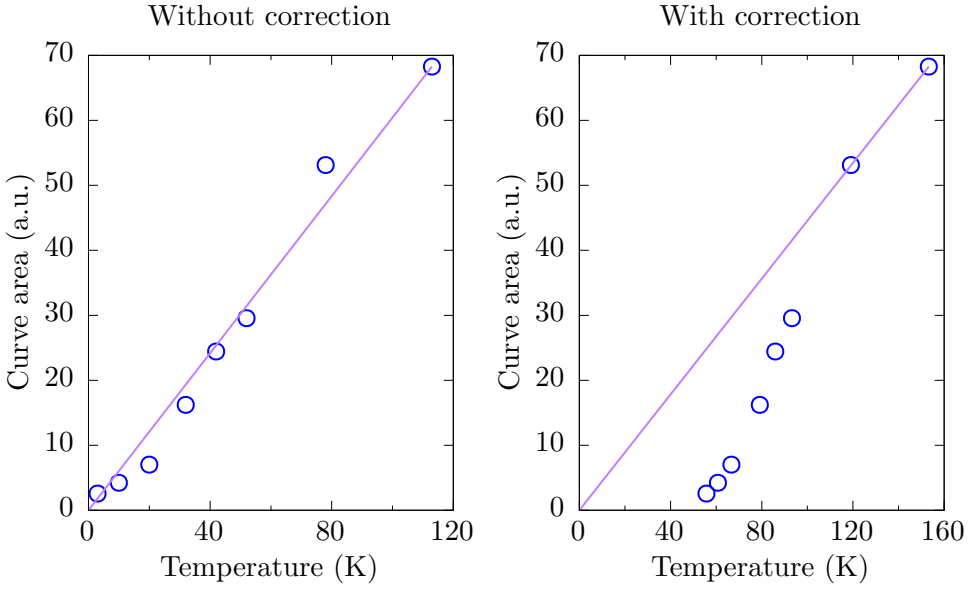

Figure 7.5 – Mechanical mode thermalization measurements. The displacement area, $\int S_{xx}(\Omega)d\Omega$, which is proportional to k_BT, is measured for different temperatures. The left and right panels respectively show data without and with heating effects correction.

However, the optical power necessary to perform a mechanical displacement readout is accountable for some heating in the disk, which does not show on the cryostat temperature sensor. We used thermo-optic shifts (see §1.3.3 and 7.2.2) to determine the (supposedly) real temperature of the disk. The results are shown on the right panel of figure 7.5. The temperatures obtained from the cryostat temperature sensor are lower that the temperatures calculated from the thermo-optic shift, as expected. But surprisingly, the area under the curve does not evolve linearly with that second temperature deduced from thermo-optic shifts. The reason for this discrepancy could be that the disk is out of equilibrium when illuminated and heated by laser absorption: the temperature of electrons and THz phonons of the disk might in this case be higher than the "temperature" of our GHz phonon of interest. The optical index (which depends on the electron temperature) is therefore shifted, but the GHz mechanical mode is not "heated" to the same extent. This calibration measurement should anyways be carried again with a resonator that heats less (an ALD passivated one for instance). Moreover, the measurements shown on figure 7.5 were carried at λ=1.3 µm with the optical booster as the light amplification device, which is far less efficient than the EDFA employed in our team at 1.5 µm. We can therefore expect to measure mechanical motion with less optically-induced thermal perturbation if we use the EDFA and an ALD passivated sample.

7.4 Optomechanical cooling experiment

7.4.1 Results

One of the main objectives of this doctoral work was to perform optomechanical cooling of a device to less than one phonon average occupancy of the mechanical oscillator. Figure 7.6 shows experimental cooling results obtained with a starting temperature of 3 K. Γ_{eff} is plotted vs. P_{drop} for blue and red detuning measurements. Γ_{eff} increases for blue detuned measurements, although canonical

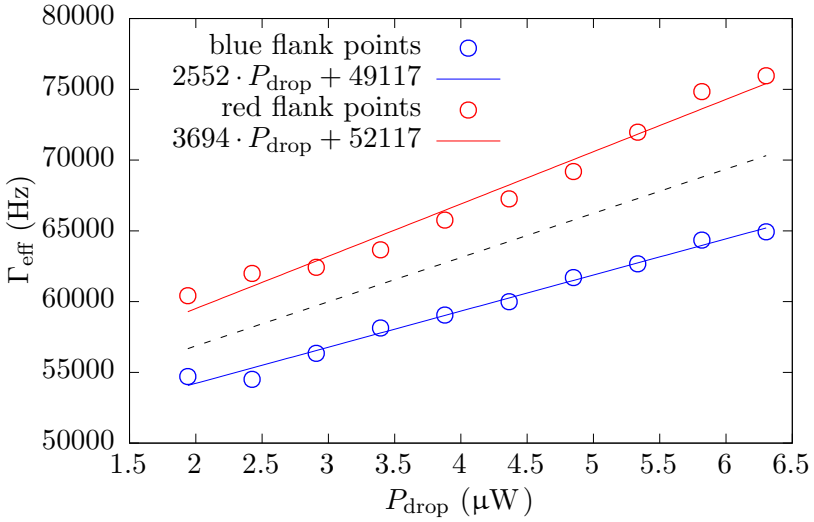

Figure 7.6 – Experimental cooling results, measured on the 1st RBM of a 1.3 µm radius disk. The dashed black line is the "intrinsic" linewidth for a given P_{drop}, i.e. without optomechanical linewidth modification.

optomechanics predict that is should decrease. The reason for this unexpected behavior might be the free carrier optical generation resulting from light absorption that increases the mechanical linewidth linearly with P_{drop}. We will refer to this effect as the "added" effect in the following. The linewidth for blue ($-$) and red ($+$) detuning can therefore be expressed as:

$$\Gamma_{\text{eff}\pm} = \Gamma_{\text{int}} + (\alpha_{\text{added}} \pm \alpha_{\text{OM}}) P_{\text{drop}} \tag{7.10}$$

For the device in use in figure 7.6, $\alpha_{\text{added}} > \alpha_{\text{OM}}$, so that both Γ_{eff} curves have a positive slope. α_{added} can be derived from the average of these two slopes. An "intrinsic" linewidth can be deduced as well by averaging the optomechanical contribution $\pm\alpha_{\text{OM}} P_{\text{drop}}$, it is represented as a dashed black line on figure 7.6. We know that for $\hbar\Omega_{\text{m}} \ll k_B T$ (which is the case for DES BETISES Ω_{m}=2π GHz at T=3 K) the OM cooled phonon number is given by: $\bar{n}_{\text{cooled}} = \bar{n}_{\text{th}}(\Gamma_{\text{int}}/\Gamma_{\text{eff}})$. At 3 K, $\bar{n}_{\text{th}} = 60$, so that, for the maximal used power of 6.3 µW (see figure 7.6):

$$\bar{n}_{\text{cooled}} = \bar{n}_{\text{th}} \frac{\Gamma_{\text{int}}}{\Gamma_{\text{eff}}} \approx 60 \cdot \frac{65\,000}{75\,000} \approx 52 \tag{7.11}$$

This result requires a correction because the dropped laser power of 6.3 µW heats the cavity. From thermo-optic shift measurements, we could estimate that for this P_{drop} the cavity is heated to a temperature of ≈10 K. At this temperature $\bar{n}_{\text{th}} \approx 200$, and the average phonon number after OM cooling is thus: $\bar{n}_{\text{cooled}} = 200 \times (65/75) = 173$. In this example the optomechanical cooling power is actually weaker than the heat rate induced by photon absorption. Efforts made to reduce heat generation through absorption (ALD) and optimize heat dissipation (large pedestals) must therefore be pushed.

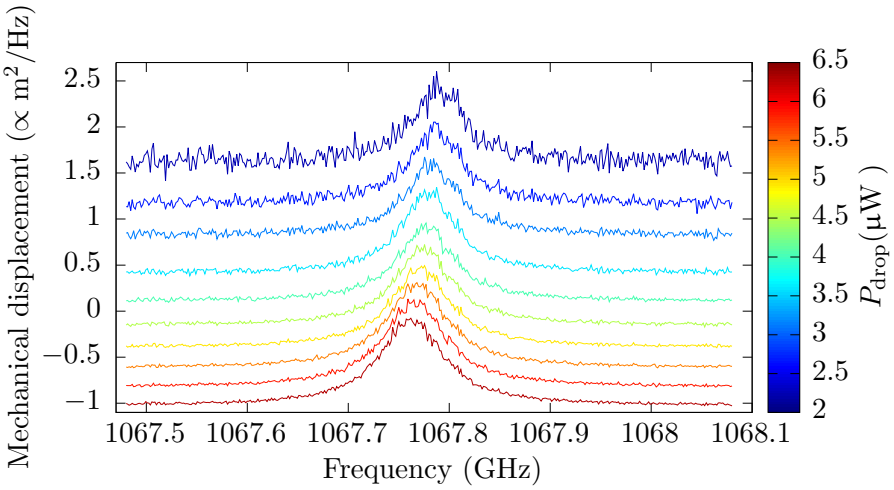

Figure 7.7 – Cooling traces corresponding to the red detuned points of 7.6. The trace linewidth Γ_{eff} as well as the area under the curve (with noise floor corrected) increase slightly with dropped laser power. For red detuned operation the area under the curve should decrease with incident laser power. This discrepancy can be attributed to the absorption of light that raise the sample thermodynamic temperature to ≈10 K.

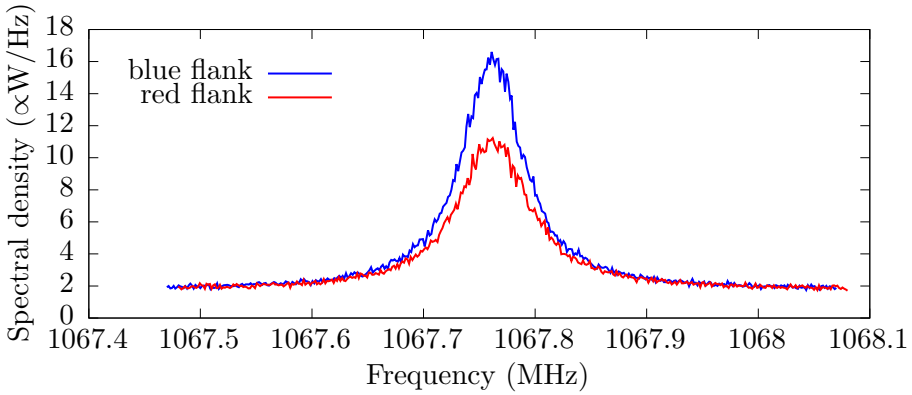

Figure 7.8 – Mechanical spectral densities for red and blue detuned measurements. Both traces were acquired for the maximum dropped power of 6.5 μW. The red-detuned area is smaller than the blue-detuned area, which is characteristic of optomechanical cooling.

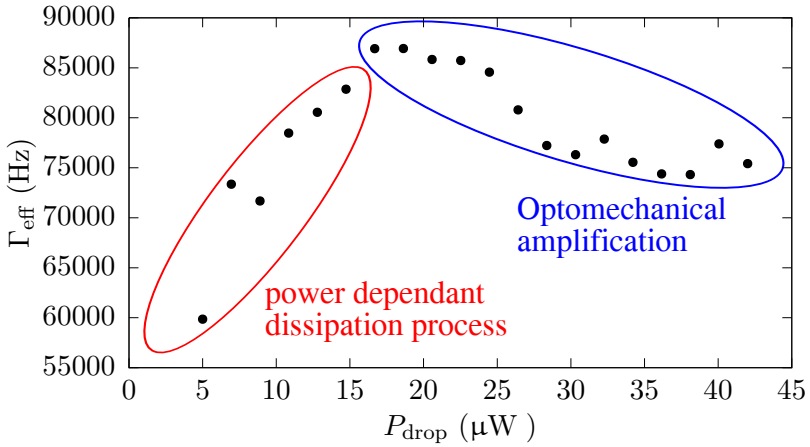

Figure 7.9 – Effective damping rate vs. dropped power in the blue detuned case. The data is measured for a 1st order RBM. Two regimes corresponding to a Γ_{eff} increase due to unknown power-dependent effects, followed by a decrease due to OM effects, can be observed.

7.4.2 Perspectives

Cooling the system to $\bar{n}_{\text{cooled}} < 1$ has revealed to be quite difficult, and the improvements brought during this doctoral work are still insufficient to perform sufficient OM cooling. The main limitations are thermo-optic instability and residual optical absorption in our high Q_{opt} resonators. However, attaining a value of $\sim 10^5$ for Q_{m} should allow, with all other parameters at our state of the art, to cool under the symbolic one phonon limit. Table 7.1 shows theoretical phonon numbers attained for the best detuning $\Delta = \omega_{\text{L}} - \omega_0$ in different cases. The disk dimension on which we invested most efforts is R=1.3 µm. Having 13 000 photons circulating in the system is feasible (it is the number of photons injected in the system for the maximum power in figure 7.6). The mechanical quality factors reached $2 \cdot 10^4$ in this work using mechanical shields, but the deleterious ICP etching effects impact the Q_{opt} which drops to $\sim 3 \cdot 10^4$. The best optical quality factors of $\sim 3 \cdot 10^5$ (for disks of 1.3 µm radius) were only measured on simple disks (without MS). Reaching both states of the art for optical and mechanical quality factors on a same optomechanical device was not yet achieved, and efforts are currently made to overcome this problem, with further optimization of the e-beam resist exposure and ICP etching step.

R(µm)	T(nm)	λ_0(nm)	Q_{opt}	f_{m}(GHz)	Q_{m}	$\frac{g_0}{2\pi}$(MHz)	N_{phot}	$\bar{n}_{\text{cooled}}$
0.6	250	970	10^5	2.3	10^5	13.3	10000	0.1
1.3	320	1550	$3 \cdot 10^5$	2.8 (RBM2)	10^5	2	13000	0.07
5	200	1550	$3 \cdot 10^6$	0.282	10^5	0.211	10^5	0.09

Table 7.1 – Minimal attainable phonon number after cooling $\bar{n}_{\text{cooled}}$ for different disk sizes. For each disk size, the parameters used to calculate $\bar{n}_{\text{cooled}}$ are listed. T is the disk thickness.

7.5 Optomechanically induced transparency

7.5.1 Principle

The standard technique used to derive the mechanical properties of the system is to analyze the spectral information of the transduced optical signal, as was explained in §1.1.2[4]. OMIT is a complementary technique, based on the use of a modulated laser source, which allows to extract information about the mechanical oscillator.

The general procedure for an OMIT measurement is the following: a strong laser beam with pulsation ω_{L} is sent with a detuning Δ from the cavity resonance ω_0: $\Delta = \omega_{\text{L}} - \omega_0$. While this strong laser beam – the *pump* – is kept at a constant pulsation, a second, weak laser beam – the *probe*, pulsation ω_{p} – is swept across the cavity resonance. Pump and probe beams must be optically coherent, in practice the probe will be a sideband of the pump obtained by modulation. If the pump is off, then the scan performed with the probe should reveal the well known Lorentzian shape of the optical cavity. However, the presence of the pump modifies the dynamics of the optomechanical system and a very narrow transparency window is observed at a probe pulsation verifying: $\omega_{\text{p}} - \omega_{\text{L}} = \pm\Omega_{\text{m}}$.

The origin of this transparency window can be intuitively understood in the following way: probe and pump beams are coherent and therefore beat with each other at a pulsation $\Omega = \omega_{\text{p}} - \omega_{\text{L}}$. The intensity within the cavity, and therefore the radiation pressure force, evolves with a pulsation Ω. As long as $|\Omega - \Omega_{\text{m}}| \gtrsim \Gamma_{\text{m}}$, this pulsating force does not excite the mechanical mode of the system (the drive is off-resonance). The transmission of the probe is the Lorentzian shape expected from a *static* optical cavity. Now when $|\Omega - \Omega_{\text{m}}| \lesssim \Gamma_{\text{m}}$, the mechanical mode is driven resonantly and the mechanical oscillation amplitude rises to high values if Q_{m} is high. This large mechanical oscillation

[4]This explanation in however limited to the bad cavity limit case, a more general expression is derived in §5.4.1

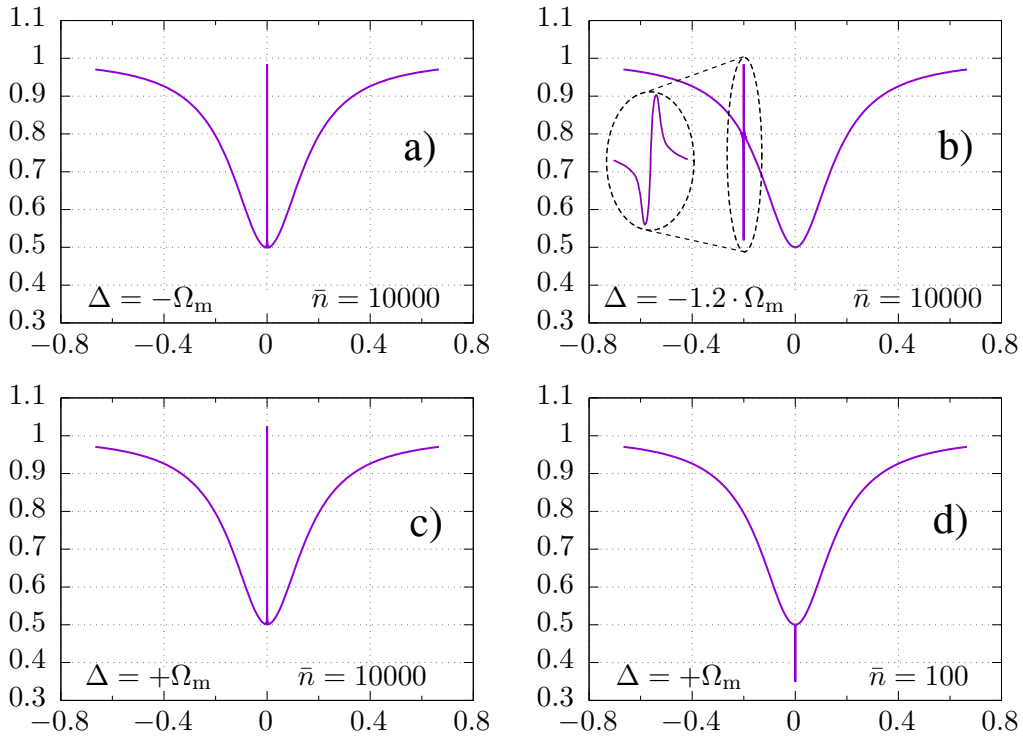

Figure 7.10 – OMIT spectra for different configurations. The transmission of the probe T_p is plotted against $(\omega_p - \omega_0)/\Omega_m$. The optomechanical system parameters are: $\kappa/2\pi$=1 GHz, $\Omega_m/2\pi$=3 GHz, $g0/2\pi$=200 kHz, Q_m=10^5. This curves are plotted using formula 7.12.

modulates in turn, via the optomechanical coupling, the intensity of the field *within the cavity* with a pulsation Ω_m. This modulation creates two sidebands of the intracavity field, respectively at $\omega_L - \Omega_m$ and $\omega_L + \Omega_m$. In the red detuning case ($\Delta < 0$), the upper sideband ($\omega_L + \Omega_m$) and the probe have the same frequency[5], and interfere with each other. This interference, if destructive, has for consequence that no optical field at $\omega_p = \omega_L + \Omega_m$ can build up in the optical cavity. The cavity therefore cannot dissipate any energy and the transmission T_p at ω_p is 100%, hence the transparency window.

Figure 7.10 displays several transmission curves of the probe beam for different configurations:

- **(a)**: the pump beam is detuned by $\Delta = -\Omega_m$, i.e. it is located at an abscissa of -1 (out of the graph limits). A very narrow transparency window can observed for $\omega_p = \omega_0$, where the transmission almost reaches 1.

- **(b)**: the pump is now detuned further to the left. As was mentioned earlier, the excitation of the mechanical oscillator happens when $\omega_p - \omega_L \approx \Omega_m$, which does not correspond to $\omega_p = \omega_0$ if $\omega_0 - \omega_L \neq \Omega_m$. This is the case here, and the OMIT feature can be seen to happen on the flank of the optical resonance. Interestingly, it is not a transparency nor an absorption window anymore, but rather a combination of the two, taking the form of a dispersive Fano resonance.

- **(c)**: on this graph the pump is detuned by $\Delta = +\Omega_m$. The *transparency* window still exists, but this time the transmission can be seen to reach a value slightly above 1. Indeed, the sidebands created by the modulation of the pump photons by the mechanical motion can have an amplitude larger than that of the probe if the mechanical motion is large enough. Therefore the transmission, which is normalized to the probe beam intensity away from the

[5] $|\Omega - \Omega_m| \lesssim \Gamma_m \equiv \omega_p \approx \omega_L + \Omega_m$, because $\Gamma_m \ll \Omega_m, \omega_L$

cavity optical resonance, can reach values higher than 1. We see that OMIT can therefore be used to perform *coherent* amplification of weak signals.

- **(d)**: the pump is still at positive detuning but now we use a lower phonon number. The result is an *absorption* peak instead of the transmission peak obtained earlier. The reason is that probe and sideband are now interfering *constructively* in the disk. The sideband therefore helps the probe to interfere *destructively* with itself at the *output* of the optomechanical system, locally increasing the contrast.

The intuitive explanation provided above allows to understand the following dependence of the OMIT peak with the optomechanical system parameters:

- The amplitude of the OMIT peak increases with g_0 and Q_m. Indeed, a higher Q_m corresponds to a larger amplitude of the driven mechanical mode, and a larger optomechanical coupling constant (g_0) leads to a stronger optical modulation for a given mechanical motion.
- The width of the OMIT peak is equal to $\Gamma_\mathrm{m}+\Gamma_\mathrm{om}$, with $|\Gamma_\mathrm{om}| \approx 4g_0^2\bar{n}/\kappa$, with a sign depending on the detuning. We see that the peak width therefore depends on g_0 and on the photon number launched in the cavity.

A detailed treatment of the calculations that yield the full OMIT trace analytic formula can be found in the supplements of [75]. The main idea is to write the input field to the cavity as: $s_\mathrm{in}(t) = e^{-i\omega_\mathrm{L}t}(\bar{s}_\mathrm{in} + \delta s_\mathrm{in}(t))$, with $\delta s_\mathrm{in}(t) = s_\mathrm{p}e^{-i\Omega t}$ ($\Omega \equiv \omega_\mathrm{p} - \omega_\mathrm{L}$), and to solve for the response of the system to the perturbation $\delta s_\mathrm{in}(t)$ with the ansatz: $\delta a(t) = A^- e^{-i\Omega t} + A^+ e^{+i\Omega t}$. One finally finds the transmission for the probe to be:

$$T_\mathrm{p} = \left| 1 - \frac{1 + if(\Omega)}{-i(\Delta+\Omega) + \kappa/2 + 2\Delta f(\Omega)} \right|^2 \qquad (7.12)$$

$$\text{with} \quad f(\Omega) = \frac{\hbar g_0^2 \bar{n}}{m_\mathrm{eff} x_\mathrm{ZPF}} \frac{(\Omega_\mathrm{m}^2 - \Omega^2 - i\Omega\Gamma_\mathrm{m})^{-1}}{i(\Delta-\Omega) + \kappa/2}$$

The above formula is not entirely exact, because in the calculation only one of the two sidebands generated in the cavity is taken into account. This approximation is valid in the good cavity limit. Indeed, in this regime, the other sideband is far off-resonance (see figure 7.11), such that it cannot buildup in the cavity and interfere significantly with the probe beam. Another limitation of formula 7.12 is that only one of the two probes is considered. Experimentally, however, the creation of a coherent probe at $\omega_\mathrm{L} + \Omega$ automatically induces the creation of another one at $\omega_\mathrm{L} - \Omega$, as will be shown in the next section. The sum of the transmissions for both probes must therefore be taken into account to get the overall transmission. A derivation of the formula that takes the two probes into account can be found in E. It is this latter formula that will be used to fit the experimental data in the next sections.

7.5.2 Experimental setup

The first requirement in order to perform OMIT experiments is the ability to generate a weak probe signal, detuned from the laser main frequency, and *coherent* with it. We use an EOM (see §5.5). Such a device modulates the intensity, (or the phase) of the laser beam passing through it. In the case of amplitude modulation, the output of the EOM, when a electric signal of pulsation $\Omega \ll \omega_\mathrm{L}$ is sent to it is:

$$E_\mathrm{out} = E_0 \cos(\omega_\mathrm{L}t)[1/2 + \beta\cos(\Omega t)] \qquad (7.13a)$$

$$= \frac{1}{2}E_0\cos(\omega_\mathrm{L}t) + \frac{E_0\beta}{2}\{\cos[(\omega_\mathrm{L}+\Omega)t] + \cos[(\omega_\mathrm{L}-\Omega)t]\} \qquad (7.13b)$$

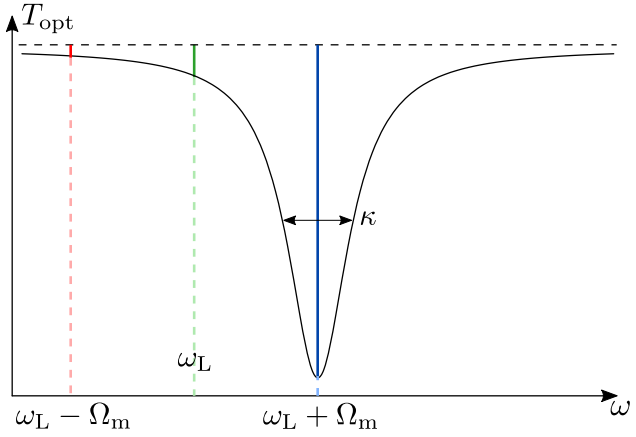

Figure 7.11 – Sideband intensity asymmetry for a system barely in the good cavity limit ($\Omega_{\mathrm{m}} \gtrsim \kappa$), pumped with a laser (green line) detuned from cavity resonance by Ω_{m}. The strong asymmetry between red and blue sidebands will be further enhanced for systems more deeply in the good cavity limit.

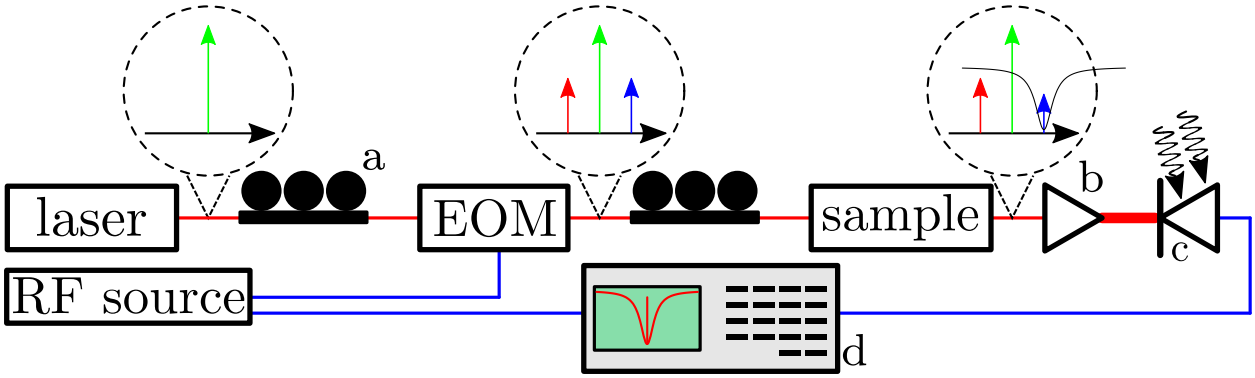

Figure 7.12 – OMIT experimental setup. **a**: Polarization control. **b**: EDFA optical amplifier. **c**: Fast photo-diode. **d**: Electronic spectrum analyzer. **Red lines**: optical fiber. **Blue lines**: electric coaxial cable. A RF source drives the EOM at frequency Ω, creating two sidebands in the optical field at frequencies $\omega_{\mathrm{L}} \pm \Omega$. After going through the sample, the blue sideband's weight is changed according to the optical cavity transmission $T_{\mathrm{p}}(\Omega)$. The beating amplitude of the blue sideband with the main laser beam therefore changes with Ω. For each Ω, the RF source sends its frequency as reference to the spectrum analyzer, which will then look for the beating power in a very narrow bandwidth (a few 10s of Hz) around Ω. The trace of the this beating power as a function of Ω therefore reconstructs the OMIT response.

We therefore notice the appearance of two sidebands at pulsations $\omega_{\mathrm{L}} + \Omega$ and $\omega_{\mathrm{L}} - \Omega$. In the case of phase modulation, it can be shown that two sidebands at same frequencies are also created. Figure 7.12 shows the experimental setup used for OMIT measurements. At the sample output, two different methods can be used to retrieve the blue sideband amplitude:

- The first method consists in filtering out the laser pump with a narrow optical filter. The optical intensity impinging on the photo-diode is therefore the square of the transmitted sidebands amplitude. Filtering is necessary because of energy conservation: the sum of pump and sideband energies being unchanged, if one wants to quantify an energy transfer from the pump to one of the sidebands, the pump must be filtered out. Such a technique avoids the use of a spectrum analyzer and of any fast electronic components (it could therefore be possible to use slow photo-diodes with a high trans-impedance gain). All-fibered optical filters with a linewidth under 50 MHz are readily available for purchase.

- The second method consists in measuring the beating of the sidebands with the pump. This beating, for our system, happens at GHz frequencies and can therefore be followed with a fast photo-diode. The power density of the beating is then detected by a spectrum analyzer, as

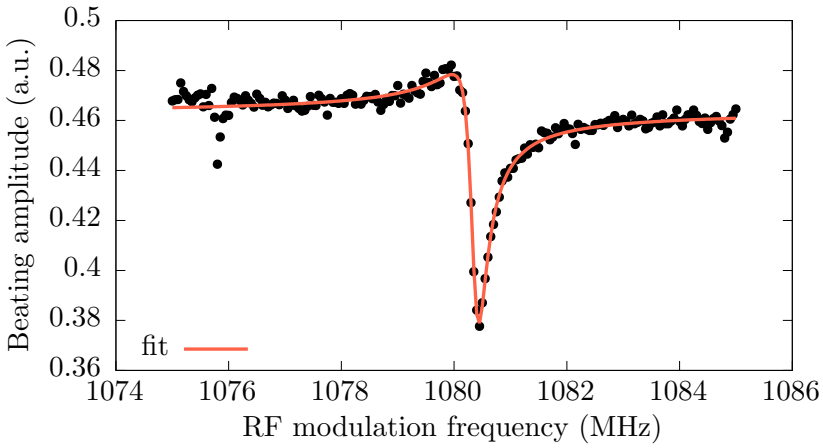

Figure 7.13 – Experimental OMIT trace around the mechanical resonance at ∼1.08 GHz. The pump is blue detuned from the cavity resonance: $\Delta = \Omega_m$. The little peak at 1076 MHz is an artifact that was not taken into account in the fit.

explained in figure 7.12. A nice feature of this technique is that the intensity of the beating component is equal to[6] $\sqrt{I_p I_s}$, which is greater than I_s, because $I_p > I_s$.

7.5.3 Experimental results

Although operation in the good cavity limit is not necessary in order to see OMIT, it simplifies the situation because of the generation of the two probes inherent to the use of an EOM. Indeed, in the good cavity limit, the transmission of the red probe is roughly constant (see figure 7.11[7]), so it does not need to be taken into account.

Operating in resolved sideband regime requires that we fabricate structures with $Q_{opt} \gtrsim 200\,000$. Unfortunately we have been unable to obtain these Q_{opt} on mechanically shielded structures, because the longer ICP process supposedly increases upper disk irregularities and asymmetries. The results shown below therefore correspond to MS structures, with a high Q_m but operating in the bad cavity limit. We preferred such a system because the strength of the OMIT peak depends on Q_m. As such a system does not operate in the good cavity limit, a generalized formula which takes both probes into account was used for the curve fitting displayed in the following figures (see appendix E).

Figure 7.13 displays an experimental omit trace obtained with a blue detuned pump. Although we observed OMIT with a red detuned pump (see figure 7.14), the amplitude of the OMIT peak was lower because of the limited pump power affordable before triggering thermo-optic instability. Figure 7.13 therefore displays an OMIT absorption window with high signal to noise ratio on a tiny dispersive Fano feature. The model can be seen to fit accurately the data. Figure 7.14 displays experimental OMIT traces for blue and red detuning. The inversion from transparency to absorption in the OMIT window can be observed.

Figures 7.15 shows OMIT absorption windows for different laser powers, but constant detuning on the blue flank. Figure 7.16 is the inverse: the power is kept constant but the detuning is changed, this time on a 2nd order RBM close to 3 GHz. The fits of the traces from figure 7.15 allowed to extract the values shown in table 7.2. For the maximum guide power of 113 µW, a cooperativity of $C = 26$ is achieved.

[6] I_p ans I_s are the intensities of the pump and the sideband, respectively.

[7] note that figure 7.11 is used here to picture the probes transmission asymmetry, although it was design originally to represent the buildup factor asymmetry of the sidebands that are generated *inside the cavity*.

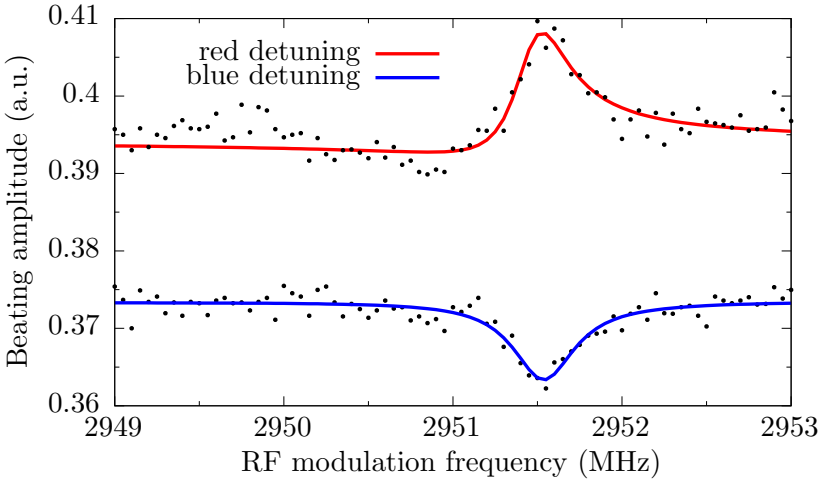

Figure 7.14 – OMIT transmission measured with red and blue detuning. A peak can be observed for red detuning, as predicted by theory.

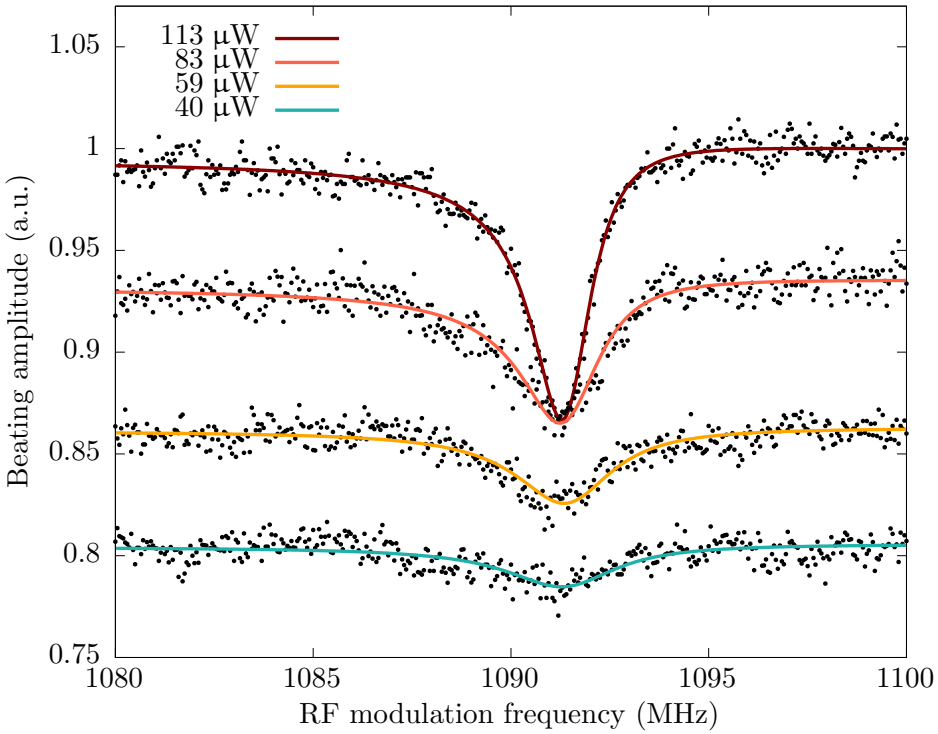

Figure 7.15 – Experimental OMIT traces near the RBM1 resonance frequency at 1092 MHz for different laser powers. The pump detuning is constant at $\Delta = +\Omega_m$ (bottom right graph in figure 7.10). The OMIT dip is more pronounced as the power is increased.

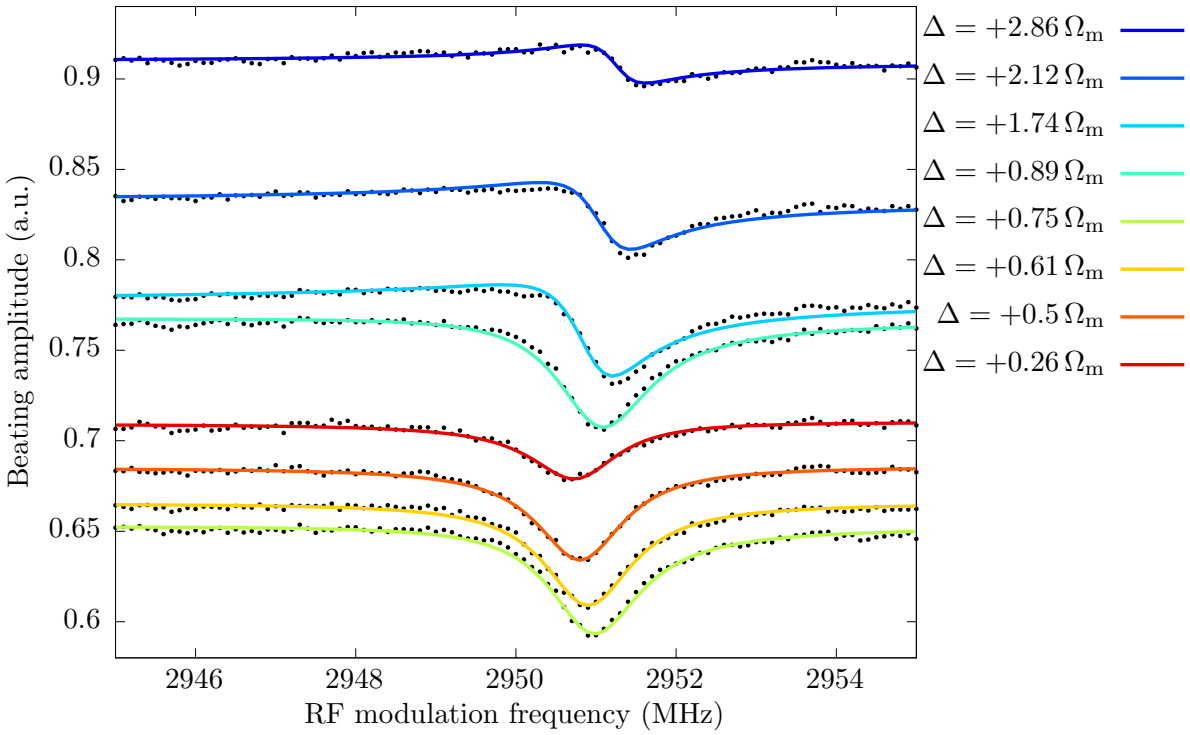

Figure 7.16 – Experimental OMIT traces near the RBM2 resonance frequency at 2951 MHz for different pump detunings. The laser power is kept constant at 255 µW. The skewed shapes correspond to detunings far from Ω_m and are predicted by the model.

P_{laser} (µW)	Q_{opt}	Q_m	Ω_m (GHz)	g_0 (MHz)	N_{cav}	C
40	230 000	264	1.09	1.5	1070	3
59	230 000	264	1.09	1.5	2020	5.6
83	230 000	264	1.09	1.5	4400	12
113	230 000	264	1.09	1.5	9500	26.5

Table 7.2 – System parameters extracted from the fits in figure 7.15.

This chapter reviewed several optomechanical experiments that can be performed at cryogenic temperatures. One of the main goals of this doctoral work was to achieve quantum ground state cooling. This goal is approached but not fulfilled yet, many perspectives are nevertheless left in order to fabricate devices with enhanced figures of merit.

Conclusion

This doctoral work has been focused on the design, fabrication, characterization and operation of nano-resonators optimized for optomechanical cooling, i.e. extraction of mechanical quanta via the interaction between optical and mechanical degrees of freedom. The main goal of this work was to achieve ground state cooling, where the occupancy of the mechanical system is in average less than one. Such an achievement necessitates devices of high quality (low roughness, high material purity, optimized surfaces, precision of dimensions) so that the following figures of merit are maximized:

– the optical quality factor Q_{opt}
– the mechanical quality factor Q_{m}
– the mechanical frequency f_{m}
– the optomechanical coupling constant g_0
– the number of photons N_{cav} in the cavity
– optical injection/collection efficiency T_{opt}

Some other figures of merit impact the cooling performance but are independent from the device:

– the cryostat bath temperature T_{bath}
– the performance of the detection system
– the laser noise
– the stability of the overall setup

The figures of merit of the best devices fabricated in our team as of today do not allow to cool to the ground state yet. Some perspectives intended at enhancing the figures of merit of our devices are listed below.

- $\boldsymbol{Q_{\mathrm{opt}}}$**:** Thanks to a good control of e-line resist reflow and to ALD, quality factors as high as $3 \cdot 10^5$ were measured on on 1 µm radius disks and $5 \cdot 10^6$ on 5 µm radius disks. This stands close to the state of the art in terms of $Q_{\mathrm{opt}}/\mathrm{V}$ (V is the mode volume). Unfortunately, this Q_{opt} level cannot be achieved on devices *with* mechanical shield (which are the devices that show the best Q_{m}) because the mask gets damaged during the long ICP etch. Some possibilities would be to use hydrogen silsesquioxane (HSQ) based resists, which provide better hardness than Ma-N resists, or to transfer the Ma-N pattern to a hard mask made of silica or SiN.

- $\boldsymbol{Q_{\mathrm{m}}}$**:** Mechanical shields have enhanced Q_{m} of produced devices already, but they have not shown their full potential yet. We believe the main reason is a slight departure of the fabricated structures dimensions from the ones obtained from simulations. The use of a hard mask (see previous bullet) would allow to explore new sets of ICP etching parameters, in particular recipes with higher power, which should yield straighter flanks, i.e. more regular structures. Additionally, a shift from $Al_{0.8}Ga_{0.2}As$ to $Al_{0.5}Ga_{0.5}As$ could reduce ICP lateral undercutting effects which affect the dimensions and shape of the shield. Liquid HF under-etching on $Al_{0.8}Ga_{0.2}As$ produced some irregular pedestals, so the etching of $Al_{0.5}Ga_{0.5}As$ should be tried. Another technique that should be tested is vapor HF etching. It has been reported to etch silica in a reproducible and anisotropic fashion [61]. Unfortunately no trial on AlGaAs has been reported yet, so we will have to try it for ourselves.

- **f_m & g_0:** These two parameters depend essentially on the disk radius and on the RBM order that is measured. Fabrication of ultimately small disks would allow to push f_m and g_0 respectively to 2.5 GHz and 20 MHz, but at the cost of a Q_{opt} and Q_m reduction. Another approach is to optimize the mechanical shield to yield high Q_m on RBM orders > 1. The mechanical frequency is thus enhanced, but g_0 generally decays. 2^{nd} order RBM devices have been fabricated during this work and characterized quite successfully, but raising the RBM to 3^{rd} is not interesting according to simulations.

- **N_{phot}:** The maximum number of photons that can be input to the optical cavity *in red detuned operation* impacts the cooling power linearly. ALD, by reducing the optical absorption, allows to send more power in the disk before the red flank instability is triggered (see §7.2.2). Another way to limit the disk temperature increase is to enhance the disk's thermal dissipation to the substrate, with the use of a wide pedestal. High Q_m and wide pedestals are compatible via the use of mechanical shields.

- **T_{opt}:** The optical transmission through the sample was raised to high values with the development of FSW during this doctoral work, with full transmission through the setup reaching 25% (50% of transmission efficiency on both input and output ports). This is close to the state of the art for nanophotonics, so we do not aim at increasing this figure further for now. However, for MS structures, the presence of a duplicate waveguide just under the top waveguide of interest can perturb the transmission efficiency. Techniques to remove this duplicate waveguide must therefore be found (see figure 4.20).

One of the possible follow-ups on quantum ground state cooling would be the preparation of two macroscopic entangled mechanical states [76, 77, 78]. The interest would reside in the fact that although quantum mechanics have been very successful in predicting the behavior of microscopic systems, macroscopic manifestations are still scarce, and entanglement of macroscopic mechanical systems has not been observed yet.

The setup proposed in ref. [76] is schematized in figure 7.17. Laser radiation impinges simultaneously on two independent optomechanical cavities (the mechanical system is a membrane that can move within the optical cavity). The outputs of the OM cavities are then combined on a 50-50 beam splitter, from which two paths emerge. For each of the paths a filter is positioned, which redirects red or blue scattered photons on two different photomultipliers depending on the photon frequency. The non-shifted laser photons are blocked by the filters.

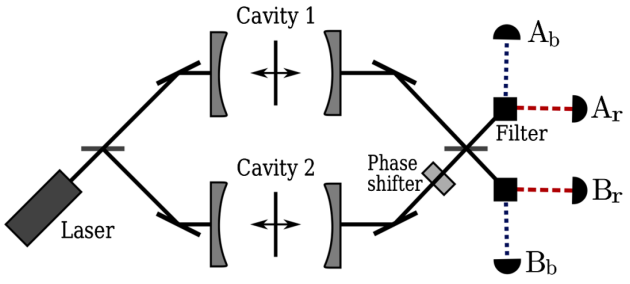

Figure 7.17 – Setup for measurement of two entangled mechanical systems.

Let us suppose that the ensemble of both OM systems is in the mechanical state $|0\rangle \otimes |0\rangle$. If a red-detuned photon is then detected on detector A_r, it means that one of the two mechanical oscillators has red-scattered one of the laser photons and therefore acquired one quantum of mechanical energy. However, because of the probabilistic nature of photon interactions with the beam splitter, it is not possible to know which mechanical oscillator did so. Indeed, the red-detuned photon could come from cavity 1 and then reflect on the beam splitter, or it could come from cavity 2 and then be transmitted through the beam splitter. The state of the mechanical system after such a

measurement is therefore $|0\rangle \otimes |1\rangle + |1\rangle \otimes |0\rangle$, which is a typical entangled state. Naturally this experiment is idealized, in real experiments:

- Both oscillators cannot be prepared in the exact ground state because of mechanical dissipation to the substrate. The state achieved on each oscillator is therefore a statistical mixture, with a certain *probability* to be in the ground state only.
- A sideband photon created in one of the optomecanical cavities is not necessarily detected by one of the 4 photomultipliers. Indeed the path linking the cavities to the photodetectors is lossy and therefore there is only a given probability that a generated sideband photon will be detected.

For these reasons the degree of entanglement achievable in such an experiment is only partial. This proposal however underlines the importance of controlling quantum ground state cooling for the realization of quantum experiments with mechanical oscillators, as well as the importance of high fidelity in optical experiments.

Glossary

$Q_{\mathbf{bend}}$ bending quality factor. 30–32, 100, 104

$Q_{\mathbf{clamp}}$ clamping loss quality factor. 41, 77, 99, 100, 102–112

$Q_{\mathbf{m}}$ mechanical quality factor. 37–40, 42, 74–76, 80, 81, 85, 100, 108, 110, 117, 122, 124, 126, 129, 130

$Q_{\mathbf{opt}}$ optical quality factor. 31, 32, 34, 35, 49, 50, 53, 62, 65–67, 74, 84, 86, 90, 104, 112–115, 122, 126, 129, 130

g_0 optomechanical coupling constant. 124

$g_{\mathbf{om}}$ optical frequency-pull parameter. 113

AFM atomic force microscope. 9

Al Aluminium. 9, 11

Al_2O_3 aluminum oxide. 34, 65, 81, 84

ALD atomic layer deposition. 34, 45, 65, 81, 84, 112, 117, 119, 120, 129, 130

AlGaAs aluminum gallium arsenide. 10, 35, 53, 54, 56, 59, 61, 64–66, 70, 73, 74, 76, 77, 79, 99–101, 103, 118, 129

AlN Aluminium Nitride. 9

AR anti reflection. 90

Ar argon. 64, 77

ASE amplified spontaneous emission. 97

BCK chemical etchant realized by isovolumic mixing of hydrobromic acid (H**B**r), acetic acid (**C**H_3COOH) and potassium dichromate (**K**$_2Cr_2O_7$) aqueous solutions. 69, 70, 72, 83

BRF bi-refringent filter. 91–93

CCW counter-clockwise. 33, 44

CMT coupled mode theory. 47–53

CO_2 carbon dioxide. 83

CW clockwise. 33, 44

DPSSL diode pumped solid state laser. 91

e-beam electron beam. 59–62, 64, 66–68, 74, 83, 104, 122

ECDL external cavity diode laser. 90, 91, 93, 94, 146

EDFA erbium doped fiber amplifier. 90, 97, 98, 114, 119, 125

EM electro-magnetic. 16, 18, 23–25, 28, 30, 31, 33, 42–44, 46, 47, 50, 51, 53, 54, 58, 101, 112, 141, 143

EOM electro-optic modulator. 85, 91, 98, 124–126, 146, 148

FBMS fixed beam moving stage. 62, 67

FDTD Finite Differences - Time Domain. 55–58

FEM finite element method. 27, 30–32, 37–43, 45, 51–53, 100, 103, 107, 112, 117, 141–143

FPC fiber polarization controller. 85, 86

FSR free spectral range. 19, 54, 91, 92

FSW fully suspended waveguide. 53, 55–59, 62, 67–69, 73, 82, 108, 130

FWHM full width at half maximum. 14, 23, 35, 41, 54, 96

GaAs gallium arsenide. 5, 10, 11, 25, 28, 29, 31, 33–38, 40–46, 49–54, 56, 57, 59–68, 70, 72, 74, 76, 77, 79, 82, 84, 90, 101–103, 111, 117

HF hydrofluoric acid. 54, 60, 61, 65–67, 69, 73, 74, 76, 77, 79–81, 83, 100, 103, 104, 109, 129

HSQ hydrogen silsesquioxane. 129

ICP inductively coupled plasma. 6, 52, 63–67, 72, 74–78, 80, 83, 84, 100, 103, 104, 108, 109, 122, 126, 129

InGaAs Indium Gallium Arsenide. 10

KOH potassium hydroxide. 66

$LiNbO_3$ lithium niobate. 98

LW long waveguide. 53–57, 59, 61, 62, 67, 108

MBE molecular beam epitaxy. 32

MEMS micro electro-mechanical systems. 39, 80

MS mechanically shielded. 54–56, 58, 59, 74–82, 84, 99, 102, 103, 105, 108–111, 122, 126, 130

N_2 nitrogen. 77, 81, 82, 100

NA numerical aperture. 69, 86

NEP noise equivalent power. 96–98

NF noise figure. 97

NH_4-OH ammonium hydroxide. 84

O_2 oxygen. 66, 67, 77, 78, 84

OM optomechanical. 11–14, 16–26, 28, 29, 32, 36, 39, 42–45, 59, 61, 65, 66, 68, 84–86, 90, 91, 94–96, 98, 99, 101, 102, 104, 110, 111, 113, 120–122, 130, 148

OMIT optomechanically induced transparency. 85, 122–128

OMs optomechanics. 12, 23, 29, 89, 90

PAC photo-active compound. 61

PDE partial differential equation. 141–144

PhD philosophiæ doctor. 53, 76, 84

PID proportional integral derivative. 88

PML perfectly matched layer. 31, 41, 52, 143, 144

PTFE polytetrafluoroethylene. 71, 81

RBM radial breathing mode. 29, 37–40, 43, 44, 82, 99–101, 103, 104, 106–109, 111, 112, 114, 120, 121, 126–128, 130

RF radio frequency. 63–66, 72, 76, 125, 146

RIE reactive ion etching. 63, 66

RMS root mean square. 19, 32, 93

SEM scanning electron microscope. 10, 65–67, 73, 75, 76, 78, 79, 81, 84, 100, 109–112

$SiCl_x$ neutral, chemically reactive molecules resulting from collisions between $SiCl_4$ and electrons in the plasma. 64, 76

$SiCl_4$ silicon tetrachloride. 64, 76, 77

SiN silicon nitride. 11, 129

SiO_2 silicon dioxide. 79

SiO_x silicon oxide. 77

SNR signal to noise ratio. 58, 96–98

TE transverse electric. 29–32, 44, 50, 51, 57, 85

Ti:S titanium sapphire. 90, 91, 94

TM transverse magnetic. 29–32, 50, 51, 57, 85

TPA two photon absorption. 34, 35, 90, 114–117

UV ultra violet. 66, 68, 83, 84

WGM whispering gallery mode. 29–35, 42–44, 46–52, 54, 55, 85, 90, 91, 115, 144

Bibliography

[1] Ernest Fox Nichols and GF Hull. A preliminary communication on the pressure of heat and light radiation. *Physical Review (Series I)*, 13(5):307, 1901.

[2] VB Braginsky. Classical and quantum restrictions on the detection of weak disturbances of a macroscopic oscillator. *Zh. Eksp. Teor. Fiz*, 53:1434–1441, 1967.

[3] Vladimir Borisovich Braginsky and Anatoli Borisovich Manukin. Measurement of weak forces in physics experiments. 1977.

[4] Carlton M Caves. Quantum-mechanical radiation-pressure fluctuations in an interferometer. *Physical Review Letters*, 45(2):75, 1980.

[5] Aaron D O'Connell, Max Hofheinz, Markus Ansmann, Radoslaw C Bialczak, Mike Lenander, Erik Lucero, Matthew Neeley, Daniel Sank, H Wang, M Weides, et al. Quantum ground state and single-phonon control of a mechanical resonator. *Nature*, 464(7289):697–703, 2010.

[6] JD Teufel, Tobias Donner, Dale Li, JW Harlow, MS Allman, Katarina Cicak, AJ Sirois, Jed D Whittaker, KW Lehnert, and Raymond W Simmonds. Sideband cooling of micromechanical motion to the quantum ground state. *Nature*, 475(7356):359–363, 2011.

[7] Jasper Chan, TP Mayer Alegre, Amir H Safavi-Naeini, Jeff T Hill, Alex Krause, Simon Gröblacher, Markus Aspelmeyer, and Oskar Painter. Laser cooling of a nanomechanical oscillator into its quantum ground state. *Nature*, 478(7367):89–92, 2011.

[8] Daniel Ramos, Eduardo Gil-Santos, Valerio Pini, Jose M Llorens, Marta Fernández-Regúlez, Álvaro San Paulo, Montserrat Calleja, and Javier Tamayo. Optomechanics with silicon nanowires by harnessing confined electromagnetic modes. *Nano letters*, 12(2):932–937, 2012.

[9] Fenfei Liu, Seyedhamidreza Alaie, Zayd C Leseman, and Mani Hossein-Zadeh. Sub-pg mass sensing and measurement with an optomechanical oscillator. *Optics express*, 21(17):19555–19567, 2013.

[10] Kartik Srinivasan, Houxun Miao, Matthew T Rakher, Marcelo Davanco, and Vladimir Aksyuk. Optomechanical transduction of an integrated silicon cantilever probe using a microdisk resonator. *Nano letters*, 11(2):791–797, 2011.

[11] Alexander G Krause, Martin Winger, Tim D Blasius, Qiang Lin, and Oskar Painter. A high-resolution microchip optomechanical accelerometer. *Nature Photonics*, 6(11):768–772, 2012.

[12] Ignacio Wilson-Rae, Nima Nooshi, W Zwerger, and Tobias J Kippenberg. Theory of ground state cooling of a mechanical oscillator using dynamical backaction. *Physical Review Letters*, 99(9):093901, 2007.

[13] Florian Marquardt, Joe P Chen, AA Clerk, and SM Girvin. Quantum theory of cavity-assisted sideband cooling of mechanical motion. *Physical Review Letters*, 99(9):093902, 2007.

[14] Ewold Verhagen, Samuel Deléglise, Stefan Weis, Albert Schliesser, and Tobias J Kippenberg. Quantum-coherent coupling of a mechanical oscillator to an optical cavity mode. *Nature*, 482(7383):63–67, 2012.

[15] RW Peterson, TP Purdy, NS Kampel, RW Andrews, P-L Yu, KW Lehnert, and CA Regal. Laser cooling of a micromechanical membrane to the quantum backaction limit. *Physical review letters*, 116(6):063601, 2016.

[16] T Rocheleau, T Ndukum, C Macklin, JB Hertzberg, AA Clerk, and KC Schwab. Preparation and detection of a mechanical resonator near the ground state of motion. *Nature*, 463(7277):72–75, 2010.

[17] Mingyun Yuan, Vibhor Singh, Yaroslav M Blanter, and Gary A Steele. Large cooperativity and microkelvin cooling with a three-dimensional optomechanical cavity. *Nature communications*, 6, 2015.

[18] Juan Restrepo, Julien Gabelli, Cristiano Ciuti, and Ivan Favero. Classical and quantum theory of photothermal cavity cooling of a mechanical oscillator. *Comptes Rendus Physique*, 12(9):860–870, 2011.

[19] Constanze Metzger, Ivan Favero, Alexander Ortlieb, and Khaled Karrai. Optical self cooling of a deformable fabry-perot cavity in the classical limit. *Physical Review B*, 78(3):035309, 2008.

[20] Christopher Baker. *On-chip nano-optomechanical whispering gallery resonators*. PhD thesis, Université Paris Diderot - Laboratoire Matériaux et Phénomènes Quantiques, 2013.

[21] CK Law. Interaction between a moving mirror and radiation pressure: A hamiltonian formulation. *Physical Review A*, 51(3):2537, 1995.

[22] Juan Sebastián Restrepo. *Theory of quantum optomechanics with unconventional nonlinear coupling schemes*. PhD thesis, Université Paris Diderot, 2014.

[23] Warwick P Bowen and Gerard J Milburn. *Quantum optomechanics*. CRC Press, 2015.

[24] Gilbert Grynberg, Alain Aspect, and Claude Fabre. *Introduction to quantum optics: from the semi-classical approach to quantized light*. Cambridge university press, 2010.

[25] John David Jackson. *Classical electrodynamics*. Wiley, 1999.

[26] Robert E Newnham. *Properties of Materials: Anisotropy, Symmetry, Structure: Anisotropy, Symmetry, Structure*. OUP Oxford, 2004.

[27] Peter T Rakich, Paul Davids, and Zheng Wang. Tailoring optical forces in waveguides through radiation pressure and electrostrictive forces. *Optics express*, 18(14):14439–14453, 2010.

[28] Steven G Johnson, Mihai Ibanescu, MA Skorobogatiy, Ori Weisberg, JD Joannopoulos, and Yoel Fink. Perturbation theory for maxwell's equations with shifting material boundaries. *Physical review E*, 65(6):066611, 2002.

[29] Alessio Andronico. *Etude Électromagnetique d'émetteurs intégrés infrarouges et terahertz en AlGaAs*. PhD thesis, Université Paris Diderot - Laboratoire Matériaux et Phénomènes Quantiques, 2008.

[30] David Parrain. *Optomécanique fibrée des disques GaAs : dissipation, amplification et nonlinéarités*. PhD thesis, Université Paris Diderot - Laboratoire Matériaux et Phénomènes Quantiques, 2014.

[31] VL Berkovits, D Paget, AN Karpenko, VP Ulin, and OE Tereshchenko. Soft nitridation of gaas (100) by hydrazine sulfide solutions: Effect on surface recombination and surface barrier. *Applied physics letters*, 90(2):022104, 2007.

[32] Gijs Dingemans and WMM Kessels. Status and prospects of al2o3-based surface passivation schemes for silicon solar cells. *Journal of Vacuum Science & Technology A*, 30(4):040802, 2012.

[33] Biswarup Guha, Felix Marsault, Fabian Cadiz, Laurence Morgenroth, Vladimir Ulin, Vladimir Berkovitz, Aristide Lemaïtre, Carmen Gomez, Alberto Amo, Sylvian Combrié, Bruno Gérard, Giuseppe Leo, and Ivan Favero. Surface-enhanced gallium arsenide photonic resonator with a quality factor of six million. *arXiv preprint arXiv:1605.00477*, 2016.

[34] Walter C Hurlbut, Yun-Shik Lee, KL Vodopyanov, PS Kuo, and MM Fejer. Multiphoton absorption and nonlinear refraction of gaas in the mid-infrared. *Optics letters*, 32(6):668–670, 2007.

[35] Srini Krishnamurthy, Zhi Gang Yu, Leonel P Gonzalez, and Shekhar Guha. Temperature-and wavelength-dependent two-photon and free-carrier absorption in gaas, inp, gainas, and inasp. *Journal of Applied Physics*, 109(3):033102, 2011.

[36] Sivia Mariani. *Three-wave mixing in semiconductor whispering gallery mode microcavities*. PhD thesis, Université Paris Diderot, 2014.

[37] Augustus Edward Hough Love. *A treatise on the mathematical theory of elasticity*, volume 1. Cambridge University Press, 2013.

[38] Morio Onoe. Contour vibrations of isotropic circular plates. *the Journal of the Acoustical Society of America*, 28(6):1158–1162, 1956.

[39] JS Blakemore. Semiconducting and other major properties of gallium arsenide. *Journal of Applied Physics*, 53(10):R123–R181, 1982.

[40] Markus Aspelmeyer, Tobias J Kippenberg, and Florian Marquardt. Cavity optomechanics. *Reviews of Modern Physics*, 86(4):1391, 2014.

[41] Lev D Landau and JB Sykes. Fluid mechanics: Vol 6. 1987.

[42] D Parrain, C Baker, T Verdier, P Senellart, A Lemaitre, S Ducci, G Leo, and I Favero. Damping of optomechanical disks resonators vibrating in air. *Applied Physics Letters*, 100(24):242105, 2012.

[43] E Gil-Santos, C Baker, DT Nguyen, W Hease, C Gomez, A Lemaître, S Ducci, G Leo, and I Favero. High-frequency nano-optomechanical disk resonators in liquids. *Nature nanotechnology*, 2015.

[44] Zhili Hao and Farrokh Ayazi. Support loss in the radial bulk-mode vibrations of center-supported micromechanical disk resonators. *Sensors and Actuators A: Physical*, 134(2):582–593, 2007.

[45] P Mohanty, DA Harrington, KL Ekinci, YT Yang, MJ Murphy, and ML Roukes. Intrinsic dissipation in high-frequency micromechanical resonators. *Physical Review B*, 66(8):085416, 2002.

[46] Quirin P Unterreithmeier, Thomas Faust, and Jörg P Kotthaus. Damping of nanomechanical resonators. *Physical review letters*, 105(2):027205, 2010.

[47] Hermann A Haus. Waves and fields in optoelectronics. 1983.

[48] C Manolatou, MJ Khan, Shanhui Fan, Pierre R Villeneuve, HA Haus, and JD Joannopoulos. Coupling of modes analysis of resonant channel add-drop filters. *Quantum Electronics, IEEE Journal of*, 35(9):1322–1331, 1999.

[49] Emmanuel Rosencher and Borge Vinter. *Optoelectronics*. Cambridge University Press, 2002.

[50] JD Love, WM Henry, WJ Stewart, RJ Black, S Lacroix, and F Gonthier. Tapered single-mode fibres and devices. i. adiabaticity criteria. In *Optoelectronics, IEE Proceedings J*, volume 138, pages 343–354. IET, 1991.

[51] P Kumar, S Kanakaraju, and DL DeVoe. Sacrificial etching of $Al_xGa_{1-x}As$ for III–V MEMS surface micromachining. *Applied Physics A*, 88(4):711–714, 2007.

[52] F Reinhardt, B Dwir, and E Kapon. Oxidation of gaas/algaas heterostructures studied by atomic force microscopy in air. *Applied physics letters*, 68(22):3168–3170, 1996.

[53] Alexander Gondarenko, Jacob S Levy, and Michal Lipson. High confinement micron-scale silicon nitride high q ring resonator. *Optics express*, 17(14):11366–11370, 2009.

[54] Vincent M Donnelly and Avinoam Kornblit. Plasma etching: Yesterday, today, and tomorrow. *Journal of Vacuum Science & Technology A*, 31(5):050825, 2013.

[55] UK Khankhoje, Se-Heon Kim, BC Richards, J Hendrickson, J Sweet, JD Olitzky, G Khitrova, HM Gibbs, and Axel Scherer. Modelling and fabrication of gaas photonic-crystal cavities for cavity quantum electrodynamics. *Nanotechnology*, 21(6):065202, 2010.

[56] Sadao Adachi. Chemical etching of inp and ingaasp/inp. *Journal of The Electrochemical Society*, 129(3):609–613, 1982.

[57] Gyorgy A Porkolab, Paveen Apiratikul, Bohan Wang, SH Guo, and Christopher JK Richardson. Low propagation loss algaas waveguides fabricated with plasma-assisted photoresist reflow. *Optics express*, 22(7):7733–7743, 2014.

[58] Laurent Jalabert, Pascal Dubreuil, Franck Carcenac, Sébastien Pinaud, Ludovic Salvagnac, Hugues Granier, and Chantal Fontaine. High aspect ratio gaas nanowires made by icp-rie etching using cl 2/n 2 chemistry. *Microelectronic Engineering*, 85(5):1173–1178, 2008.

[59] Maïté Volatier, David Duchesne, Roberto Morandotti, Richard Ares, and Vincent Aimez. Extremely high aspect ratio gaas and gaas/algaas nanowaveguides fabricated using chlorine icp etching with n2-promoted passivation. *Nanotechnology*, 21(13):134014, 2010.

[60] A Crockett, M Almoustafa, and W Vanderlinde. Plasma delayering of integrated circuits. *Microelectronics Failure Analysis Desk Reference*, 4:243–25, 2004.

[61] Yamato Fukuta, Hiroyuki Fujita, and Hiroshi Toshiyoshi. Vapor hydrofluoric acid sacrificial release technique for micro electro mechanical systems using labware. *Japanese journal of applied physics*, 42(6R):3690, 2003.

[62] Niels Tas, Tonny Sonnenberg, Henri Jansen, Rob Legtenberg, and Miko Elwenspoek. Stiction in surface micromachining. *Journal of Micromechanics and Microengineering*, 6(4):385, 1996.

[63] William E Gifford and RC Longsworth. Pulse-tube refrigeration. *Journal of Engineering for Industry*, 86(3):264–268, 1964.

[64] http://www.attocube.com/attomotion/premium-line/introduction/#tab-2.

[65] Arthur L Schawlow and Charles H Townes. Infrared and optical masers. *Physical Review*, 112(6):1940, 1958.

[66] KJ Weingarten, B Braun, and U Keller. In situ small-signal gain of solid-state lasers determined from relaxation oscillation frequency measurements. *Optics letters*, 19(15):1140–1142, 1994.

[67] Carl E Wieman and Leo Hollberg. Using diode lasers for atomic physics. *Review of Scientific Instruments*, 62(1):1–20, 1991.

[68] Eric D Black. An introduction to pound–drever–hall laser frequency stabilization. *American Journal of Physics*, 69(1):79–87, 2001.

[69] Tobias J Kippenberg, Albert Schliesser, and ML Gorodetsky. Phase noise measurement of external cavity diode lasers and implications for optomechanical sideband cooling of ghz mechanical modes. *New Journal of Physics*, 15(1):015019, 2013.

[70] Amir H Safavi-Naeini, Jasper Chan, Jeff T Hill, Simon Gröblacher, Haixing Miao, Yanbei Chen, Markus Aspelmeyer, and Oskar Painter. Laser noise in cavity-optomechanical cooling and thermometry. *New Journal of Physics*, 15(3):035007, 2013.

[71] Lawrence Davis. Handbook of genetic algorithms. 1991.

[72] Dac Trung Nguyen, Christophe Baker, William Hease, Selsabil Sejil, Pascale Senellart, Aristide Lemaitre, Sara Ducci, Giuseppe Leo, and Ivan Favero. Ultrahigh q-frequency product for optomechanical disk resonators with a mechanical shield. *Applied Physics Letters*, 103(24):241112, 2013.

[73] Dac Trung Nguyen, William Hease, Christopher Baker, Eduardo Gil-Santos, Pascale Senellart, Sara Ducci, Giuseppe Leo, Ivan Favero, et al. Improved optomechanical disk resonator sitting on a pedestal mechanical shield. *New Journal of Physics*, 17(2):023016, 2015.

[74] David G. Cahill, Wayne K. Ford, Kenneth E. Goodson, Gerald D. Mahan, Arun Majumdar, Humphrey J. Maris, Roberto Merlin, and Simon R. Phillpot. Nanoscale thermal transport. *Applied physics reviews*, 2002.

[75] Stefan Weis, Rémi Rivière, Samuel Deléglise, Emanuel Gavartin, Olivier Arcizet, Albert Schliesser, and Tobias J Kippenberg. Optomechanically induced transparency. *Science*, 330(6010):1520–1523, 2010.

[76] K Børkje, A Nunnenkamp, and SM Girvin. Proposal for entangling remote micromechanical oscillators via optical measurements. *Physical review letters*, 107(12):123601, 2011.

[77] Michael J Hartmann and Martin B Plenio. Steady state entanglement in the mechanical vibrations of two dielectric membranes. *Physical review letters*, 101(20):200503, 2008.

[78] Max Ludwig, K Hammerer, and Florian Marquardt. Entanglement of mechanical oscillators coupled to a nonequilibrium environment. *Physical Review A*, 82(1):012333, 2010.

Appendix A

Electrostriction: derivation of the striction pressure

Electrostriction can be apprehended as the tendency of optical forces to strain materials. To provide some insight we derive here the expression of the force induced by electrostriction in the simple case of a polarizable liquid. Consider a polarizable particle evolving in a field distribution (see figure A.1a). It can be easily proven that the force exerted on this particle is : $\mathbf{F} = \frac{1}{2}\varepsilon_0\alpha\nabla(|\mathbf{E}|^2)$, where α is the particle's polarizability. This expression can be understood intuitively : the net force exerted on the dipole goes like $\nabla\mathbf{E}.d$, and the distance d between the two charges of the dipole is proportional to this force. We call this force a field gradient force.

Now consider a parallel plate capacitor immersed in a polarizable liquid (figure A.1b). The fields lines decay in strength near the edges of the parallel plates, which induces a field gradient force, which in turn compresses the liquid. The fluid density therefore changes by an amount $\Delta\rho$, and the corresponding change in the relative permittivity of the liquid is : $\Delta\varepsilon_r = (\partial\varepsilon_r/\partial\rho)\Delta\rho$. A change in the field energy density is associated to $\Delta\varepsilon_r$: $\Delta u = (1/2)\varepsilon_0 E^2\Delta\varepsilon_r$ (we write $E^2 = |\mathbf{E}|^2$). Now according to the first law of thermodynamics, this change in energy density must be equal to the work per unit volume exerted by the optical force : $\Delta w = -p_{st}(\Delta\rho/\rho)$, where p_{st} is the "striction" pressure exerted by the optical force. Equalizing Δu and Δw yields :

$$p_{st} = -\frac{1}{2}\varepsilon_0\eta_e E^2 \quad \text{with} \quad \eta_e = \rho\frac{\partial\varepsilon_r}{\partial\rho} \tag{A.1}$$

We were able to link the strictive pressure to the electric field via the derivative of the dielectric constant with density, using energy conservation. Because the fluid has no crystalline structure an isotropic approach is sufficient.

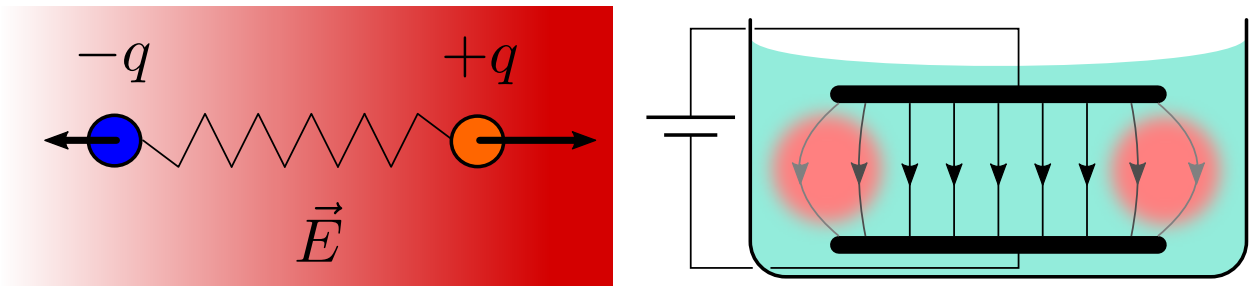

(a) Dipole surrounded by a field gradient. The red hue is deeper where the field is more intense. The net force exerted on the dipole is directed to the right.

(b) Parallel plates capacitor immersed in a polarizable liquid. Elecrtic field gradients produce a local increase of the fluid's pressure (red circle areas).

Figure A.1 – Field gradient force and its consequences

Appendix B

Brief presentation of the Finite Element method

The Finite Element Method (FEM) is a technique aimed at finding numerical approximations to partial differential equations (PDEs). The resolution of Maxwell's equations in frequency domain involves the Helmholtz equation, which is a PDE:

$$\nabla \cdot (\boldsymbol{\nabla} E) + n^2 \left(\frac{\omega}{c}\right)^2 E = 0 \tag{B.1}$$

with $\nabla \cdot$ the divergence operator, $\boldsymbol{\nabla}$ the gradient operator, ω the pulsation of the EM field, c the speed of light in vacuum, and n the index of the material, which is a function of spatial variables. In the following we will write $n^2 \left(\frac{\omega}{c}\right)^2 \equiv k$. The quantity to solve for is E, which is one of the 3 components of the electric field.

Now let's multiply equation B.1 by a function ϕ of the spatial variables, and integrate it on the full space relevant to the problem, Ω. It can be shown (Lax-Milgram theorem) that if E is such that the following equation:

$$\int_\Omega \nabla \cdot (\boldsymbol{\nabla} E)\phi dV + k \int_\Omega E\phi dV = 0 \tag{B.2}$$

is satisfied for *any* function ϕ, then E is solution of equation B.1. This result can be somewhat intuited by considering the case of functions ϕ that are very peaked (like Dirac delta functions). For these functions the integrals are equivalent to an estimation of the integrand value at the position where the Dirac delta is defined, which yields back equation B.1. Requiring B.2 to be satisfied for *any* function ϕ is a strong condition, and it is actually merely required to have B.2 satisfied for a set of functions constituting a basis of the vector space of solutions.

We now write E on such a basis $\{\psi_i\}_{i=[1..N]}$: $E = \sum_i E_i \psi_i$[1]. By choosing $\phi = \psi_j$ for $j = [1..N]$, we end up with a set on N equations (we use $\Delta \equiv \nabla \cdot \boldsymbol{\nabla}$):

$$\forall j, \quad \sum_i E_i \int_\Omega \Delta(\psi_i) \cdot \psi_j dV + \sum_i E_i \int_\Omega \psi_i \cdot \psi_j dV = 0 \tag{B.3}$$

This set of linear equations can be re-written in matrix form:

$$M \cdot e = 0 \tag{B.4}$$

with e the vector containing the E_i components, and M the matrix of elements $m_{ij} = \int_\Omega (\Delta(\psi_i) - \psi_i) \cdot \psi_j dV$.

[1] Here the $\{E_i\}$ are the coefficients of E in the basis, not the different components of $\boldsymbol{E}$ in 3-D space.

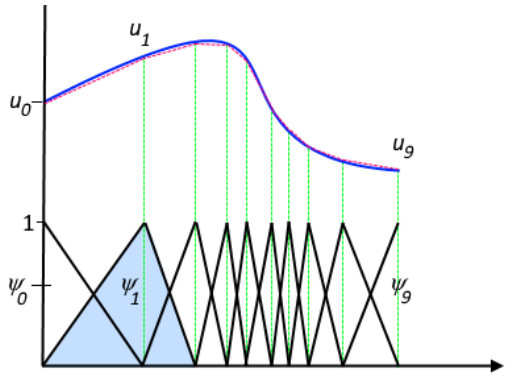

(a) The nodes where the basis functions take nonzero values can be made denser in areas where high derivatives of the solution are expected.

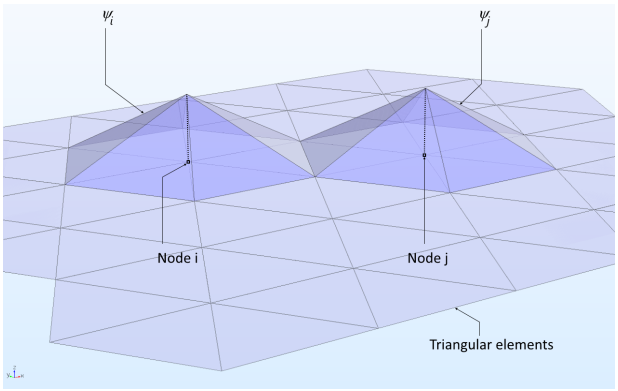

(b) Basis functions for a 2D triangular mesh. Overlaps are non-zero only for basis functions centered on adjacent nodes.

Figure B.1 – Example of finite-support basis functions that can be used for FEM.

Two advantages of FEM are:

- The basis of functions can be chosen to match the geometry of the problem. For instance one can choose a basis of peaked functions that is denser where the derivatives of the solution are expected to be higher (see figure B.1a). Other example: a basis of quadratic piecewise functions can be used to approximate a smooth problem more efficiently.
- If a basis of functions with small finite support is chosen, then overlap integrals are zero except for nodes i and j that are adjacent (see figure B.1b). This results in most elements m_{ij} being zero. In other words the matrix M is sparse, which allows to use efficient algorithms to solve system B.4.

FEM was presented in the example above in the particular case of the Helmholtz equation, but it can be implemented for a variety of PDEs. The function found by solving system B.4 are *approximations* of the solution of B.1. The precision of the approximation typically increases with the dimension of the basis used to represent potential solutions. In the example of finite support peaked functions, an increase of the basis dimension corresponds to a denser mesh.

Appendix C

Perfectly Matched Layers

The previous appendix briefly presented the FEM, which allows to find numerical approximations to PDE solutions. PDEs being differential equations, spatial (and temporal) boundary conditions must be defined (temporal boundary conditions are clearly not a problem when PDEs are solved in frequency domain, as is often the case). For some problems, as for instance the EM distribution in a metallic perfectly reflective cavity, the definition of boundary conditions can be simply implemented (zero electric field in the metal). For problems like the search of eigenmodes of a miniature disk, the boundary conditions are more problematic. Indeed, we know that the electric field is arbitrarily close to zero *at infinity*, but obviously the computation of an infinitely large domain in not realistic. One has to work in a finite domain with boundary condition on its edges. One solution is to use a domain sufficiently large so that the evanescent field from the disk's mode should be very small, and then impose a zero electric field on the boundaries. This will yield reflections that will perturb the solutions anyways, and necessitates to compute a quite large domain.

Another solution is to define a *layer*, called PML, which has the two following properties:

- this layer has a *constitution* that is different from free space, so that waves that normally propagate in free space are absorbed exponentially within this layer.
- the interface between the normal computation space and the PML does not generate reflections.

The first condition can be quite easily fulfilled, by e.g. setting an imaginary part in the impedance of the layer. However this would generate reflections at the interface between the free space and the layer because of the impedance mismatch.

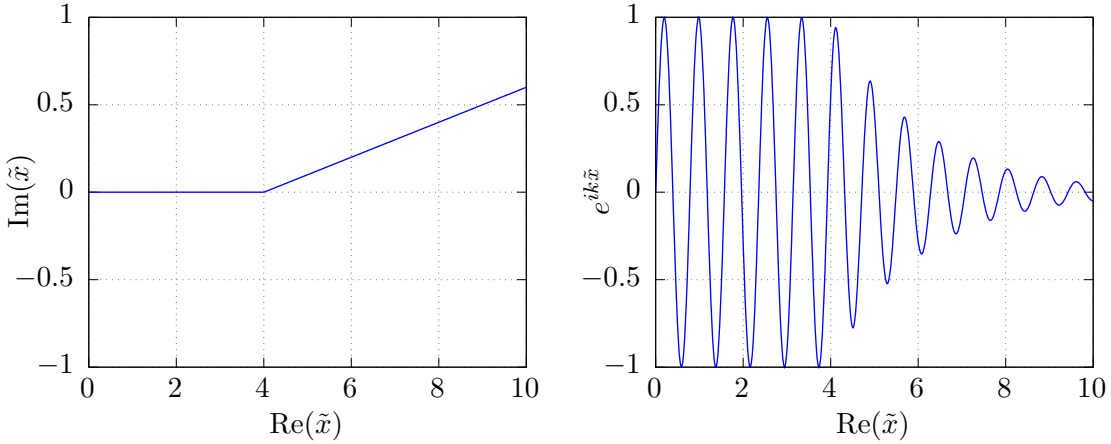

Figure C.1 – Complex contour $\tilde{x}$ and corresponding values for the plane wave $e^{-ik\tilde{x}}$. The semi-space $\mathrm{Re}(\tilde{x}) < 4$ corresponds to the normal simulation space, while $\mathrm{Re}(\tilde{x}) > 4$ corresponds to the PML space.

The starting idea with the PML is to perform an analytic continuation of the spatial variable, *in complex space*. Consider a wave that has a spatial dependency e^{-ikx}. Now we let x evolve in the complex plane, and we write the new complex variable $\tilde{x}$. Figure C.1 left graph represents a given *contour* in the complex plane, for which the imaginary part starts to increase for $\mathrm{Re}(\tilde{x}) > 4$. The right graph represents the values of $e^{ik\tilde{x}}$. It can be seen that the wave is exponentially attenuated in the semi-space $\mathrm{Re}(\tilde{x}) > 4$. This attenuation can in theory be made as strong as desired. The key fact is that $e^{-ik\tilde{x}} = e^{-ikx}$ in the semi-space $\mathrm{Re}(\tilde{x}) < 4$ which is precisely what is required for a good absorbing layer: the solution is not changed in the central space of interest.

However we did explicit a solution here (e^{-ikx}). In a real situation a solution has to be found. We must therefore modify the differential operators within the PML in order to get a solution of the type shown on figure C.1. A complex contour can be parameterized as: $\tilde{x}(x) = x + if(x)$ (in the case of figure's C.1 left graph, f is a linear function). The differential $\partial\tilde{x}$ element can therefore be expressed as: $\partial\tilde{x} = (1 + \frac{df}{dx})\partial x$. The position differential operator must therefore be changed in the PML in the following way:

$$\boxed{\frac{\partial}{\partial x} \rightarrow \frac{1}{1 + i\frac{df}{dx}} \frac{\partial}{\partial x}} \tag{C.1}$$

Several remarks:

- The function f can be made dependent on the frequency ω when solving PDEs in frequency domain, in order to have the same characteristic attenuation in the PML for different frequencies.

- f can be chosen linear or even quadratic or cubic; in theory the attenuation strength in the PML can be set to be arbitrarily high. However, if the numerical sampling (discretization) in the PML is not fine enough, some reflections can occur and perturb the solution in the region of interest.

- The PML presented above is a 1D PML in the $+x$ direction. For 3D problems, 6 PMLs must be implemented: $\pm x, \pm y, \pm z$. The problem of the *angle of incidence* then arises. In 1D the wave has no angle, it merely propagates either in the $+x$ or $-x$ direction. In 2D or 3D though, an infinity of propagation directions are possible: waves do not necessarily propagate in the x, y, or z direction. In this case the PML absorption rate of the wave is proportional to the projection of the wave vector $\boldsymbol{k}$ upon the direction of the PML. So we see that waves with a high angle of incidence are not absorbed by the PML. In practice this is not necessarily a concern if the region of the simulation with the source of waves is far away from the PMLs. In the limit where the ratio of total computation volume over source volume goes to infinity, the maximum angle of incidence for plane waves impinging on a PML in 3D is $\cos^{-1}(1/\sqrt{3}) \approx 55°$.

- An alternative to PMLs would be to increase adiabatically the imaginary part of the impedance in the absorbing layer. The imaginary part would absorb the waves, and its adiabatic increase would avoid reflections. However such a technique has a poor efficiency, because the imaginary part must be increased very slowly in order to avoid reflections.

- Last but not least, a very interesting feature of PMLs is their ability to *quantify* the amount of energy that they absorb. For 2D axisymmetric simulations of WGMs (see figure 2.3), the mode shapes can be computed quite accurately without the use of a PML, by simply defining a perfect conductor condition ($E = 0$) on the boundaries. However in this case the system is closed, so that the energy scattered at infinity cannot be computed. The interest of PMLs resides in the fact that the resolution of frequency domain PDEs with PMLs yields an imaginary part to the eigeinfrequencies of the modes found, which is related to the loss rate of the mode.

Appendix D

Stabilization of the thermo-optic instability

The variation of the index of refraction with the temperature (i.e. the thermo-optic effect) is accountable for an instability that arises when the laser is red-detuned from the cavity resonance (see §7.2.2 for details). This instability sets a limit on the maximum power that can be sent in the optical cavity when detuned on the red flank. Unfortunately, the red flank is the one of interest to us, because optomechanical cooling happens when the laser is red detuned. In order to be able to send more power to the red flank, some attempts were made to actively stabilize the mode.

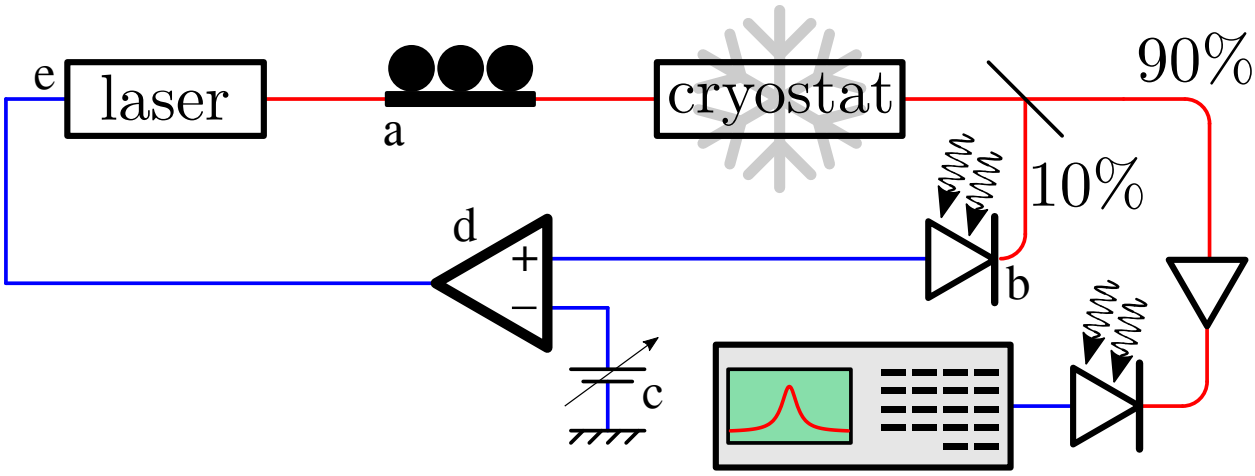

Figure D.1 – Setup for active stabilization on the red flank. **a:** fibered polarization controller. **b:** fast photo-diode. **c:** variable voltage source. **d:** fast electronic difference amplifier. **e:** fast input for laser diode intensity modulation.— telecom optical fiber. — electric co-ax cable.

The general idea of the stabilization technique can be seen on figure D.1. At the output of the cryostat, within which the optomechanical sample is nested, 10% of the signal is directed to a fast photodiode. The photodiode output V_{PD} is compared to a constant setpoint V_{SP} via a difference amplifier, which output V_{amp} is then re-injected in the laser to modulate the current send through the laser diode. The constant setpoint is the transmission level that we wish to lock the system on. Let's assume that the system is stabilized: $V_{\mathrm{PD}} = V_{\mathrm{SP}}$. If the mode starts to drift e.g. to the left (see figure 7.3), then V_{out} increases, so V_{amp} becomes positive. The laser intensity therefore increases, which is what is needed to heat the disk more and push back the mode resonance to the right.

Unfortunately this stabilization was not achieved successfully in practice, for the following reasons:

- Stabilization based on laser intensity control, like presented in the previous paragraph, leads to diverging loops. Indeed, if V_{amp} starts to be positive, then the laser sends more power, which results in a direct increase of V_{SP}, which increases V_{amp}, etc...
- Another possibility is to work at constant intensity, but to change the *wavelength* of the laser output in order to track the unstable flank of the mode.
  - The wavelength of out ECDLs can be tuned by a piezo-mounted mirror, but this tuning is too slow (∼kHz) to follow the the instability.
  - When the laser diode current is modulated, it results in a change of the carrier density, which changes the index of the gain medium and eventually changes the wavelength of emission. This technique is fast (∼ 100 MHz) but the wavelength shift induced by current modulation is too small if compared to the width of our typical optical modes, and therefore it does not have the leverage to bring the mode back. Besides, current modulation changes the intensity linearly so that the problem exposed in the first point dominates.
  - Wavelength modulation can also be obtained by the use of an EOM[1]. This technique resolves a priori all problems. The modulation is in wavelength only (no parasitic intensity changes), it can be very fast (GHz), and the tuning can be done on a range of a few tens of pm, which is enough given the typical 10 pm width of our modes.

  The two first techniques were tried experimentally, without success. The third technique was not tried because it requires two EOMs and a sophisticated RF source, which were not available at the time.
- Even if the EOM technique was implemented, the mode stabilization would remain difficult because of the thermo-optic unstability swiftness. The typical thermal time (i.e. the characteristic time of temperature decay for a 1 µm radius disk) is of the order of a µs. But the time needed for the mode to move (in wavelength) by an amount on the order of its own width is a factor 100 to 1000 shorter[2]. This requires a GHz speed feedback loop, which is difficult to implement electronically. Moreover, the propagation of light and electric signals is another limitation: it takes 1 ns to the light to propagate by ∼30 cm, and the loop of the setup is rather on the order of several meters...

The stabilization on the red flank was therefore not implemented successfully yet. However if the power at which one wishes to stabilize the mode is lower, a feedback with a bandwidth of 10 MHz can be enough. This might allow to send a bit more power in the system, therefore increasing the cooling power.

[1] some schemes involving two EOMs allow to suppress the carrier, so that only the sidebands remain, which wavelength can be varied by changing the frequency of the electronic source applied to the EOM

[2] the mode will typically sweep the full thermo-optic shift, which can be ∼10 nm for a typical power of 1 mW, in 1 µs. The mode will therefore move by its own width (which is typically 10 pm) in 1 ns

Appendix E

Derivation of OMIT transmission expressions

We start from the linearized equations 1.18 for small amplitudes, to which we make two modifications:

- We add a term δs_{in} to equation 1.18a to account for the added sidebands to the input fields.
- We drop the term $F_{\mathrm{th}}(t)$ which is not of interest here, in other words we suppose that the temperature of the mechanical bath is zero.

The linearized equations are therefore (in the reference frame spinning at ω_L):

$$\delta\dot{a}(t) = [i\bar{\Delta} - \kappa/2]\delta a(t) + ig_{\mathrm{om}}\bar{a}\delta x(t) + \sqrt{\kappa_{\mathrm{ext}}}\delta s_{\mathrm{in}}(t) \tag{E.1a}$$

$$\delta\ddot{x}(t) = -\Omega_{\mathrm{m}}^2\delta x(t) - \Gamma_{\mathrm{m}}\delta\dot{x}(t) + \frac{g_{\mathrm{om}}}{m\omega_0}[\bar{a}^*\delta a(t) + \bar{a}\delta a^*(t)] \tag{E.1b}$$

We now suppose an input field of the form $\delta s_{\mathrm{in}}(t) = s_p e^{-i\Omega t}$, with $\Omega = \omega_p - \omega_L$. This expression accounts for the sideband of the input field at frequency $\omega_L + \Omega$. Now the *intracavity* field will respond to this excitation at Ω with a priori two sidebands at $\pm\Omega$. We therefore suppose that $\delta a(t)$ and $\delta x(t)$ can be respectively expressed as:

$$\delta a(t) = A^- e^{-i\Omega t} + A^+ e^{+i\Omega t} \tag{E.2a}$$

$$\delta x(t) = X e^{-i\Omega t} + X^* e^{+i\Omega t} \tag{E.2b}$$

A^+ and A^- are the coefficients for the two sidebands of the intracavity fields. $a(t)$ is derived from the average value of an operator which is not hermitian, so in general $\delta a(t) \neq \delta a^*(t)$, and therefore no simple relation links A^+ to A^-. $x(t)$ is derived from an hermitian operator, therefore $\delta x(t) = \delta x^*(t)$, and the two coefficients are therefore each other's complex conjugate. Inserting expressions E.2 (to which we add the expression $\delta a^*(t) = (A^+)^* e^{-i\Omega t} + (A^-)^* e^{+i\Omega t}$) in equations E.1 yields 6 equations, once sorted by positive and negative frequency terms. The set for negative frequency terms is:

$$[-i(\bar{\Delta} + \Omega) + \kappa/2]A^- = -ig_{\mathrm{om}}\bar{a}X + \sqrt{\kappa_{\mathrm{ext}}}s_p \tag{E.3a}$$

$$[-i(\bar{\Delta} - \Omega) + \kappa/2](A^+)^* = +ig_{\mathrm{om}}\bar{a}X \tag{E.3b}$$

$$m_{\mathrm{eff}}(\Omega_{\mathrm{m}}^2 - \Omega^2 - i\Gamma_{\mathrm{m}}\Omega)X = -\frac{g_{\mathrm{om}}}{\omega_0}(A^- + (A^+)^*) \tag{E.3c}$$

The system can be solved to yield:

$$A^- = \frac{1 + if^-(\Omega)}{-i(\bar{\Delta} + \Omega) + \kappa/2 + 2\bar{\Delta}f^-(\Omega)}\sqrt{\kappa_{\mathrm{ext}}}s_p \quad \text{with} \quad \begin{array}{ll} f^-(\Omega) & = g_{\mathrm{om}}^2\bar{a}^2\frac{\chi^-(\Omega)}{i(\bar{\Delta}-\Omega)+\kappa/2} \\ \chi^-(\Omega) & = \frac{1}{m_{\mathrm{eff}}(\Omega_{\mathrm{m}}^2 - \Omega^2 - i\Gamma_{\mathrm{m}}\Omega)} \end{array} \tag{E.4}$$

The set of equations for positive frequency terms (not shown here) can be solved to yield:

$$A^+ = \frac{if^+(\Omega)}{i(\Omega-\bar{\Delta})+\kappa/2+2\bar{\Delta}f^+(\Omega)}\sqrt{\kappa_{\rm ext}}s_p \quad \text{with} \quad \begin{array}{ll} f^+(\Omega) & = g_{\rm om}^2\bar{a}^2\frac{\chi^+(\Omega)}{i(\bar{\Delta}+\Omega)+\kappa/2} \\ \chi^+(\Omega) & = \frac{1}{m_{\rm eff}(\Omega_{\rm m}^2-\Omega^2+i\Gamma_{\rm m}\Omega)} \end{array} \tag{E.5}$$

We can therefore find the expressions for the sidebands transmissions through the OM system. In practical experiments though, two sidebands are simultaneousy generated at frequencies $\omega_L+\Omega$ and $\omega_L-\Omega$. In the good cavity limit one of the sidebands is filtered out, but in bad cavity limit both sidebands interact with the cavity, and a full expression must be derived in order to fit experiments. The set of equations E.3 should be considered again, but this time with the input term $\sqrt{\kappa_{\rm ext}}s_p$ situated in the equation E.3b. In the end we get 4 sidebands terms, corresponding to the two sidebands generated in the cavity for *each* of the sidebands generated by the EOM. The beating of these 4 sideband terms with the pump must be evaluated to yield the exact power that is detected by our electrical spectrum analyzer.